

**X-ray Observations of MeV Electron Precipitation with a Balloon-Borne
Germanium Spectrometer**

by

Robyn Margaret Millan

B.A. (University of California) 1995
M.A. (University of California) 1999

A dissertation submitted in partial satisfaction of the
requirements for the degree of
Doctor of Philosophy

in

Physics

in the

GRADUATE DIVISION
of the
UNIVERSITY of CALIFORNIA at BERKELEY

Committee in charge:

Professor Robert P. Lin, Chair
Professor Forrest Mozer
Professor Imke de Pater

Spring 2002

The dissertation of Robyn Margaret Millan is approved:

Chair

Date

Date

Date

University of California at Berkeley

Spring 2002

**X-ray Observations of MeV Electron Precipitation with a Balloon-Borne
Germanium Spectrometer**

Copyright Spring 2002

by

Robyn Margaret Millan

Abstract

X-ray Observations of MeV Electron Precipitation with a Balloon-Borne
Germanium Spectrometer

by

Robyn Margaret Millan

Doctor of Philosophy in Physics

University of California at Berkeley

Professor Robert P. Lin, Chair

The MAXIS (MeV Auroral X-ray Imaging and Spectroscopy) balloon payload was launched on a long duration balloon from McMurdo, Antarctica on Jan. 12, 2000. The high spectral resolution germanium spectrometer aboard MAXIS detected nine X-ray bursts with significant flux extending above 0.5 MeV during the 18 day flight. The X-rays are bremsstrahlung produced by precipitating electrons and the events are characterized by an extremely flat X-ray spectrum ($\sim E^{-2}$) similar to the first MeV event discovered in 1996, indicating relativistic parent electrons. The bursts were detected between magnetic latitudes 58° - 68° (IGRF L-values of 3.8-6.7) with durations varying from several minutes to several hours and occurred only in the late afternoon/dusk sectors (14:30-00:00 MLT) while softer precipitation was detected at all magnetic local times. In addition, the MeV events were associated with substorm activity and several events showed Ultra Low Frequency (mHz)

modulation of the X-ray count rate. Spacecraft and ground-based observations indicate the presence of ULF wave activity near the time and location of the events which may be causing the modulation by some mechanism that is not understood.

The MeV events are well modeled by a very flat exponential precipitating electron distribution and the average flux of precipitating electrons with $E \geq 0.5$ MeV is estimated to be $\sim 360 \text{ cm}^{-2}\text{s}^{-1}$. This corresponds to about 5×10^{25} precipitated electrons in this latitude range during the eight day observing interval compared to $\sim 2 \times 10^{25}$ trapped 0.5-3.6 MeV electrons estimated using GPS electron measurements. The MAXIS observations indicate that these electron precipitation events are common and may be the primary loss mechanism for outer zone relativistic electrons. Individual events were also compared with measurements of the trapped electrons from which it is estimated that only a few percent of the loss cone is being filled by the mechanism acting to precipitate the particles. This indicates that if the mechanism is wave-particle interaction, it is not in the strong diffusion regime.

Looking towards the future, a Compton telescope for imaging MeV X-ray bursts at high energies is also investigated. Such an instrument may also be used to measure polarization and thus may provide a method for inferring the precipitating electron pitch angle distribution.

Professor Robert P. Lin
Dissertation Committee Chair

To the memory of Bob Campbell.

Contents

List of Figures	vii
List of Tables	xii
1 Introduction	1
1.1 The Magnetosphere and Geomagnetic Activity	3
1.1.1 Overview of the Magnetosphere	3
1.1.2 Magnetic Reconnection	7
1.1.3 Magnetospheric Substorms	8
1.1.4 Geomagnetic Storms	10
1.2 The Earth's Radiation Belts	12
1.2.1 Properties of the Radiation Belts	12
1.2.2 Adiabatic Invariants	14
1.2.3 Spacecraft Measurements	20
1.2.4 Acceleration Mechanisms	22
1.2.5 Loss of Trapped Particles	26
1.3 Energetic Electron Precipitation	27
1.3.1 Observations	27
1.3.2 Precipitation Mechanisms	30
1.4 Discovery of Terrestrial MeV X-rays	34
1.4.1 Observations	34
1.4.2 Interpretation	34
1.5 Scope of Research	38
2 The MAXIS Balloon Experiment	40
2.1 Introduction	40
2.2 Instrumentation	41
2.2.1 Germanium Spectrometer	42
2.2.2 X-ray Imagers	47
2.2.3 BGO Scintillator	47
2.3 Power System	48
2.4 Housekeeping Data	48

2.5	Data Acquisition	49
2.5.1	Main Flight Computer	49
2.5.2	Telemetry	49
2.5.3	Ground Support Equipment	50
2.6	GeV Calibration	51
2.6.1	Detector Bias	51
2.6.2	Effective Area	52
2.6.3	Detector Scans	53
2.6.4	Environmental Tests	54
2.7	Flight Summary	57
2.8	Data Analysis	58
2.8.1	Background Selection	61
2.8.2	Gain Calibration	61
2.8.3	Live Time	63
2.8.4	Instrument and Atmospheric Response Matrices	65
3	MAXIS Observations of MeV Electron Precipitation	67
3.1	Event Classification	72
3.2	Magnetic Local Time Distribution	80
3.3	Magnetic Latitude and L Distribution	82
3.4	Location with respect to the Trapping Boundary	84
3.5	Location with respect to the Plasmapause	87
3.6	Relation to Geomagnetic Activity	88
3.7	Summary	94
4	Spectral Modeling of MAXIS MeV Events	97
4.1	Description of the Model	98
4.1.1	Ionization Losses	98
4.1.2	Bremsstrahlung Production	99
4.1.3	Atmospheric and Instrument Response	100
4.2	Forward-Folding Method	101
4.2.1	Some Examples and Discussion	101
4.2.2	Model Results for MAXIS MeV Events	111
4.2.3	Average Precipitating Relativistic Electron Flux	116
4.3	Direct Inversion Method	120
4.3.1	Direct Inversion results for MAXIS MeV Events	125
4.4	Comparison with Measurements of Trapped Electrons	132
4.5	Summary	138
5	Temporal Analysis	139
5.1	Fourier Analysis	141
5.1.1	Overview	141
5.1.2	Example: Kiruna Event	142
5.1.3	Limitations of the Fourier Transform	145
5.2	Wavelet Analysis	146

5.2.1	Overview: Time-Frequency analysis	146
5.2.2	Analytic Example	149
5.2.3	Example: The Kiruna Event	150
5.2.4	Wavelet Analysis of MAXIS MeV Events	152
5.3	Spacecraft and Ground-Based Observations	158
5.4	Mechanisms for Modulating Precipitation	163
6	A Compton Telescope for Imaging MeV Electron Precipitation	166
6.1	Characteristics of the Compton Telescope	168
6.1.1	Angular Resolution	170
6.1.2	Field of View	173
6.2	Monte Carlo Simulation of a Compton Telescope	173
6.2.1	Instrument Configuration	173
6.2.2	Effective area	174
6.2.3	Angular Resolution	177
6.2.4	Field of View	178
6.2.5	Instrument Background	179
6.2.6	Instrument Sensitivity	182
6.2.7	Other Configurations	184
6.3	Polarization	185
6.3.1	Measuring Polarization	186
6.3.2	Polarization of an Overhead Source	188
6.3.3	Electron Scattering	192
7	Conclusion and Future Work	195
7.1	Summary	195
7.2	Future Work	197
7.2.1	Relation to Other Types of Precipitation	197
7.2.2	Other Observations	199
Bibliography		200
A Geomagnetic Activity Indices		210
A.1	Indices	210
B Frequently Used Acronyms		212

List of Figures

1.1	Schematic of Earth's magnetosphere.	4
1.2	Equipotentials of the combined convection and corotation electric fields. The separatrix between open and closed equipotentials defines the plasmapause [Spjeldvik and Rothwell, 1985].	6
1.3	The sequence of a substorm [Tsurutani, 2001].	9
1.4	AU and AL indices during a substorm. The phases of the substorm are identified by a change in slope of the AL index [Kivelson and Russell, 1995].	10
1.5	Dst index during a geomagnetic storm [Tsurutani, 2001].	11
1.6	Schematic of the earth's radiation belts [Daglis, 2001b].	12
1.7	Radial profiles of the electron and ion equatorial omni-directional flux (from Panasyuk [2001])	13
1.8	The motion of a trapped particle [Spjeldvik and Rothwell, 1985].	15
1.9	Frequencies of gyration, bounce and drift motion for electrons and protons as a function of energy [Schulz and Lanzerotti, 1974].	19
1.10	GOES 8 >2 MeV electron fluence [Baker et al., 1997].	20
1.11	Relativistic electron flux as measured by the CPA instrument on LANL 1984-129 during a geomagnetic storm along with Dst for the same period [Horne, 2001].	21
1.12	Electron interacting with a whistler wave [Walt, 1996].	25
1.13	Location of whistler and EMIC waves in local time and in relation to plasmapause [Summers et al., 1998].	33
1.14	Top panel: The X ray count rate for the Kiruna event. Also shown residual countrate after subtracting smoothed data. Middle panel: Power spectrum of count rate as a function of time. Bottom panel: Spectral hardness [Foat et al., 1998].	35
1.15	Count spectrum and Photon spectrum from Kiruna event with model spectra superposed [Foat et al., 1998].	36
2.1	The MAXIS gondola during payload integration. The instruments were mounted on the top platform. The GeD and dewar are on the right, the X-ray imagers and BGO are under the foam box on the left.	43

2.2	(A) Close-up of Imagers and BGO: PXRI(right), CXRI(left) and BGO (center). (B) The GeD	44
2.3	Determination of detector operating voltage: photopeak position for 835 keV ^{54}Mg line as a function of bias voltage.	51
2.4	Detector effective area as a function of energy. The solid line shows the modeled response.	53
2.5	Horizontal scan across top of detector at 17.6 keV. Contour levels show counts in photopeak at each x-y position across the detector in 0.5 cm increments.	54
2.6	Vertical scan across detector at several different gamma ray energies. The x-axis shows position in mm with the origin located at the detector center and negative positions refer to the top half.	55
2.7	Test pulse PHA channel number as a function of temperature for three cold and two hot thermal cycles.	56
2.8	Inflation and launch of the MAXIS balloon.	58
2.9	Trajectory of MAXIS balloon flight on an orthographic plot of the Antarctic continent with X-ray events indicated by asterisks and triangles. Also shown are lines of geographic longitude and latitude (dashed) and magnetic latitude (solid) every 10°.	59
2.10	Top panels: GeD count rate for Jan.12-Jan.27, 2000. MeV events are indicated by arrows and described in Chapter 3. Bottom panels: CGM latitude and Dst index during the flight.	60
2.11	Example background spectrum	61
2.12	Temperature profile of GeD electronics during the first four days of the MAXIS flight.	62
2.13	Gain and offset as a function of temperature. Solid line is quadratic fit. . .	62
2.14	Atmospheric depth measured every hour. The points blow 36 km were measured during the ascent of the balloon	66
3.1	GeD count rate on Jan.15-17, 2000 in two energy channels: 20-1300 keV (top) and 180-1300 keV (bottom).	68
3.2	GeD count rate on Jan.18-20, 2000 in two energy channels: 20-1300 keV (top) and 180-1300 keV (bottom). MeV events are labeled and indicated by arrows.	69
3.3	GeD count rate on Jan.21-23, 2000 in two energy channels: 20-1300 keV (top) and 180-1300 keV (bottom).	70
3.4	GeD count rate on Jan.24-26, 2000 in two energy channels: 20-1300 keV (top) and 180-1300 keV (bottom).	71
3.5	Background subtracted spectra for an MeV event and a soft event. The lead collimator lines are still evident in the background subtracted MeV event spectrum since the line strength is actually increased by the MeV event.	73
3.6	Spectrum and count rate for events on January 25, 2000. The short spike evident in the 180-1300 keV count rate is the MeV event (crosses) and occurred during a period of low energy precipitation (diamonds).	75
3.7	Count spectra and power law index between 100-180 keV	76
3.8	Count spectra and power law index between 100-180 keV	76
3.9	Count spectra and power law index between 100-180 keV	77

3.10	Count spectra and power law index between 100-180 keV	77
3.11	Count spectra and power law index between 100-180 keV	78
3.12	Count spectra and power law index between 100-180 keV	78
3.13	Spectral power law index (PLI) for each event and histogram for all of the 25 MAXIS event intervals	79
3.14	Magnetic local time distribution of 25 MAXIS events. MeV events are represented by an asterisk and soft events by triangles (the 1996 Kiruna event is also included).	81
3.15	Occurrence probability as a function of magnetic latitude and magnetic local time for MeV events (top) and soft events (bottom). Grey indicates no data.	83
3.16	Electron flux measured in four energy channels for four GPS passes through the radiation belts. GPS data were provided courtesy of R. Friedel.	84
3.17	Trapping boundary location in four energy channels as measured by GPS. Asterisks mark the MeV X-ray event times and locations.	86
3.18	L-value of the inner edge of the plasmapause (solid line) and where density has fallen by a factor ~ 50 (dashed line) determined using POLAR EFI data. The MeV event locations are shown with asterisks.	88
3.19	AL index from Jan 17-26,2000. The shaded regions indicate when the balloon was between ~ 1500 -0000 MLT and stars show the location of the MeV events	89
3.20	GeD count rate (top) AL index (middle) and horizontal component of surface magnetic field conjugate to balloon (bottom) on January 19, 2000. The Greenland ground-based magnetometer array is operated by the Danish Meteorological Institute (DMI). Magnetometer data for this study were provided by J. Watermann, DMI.	91
3.21	LANL electron flux 50-315 keV.	93
3.22	GeD count rate and AL index on January 22-23,2000. MeV events are indicated by arrows.	94
3.23	LANL proton flux	95
3.24	GeD count rate and AL index on January 24-26,2000. MeV events are indicated by arrows.	96
4.1	Equilibrium electron flux for monoenergetic, exponential and flat initial electron distributions.	103
4.2	Bremsstrahlung spectra for monoenergetic, exponential and flat initial electron distributions.	105
4.3	Equilibrium electron flux for monoenergetic, power law ($\alpha = 6$) and power law with a lower energy cutoff of 400 keV initial electron distributions.	106
4.4	Bremsstrahlung spectra for monoenergetic, power law ($\alpha = 5$) and power law with a lower energy cutoff of 400 keV initial electron distributions.	107
4.5	Simulated count spectra for an event similar to the Kiruna event. Models shown here use monoenergetic (1.5 MeV) and broken power law ($\sim E^{-3}$, 0.75-1.5 MeV, and E^{-6} above 1.5 MeV with a low energy cut-off at 1 MeV) electron distributions.	109

4.6 Simulated count spectra for an event similar to the Kiruna event. Models shown here use monoenergetic (1.5 MeV) and Flat (up to 2 MeV) electron distributions.	109
4.7 Simulated count spectra for an event similar to the Kiruna event. Models shown here use monoenergetic (1.5 MeV) and exponential (with e-folding at 600 keV) electron distributions.	110
4.8 Observed and model count spectra. Q is the chi-square probability described in the text.	113
4.9 Observed and model count spectra	114
4.10 Observed and model count spectra	115
4.11 Observed and model count spectra	115
4.12 GeD (crosses) and BGO (diamonds) photon spectra on Jan. 19, 2000.	121
4.13 Combined GeD and BGO photon spectrum.	122
4.14 Equilibrium (bremsstrahlung-producing) electron spectrum.	124
4.15 Precipitating electron spectrum.	125
4.16 Combined GeD and BGO photon spectrum.	126
4.17 Equilibrium (bremsstrahlung-producing) and precipitating electron spectra.	127
4.18 Combined GeD and BGO photon spectrum	128
4.19 Equilibrium (bremsstrahlung-producing) and precipitating electron spectra.	129
4.20 Combined GeD and BGO photon spectrum.	130
4.21 Equilibrium (bremsstrahlung-producing) and precipitating electron spectra.	131
4.22 GPS electron flux in four energy channels averaged over L=5.1-5.3 on January 19, 2000.	132
4.23 GPS electron flux averaged over L=5.1-5.3 on January 19, 2000 from 13:10-18:00 UT (bar with diamonds) and precipitating electron flux (crosses).	133
4.24 Scattering efficiency as a function of energy.	134
4.25 Scattering efficiency as a function of energy.	135
4.26 Scattering efficiency as a function of energy	136
4.27 Scattering efficiency as a function of energy	136
 5.1 X-ray count rate (top), Fourier power spectrum (middle) and wavelet power spectrum (bottom) for the Kiruna Event. The 3σ level corresponds to a normalized power of 5.8.	144
5.2 Morlet wavelet in time and frequency domains.	148
5.3 X-ray count rate (top) and wavelet power spectrum for periods between 20-200 seconds (bottom) for the Kiruna event.	151
5.4 X-ray count rate (top) and wavelet power (in units of variance) (bottom) for one 4096 point background interval.	153
5.5 Average wavelet power (crosses) shown with theoretical curve for white noise (solid line).	154
5.6 X-ray count rate (top) and wavelet power spectrum for periods between 1-35 s (middle) and 20-200 s (bottom) for event on Jan. 19, 2000.	155
5.7 X-ray count rate (top) and wavelet power spectrum for periods between 1-35 s (middle) and 20-200 s (bottom) for the event on Jan. 20, 2000.	157

5.8	POLAR trajectory over Antarctica and balloon location (star) on January 19, 2000.	158
5.9	POLAR EFI data transformed into frame where z is in the direction of the magnetic field. The x and y directions are arbitrary.	160
5.10	Raw electric field data (unrotated and without baseline removed) and it's wavelet power spectrum (from POLAR EFI). In this case, the z-direction is measured in the spacecraft frame not with respect to the magnetic field.	161
5.11	X-ray count rate (top), 10 minute bandpass-filtered (H-component) magnetometer data (middle) and normalized wavelet power for the magnetometer data (bottom). The Greenland ground-based magnetometer array is operated by the Danish Meteorological Institute (DMI). Magnetometer data for this study were provided by J. Watermann, DMI.	162
6.1	Schematic of a Compton telescope [Boggs, 1998].	168
6.2	Uncertainty in the reconstructed scattering angle for a 1 MeV photon as a function of scattering angle due to energy resolution of detector (assumed to be 2 keV).	170
6.3	Uncertainty in reconstructed scattering angle for a normally incident 1 MeV photon as a function of scattering angle due to spatial resolution of detector ($x,y=1.5$ mm, $z=0.5$ mm). Shown for three different values of distance, r , between the first and second scatter.	171
6.4	Schematic of model instrument geometry. Germanium detectors are shaded with angled lines and cold plates are shaded gray. A normally incident 1 MeV photon is also shown.	174
6.5	Effective area for three cases: all photopeak (fully absorbed) events, events with 3 or more interactions, and events with 3+ interactions that have a 1 cm minimum lever arm (MLA).	175
6.6	The ARM (angular resolution measure) distribution for normally incident 1 MeV photons.	177
6.7	Effective area at 1 MeV as a function of incident angle. Only events with 3 or more interactions and 1 cm minimum lever arm were included.	178
6.8	Background component for zenith angles 0° - 70° including all events (solid), unrejected events that satisfy 3+ interaction site, 1 cm minimum lever arm, and valid event requirements (dashed) and unrejected events within 2.5° of zenith (dot-dashed). Calculated assuming 5gcm^{-2} atmospheric depth in Antarctica.	179
6.9	Total background (solid) and background components for different zenith angle ranges at 5 gcm^{-2} atmospheric depth in Antarctica assuming an on-axis point source.	181
6.10	Mean modulation amplitude as a function of energy for normally incident photons.	186
6.11	Fractional polarization sensitivity as a function of energy for an on-axis source.	187
6.12	Total bremsstrahlung cross section as a function of photon emission angle for photon energies ranging from 0.1 to 0.9 of the initial electron energy (1 MeV).	188

6.13 Fractional polarization as a function of emission angle for different values of the emitted photon energy (expressed as a fraction of initial electron energy) [Lichtenberg et al., 1975].	189
---	-----

List of Tables

1.1	Plasma properties of main regions of the magnetosphere.	5
1.2	Precipitation Mechanisms and their characteristics (courtesy of K.R.Lorentzen)	31
2.1	MAXIS Instrument Specifications	42
3.1	MAXIS event intervals with peak count rate > 500 cps	72
3.2	K _p and L-value calculated from T89 magnetic field model for MeV events. .	82
4.1	Best fit and acceptable range of fit parameters (in keV) for MeV events (E signifies exponential, F flat, and M monoenergetic). Also listed is >500 keV electron fluence from best fit model and the range of model electron fluence from all acceptable models.	112

Acknowledgements

Many thanks to my dissertation committee, especially my advisor, Robert P. Lin for his undying patience and optimism. I would also like to thank David Smith for answering so many of my questions and for being a good friend, Steve Boggs, Henry Primbsch and Steve McBride for sharing advice and stories about ballooning and Marsha Colby for organizing all those Wednesday balloon lunches. My deepest gratitude goes to the MAXIS team, especially Kirsten Lorentzen, Michael McCarthy and Rick Sterling for devoting the many sleepless nights that made MAXIS a success, and Stuart Banks for teaching me more than I ever wanted to know about pipe fittings, vacuum grease and fiberglass. Last but not least, thanks to my family and friends, especially Julie who has always been there for me and Karl for your love and support.

This work was supported by NASA grants, NGT5-30110, FDNAG5-6870-1/99, and NAG5-10428-02/02. The University of Washington contributions to MAXIS were supported by the National Science Foundation.

Chapter 1

Introduction

In the region of space surrounding the earth lie the Van Allen radiation belts, where very energetic particles are trapped by Earth's magnetic field. The radiation belts were discovered in 1958 at the dawn of the Space Age and since that time, an increasing number of satellites pass through the region as they orbit the earth. Here they are bombarded by the energetic particles which pose a hazard both to satellite instrumentation and also to astronauts. With our increasing dependence on satellites, understanding the radiation belts and the dynamics of these energetic particles has become a topic of great interest. Despite the more than forty years since the radiation belts were discovered, the processes that accelerate electrons to relativistic energies are not understood, but the evidence points to them being accelerated near the earth. This is quite remarkable; Earth, a small benign planet, can accelerate particles to relativistic energies very quickly. Understanding these processes is important for understanding not only the radiation belts, but particle acceleration in general, a process ubiquitous throughout the universe.

In 1957, before the discovery of the radiation belts, X-rays were detected by a balloon-borne particle detector launched near Minneapolis; they were thought to be bremsstrahlung produced by energetic electrons as they enter the earth's atmosphere and collide with neutrals. Since then, many more balloon observations of X-rays up to a few hundred keV and peaking at energies \sim tens of keV have been made. The lower energy X-rays were thought to be produced by the electron population that also produces the Aurora Borealis and Aurora Australis in the northern and southern hemispheres but the \sim 100 keV particles probably come from the radiation belts. On August 20, 1996 an X-ray burst with energies extending above 1 MeV and one of the hardest spectra ever detected for a terrestrial source ($\sim E^{-1.7}$ below 150 keV) was observed by a LN₂-cooled germanium spectrometer carried by a high altitude balloon launched from Kiruna, Sweden. The balloon was launched as part of a French balloon campaign, InterBOA, to study aspects of the aurora including ionospheric currents and auroral X-rays. However, the X-rays produced in the MeV burst were so energetic that the electrons producing the radiation must have been relativistic. The event was well described by 1.7 MeV electrons whose most likely source is the radiation belts.

The observation of such energetic terrestrial X-rays was completely unexpected and demonstrated that balloons could provide a tool for studying the loss of relativistic electrons from the radiation belts. The observations also raised many questions including: What mechanism is responsible for scattering the electrons into the atmosphere? How common are the MeV X-ray bursts and under what geomagnetic conditions do they occur? Is there a relation between these X-ray bursts and the relativistic electron precipitation (REP)

events and electron microbursts seen by low-Earth-orbiting spacecraft? This dissertation describes a long-duration balloon experiment, MAXIS, that was designed to search for MeV X-ray bursts and address these questions. In order to understand the significance of the MAXIS observations it is necessary to first give a brief introduction to the earth's magnetosphere. In this chapter, the important regions of the magnetosphere are introduced along with an overview of geomagnetic activity. We then focus in Section 1.2 on the part of the magnetosphere most relevant to the current topic: the radiation belts. The concept of particle motion in the radiation belts is introduced along with a review of observations and some proposed mechanisms for creating and depleting the radiation belts. Finally, in Section 1.4, the observations of the 1996 Kiruna MeV X-ray burst are described in detail. Descriptions of some of the geomagnetic indices commonly used to identify and measure geomagnetic activity can be found in Appendix A.

1.1 The Magnetosphere and Geomagnetic Activity

1.1.1 Overview of the Magnetosphere

The earth's internal magnetic field is nearly dipolar and tilted by about 11° with respect to the spin axis of the earth. Near the earth, particle motion is dominated by the terrestrial magnetic field and this region is known as the *magnetosphere*. Outside the magnetosphere, the *solar wind*, a tenuous plasma composed mainly of protons and electrons with average densities $\sim 7\text{cm}^{-3}$, flows away from the sun reaching an average speed of 400 km/s at 1 AU [Kivelson and Russell, 1995]. Fast solar wind streams also flow from coronal hole and polar regions on the sun at typical speeds of 800 km/s. The solar magnetic field

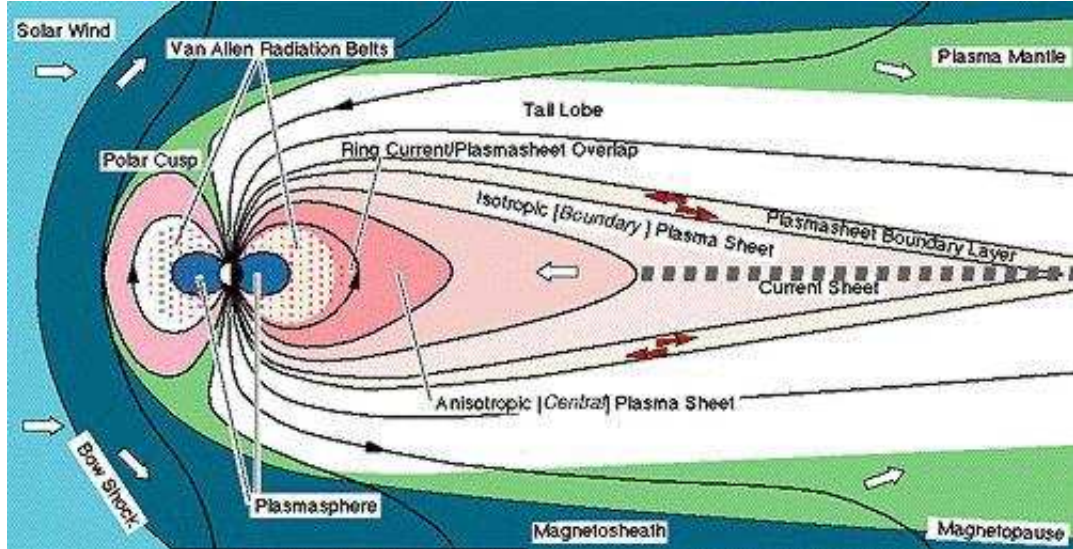


Figure 1.1: Schematic of Earth’s magnetosphere.

is “frozen into” the solar wind plasma meaning the field is dragged along with the plasma as it flows out into the solar system. This interplanetary magnetic field (IMF) lies mostly in the ecliptic plane and has an average strength of $\sim 7\text{nT}$ at the earth’s distance. As we will see, both the strength and orientation of the IMF are important for the coupling of the solar wind to the magnetosphere and the resulting geomagnetic activity.

When the supersonic solar wind encounters the terrestrial magnetic field, a shock called the bow shock, forms upstream converting the energy of the flow into thermal energy and slowing the solar wind to subsonic speeds. The solar wind can then be deflected around the earth. The region behind the bow shock is filled with shocked plasma and is called the magnetosheath. The *magnetopause* is the boundary of the magnetosphere and occurs to zeroth approximation where there is pressure balance between the solar wind ram pressure and the magnetic pressure of the earth’s field. This boundary is a current sheet that

Region	Density (cm^{-3})	T_e	T_p	B (nT)
Magnetosheath	8	25 eV	150 eV	15
Tail lobes	0.01	50 eV	300 eV	20
Plasma sheet	0.3	0.6 keV	4.2 keV	10
Plasmasphere	10^3	~ 1 eV	~ 1 eV	500

Table 1.1: Plasma properties of main regions of the magnetosphere.

separates the regions where the earth's field and the IMF are frozen into their respective plasmas. The magnetopause current sheet increases the field strength on the earthward side of the boundary thus compressing the field on the dayside of the earth. As the solar wind flow is deflected around the earth, momentum is transferred to the magnetospheric plasma causing it to flow away from the earth forming the *geomagnetic tail* on the nightside. Figure 1.1 shows a schematic of the magnetosphere and labels the different regions which are identified by differing plasma properties (summarized in Table 1.1).

The outer magnetosphere consists of the tail lobes where the density is very low ($\sim 0.1 \text{ cm}^{-3}$), and the plasma sheet which separates the northern and southern tail lobes. In the plasma sheet, hot plasma ($\sim \text{keV}$) balances the magnetic pressure of the lobes. Since there is a discontinuity in the field (as the field lines are dragged out from the earth) the plasma sheet is also a current sheet with the “cross-tail current” flowing across the tail from dawn-to-dusk and a return current flowing around the tail lobes. A dawn-to-dusk convection electric field maintains the cross-tail current and the strength of this convection electric field depends on the solar wind velocity and the north-south component of the magnetic field.

Two plasma populations lie in the inner magnetosphere ($< 8 R_E$); the first of these, called the plasmasphere, is made up of cold (\sim few eV) plasma of ionospheric origin that

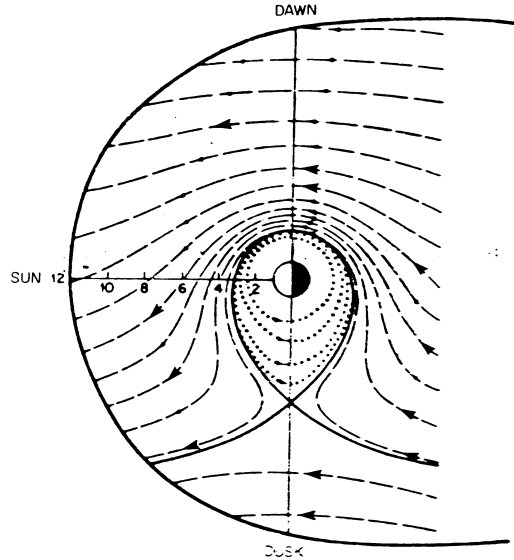


Figure 1.2: Equipotentials of the combined convection and corotation electric fields. The separatrix between open and closed equipotentials defines the plasmapause [Spjeldvik and Rothwell, 1985].

corotates with the earth. The rotating magnetic field of the earth creates a radial electric field in the non-rotating frame and the superposition of this “corotation” electric field and the dawn-to-dusk convection field gives rise to closed equipotentials near the earth with a bulge near dusk (Figure 1.2). Further from the earth, the equipotentials are open and intersect the magnetopause. The boundary between open and closed regions is known as the plasmapause. Plasma inside the plasmapause is trapped and across this boundary, the plasma density drops by a factor $\sim 10^3$. During periods of high activity, the convection electric field strength is increased and the plasmapause moves inward.

The second plasma population of the inner magnetosphere is the energetic population that makes up the radiation belts and the ring current. For particles with energies above ~ 200 keV, the magnetospheric electric fields are not so important; the motion of

these particles is dominated by magnetic effects such as gradient and curvature drifts which will be discussed in detail in Section 1.2.2 [Schulz and Lanzerotti, 1974]. A ring current is produced by electrons and ions as they gyrate and oppositely gradient/curvature drift around the earth and the effects of this current can be measured as a decrease in the horizontal component of the magnetic field at the surface of the earth near the equator. The depression in the field is proportional to the total energy in the ring current and is mostly due to ions with energy between 15-250 keV [Daglis, 2001b]. During times of high geomagnetic activity, the strength of the ring current increases, further depressing the equatorial magnetic field strength. Coexisting with the ring current, the radiation belts consist of very energetic particles or “penetrating radiation” which pose a hazard to both spacecraft and humans in the near-earth environment. Properties of the radiation belts will be discussed further in Section 1.2.

1.1.2 Magnetic Reconnection

As mentioned previously, properties of the solar wind such as the IMF strength and direction as well as the solar wind velocity and density are important in determining how much energy and plasma are transferred from the solar wind to the magnetosphere. This coupling reveals itself on earth in many forms including the aurora, surface magnetic field fluctuations and many others which are broadly categorized as geomagnetic activity. Before discussing geomagnetic activity, we must first introduce the concept of magnetic reconnection.

The magnetosphere was described earlier as an isolated bubble separated from the solar wind by the magnetopause. However, in 1961 Dungey proposed that if the IMF and

earth's magnetic fields were anti-parallel (meaning the IMF had a southward component), the earth's field lines could become "reconnected" to the IMF [Kivelson and Russell, 1995]. This process, called reconnection, would then lead to open magnetic field lines (connected back to the sun) whereby energy and plasma from the solar wind could enter the magnetosphere. The details of the reconnection process are beyond the scope of this discussion but are reviewed in e.g. Kivelson and Russell [1995] and Parks [1991]. Various types of magnetic activity have been shown to correlate with the southward turning of the IMF thus supporting the importance of magnetic reconnection. Magnetospheric substorms and geomagnetic storms will be discussed in the next two sections.

1.1.3 Magnetospheric Substorms

A *magnetospheric substorm* is a sequence of events in both the magnetosphere and ionosphere that occurs as energy and plasma are stored in the tail and then suddenly released to the inner magnetosphere. The substorm is a global reconfiguration of the magnetosphere and represents the magnetospheric response to a change in the dayside reconnection rate. This global phenomenon has many different manifestations including bright aurora, fluctuations of the surface magnetic field and generation of plasma waves.

When the IMF turns southward, the newly opened magnetic field lines are dragged across the polar cap by the solar wind allowing magnetic flux to enter the magnetosphere and be transported to the tail lobes (Figure 1.3). As flux is transferred to the tail lobes, the plasma sheet is squeezed down and thins due to the increased magnetic pressure [Kivelson and Russell, 1995]. This is the growth phase where energy is being stored in the tail. As the plasma sheet thins, geosynchronous spacecraft which usually lie a few de-

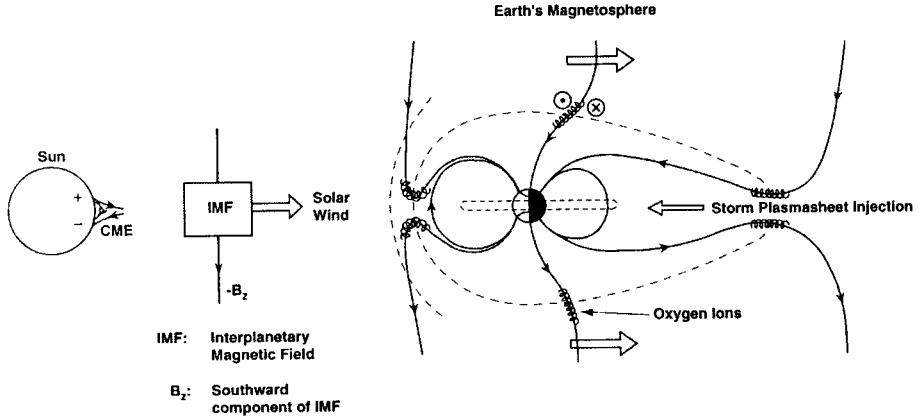


Figure 1.3: The sequence of a substorm [Tsurutani, 2001].

grees off the magnetic equator, measure a dropout of particle flux during this phase of the substorm. In addition, weak magnetic “bay” signatures are measured on the ground with magnetometers as a result of currents in the ionosphere, weak short duration aurora are seen and the size of the polar cap increases slowly.

During the expansion phase, energy is suddenly released and the aurora becomes suddenly bright and active. The process is not fully understood, but one theory is that either due to current instability or northward turning of the IMF, reconnection at a near earth neutral line ($8-10 \text{ Re}$) causes both the dipolarization of the field and the ejection of a plasmoid tailward. At the onset of the expansion phase, the inner boundary of the plasma sheet moves earthward as the field lines snap back to a more dipolar configuration. Spacecraft in geosynchronous orbit near this boundary see an increase in particle density or “injection” of particles when the plasma sheet moves past.

A typical substorm lasts for a few hours and the magnetosphere relaxes to its ground state in the recovery phase. Figure 1.4 shows the phases of a substorm as measured

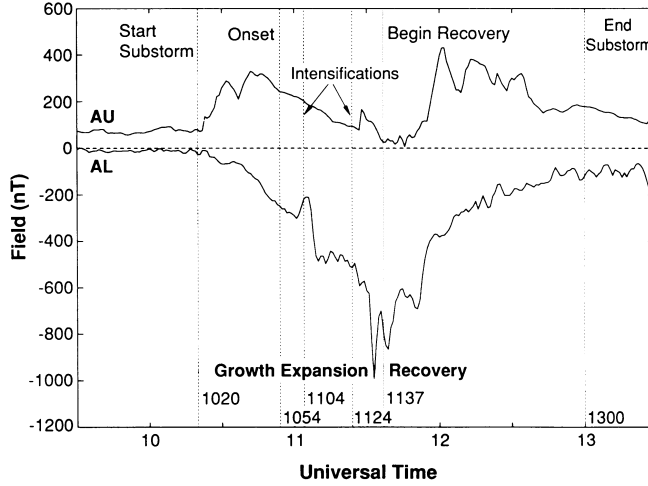


Figure 1.4: AU and AL indices during a substorm. The phases of the substorm are identified by a change in slope of the AL index [Kivelson and Russell, 1995].

by the AU and AL magnetic indices. These indices are determined by measuring changes in the horizontal component of the surface magnetic field due to ionospheric currents. A change in the rate of decrease of AL marks the onset of the storm.

1.1.4 Geomagnetic Storms

When the IMF remains southward for a long period or turns southward multiple times in a short interval, energy and plasma are transported to the magnetosphere faster than it can return to its ground state and a *geomagnetic storm* follows. During a storm, overlapping particle injections cause the ring current to grow. A storm is thus identified by the Dst index which is based on magnetic field measurements at stations along the earth's equator. The phases of a storm are shown in Figure 1.5 which shows an idealized Dst profile. The “main phase” of the storm is characterized by a rapid decrease in the field and Dst due to the pumping up of the ring current. When the IMF turns northward or the southward

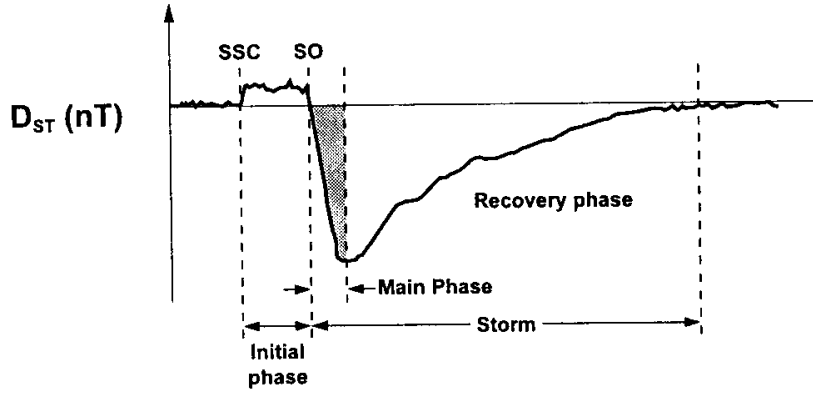


Figure 1.5: Dst index during a geomagnetic storm [Tsurutani, 2001].

component weakens, the “recovery phase” begins and the ring current stops growing and decays as particles are lost to the magnetopause or Earth’s atmosphere. During the recovery phase of a storm geosynchronous satellites also measure an *increase* in the energy density of the radiation belts. In particular, the relativistic electron flux increases in the days following a storm. These relativistic electron enhancements are not well understood and will be discussed further in Section 1.2.

Geomagnetic storms are often preceded by the arrival of an interplanetary shock (produced by activity on the sun). The density and magnetic field increase abruptly across the shock and the increase in pressure forces the magnetopause to move inward causing the magnetic field measured at the surface of the earth to increase ~ 10 nT. This is called the “initial phase” of the storm (Figure 1.5) and is also called a Storm Sudden Commencement (SSC). The initial phase is not present for all storms [Kamide, 2001]. The effects of a geomagnetic storm last for about a week although high energy particles can hang around for many months [Looper et al., 1994].

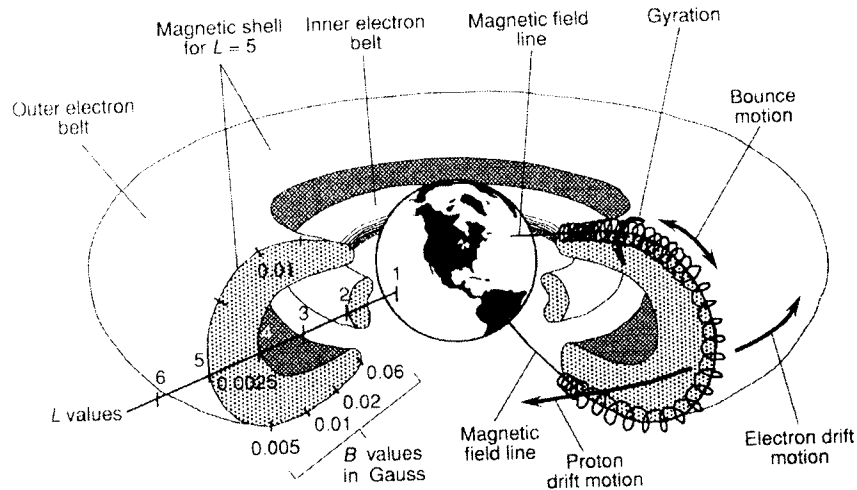


Figure 1.6: Schematic of the earth’s radiation belts [Daglis, 2001b].

1.2 The Earth’s Radiation Belts

The earth’s radiation belts or “Van Allen belts” were discovered in 1958 using the Geiger counter flown on Explorer 1 when the count rate dropped nearly to zero. James Van Allen correctly deduced the presence of the belts which produced $\sim 100\%$ dead time upon encountering the very high particle fluxes. This was confirmed a few months later with the launch of Explorer 3 [Lemaire, 2001]. Figure 1.6 shows a schematic of the radiation belts where particles are confined by the earth’s nearly-dipolar magnetic field.

1.2.1 Properties of the Radiation Belts

As mentioned in Section 1.1.1, the radiation belts consist of energetic ions and electrons that are trapped as long as the conditions described in the next section (1.2.2) are met. In the radiation belts, the earth’s magnetic field is nearly dipolar and particle

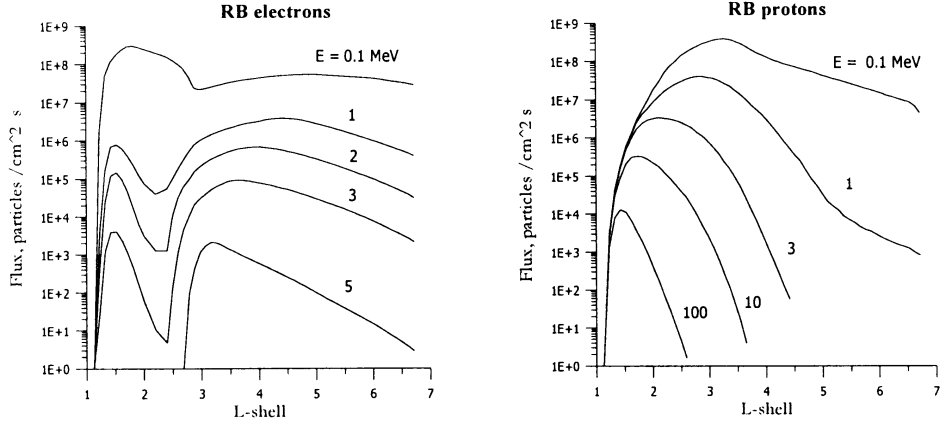


Figure 1.7: Radial profiles of the electron and ion equatorial omni-directional flux [Panasyuk, 2001].

trajectories follow the field lines. Therefore, the radiation belts are field-aligned structures and it is useful to define a coordinate system with coordinates labeling the magnetic field lines. The McIlwain L parameter is defined as the distance, measured in Earth radii, from the center of Earth to the point where a magnetic field line crosses the equator. With this definition, the equation for the dipole magnetic field strength at the equator can simply be written

$$B = \frac{B_0}{L^3}$$

where B_0 is the magnetic field strength at the earth's surface ($L=1$) and has an average value of ~ 0.31 Gauss. The definition of L can be extended to non-dipolar field but L still labels a particular "shell" of magnetic field lines.

Figure 1.7 shows the radial profile for electrons and protons measured at the equator. Ions (mostly protons) are found between $L \sim 1-7$ with the more energetic particles concentrated closer to Earth. The main source for protons above 30 MeV, which are found

in the inner zone, is the cosmic ray albedo neutron decay source or CRAND [Walt, 1996]. Neutrons, produced by cosmic rays colliding with the atmosphere, can sometimes escape and beta decay close to Earth. The resulting protons and electrons will become trapped.

Electrons are found in two main belts separated by the slot region. The inner belt (sometimes referred to as the inner zone) extends between $L \sim 2$ down to a few hundred kilometers above the Earth's surface. The outer zone is located between $L \sim 2.5-7$ and peaks near $L=4$. The CRAND source is not sufficient to account for electrons or \sim MeV ions in the outer radiation belts and their origin is still not fully understood. The slot region is believed to be a result of scattering of electrons out of the radiation belts by a type of VLF wave known as plasmaspheric hiss [Lyons et al., 1972]. The scattering of particles by plasma waves will be discussed in more detail in Section 1.3.2. The outer edge of the outer zone occurs where the magnetic field deviates from a dipole and drift paths are no longer closed.

Observations of the flux and spectrum of relativistic electrons in the radiation belts will be described in Section 1.2.3, but, first, in order to understand the existence of the radiation belts we need review the concept of trapped particle motion and the associated adiabatic invariants.

1.2.2 Adiabatic Invariants

The motion of a geomagnetically trapped particle can be separated into three types of periodic motion with different timescales: gyration about a field line (cyclotron motion), bounce along the field line and longitudinal drift around the earth (Figure 1.8). Associated

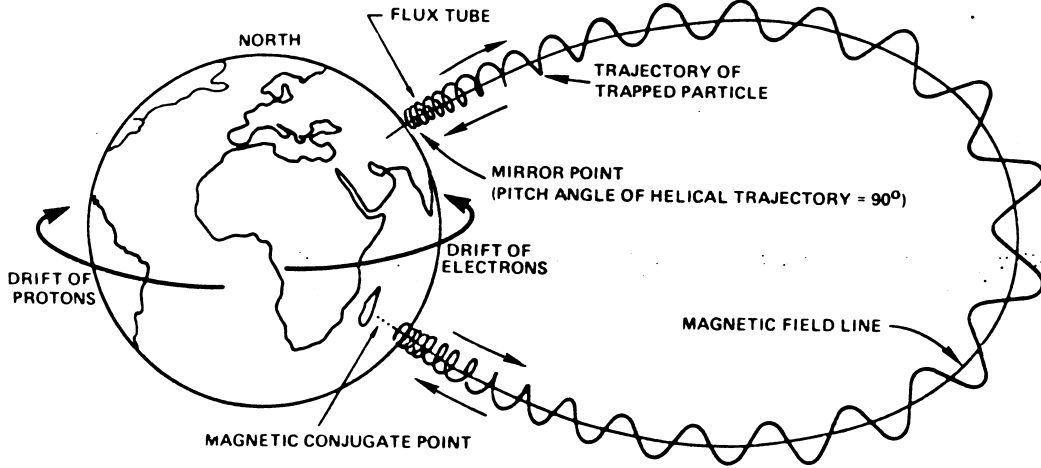


Figure 1.8: The motion of a trapped particle [Spjeldvik and Rothwell, 1985].

with each of these motions is an action variable given by

$$J_i = \oint [\vec{p} + \frac{q}{c} \vec{A}] \cdot d\vec{l} \quad (1.1)$$

where \vec{p} is the momentum, \vec{A} is the vector potential and the integral is taken along the particle path. As long as the magnetic field changes slowly compared to these periodic motions, the action or “adiabatic invariant” associated with each is conserved. The next sections give a conceptual picture of trapped particle motion and the associated adiabatic invariants. A full discussion is given by e.g. Shultz and Lanzerotti [1974].

Gyration

Gyration is the motion of a particle about the field line due to the Lorentz force with the frequency of motion given by the usual relativistic cyclotron frequency,

$$\Omega = \frac{qB}{\gamma m_0 c} \quad (1.2)$$

The particle gyration is perpendicular to the magnetic field and the particle path is a circle with radius $R_g = p_\perp c / |q|B$ where p_\perp is the momentum perpendicular to B . Using Equation 1.1, the action is then

$$J_1 = 2\pi p_\perp R_g + \frac{q}{c} \int B \cdot dA$$

where Stokes' theorem has been used in the second term.

$$\begin{aligned} \int B \cdot dA &= B\pi R_g^2 \\ \Rightarrow J_1 &= \frac{\pi p_\perp^2 c}{|q|B} \end{aligned}$$

From this expression and the particle rest mass, m_0 we define the “first adiabatic invariant”

$$\mu = \frac{p_\perp^2}{2m_0 B} \quad (1.3)$$

which is equivalent to the first action variable since m_0, q, c and π are constants and is also related to the particle's magnetic moment by

$$M = \frac{\mu}{\gamma}$$

As long as the magnetic field is constant on the timescale of gyration, the first adiabatic invariant (which is essentially the magnetic flux contained in the gyro-orbit) is conserved.

Bounce Motion

Since the earth's magnetic field is nearly dipolar, a particle moving parallel to the magnetic field experiences converging field lines as it approaches the poles. As a result, there is a force that acts to reflect the particle and the particle bounces between so called “mirror points”. In this case, the particle path is parallel to the magnetic field and encloses

no magnetic flux so the action is just given by

$$J_2 = \oint p_{\parallel} ds$$

where s is the coordinate along the magnetic field line. J_2 or the “second adiabatic invariant” depends on the magnetic field configuration and for a perfect dipole is

$$J = 2pLR_e Y(\alpha)$$

where p is the total momentum, L is the McIlwain L parameter, R_e is the radius of the earth and Y is of order unity and is a function of the equatorial pitch angle, α , which is defined as the angle between the velocity vector and magnetic field at the equator [Schulz and Lanzerotti, 1974]. Similarly, the frequency of bounce motion in a dipole is

$$\Omega_b = \frac{2\pi p}{4mLR_e T(\alpha)} \quad (1.4)$$

where $m = \gamma m_0$ and $T(\alpha)$ is another function of the pitch angle given approximately by

$$T(\alpha) \approx 1.38 - 0.3198(\sin\alpha + \sqrt{\sin\alpha})$$

Conceptually, the second adiabatic invariant is proportional to the length of the field line between the mirror points.

The mirror point, or point where the particle is reflected, can be calculated assuming both the first adiabatic invariant and particle energy are conserved. Then

$$\frac{p_{\perp}^2(s)}{2m_0B(s)} = \frac{p^2}{2m_0B_m}$$

at any point, s , along the field line where B_m is the magnetic field strength at the mirror point. At the equator,

$$p_{\perp}^2 = p^2 \sin^2 \alpha$$

$$\Rightarrow \frac{B_m}{B_e} = \frac{1}{\sin^2 \alpha} \quad (1.5)$$

In other words, the mirror point is determined by a particle's equatorial pitch angle; particles with $\alpha=90^\circ$ gyrate at the equator and have no bounce motion while particles with small pitch angles are reflected near the poles. Conservation of the second adiabatic invariant means the particle will always be reflected where the magnetic field has the value, B_m , and will preserve it's equatorial pitch angle.

Particle Drift

The final and slowest particle motion is the gradient/curvature drift around the earth due to the inhomogeneity of a dipolar field. Consider a particle with $\alpha=90^\circ$ that gyrates at the equator. As the particle moves closer to Earth where the magnetic field is stronger, the gyroradius gets smaller. The magnetic field gradient causes the gyro-orbit to not quite close on itself and the particle drifts; electrons to the east and ions to the west. Similarly, a particle mirroring at high latitudes experiences the curvature of the magnetic field and a resulting centrifugal force which causes the particle to drift in longitude. The combined drift motion of the particle defines a "drift shell".

In this case the integral in Equation 1.1 is evaluated along any closed curve that lies on the drift shell. The firsts term is small and the second term gives

$$J_3 = \frac{q}{c} \Phi_m \quad (1.6)$$

where Φ_m is the magnetic flux. Thus, in a dipolar magnetic field, the "third adiabtic invariant", Φ , is given by

$$\Phi = -\frac{2q\pi B R_e^2}{Lc}$$

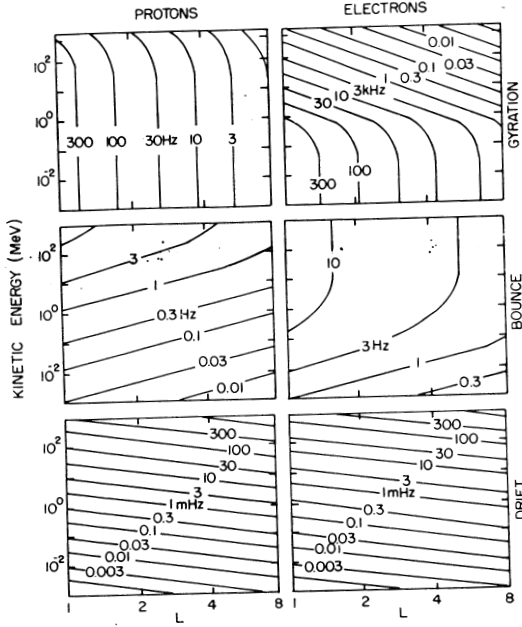


Figure 1.9: Frequencies of gyration, bounce and drift motion for electrons and protons as a function of energy [Schulz and Lanzerotti, 1974].

Conservation of the third adiabatic invariant is equivalent to conservation of the magnetic flux contained in the particle drift orbit. If the magnetic field decreases as in the case of a geomagnetic storm, a particle moves radially outward to conserve the third adiabatic invariant.

The drift frequency for a particle in a dipole magnetic field can be calculated [Schulz and Lanzerotti, 1974]

$$\Omega_d = -\frac{3L}{\gamma}(\gamma^2 - 1) \left(\frac{c}{R_e} \right)^2 \left(\frac{m_0 c}{q B_0} \right) \frac{D(\alpha)}{T(\alpha)} \quad (1.7)$$

where for an equatorially mirroring particle ($\alpha=90^\circ$), $\frac{D}{T}=0.5$.

The frequencies of gyration, bounce and drift motions as a function of energy are shown in Figure 1.9. For a 1 MeV electron at $L=6$, the gyration, drift and bounce periods

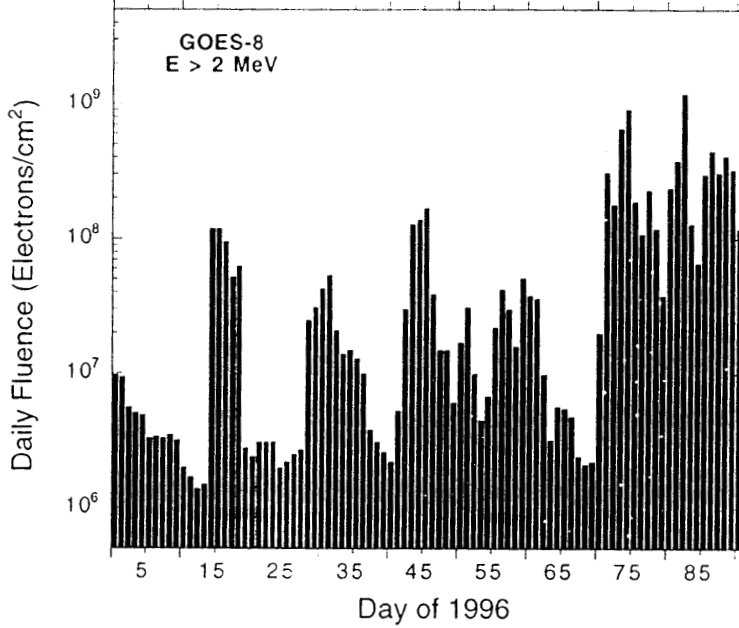


Figure 1.10: GOES 8 >2 MeV electron fluence [Baker et al., 1997].

are $\tau_g \sim 1$ ms, $\tau_b \sim 1$ s and $\tau_d \sim 1000$ s. Violation of an adiabatic invariant can occur if particles are subjected to forces which vary on short enough spatial or temporal scales such that particles at different phases respond differently. Such processes can change both the pitch angle and energy of a particle and will be discussed further in Sections 1.3.2.

1.2.3 Spacecraft Measurements

The flux of relativistic electrons in the radiation belts is highly variable and can increase by up to two orders of magnitude on a timescale of a few hours to days. Figure 1.10 shows the daily average fluence of >2 MeV electrons measured by the GOES-8 geosynchronous spacecraft. The sharp increases and drops are typical with the relativistic electron flux peaking 1-3 days after the onset of a geomagnetic storm [Friedel et al., 2002].

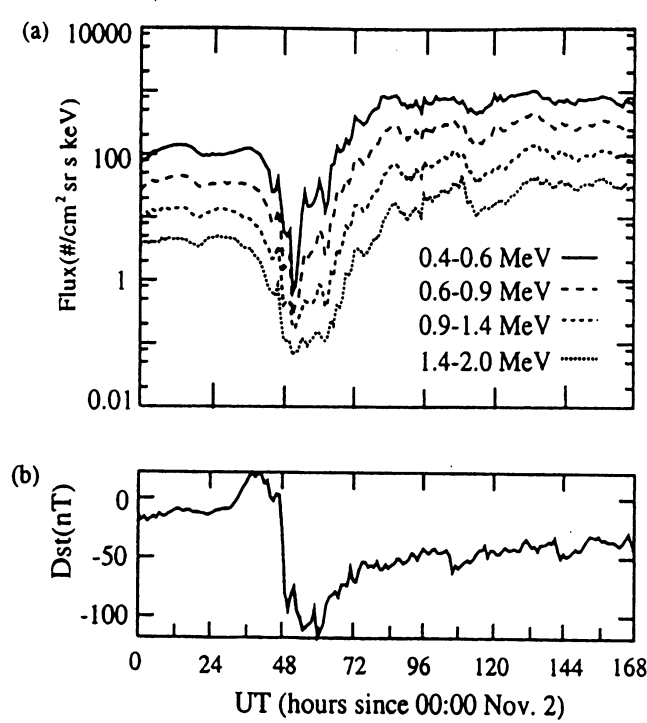


Figure 1.11: Relativistic electron flux as measured by the CPA instrument on LANL 1984-129 during a geomagnetic storm along with Dst for the same period [Horne, 2001].

Figure 1.11 shows the relativistic electron flux enhancement measured by the Los Alamos National Lab (LANL) spacecraft 1984-129 during a particular storm in November 1998 along with the Dst index during the same period. A decrease in the relativistic electron flux is first observed during the main phase followed by an increase to above pre-storm level during the recovery phase. The initial decrease can be partly understood as an adiabatic effect known as the “Dst effect”; as the magnetic field decreases, particles move outward to conserve their third adiabatic invariant. Conservation of the 1st and 2nd invariants means the energy must also decrease and since the particle flux drops steeply with energy, a drop in the flux at a fixed energy is measured. The initial decrease, however, may also be partly due to the loss of particles.

Though this type of observation is common and all relativistic electron enhancements are associated with magnetic storms, every storm does not show an increase [Reeves, 1998]. This difference in effectiveness in accelerating electrons between different storms is not understood and the lack of increase in the relativistic electron flux for some storms may not be due to a lack of acceleration of particles but rather to heavy losses. The variability of the relativistic electron flux in the radiation belts is a major driver for the current focus placed on understanding both acceleration and loss mechanisms.

1.2.4 Acceleration Mechanisms

One possible explanation for the increase of relativistic electrons observed in the outer radiation belts is an injection of particles from an external source. The solar wind can be ruled out as a source because the phase space density of MeV electrons is too low [Li et al., 1997]. Another suggestion was made by Baker et al. [1979] that Jovian electrons can enter the earth's magnetosphere when Earth and Jupiter are connected by the same IMF field line. Jovian electrons have been observed over the poles but cannot account for the increases associated with geomagnetic activity. Moreover, the electron enhancements do not correlate with the location of Jupiter [Friedel et al., 2002]. Therefore, it is generally believed that the relativistic electrons in the radiation belts are being accelerated internally by the Earth's magnetosphere. In this section some of the theories suggested to explain the relativistic electron enhancements are described.

The source for radiation belt particles is thought to be the plasma sheet. Particles of ~ 10 keV can be accelerated to ~ 100 keV by increases in the convection electric field but not to the required \sim MeV energies [Horne, 2001]. Therefore, acceleration must be due to

breaking of one or more adiabatic invariants.

Radial Diffusion

Consider some process that can transport a particle radially inward violating the third adiabatic invariant but preserving the first and second. Such a process could involve, for example, electric and magnetic fields fluctuating on the particle drift timescale. Moving a particle radially inward moves it to a region of stronger magnetic field and if the first and second adiabatic invariants are conserved, the particle energy must increase (see Section 1.2.2). Fluctuating fields would act to move some particles inward but others radially outward. However, if the phase space density gradient is inward such that more particles are found at larger Φ (or higher L), more particles overall will be transported inward. This process is known as radial diffusion and leads to a net increase in particle energy at the expense of the energy from the fluctuating fields.

In order to accelerate particles to relativistic energies, Fujimoto and Nishida [1990] proposed a recirculation model whereby particles are diffused inward via conventional radial diffusion, then transported back out by some mechanism that preserves the third adiabatic invariant (and thus the energy) and then the whole process repeats. After many cycles, the particle energy can be increased substantially. The radial recirculation model was originally proposed to explain the presence of energetic electrons in Jupiter's radiation belts. The recirculation process is very slow and on Earth, it may be able to explain enhancements over several days at $L=6.6$ but cannot explain the rapid enhancements often observed at $L=4$ [Friedel et al., 2002].

Another model proposed involves resonant interaction of electrons with Ultra Low

Frequency (ULF) waves on the drift timescale. ULF waves are global oscillations of the earth's magnetic field and are observed to be enhanced during times of high geomagnetic activity. Elkington and Hudson [1999] have recently shown that this "enhanced" radial diffusion can accelerate particles much more quickly than the classic radial diffusion model and is thus a good candidate for explaining the relativistic electron enhancements.

On March 24 1991, an injection of electrons with energies up to 15 MeV was observed deep in the radiation belts ($L < 4$) following a very large magnetic storm [Blake et al., 1992]. The electrons are believed to have been accelerated by a large electric field produced when an interplanetary shock rapidly compressed the magnetosphere. However, such events are rare and do not explain the regular enhancements [Li et al., 1996].

Electron Cyclotron Heating

Gyroresonant interaction with plasma waves has also been suggested as the mechanism responsible for accelerating electrons to MeV energies [Horne, 2001]. For example, whistler waves are R mode electromagnetic waves that have frequency less than the electron gyrofrequency (VLF band: 3-30kHz) and can thus violate the electron's first adiabatic invariant. Parallel propagating whistler waves are circularly polarized and an electron travelling towards the wave sees the wave electric field rotating at the Doppler shifted wave frequency in the same direction as the particle's gyration motion (Figure 1.12). If the particle velocity is just right, the electric field will be rotating at the same frequency as the particle, so the electric field will appear stationary. When this resonance condition is met, the wave and particle can exchange energy. The resonance condition can be written as

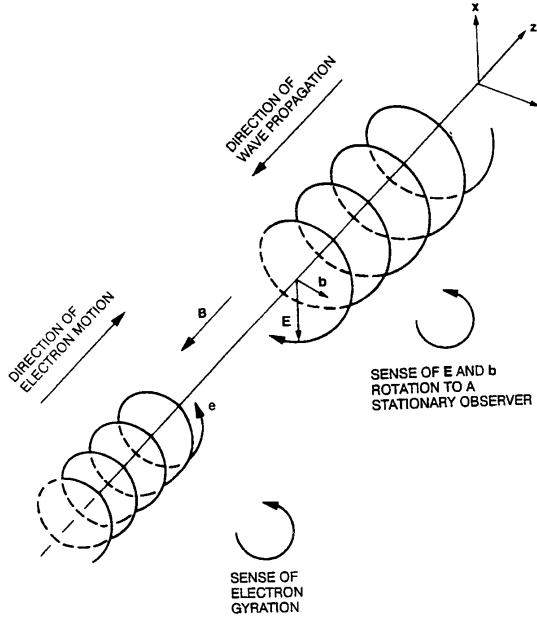


Figure 1.12: Electron interacting with a whistler wave [Walt, 1996].

follows

$$\omega - \frac{\vec{v} \cdot \vec{k}}{c} = \frac{n\Omega}{\gamma} \quad (1.8)$$

where \vec{v} is the particle velocity, \vec{k} is the wavenumber, n is an integer and Ω is the non-relativistic cyclotron frequency. Waves will therefore interact strongly with particles that have

$$v_{||} = \frac{c}{k_{||}} \left(\omega - \frac{n\Omega}{\gamma} \right) \quad (1.9)$$

In general, particles at different gyrophases will see different electric field strengths; some particles will be accelerated while others will be decelerated. The evolution of the distribution of particles is often modeled as a diffusion process where the diffusion coefficient is proportional to the wave power. Diffusion generally acts to isotropize a distribution and since there are fewer particles at higher energies in the radiation belts, interaction with

waves will tend to increase the flux at higher energies [Horne and Thorne, 1998].

Whistlers have been shown to be capable of accelerating electrons from ~ 100 keV to > 1 MeV outside the plasmasphere [Summers et al., 1998], and are also observed during geomagnetic storms [Horne, 2001]. They can accelerate electrons in the required 1-3 day timescale provided the waves are strong enough.

1.2.5 Loss of Trapped Particles

In order to explain the observed changes in flux of the trapped flux it is also necessary to consider the loss processes acting on trapped electrons. Any viable acceleration mechanism must be able to explain the actual increase in flux when the *observed* losses are considered. Particles at high L can be lost through the magnetopause, but at lower L they can be lost to the earth's atmosphere and this is called "electron precipitation". As particles bounce between mirror points, those that reach a low enough altitude (~ 100 km) will collide with the atmosphere and be lost. This occurs for particles with small equatorial pitch angles ($<$ few degrees) thus defining the "loss cone". The pitch angle distribution of particles will usually be empty at these small angles but if the first and/or second adiabatic invariants are violated, a particle's pitch angle can be lowered causing it to bounce at a lower altitude; in other words the particle can be scattered into the loss cone. Specific mechanisms acting to pitch-angle scatter outer zone relativistic electrons will be discussed in detail in the next section along with a review of observations of electron precipitation .

1.3 Energetic Electron Precipitation

The precipitation of energetic ($>100\text{keV}$) electrons has been measured both directly with particle detectors aboard spacecraft and remotely through the detection of X-rays and the effects of precipitation on the ionosphere. These different observing methods are complimentary and each has its advantages; spacecraft observations provide a global view of precipitation while a nearly-stationary balloon platform allows for the separation of temporal and spatial effects. The measurements have revealed dynamic structure both spatially and temporally and the wide range of characteristics suggest that more than one process is responsible for precipitating electrons. These measurements are reviewed in the next section followed by a discussion of some postulated scattering mechanisms responsible for the various types of precipitation observed. Finding the relationship between these different types of events is challenging but important to understanding the impact of each on the trapped population.

1.3.1 Observations

The first detection of terrestrial X-rays was made in 1957 with a balloon-borne particle detector over Minneapolis [Winckler et al., 1958]. The interpretation of the increased count rates was bremsstrahlung X rays produced by precipitating electrons colliding with neutrals in the earth's atmosphere. The source of these particles was thought to be solar at the time, since the observation was made prior to the discovery of the Van Allen belts. Subsequent observations of X rays made from balloon, rocket and satellite experiments led to a basic picture of the precipitation: the X rays are bremsstrahlung produced by the

precipitation of electrons, the typical e-folding energy of the events is \sim 20 keV indicating that most of the precipitating particles have energies of tens of keV. The particles were thought to be auroral (from the plasma sheet) rather than from the radiation belts. Different temporal structures were found to occur at different local times during auroral break-up and were interpreted as local manifestations of a global disturbance. Temporal structure was seen on many timescales from hundreds of milliseconds (“microbursts”) to modulations over minutes. Wave-particle interactions were thought to account for the microburst precipitation and modulation of the precipitation by low frequency waves to account for the variations seen on minute timescales. However, the physical processes involved are still not well understood [Parks et al., 1993].

Precipitation of more energetic electrons (0.1 to 1 MeV) was first inferred from the daytime decrease of forward scatter radio signals [Bailey, 1968]. The decrease was thought to be the result of an increase in D-region ionization due to the precipitation of >0.4 MeV electrons, thus these were called relativistic electron precipitation (REP) events. Bremsstrahlung X-rays were detected in the noon sector in direct association with REP detected by forward scatter radar, but electron e-folding energies inferred from the X-ray observations were 100-150 keV and 40-70 keV respectively for the two events reported [Rosenberg et al., 1972]. In the late 1970’s, bremsstrahlung X rays with energies up to \sim 600 keV were observed by polar orbiting spacecraft and these observations found that the precipitation often occurs near midnight at the beginning of a magnetic storm [Imhof et al., 1990]. In addition, the inferred spectrum of precipitating electrons near the trapping boundary (outer edge of the radiation belts) showed an L-dependent energy

cut-off, while the spectrum of precipitation within the outer zone indicated that electrons are precipitated at all energies with equal strength. Other balloon-based observations of bremsstrahlung inferred electron e-folding energies as high as 200 keV for precipitating electrons on the dayside [Parks et al., 1979, Matthews et al., 1988].

None of these observations showed X-ray flux extending to MeV energies, but the early balloon instrumentation was incapable of measuring X rays above \sim 200 keV and lacked the spectral resolution required to infer the precipitating electron spectrum. Smith et al. [1995] made the first high resolution spectral measurements sensitive to higher energies with a germanium spectrometer and reported several events that extended up to 300 keV. Because of an instrument live time problem, these observations were not sensitive to X-rays above 300 keV. The reported events had e-folding energies < 50 keV for the X-ray spectrum, corresponding to electron e-folding energies < 150 keV [Berger and Seltzer, 1972].

Direct spacecraft particle measurements show that most "REP" events are also dominated by electrons with energies well below 1 MeV [Thorne and Andreoli, 1980], [Imhof et al., 1991]; only four out of 313 events observed with the S3-3 satellite showed precipitation increasing with energy, from none below 160 keV to strong diffusion levels at 850 keV. These events occurred in the dusk sector and Thorne and Andreoli [1980] suggested electromagnetic ion cyclotron (EMIC) waves as the scattering mechanism. Imhof [1986] reported narrow electron spikes observed with the S81-1 and P78-1 spacecraft near the plasma-pause in the evening sector, that showed stronger precipitation above 300 keV than at lower energies. More recent high time resolution measurements from SAMPEX show two classes of energetic (> 1 MeV) electron precipitation [Blake et al., 1996, Nakamura et al., 1995]:

"bands" occur near the high latitude trapping boundary (similar to the electron spikes reported by Brown and Stone [1972]), and "relativistic electron microbursts" with <1 s temporal structure, occur both near the trapping boundary and at lower latitudes. SAM-PEX also frequently observes lower energy (<150 keV) microbursts.

1.3.2 Precipitation Mechanisms

Table 1.3.2 summarizes some of the mechanisms that can scatter radiation belt electrons into the loss cone; these mechanisms fall into two classes: current sheet scattering and wave-particle interactions. When the radius of curvature of the magnetic field becomes smaller than ~ 10 times the electron gyroradius, electrons lose their adiabaticity [Sergeev and Tsyganenko, 1982]. The current sheet scattering mechanism acts primarily on the nightside at high L-values, where the magnetic field lines are stretched and have a smaller radius of curvature. Current sheet scattering also acts selectively on higher energy-particles since they have larger gyroradii; this phenomenon has been observed by low-altitude satellites [Imhof et al., 1991].

As discussed in Section 1.2.4, a plasma wave and a particle can exchange energy if the cyclotron resonance condition (Equation 1.8) is met. Given this condition and the dispersion relation for a particular plasma wave mode, the resonant electron energies can be calculated for given values of wave frequency, plasma density and magnetic field strength. Determining the resonant electron energies places constraints on the precipitating electron energy spectra, and provides a method for distinguishing between the mechanisms.

There are several wave modes that can interact with relativistic electrons: whistlers, electromagnetic ion cyclotron (EMIC) mode waves, and electrostatic ion-cyclotron (EIC)

	References	Energy spectrum	Local time	L-shell
Current sheet scattering	Sergveev and Tsyganenko,1982 Imhof et al.,1990	preferentially high (mono-energetic?)	generally nightside	high trapping boundary
Whistler mode scattering	Kennel and Petschek,1966 Thorne and Andreoli,1980 Summers et al,Horne and Thorne,1998	stronger for low energies (100 keV) but can work for MeV	dawnside	outside plasmapause (low density)
Electromagnetic Ion Cyclotron Mode Scattering	Thorne and Kennel 1971;Thorne and Andreoli,1980 Summers et al,Horne and Thorne,1998 Lorentzen,2000	preferentially high (mono-energetic)	duskside	inside plasmapause (or detached region of density)
Electrostatic Ion Cyclotron Mode Scattering	Thorne and Andreoli,1980	stronger for low energies (100 keV) but can work for MeV	nightside	?

Table 1.2: Precipitation Mechanisms and their characteristics (courtesy of K.R.Lorentzen)

mode waves [Thorne and Andreoli, 1980]. These interactions are parasitic, meaning that the waves are generated by a different population of particles than those precipitated. Whistlers and EIC waves are most effective for scattering electrons of energy < 1 MeV, but they can also interact with electrons of higher energies. EMIC waves, however, are most effective for scattering electrons with energy > 1 MeV. The dispersion relation for EMIC waves, where $\omega < \Omega_i \ll \omega_i$, is

$$\frac{c^2 k^2}{\omega^2} = \frac{\omega_i^2}{\Omega_i(\Omega_i - \omega)}$$

where ω is the wave frequency, Ω_i is the ion gyrofrequency and $\omega_i = \sqrt{4\pi n e^2/m_i}$, is the ion plasma frequency for a plasma density, n. Combining this with the resonance condition (Equation 1.8) and assuming $\omega \ll \Omega_e$, the resonant parallel kinetic energy is then

$$\frac{E_{res}}{m_e c^2} = \left[1 + \frac{2E_m}{m_e c^2} \left(\frac{m_i}{m_e} \right) \left(\frac{\Omega_i}{\omega} \right)^2 \left(1 - \frac{\omega}{\Omega_i} \right) \right]^{1/2} - 1 \quad (1.10)$$

where $E_m = B^2/8\pi n$ is the magnetic energy per particle. Particles with this parallel kinetic energy and any perpendicular energy will interact strongly with EMIC waves. This can be understood by noting that EMIC waves are left-handed (ion waves) while electron gyration is right-handed. In order to interact, the electron must be going fast enough to overtake the wave so the apparent polarization is reversed. Since resonance only depends on the parallel energy, the resonant energy, E_{res} , defines a lower cutoff energy and any particle with $E > E_{res}$ can interact with the wave provided it has the resonant parallel velocity. Since the trapped electron distribution is rapidly falling in energy, a precipitating electron spectrum with a quasi-monoenergetic peak will result.

Both whistler waves and EMIC waves are often excited by particles that have been injected during substorms and because of the direction of gradient-curvature drift,

SUMMERS ET AL.: WAVE-PARTICLE RESONANT DIFFUSION

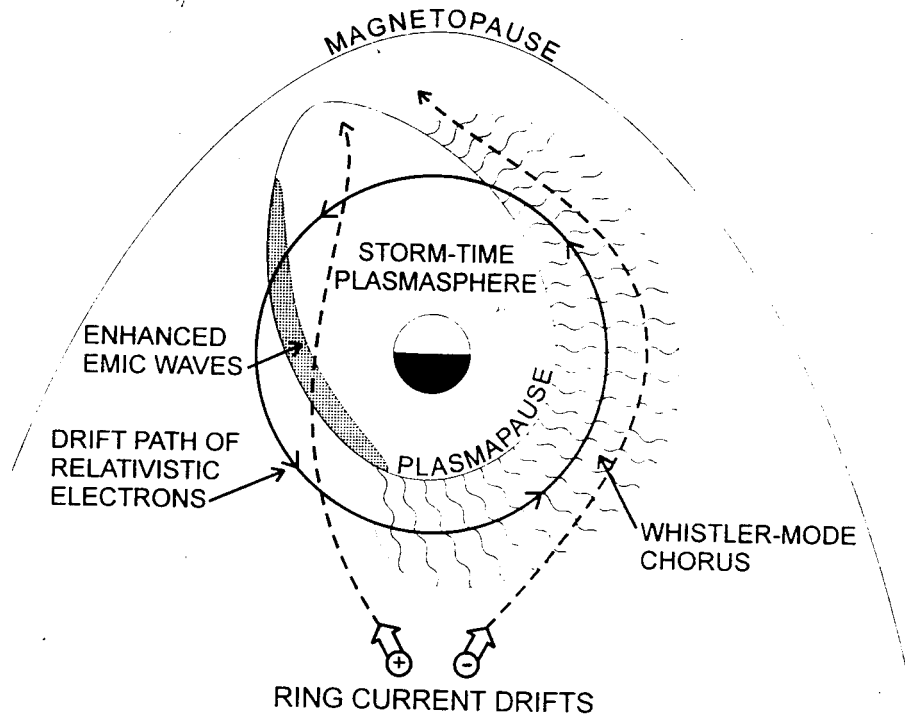


Figure 1.13: Location of whistler and EMIC waves in local time and in relation to plasma-pause [Summers et al., 1998].

whistler mode waves are usually generated on the dawnside, and EMIC mode waves on the duskside (Figure 1.13). The density needed to satisfy the cyclotron resonance condition places further constraints on the location of the interaction with electrons, such as inside or outside the plasmapause. For example, high plasmaspheric densities are required to lower the EMIC resonant energy to ~ 1 MeV.

1.4 Discovery of Terrestrial MeV X-rays

1.4.1 Observations

In 1996 the first detection of MeV X-rays produced by precipitating electrons was made by a germanium spectrometer and X-ray pinhole camera carried on a high altitude balloon over Kiruna, Sweden [Foat et al., 1998, Lorentzen, 1999]. This event had the hardest spectrum ever detected from precipitating electrons ($\sim E^{-1.7}$). Observations of gamma-ray flashes associated with lightning have been observed with similar spectral hardness and significant flux above 300 keV, but much shorter duration lasting between 1-10 ms [Nemiroff et al., 1997].

The Kiruna MeV event lasted for \sim 22 minutes and consisted of 7 bursts. Each burst was \sim 100 seconds in duration with a higher frequency 10-20 second period modulation superposed (Figure 1.14). Observations made with the X-ray pinhole camera indicate a uniform spatial distribution over the field of view (90° field of view translates to a 100 km \times 100 km spatial extent at the region of X-ray production). Thus the variations in X-ray intensity seem to be due to temporal effects rather than a source moving in and out of the field of view.

1.4.2 Interpretation

The location of the Kiruna MeV X-ray event ($L=5.8$) suggests the radiation belts as the source of the precipitating particles. The burst was observed in the dusk sector (18:35-18:57 MLT) and geomagnetic activity was low ($K_p \sim 2$). The Kiruna X-ray spectrum was so flat that it could not be reproduced by a power law of precipitating electrons; the precipitat-

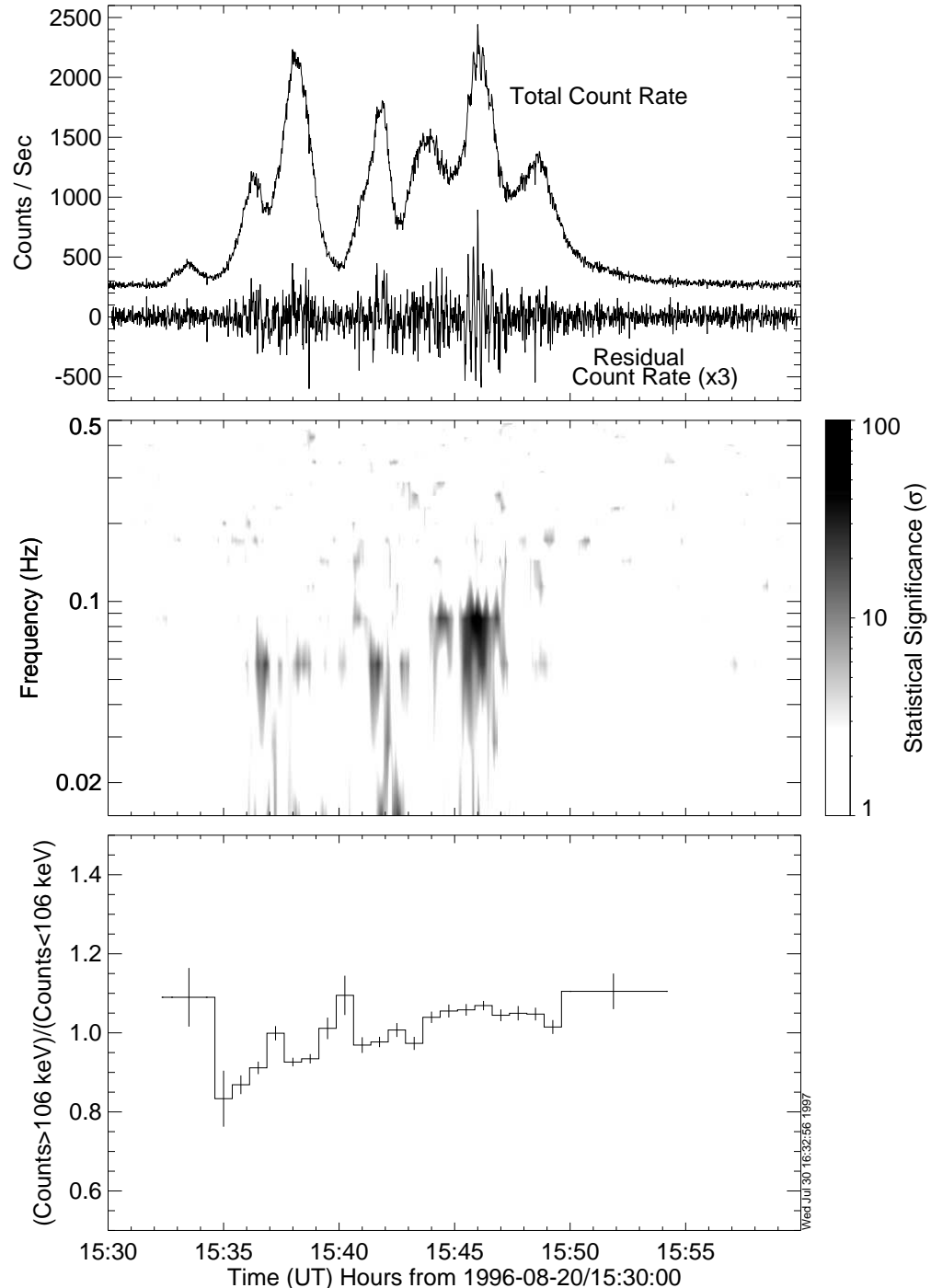


Figure 1.14: Top panel: The X ray count rate for the Kiruna event. Also shown residual countrate after subtracting smoothed data. Middle panel: Power spectrum of count rate as a function of time. Bottom panel: Spectral hardness [Foat et al., 1998].

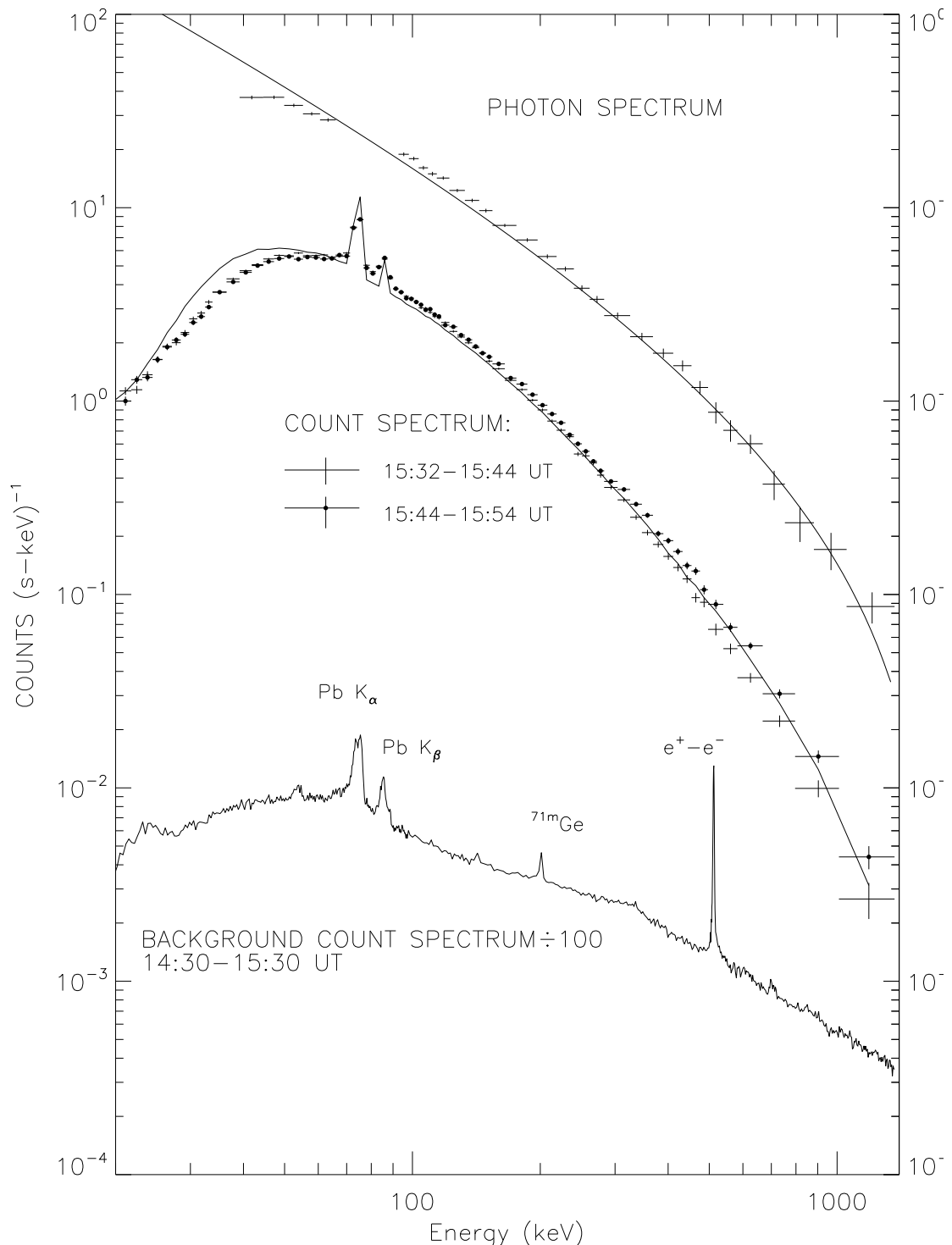


Figure 1.15: Count spectrum and Photon spectrum from Kiruna event with model spectra superposed [Foa et al., 1998].

ing electron distribution was found to be very different from that of the trapped population. The event was well modeled by a monoenergetic electron distribution at 1.7 MeV indicating that the bulk of the precipitation was at relativistic energies (Figure 1.15). The details of the modeling procedure are described in Chapter 4. We estimate that a rate of precipitation of 2×10^{17} electrons/s is required to account for the burst, which corresponds to an energy deposition of 6×10^{11} ergs/s. Particle measurements by geosynchronous spacecraft during the event indicate a flux of trapped MeV electrons sufficient to replenish the local field line by drift during the event. In addition, an increase in relativistic electron flux was not seen, thus it seems likely that the event was a result of scattering of the ambient population rather than local particle acceleration.

As discussed in Section 1.3.2, EMIC waves are a good candidate for pitch angle scattering > 1 MeV electrons. For the Kiruna event, assuming a wave period equal to the X-ray modulation period of 20 s, $E_{res} = 2$ MeV and $\Omega_i = 18$ rad/s for protons at L=5.7, Foat et al. [1998] found that resonance with EMIC waves would require plasma densities $\sim 10^4 \text{ cm}^{-3}$, about a factor of 100 higher than typical for the plasmasphere. However, Lorentzen et al. [2000] suggested that higher frequency waves (~ 1 s period) could be resonant with the electrons and this idea was supported by the observation of a small substorm injection about 24 minutes before the Kiruna X-ray event by both POLAR UVI and a Los Alamos geosynchronous spacecraft which were located near a magnetic local time (MLT) ~ 22 h. In particular, the LANL measurements indicated an increase in the 60 keV proton flux at this time. The drift time for 60 keV protons is consistent with the delay between the injection and the X-ray event and Lorentzen et al.[2000] suggested that these 60 keV protons drifted

to the balloon location, which if in a dense plasmasphere or detached plasma region would be unstable to generation of electromagnetic ion cyclotron waves. Resonant interaction between the EMIC waves and MeV electrons could then lead to pitch angle scattering and precipitation. This model was shown to be consistent with the duskside location and timing of the event as well as the precipitating electron energy. However, this model could not account for the temporal modulation of the X-ray count rate on either 10-20 s or 100 s timescales. Modulation of the wave growth rate by some as yet unknown mechanism could account for such temporal structure.

During the Kiruna MeV event, a field line resonance (FLR) was reported at about the same local time as the balloon [F. Fenrich, private communication] with frequency at 4.9mHZ roughly matching the frequency of modulation (100-200 sec) of the X-ray count rates. Foat et al. [1998] speculated that a disturbance associated with the FLR could have triggered motion of the plasmapause boundary or detachment of plasma resulting in the conditions necessary for EMIC wave growth and pitch angle scattering.

1.5 Scope of Research

This dissertation describes a Long Duration Balloon (LDB) experiment, MAXIS, which was designed to search for and study MeV bursts like the Kiruna MeV event in an effort to understand the loss rates and processes for relativistic radiation belt electrons. In the next chapter, the balloon instrumentation is described focusing on the germanium detector which was my primary responsibility. The detector was refurbished at Lawrence Berkeley Lab and electronics from a previous balloon flight were used, with the exception

of an analog peak detector board and digital interface which I built. I also performed all environmental and calibration tests of the GeD described and was assisted by J. Walawender for both the efficiency calibration and detector scans. For completeness, brief descriptions of the X-ray imagers and BGO scintillator which were built and calibrated at the University of Washington are also given. A summary of the balloon flight and data analysis techniques are also outlined in Chapter 2. Again all aspects of the data analysis were done by me with the exception of modeling the GeD and atmospheric response matrices, which were done by Dr. David Smith at U.C. Berkeley.

In Chapter 3, the details of the observations are discussed and the distribution of MeV precipitation events in magnetic local time and latitude are presented. In Chapter 4, techniques to model the X-ray spectrum are described and a model flux and energy spectrum is obtained for each event and compared with spacecraft measurements to determine the electron loss rate. In Chapter 5, the temporal structure of MeV events is analyzed and compared with ground-based and spacecraft observations of Ultra Low-Frequency (ULF) waves. Finally, in Chapter 6, a new instrument for imaging MeV electron precipitating is described. The results of this work are summarized in Chapter 7.

Chapter 2

The MAXIS Balloon Experiment

2.1 Introduction

Long duration balloon flights (LDBF) in Antarctica have been carried out almost every year since the early 1990's. The stratospheric winds carry the balloon around the pole allowing 1-3 weeks of observations from over 120,000 ft. altitude. Political issues prevented similar northern hemisphere flights for over a decade since the northern trajectory passes over Siberia. Finally, in 1997, the National Scientific Balloon Facility (NSBF) made its first successful test flight of a northern hemisphere long duration balloon flight (LDBF) from Fairbanks, AK, thus opening new opportunities for balloon based X-ray observations. The MAXIS (MeV Auroral X-ray Imaging and Spectroscopy) LDB experiment was designed to search for and study terrestrial MeV bursts like the Kiruna event and in June 1998, the balloon was launched from Fairbanks carrying the same germanium spectrometer (GeD) and pinhole X-ray (PXRI) camera that were flown in Kiruna. A coded mask X-ray imager (CXRI) was also added to increase the sensitivity of the imaging component of the

experiment. A northern hemisphere launch was considered ideal since the balloon, drifting westward around the pole, would most likely pass over Kiruna where the first MeV burst was detected. Unfortunately, there were problems with the balloon science stack, a piggyback experiment and the MAXIS power system from which the power system never recovered. Only 49 hours of data were recovered from this flight and no MeV bursts were detected. The experiments were severely damaged in the termination of the 1998 flight on Victoria Island in northern Canada; the parachute cut-away mechanism failed and the payload was dragged across the rocky tundra for about half a mile before finally landing in a lake. We were unable to determine the origin of the power system failure because of the damage but the experiments were rebuilt to fly from Fairbanks again in June 1999. A bismuth germanate (BGO) scintillator was also added to the payload to improve sensitivity at MeV energies. After flight readiness was declared and two launch attempts, the campaign was cancelled due to refusal of the Russian government to grant overflight permission, undoubtedly a result of the war in Kosovo at the time. Luckily, an opportunity opened to fly the payload in Antarctica during the 1999-2000 season and MAXIS was launched from McMurdo Station on January 12, 2000. The following sections describe the MAXIS instrumentation, calibration procedures and data analysis techniques. A summary of the MAXIS flight in January 2000 is also presented.

2.2 Instrumentation

MAXIS was designed specifically to study MeV electron precipitation and the instruments combine high spectral resolution, imaging and good sensitivity at MeV energies.

Instrument	Energy range	Energy Res.	Spatial Res.
GeD	20keV-10MeV	2.7 keV@835 keV	N/A
PXRI	20-200keV	10 keV@60 keV	10 km@100 km
CXRI	20-200keV	10 keV@60 keV	10 km@100 km
BGO	0.2-7MeV	100 keV @ 1 MeV	N/A

Table 2.1: MAXIS Instrument Specifications

The instrumentation is summarized in Table 2.1 and described below. Figure 2.1 shows a photograph of the MAXIS payload during pre-flight integration and testing. Figure 2.2 shows the X-ray imagers and BGO scintillator which are enclosed in a foam box for thermal insulation (A) and the germanium detector (B). The MAXIS instruments are mounted on the top platform of a gondola which is carried by a 29 million cubic foot helium-filled balloon. The weight of the instruments is about 300 lbs. and the total payload weight, including gondola, balloon control systems, batteries, and ballast is about 3800 lbs.

2.2.1 Germanium Spectrometer

Germanium Detector

Superb energy resolution (2.7 keV @ 835 keV) is obtained with a LN₂-cooled germanium detector (GeD). The detector is a 5.5 cm diameter × 5.5 cm unsegmented coaxial which has flown on multiple previous balloon flights including flights in both Antarctica and Kiruna. A 0.54 cm thick lead collimator limits the field of view to a 45° half-angle cone looking vertically upward. The detector is mounted in a 30 liter dewar containing enough LN₂ to cool the detector to 77K for 17 days at float altitude. Nitrogen is vented through a 5 psi pressure relief valve during flight.

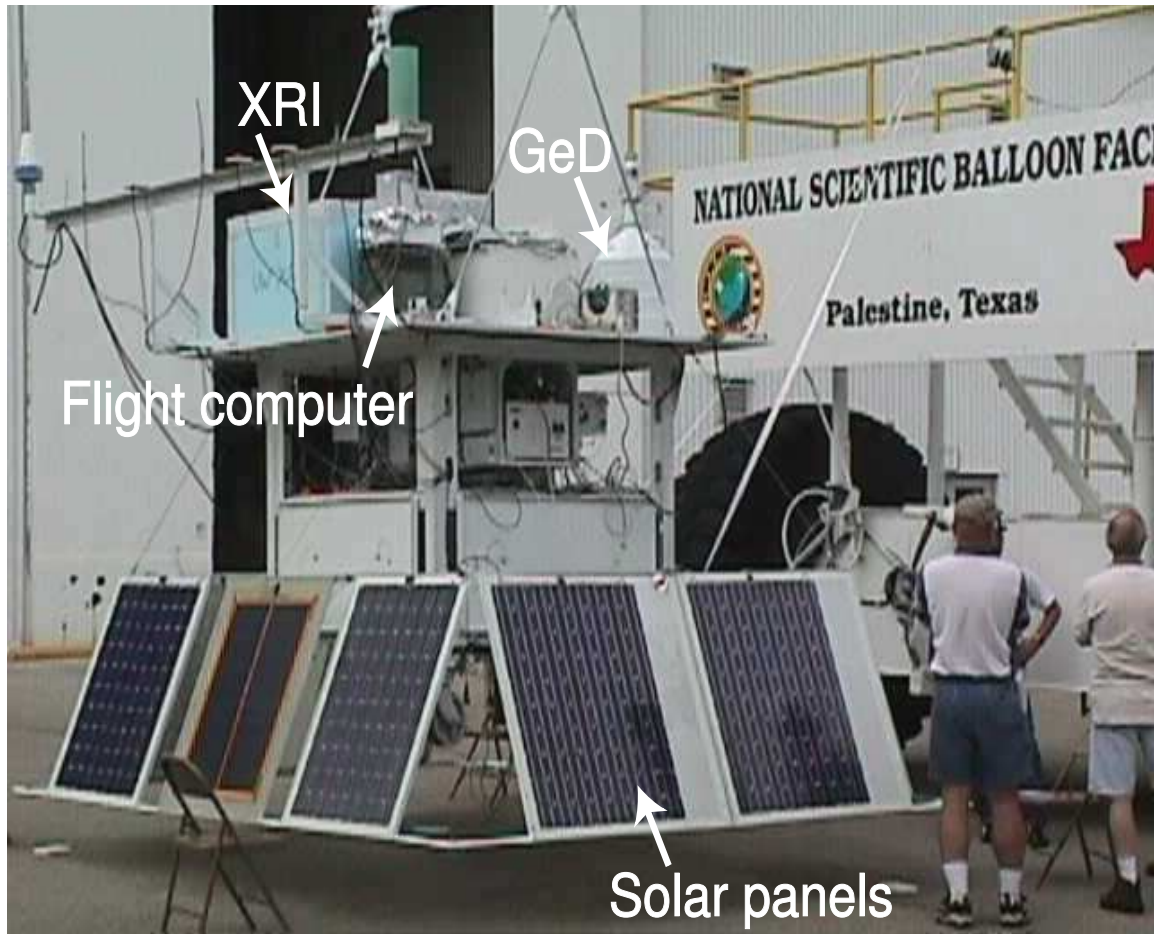


Figure 2.1: The MAXIS gondola during payload integration. The instruments were mounted on the top platform. The GeD and dewar are on the right, the X-ray imagers and BGO are under the foam box on the left.

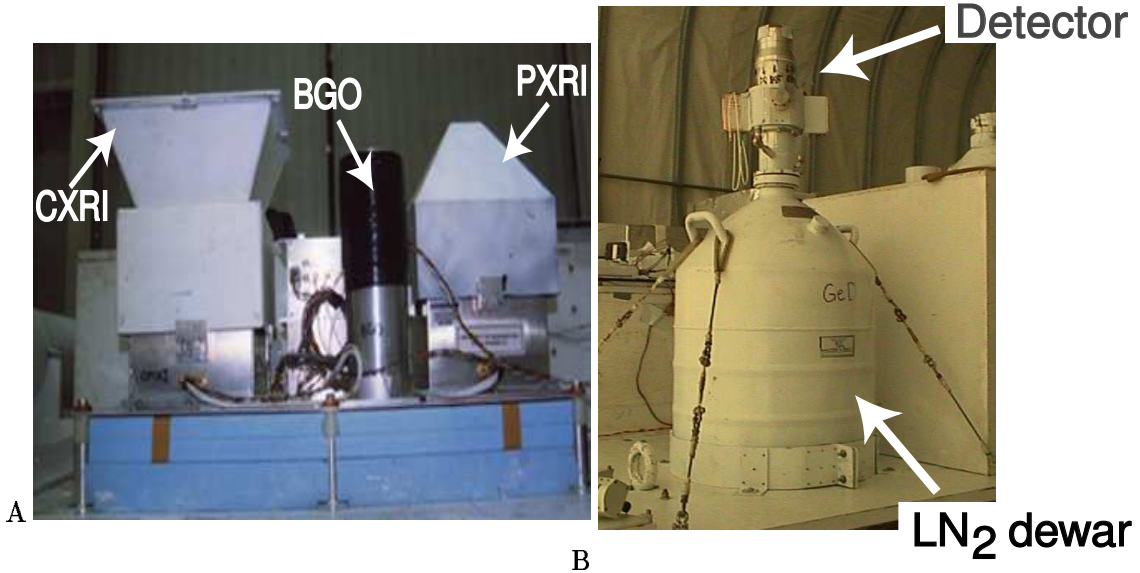


Figure 2.2: (A) Close-up of Imagers and BGO: PXRI(right), CXRI(left) and BGO (center). (B) The GeD

Analog Electronics

Processing of each detector event is carried out with standard electronics designed for high resolution gamma ray spectroscopy. The detector signal is first amplified by a charge sensitive preamplifier. Since any noise introduced at this stage will be further amplified down the electronics chain, the Johnson noise of the preamplifier, which dominates the system noise, is minimized by using a cooled Field Effect Transistor (FET). The output of the preamplifier is a “tail pulse” with a fast rise (comparable to the collection time in the detector) and a long decay to ensure complete charge collection.

The next stage is the shaper amplifier where each detector tail pulse is amplified further and shaped into a Gaussian signal with half-width (peaking time) of $4\mu s$. Shaping of the pulse preserves the signal amplitude (which contains the energy information) but reduces the effects of pulse pile-up by eliminating the long tail of the signal. Pulse shaping also

improves the signal-to-noise by reducing the signal bandwidth [Knoll, 1989]. The MAXIS GeD shaper has two outputs with different gains so that every detector pulse gives rise to two shaped pulses. The two gain channels are adjusted to record events between 20 keV-1.4 MeV for the high gain channel and 20 keV-10 MeV for the low gain channel. The shaped pulses are then passed to the peak detector where threshold circuitry determines the gain channel to be used. The peak detector sends a logic signal to the selected Pulse Height Analyzer (PHA) at the peak of the shaped pulse; events between 20 keV and 1.4 MeV are processed in one PHA and those between 1.4 MeV and 10 MeV in the other PHA.

The MAXIS GeD uses Wilkinson run-down type PHA's. A capacitor is charged by the shaped pulse until the peak detector logic signal is received. The capacitor is then discharged at a constant rate and since the total charge on the capacitor is proportional to the energy deposited in the detector, the time to fully discharge the capacitor is a measure of the energy. Pulses from a 4 MHz clock are counted for the duration of the capacitor discharge to measure the discharge time which then determines the PHA channel number for the event. The resulting 12 bit PHA channel number is sent to a Data Processing Unit (DPU) along with 4 ID bits.

Digital Interface and Data Collection

A digital interface provides data ready signals to the DPU for each PHA. The DPU reads the data and organizes a 512 byte data frame every 1/4 second. At count rates below 400 counts/s, every energy deposition in the detector is recorded with 12 bit precision (4096 channels with 0.3 keV resolution 20 keV-1.4 MeV and 2 keV resolution for 1.4 MeV-10 MeV). At higher count rates, energy depositions below 1.4 MeV are binned into 96 channel

spectra every 1/4 second with channel width increasing quasi-logarithmically from ~ 3 keV at 20 keV to ~ 43 keV at 1.4 MeV. The 16.384 kbits/s data stream is sent along with a clock signal to the main flight computer.

Instrument Livetime and Count Rate

In addition to PHA events, the GeD count rate and live time are recorded every 10 ms. The Low Level Discriminator (LLD) signal from the shaper is used to measure the count rate between 20 keV and 1.4 MeV. The instrument live time is measured using a combination of the pile-up inhibit signal from the shaper and the PHA busy signal. The pile-up rejector on the shaper board inhibits processing of further events for 22 μ sec after an event. The purpose of the pile-up rejector is to eliminate any signals riding on the tail of another signal which would produce inaccurate energy determination. However, this results in some events being thrown away and the instrument count rate and spectrum must be corrected for this effect. Events can be “lost” in two different ways at this stage. In the first case, for events separated by more than 4 μ sec but less than 22 μ sec, the first event will be retained but the second will be lost. If on the other hand, the second signal arrives before the peak of the first (within 4 μ sec), both events will be lost. In addition to the pile-up rejector, events can be lost due to the PHA processing time. The PHA processing time is energy dependent for the Wilkinson type PHA and this time is determined by the 4 MHz clock, in this case, 0.25 μ sec per PHA channel. Thus a 1.4 MeV (channel 4096) photon signal will take 1 ms to process for the high gain channel. The correction for dead time losses is discussed in more detail in Section 2.8.3.

The live time and LLD signals are sent with a 4 MHz clock signal from the PHA

to counters on the digital interface board. The counters are latched and read by the DPU every 10 ms and the 14 bit values incorporated into the data frame.

2.2.2 X-ray Imagers

A 15.24 cm × 15.24 cm × 0.64 cm thick NaI(Tl) crystal is the detector element for the Anger type pinhole X-ray imager (PXRI). A 2 cm diameter hole in the 0.32 cm thick lead collimator is situated at a height above the crystal chosen to give the instrument a 90° field of view. A plastic scintillator is used in anti-coincidence with the NaI to reject cosmic rays. Events from each of the four PMT's are recorded with 8 bit precision and compiled into a 512 byte data frame every 1/4 second. With statistics comparable to the Kiruna event, about 20 seconds are required to create an image with about 10° resolution [Lorentzen, 1999].

The CXRI is nearly identical to the PXRI just described but the collimator in this case allows ~50% transmission. The increased number of photons reaching the crystal in the coded mask configuration allows images to be made with higher time resolution.

Both the PXRI and CXRI were developed at the University of Washington and at the time of writing this dissertation, the data were not yet analyzed and are not presented.

2.2.3 BGO Scintillator

A 3" diameter by 3" BGO crystal increases the sensitivity of the experiment by a factor of 3-4 at MeV energies. A thin lead shield surrounding the crystal reduces background at low energies but the field of view at MeV energies is essentially open. Light collection is achieved with a single PMT and the BGO data are integrated into the data frames of one of

the imagers because a separate DPU was unavailable. One full BGO spectrum is acquired every 128 seconds over an energy range of 0.2-7 MeV.

The BGO scintillator was also built at the University of Washington. Background subtracted spectra were produced by Dr. Michael McCarthy and are presented in Chapter 4.

2.3 Power System

Power is provided to the entire science payload with 27 lithium battery packs (32V 30 amp-hour). Back-to-back diodes in the power cable allow for the use of a power supply during pre-flight testing. The 32 V input to the power system is down-converted to the necessary voltages for each payload component. A master power switch controls power to the entire system while individual switches for each instrument are controlled by command through the main flight computer. It was suspected that the master power control may have caused the failure in the 1998 flight so a timer was installed to automatically turn power on to the system 60 minutes after power is turned off (accidentally or otherwise). This timer circuit also employs a pressure switch so it will not be activated on termination of the flight.

2.4 Housekeeping Data

Accurate determination of the azimuthal orientation of the gondola is necessary to despin the images obtained with the PXRI and CXRI and is achieved with 8 sun sensors (built by Dr. Mike Pelling at UCSD). The sensors have partially overlapping 60° fields of view and are mounted on the corners of the gondola. A digital flag from each sensor indicates

if the sun is visible. The digital flag and an analog signal proportional to intensity at each sensor are recorded by the main flight computer every 10 seconds. Additional housekeeping read by the main flight computer includes temperatures from four temperature sensors mounted to the GeD electronics plate, power system, XRI electronics plate and main flight computer and the output voltage of each power converter. GPS position and pressure altitude are provided by the NSBF Science Instrument package (SIP) and these data are recorded in both the data frames of each instrument and a separate housekeeping frame.

2.5 Data Acquisition

2.5.1 Main Flight Computer

The three instrument data streams (each 16.384 kbits/s) and all housekeeping data are read by the main flight computer (a single board computer running DOS 5.0) where housekeeping frames, and all instrument data frames are stored to an 8.4 Gbyte hard disk. New data files are created every five minutes and named according to the time the file was opened. Time stamps are also embedded in every sixth data frame (every 1.5 sec) by the main flight computer along with other housekeeping data important for analysis (GPS, etc.). The disk is mounted in a pressure vessel held at 1 atm. and the pressure is monitored as part of the housekeeping data.

2.5.2 Telemetry

The entire data stream is sent at 56 kbits/s to an NSBF L-band transmitter when the balloon is in line-of-sight and the analog and digitized data are stored on the ground.

When the balloon is no longer in line-of-sight, the TDRSS satellite system is used to receive data and transmit commands at 4 kbits/s. Because the TDRSS data rate is limited and recovery of the payload not guaranteed, each five minute data file is prioritized by the on board flight computer into one of three priority levels based on the instrument count rates. These priority levels determine which data are sent to the SIP and telemetered. A housekeeping frame is also sent out every five minutes. The data are sent via serial link to the SIP where they are stored and telemetered.

Measurements of the battery voltage into the power system and power to the data acquisition system are also sent directly to the SIP science stack and telemetered through Inmarsat every 30 minutes. This allows verification independent of the flight computer that the system is receiving power. A master power command can also be sent to the power system through the science stack.

2.5.3 Ground Support Equipment

The TDRSS data are received at White Sands, NM, and sent on dedicated line to GSFC and to the NSBF in Palestine, Texas where they are displayed and stored by the GSE computer. Data can also be viewed in real-time from Antarctica, Berkeley, and Washington via the Internet (using LapLink). Commands can also be sent from the remote sites through TDRSS.

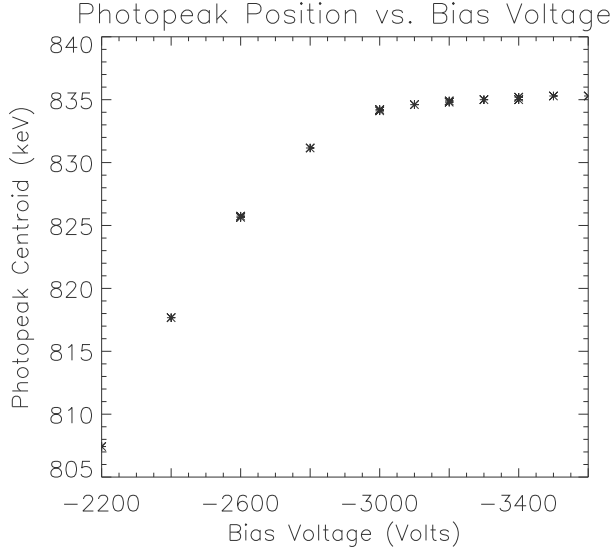


Figure 2.3: Determination of detector operating voltage: photopeak position for 835 keV ^{54}Mg line as a function of bias voltage.

2.6 GeD Calibration

Calibrations and environmental testing were performed in the laboratory both to characterize the instrument response and to ensure proper operation at balloon altitudes. These measurements are described in the following sections.

2.6.1 Detector Bias

To determine the optimal bias voltage for the GeD, a pulse height spectrum was obtained at varying voltages using ^{60}Co (1173, 1333 keV) and ^{54}Mg (835 keV) calibration sources. The position of each photopeak was determined by fitting a Gaussian lineshape (using Oxford WinMCA), and the centroid position is shown for the 835 keV line of ^{54}Mg as a function of bias voltage in Figure 2.3. At low voltages, incomplete charge collection results in the peak appearing at a lower PHA channel (calibrated to energy scale here).

As the voltage is increased, the peak moves up until the charge is fully collected. For the MAXIS flight, a bias voltage of -3200 V was selected based on these data.

2.6.2 Effective Area

Monoenergetic gamma rays incident on the detector can undergo several types of interaction which determine the total energy deposited in the detector. If the photon is photoelectrically absorbed either on its first interaction or after one or more Compton scatters, the full energy will be deposited. Both of these cases contribute counts to the “photopeak” in the spectrum. However, scattered photons may also escape the detector in which case some energy is lost. These events make up the “Compton continuum”. Since the cross sections for these interactions depend on the energy, the efficiency and effective area will be a function of energy.

To determine the true photon spectrum from any source, it is necessary to measure the efficiency as a function of energy in the lab and correct any spectrum for this instrumental response. Several radioactive sources with gamma ray lines at varying energies were used to carry out this measurement for gamma rays incident normal to the top of the detector. Figure 2.4 shows the effective area as a function of energy. In practice, we expect photons to be incident on the detector at many energies and angles. This would be cumbersome if not impossible to measure in a laboratory so the detector response is modeled using a Monte Carlo simulation. The solid line in Figure 2.4 shows the model response for photons incident normal to the detector. The measured efficiency data serve to check the accuracy of the modeled response. For a balloon-borne detector, it is also necessary to correct for the atmospheric response and this is discussed in Section 4.1.3.

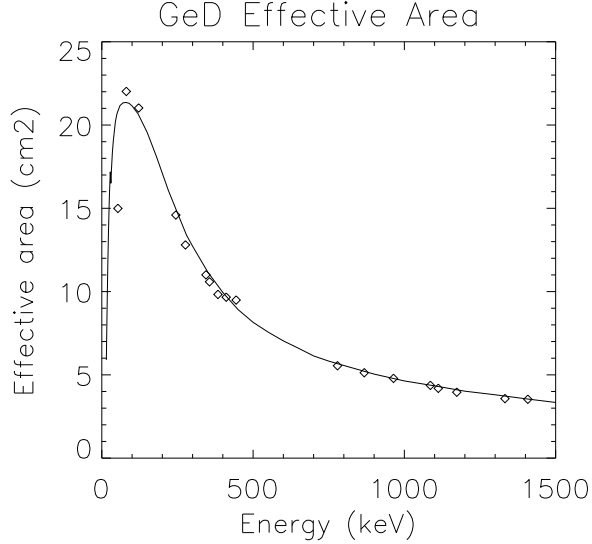


Figure 2.4: Detector effective area as a function of energy. The solid line shows the modeled response.

2.6.3 Detector Scans

In addition to the efficiency measurement described above, vertical and horizontal scans of the detector were performed to look for any properties of the detector that are not accounted for in the model such as dead layers. A horizontal scan of the top of the detector was performed manually over 37 grid points (every 0.5 cm) on the detector top using a collimated ^{241}Am source. The number of counts in the 17.6 keV photopeak across the detector is shown in the contour plot (Figure 2.5). For the vertical scan, a Ba-133 source was mounted in a computer controlled scanner and the photopeak intensity was determined at positions across the detector at six different energies (Figure 2.6). The detector is uniform except at the lowest energies where the decrease in counts at the top of the detector is apparent. This is either a result of a dead layer at the top of the detector or the mounting brackets that hold the detector in the cryostat, and is consistent with the discrepancy

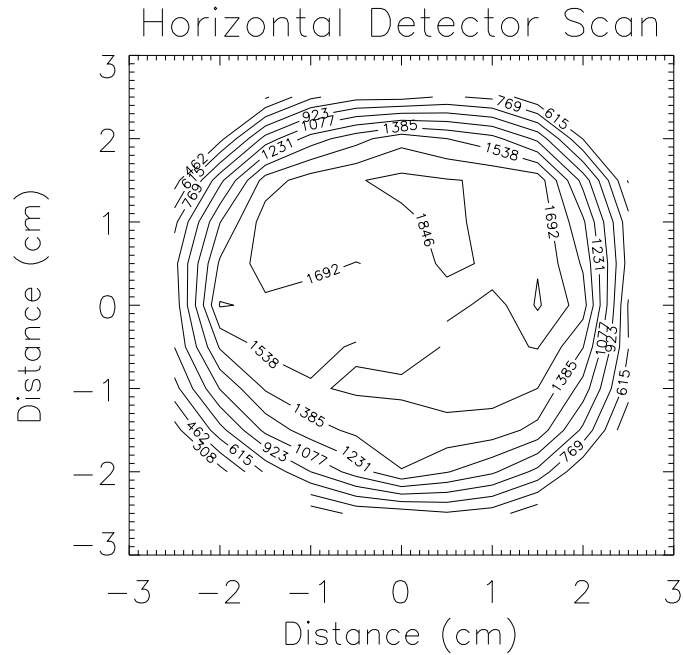


Figure 2.5: Horizontal scan across top of detector at 17.6 keV. Contour levels show counts in photopeak at each x-y position across the detector in 0.5 cm increments.

between the model and the measured efficiency at 60 keV. The rounded appearance near the top and bottom of the detector is a result of Compton scattered photons being lost.

2.6.4 Environmental Tests

In the balloon environment, instrumentation is exposed to a wide range of temperatures, pressures, and mechanical forces. The payload was designed to operate at float altitude (which is a very hot environment over Antarctica due to the reflection of sunlight off the snow), but must also endure many hours on the launch pad which is often below freezing. A series of thermal and vacuum tests were carried out to ensure the proper operation of all instrumentation during pre-launch, launch and float conditions.

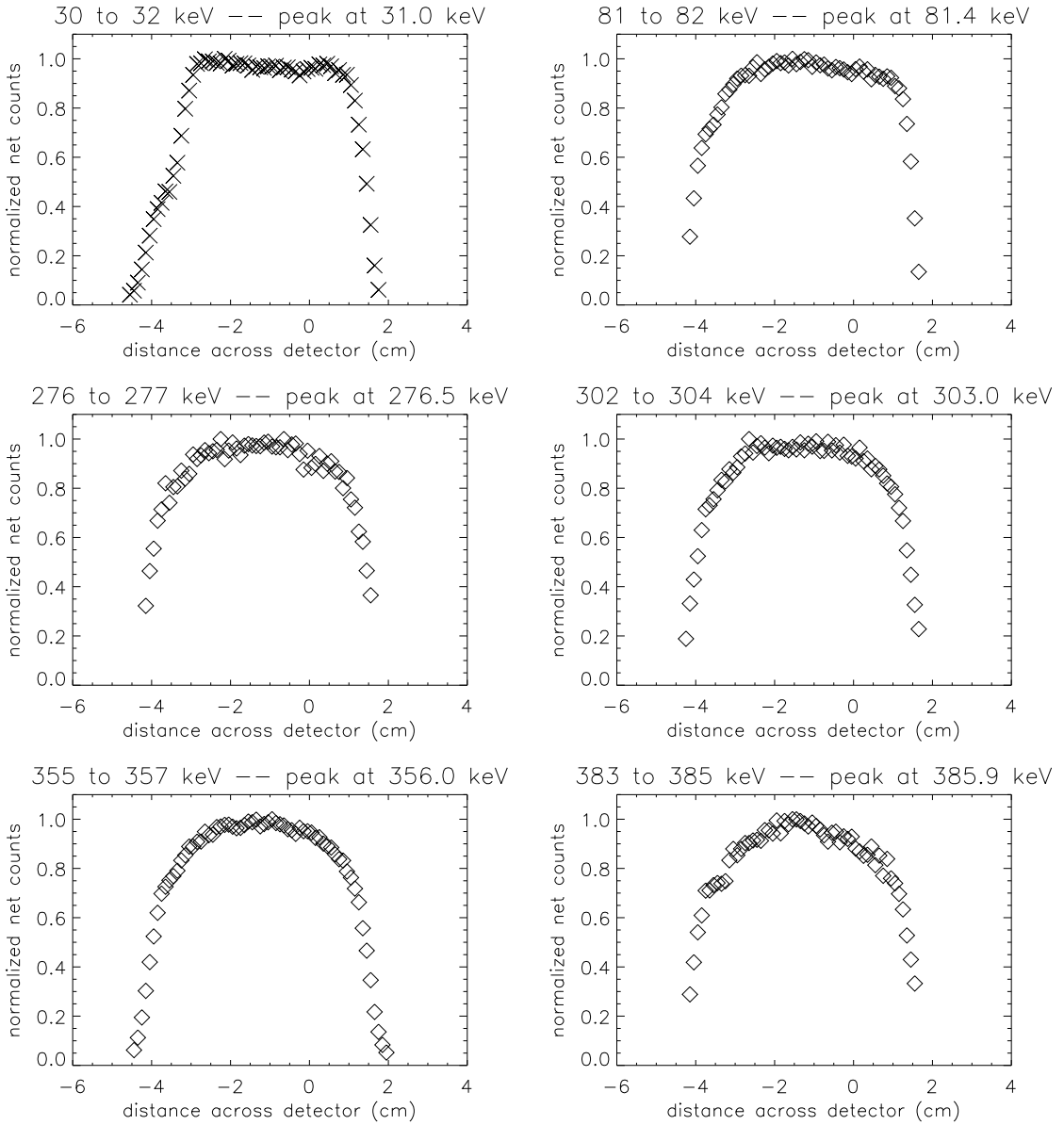


Figure 2.6: Vertical scan across detector at several different gamma ray energies. The x-axis shows position in mm with the origin located at the detector center and negative positions refer to the top half.

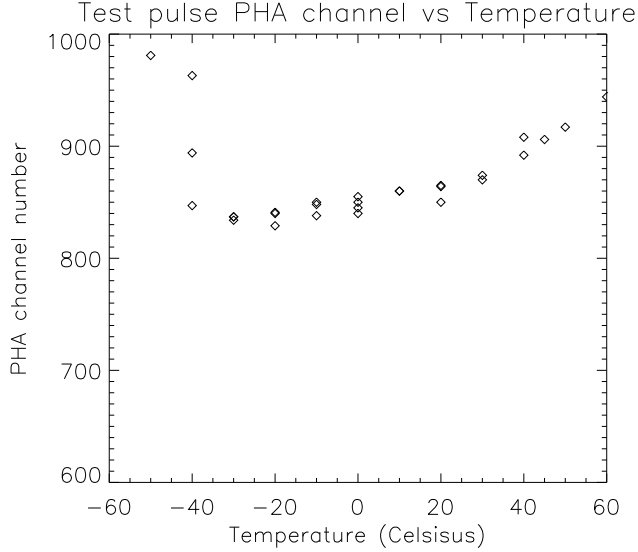


Figure 2.7: Test pulse PHA channel number as a function of temperature for three cold and two hot thermal cycles.

Thermal Tests

The GeD electronics can nominally operate over temperatures ranging from $\pm 50^{\circ}\text{C}$. A thermal test was conducted to ensure operation over this range and to measure changes in gain as a function of temperature. A signal generator tail pulse was used as the input and the PHA channel was recorded at 10°C intervals from -60°C to $+50^{\circ}\text{C}$. Figure 2.7 shows PHA channel versus temperature for two hot and three cold cycles. Below -40°C , the gain drifted severely but at all other temperatures, the gain changed in a repeatable way. In-flight data were used for the actual gain calibration and this is discussed further in Section 2.8.2.

Similar thermal tests were performed on the power system, flight computer, and other detector systems. The main temperature constraint of the experiment is the hard disks which can only tolerate temperatures down to 5° C .

Vacuum Tests

To simulate the different pressure conditions expected during the balloon flight, vacuum tests were also carried out. For the GeD, the most critical item for vacuum testing is the high voltage power supply since pressure at balloon altitudes (~ 5 mbars) is the most favorable for arcing. The high voltage supply and cables were first tested in a small vacuum chamber without the detector. The current drawn by the supply was closely monitored for pressures down to a few torr. The entire GeD system was then placed in an 8 ft. diameter vacuum chamber where the pressure was cycled between atmospheric and 1 torr multiple times over a 24 hour period. The high voltage supply current, detector resolution and LN₂ pressure were all monitored throughout the test.

2.7 Flight Summary

The MAXIS balloon payload was launched from McMurdo, Antarctica on January 12, 2000 after a month of weather delays (Figure 2.8). The balloon circumnavigated the south pole in 18 days covering magnetic latitudes ranging from 58°-90° south (Figure 2.9) with geomagnetic activity ranging from quiet to moderate storm levels. All instruments operated nominally until the 17th day of the flight when the GeD LN₂ supply was exhausted. The flight lasted longer than expected so data recording was also interrupted during the last two days to avoid filling the hard drive. The hard drive was recovered from the Antarctic plateau about 400 miles from McMurdo station resulting in the recovery of over 350 hours of data from each of four instruments. Several days of nearly continuous X-ray activity were recorded primarily in the week following a geomagnetic storm when Dst fell to -91 nT

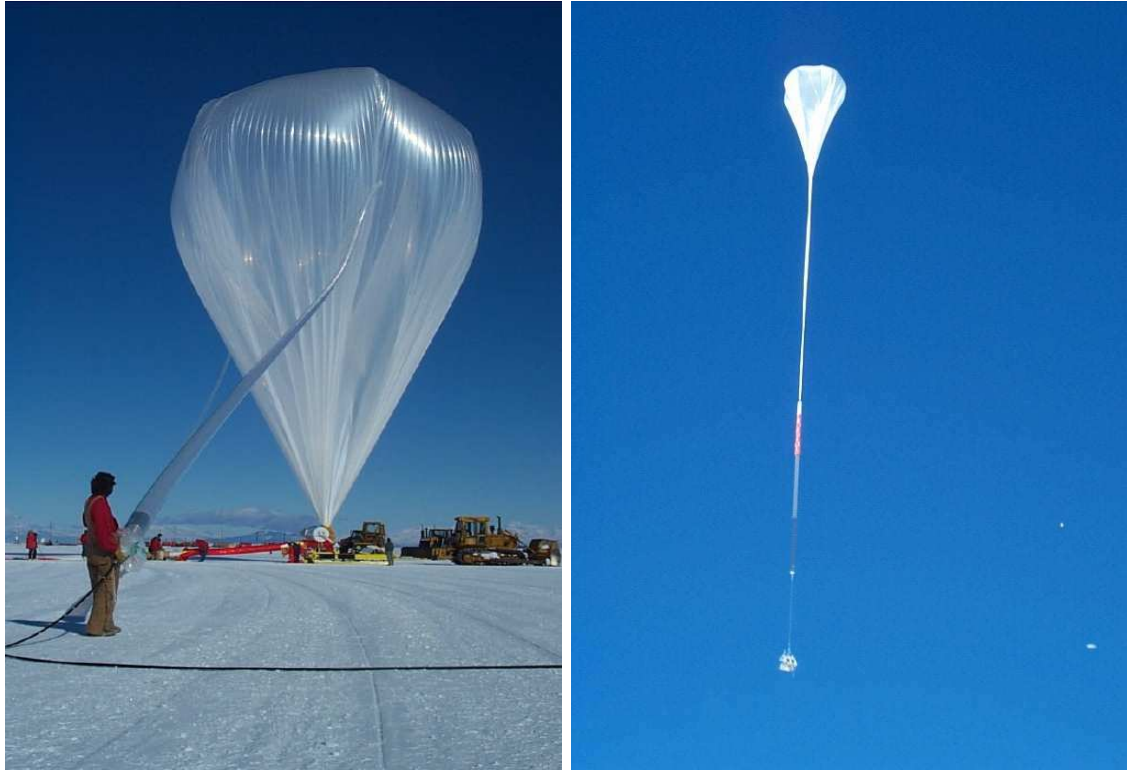


Figure 2.8: Inflation and launch of the MAXIS balloon.

(from Kyoto web site) on Jan. 23 (Figure 2.10).

2.8 Data Analysis

The GeD data were divided into event intervals based on the 20 keV-1.4 MeV count rate. In most cases, this division was made where the count rate returned to background levels. However, as shown in Figure 2.10, several hours of nearly continuous X-ray activity on January 23 and January 24 made this difficult since the count rate didn't fully return to background.

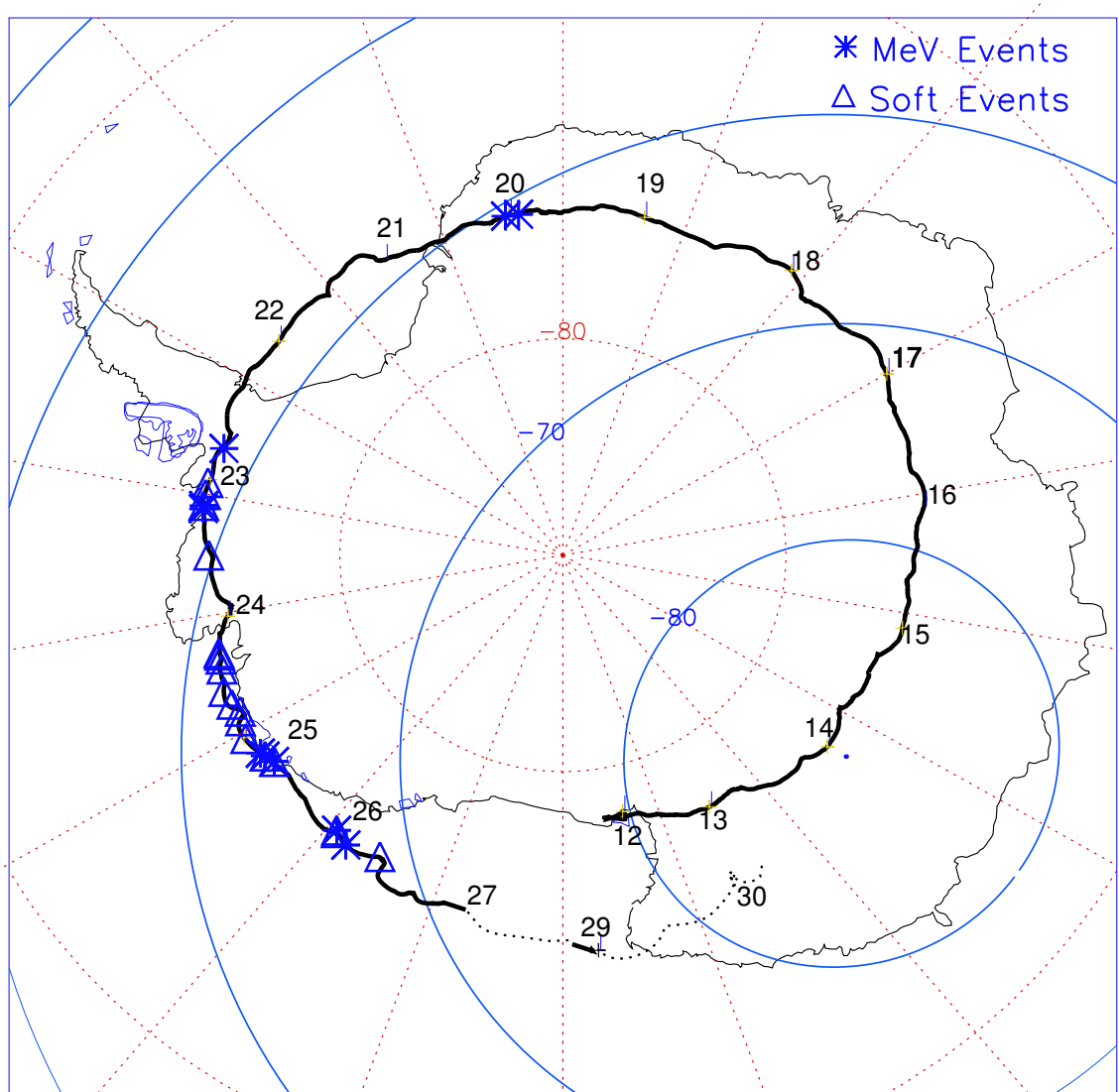


Figure 2.9: Trajectory of MAXIS balloon flight on an orthographic plot of the Antarctic continent with X-ray events indicated by asterisks and triangles. Also shown are lines of geographic longitude and latitude (dashed) and magnetic latitude (solid) every 10° .

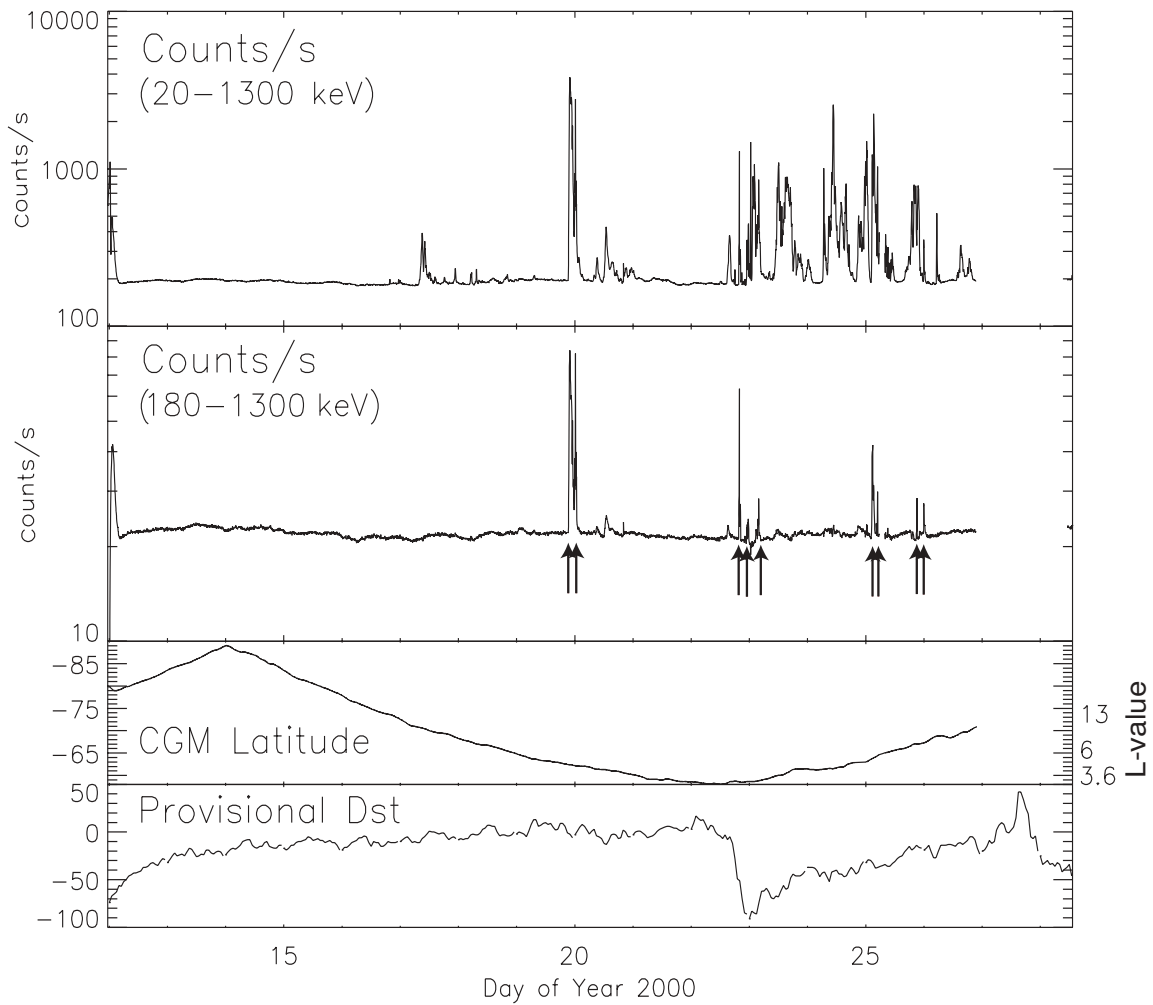


Figure 2.10: Top panels: GeD count rate for Jan.12-Jan.27, 2000. MeV events are indicated by arrows and described in Chapter 3. Bottom panels: CGM latitude and Dst index during the flight.

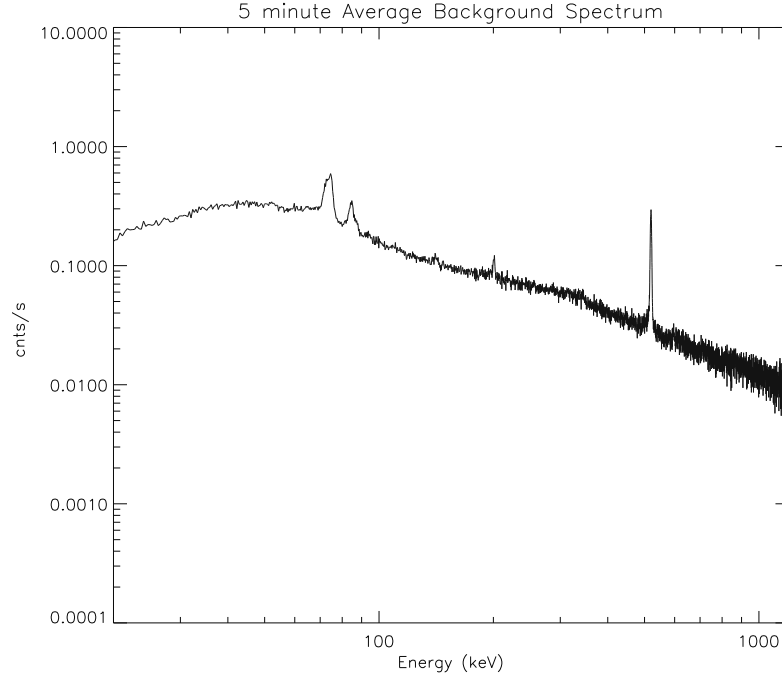


Figure 2.11: Example background spectrum

2.8.1 Background Selection

The X-ray background is due mainly to cosmic rays and depends on both geomagnetic latitude and altitude. Background intervals were chosen as either the pre-event or post-event \sim 1 hour interval closest in time to each event. An example background spectrum is shown in Figure 2.11. The \sim 75 keV and \sim 85 keV K-shell lines of the lead collimator, the 198.3 keV line from neutron inelastic scattering off ^{71}Ge , and the 511 keV atmospheric e^+e^- annihilation line are evident.

2.8.2 Gain Calibration

Figure 2.12 shows the GeD electronics temperature during a four day period of the flight. The temperature variations caused by the changing sun angle during each day give

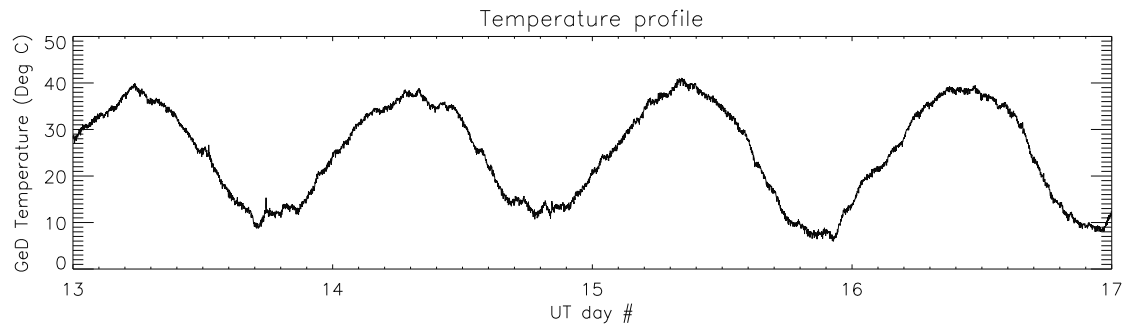


Figure 2.12: Temperature profile of GeD electronics during the first four days of the MAXIS flight.

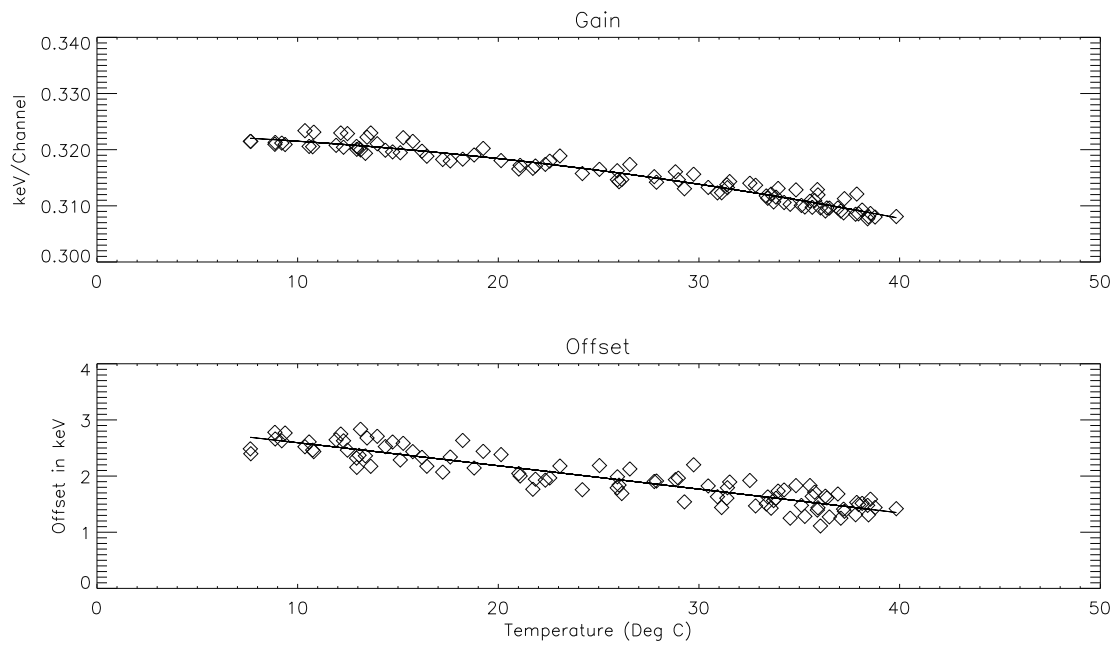


Figure 2.13: Gain and offset as a function of temperature. Solid line is quadratic fit.

rise to changes in gain of the electronics. During the first five days of the flight, the GeD count rate remained at background levels. To determine the gain calibration parameters, a spectrum was created for every five minute data file during this interval. A Gaussian was fit to the 511 keV annihilation line produced in the atmosphere and the 198.3 keV line for each file. Assuming a linear relation between PHA channel and energy, the gain and offset were then calculated using the line centroids from the Gaussian fits. Figure 2.13 shows the gain and offset as a function of temperature. Quadratic fits to the data are also shown and were used to calibrate all background and event spectra for the remainder of the flight. Note that it was not possible to calculate the gain and offset for each individual event spectrum because for any event with an average count rate greater than 400 counts/s, only 96 channel binned spectra were available and the energy resolution recorded for event spectra was not sufficient to carry out accurate spectral line fits. The gain calibration was applied using the average temperature for each five minute file during an event. After calibration, the spectra were re-binned into standard bins and summed to produce the count spectrum (counts/keV) over the event interval. Background spectra were created in a similar way but 4096 channels were retained until after the gain calibration.

2.8.3 Live Time

Before subtracting the background from each event spectrum, both must be corrected for dead time losses to convert the count spectrum from counts/keV to count/s/keV. As discussed in Section 2.2.1, events can be lost in several ways due to the processing time of the electronics. The GeD electronics most closely resemble a paralyzable system , for which the fractional live time can be estimated from the expression [Knoll, 1989]:

$$\text{fractional live time} = e^{-n\tau}$$

where n is the true count rate and τ is the dead time for each event. Since the MAXIS GeD uses a Wilkinson type PHA, the dead time, τ , is energy dependent and the total live time depends on the spectral distribution of events. The fractional live time for a given interval can be estimated based on the mean τ for a given spectral shape. For example, at background count rate (~ 180 counts/sec) the mean dead time for an event is $220 \mu\text{sec}$ giving a fractional live time of 0.96. Event spectra are much softer than the cosmic ray background and the mean dead time is $\sim 75 \mu\text{sec}$. The model would estimate a fractional live time of 0.93 for an event with a count rate of 1000 counts/s.

For the 1999/2000 MAXIS flight, a live time measurement was added to the electronics to make the correction for dead time losses more accurate and straightforward. However, the measured live times were roughly a factor of two larger than would be expected based on the model. This is probably due the LLD threshold being set below the peak detector threshold resulting in events that contributed to dead time, but not to the measured spectrum. Correcting the spectra using the measured values often resulted in an over-subtraction of the background which was easily detected by examining variations of the (assumed) steady 511 keV annihilation line.

Because the determination of the actual live time is dependent on the energy spectrum and the measured live time produced unsatisfactory results (i.e an over-subtraction of the background), the 511 keV line was used instead to correct the GeD spectra. The 511 keV line is produced by cosmic rays in the atmosphere and the MeV precipitation events contribute a negligible amount to the 511 keV flux ($\leq 10^{-5}$ counts/s assuming the flux for

the Kiruna event compared to \sim 6 counts/s from cosmic rays). Therefore, we can assume the 511 keV line flux remains unchanged during an event and use its flux to correct for live time. Since the event spectra were binned into 96 channel spectra, the 511 keV line is easily contained in one bin. The flux in the line was determined by fitting the continuum below the line and subtracting the continuum contribution from the counts in the 511 keV bin. A scale factor was then determined by dividing the event line flux by the background line flux and the event spectrum was scaled to the background spectrum before subtracting.

For events extending to sufficiently high energies, the spectrum was extended above 1.3 MeV using data from the low-gain channel. The low-gain channel calibration parameters were first determined as a function of temperature using the 1440 keV K line from a weak calibration source (imitation salt) flown with the GeD. Because the two gain channels share only some electronics, their dead time corrections were different and the low-gain channel dead time was not well characterized prior to the flight. Therefore the low-gain channel was scaled to match the high-gain channel by fitting a power law to each spectrum near the boundary. In addition, the number of counts in the bins nearest the boundary between gain channels were often much lower than expected so these were replaced using the same power law fits.

2.8.4 Instrument and Atmospheric Response Matrices

After the background has been subtracted, the event count spectrum must be corrected for scattering and attenuation in both the instrument and atmosphere to obtain the photon spectrum. As discussed in Section 2.6.2, the GeD instrument response was modeled using a 20 component mass model in a Monte Carlo simulation. Scattering in the

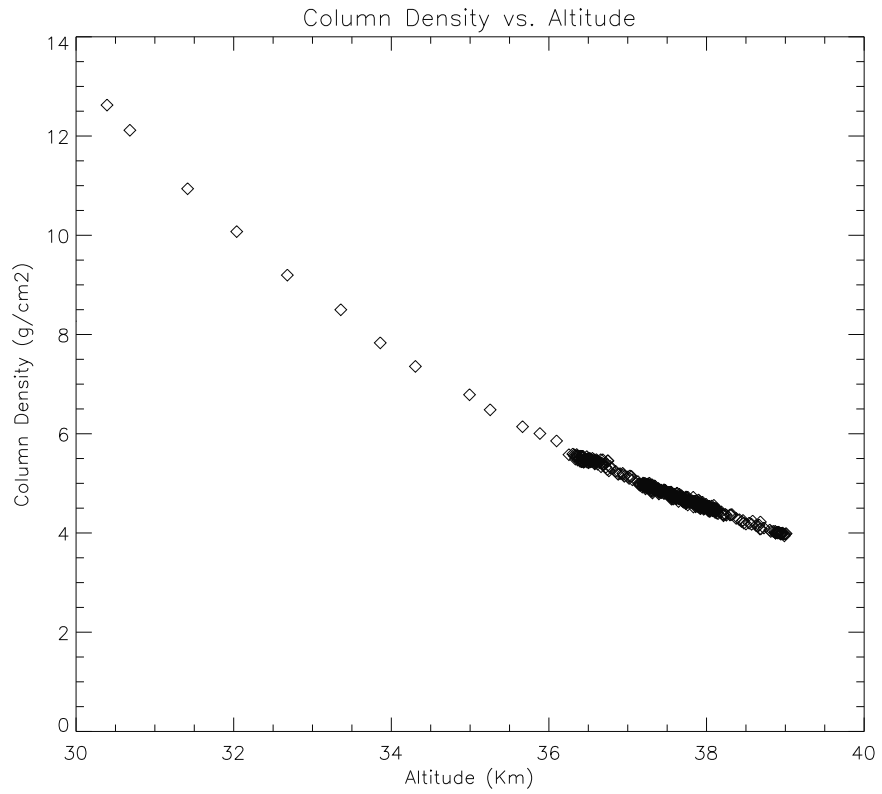


Figure 2.14: Atmospheric depth measured every hour. The points below 36 km were measured during the ascent of the balloon

atmosphere depends on the column density of atmosphere above the detector. The pressure at the balloon altitude was recorded throughout the flight and can be easily converted to atmospheric depth which in this case is the same as column density since the instrument is pointed to zenith. Figure 2.14 shows the column density as a function of GPS altitude during the flight. A Monte Carlo simulation was performed to model scattering in the atmosphere and is described in detail in Section 4.1.3

Chapter 3

MAXIS Observations of MeV Electron Precipitation

During its January 2000 balloon flight, MAXIS detected nine MeV X-ray bursts along with many hours of lower energy X-ray activity. Figures 3.1-3.4 show the X-ray count rate from January 15-26, 2000 in two energy channels. The MeV events are evident in the 180-1300 keV channel (bottom) and are indicated by arrows. These events are characterized by a very hard X-ray spectrum similar to the Kiruna event (see Section 1.4) which indicates precipitating electrons with relativistic energies. In this chapter, the method used to identify MeV events and establish that they are a distinct class of precipitation rather than the high energy tail in a distribution of softer precipitation is outlined. The distributions of MeV events in magnetic local time (MLT) and L-shell are then presented and compared with spacecraft observations (Sections 3.2, 3.3). Finally, in Section 3.6 the occurrence of MeV events in relation to geomagnetic activity is discussed.

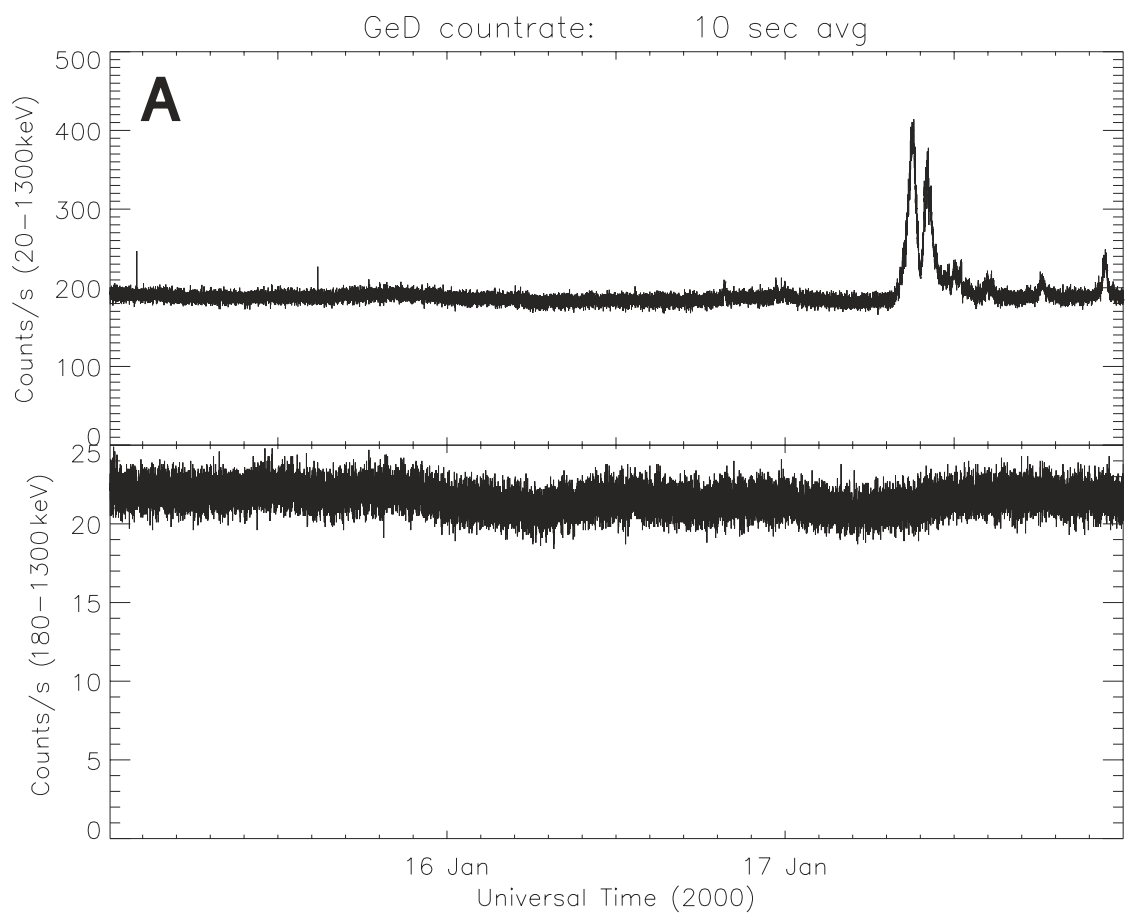


Figure 3.1: GeD count rate on Jan.15-17, 2000 in two energy channels: 20-1300 keV (top) and 180-1300 keV (bottom).

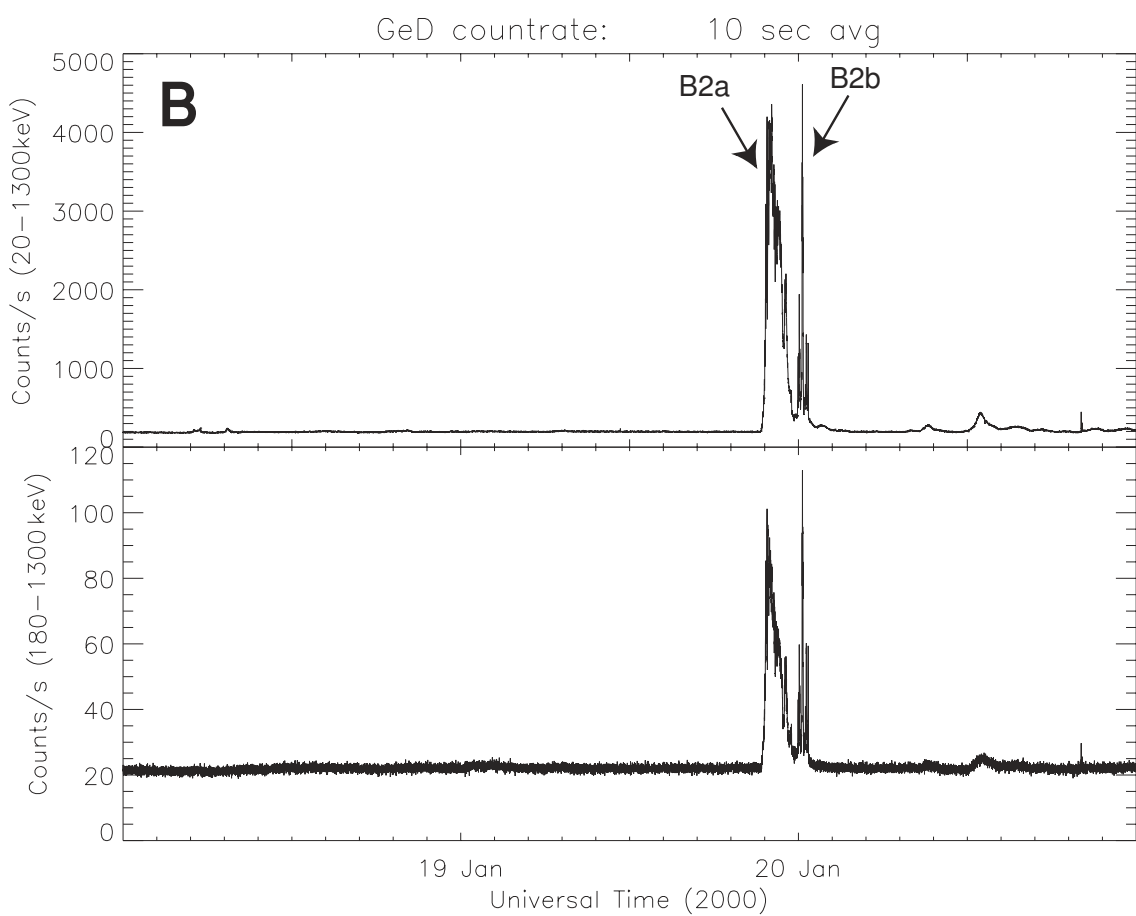


Figure 3.2: GeD count rate on Jan.18-20, 2000 in two energy channels: 20-1300 keV (top) and 180-1300 keV (bottom). MeV events are labeled and indicated by arrows.

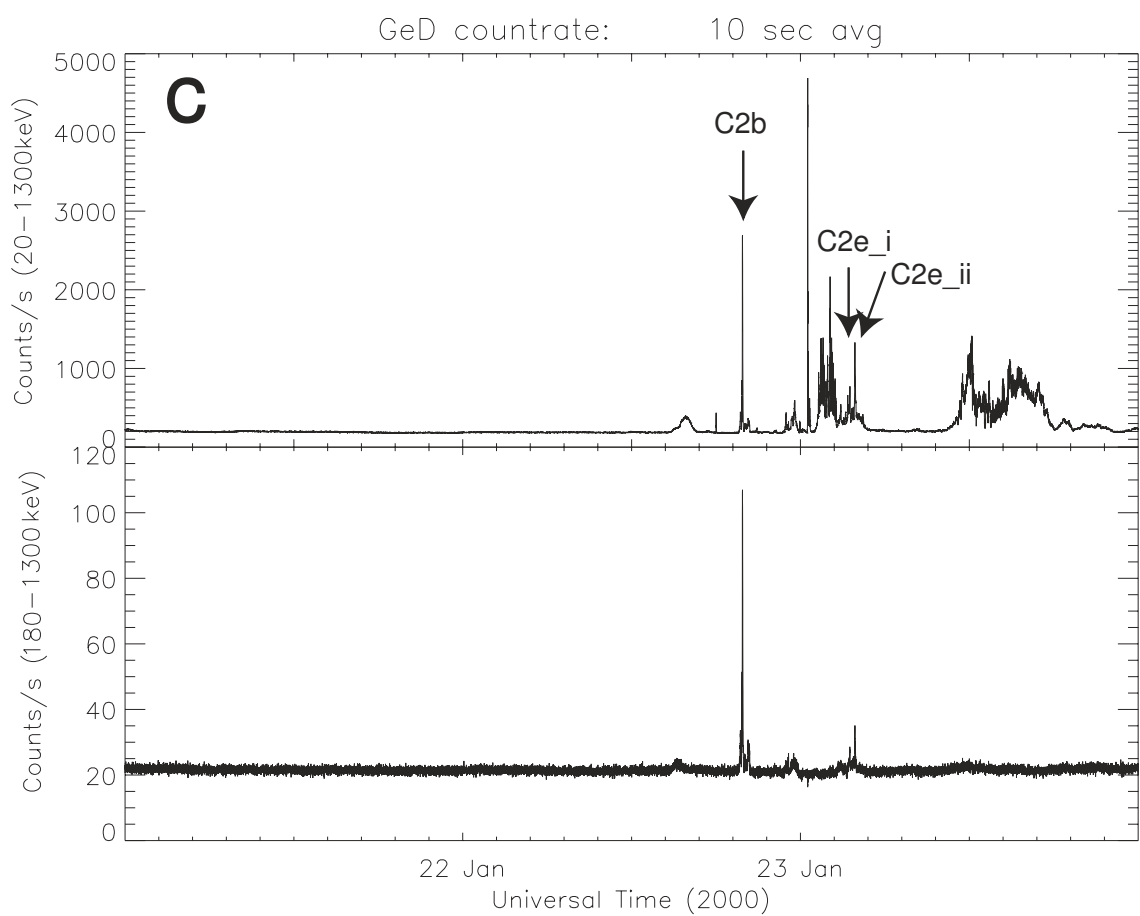


Figure 3.3: GeD count rate on Jan.21-23, 2000 in two energy channels: 20-1300 keV (top) and 180-1300 keV (bottom).

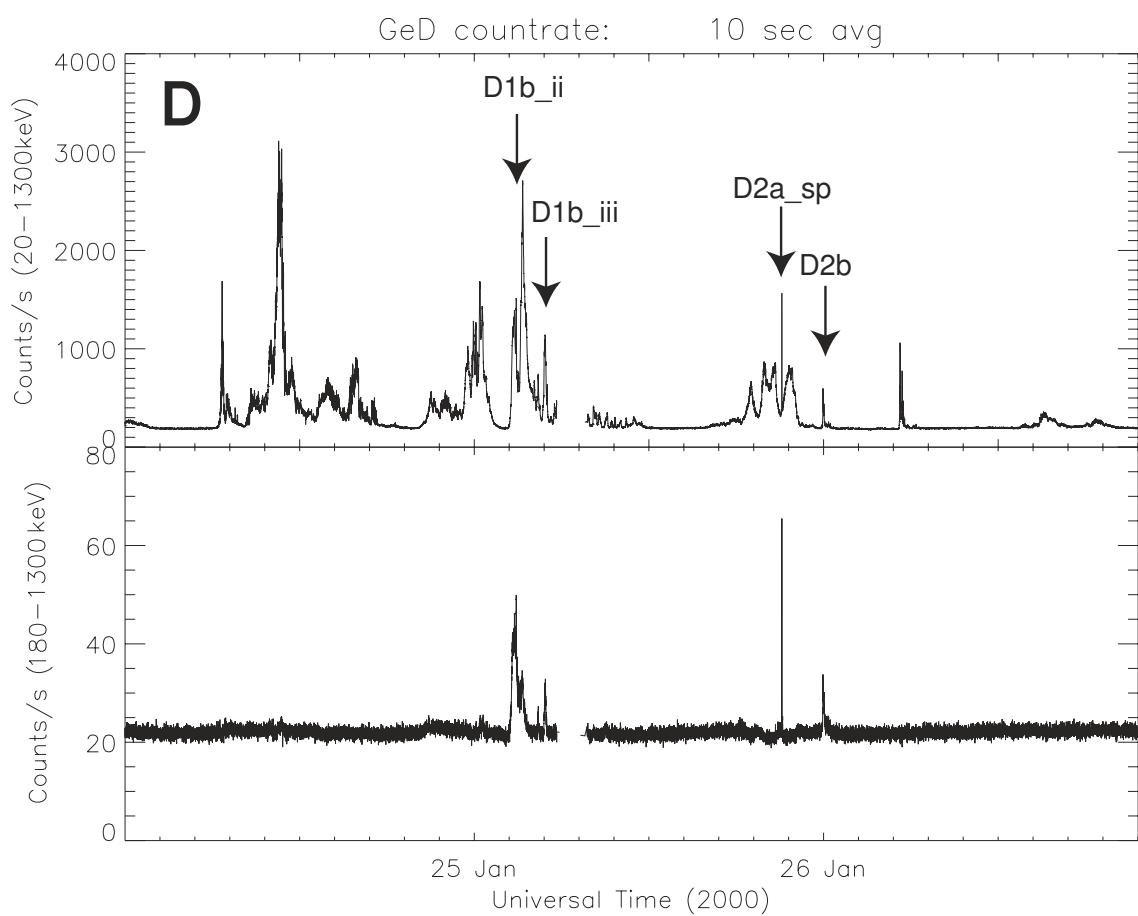


Figure 3.4: GeD count rate on Jan.24-26, 2000 in two energy channels: 20-1300 keV (top) and 180-1300 keV (bottom).

Name	DOY	Time (UT)	Lat.	Long.	Alt. (km)	L	MLT	α
B2a	019	2120-2345	-74.0	-7.17E	36.5	4.7	1920-2145	-2.2
B2b	020	2345-0045	-74.0	-9.3E	36.0	4.6	2150-2240	-2.0
C2b	022	1942-1957	-73.9	-72E	38.2	3.7	1530-1545	-1.7
C2c_v	023	0025-0045	-73.6	-78.1E	37.9	3.7	2000-2020	-5.9
C2d	023	0100-0235	-73.6	-80.1E	37.7	3.72	2031-2206	-4.1
C2e_i	023	0320-0325	-73.6	-81.9E	37.5	3.74	2247-2252	-2.4
C2e_ii	023	0325-0405	-73.6	-82.4E	37.6	3.75	2251-2331	-2.4
C3a	023	1100-1330	-73.0	-90.0E	37.4	3.96	0612-0842	-3.3
C3b	023	1330-1800	-74.5	-96.5E	37.8	4.23	0830-1300	-3.6
C4a_i	024	0625-0655	-74.8	-106.3E	36.0	4.37	0103-0133	-3.6
C4a_ii	024	0655-0720	-73.8	-106.7E	35.9	4.38	0132-0157	-3.4
C4b_i	024	0800-0930	-73.8	-107.4E	35.9	4.41	0236-0406	-3.4
C4b_ev	024	0930-1300	-73.7	-109.0E	36.3	4.45	0402-0732	-3.6
C4c_i	024	1300-1500	-73.4	-112.5E	37.4	4.51	0724-0924	-3.6
C4c_ii	024	1500-1655	-73.5	-114.9E	38.2	4.65	0919-1114	-3.7
C4c_iii	024	1655-1725	-73.7	-116.5E	38.4	4.78	1112-1142	-3.5
D1a_i	024	1910-2250	-73.5	-117.9E	38.4	4.80	1323-1703	-3.3
D1a_ii	024	2250-0150	-73.3	-120.8E	38.6	4.90	1657-1957	-3.5
D1b_i	025	0225-0305	-73.5	-124.0E	38.5	5.14	2026-2106	-2.1
D1b_ii	025	0305-0405	-73.6	-124.8E	38.2	5.22	2105-2205	-3.2
D1b_iii	025	0440-0505	-73.8	-126.4E	37.8	5.39	2237-2302	-2.8
D2a_ev	025	1800-2250	-73.5	-141.6E	38.0	6.58	1124-1614	-4.7
D2a_sp	025	2105-2110	-73.6	-141.4E	38.2	6.6	1430-1435	-2.1
D2b_ev	025	2355-0005	-73.3	-144.0E	38.4	6.76	1653-1724	-1.8
D2c_ev	026	0510-0540	-73.7	-149.5E	38.0	7.64	2219-2249	-3.6

Table 3.1: MAXIS event intervals with peak count rate > 500 cps

3.1 Event Classification

The data were divided into 25 event intervals as described in Section 2.8 and average background subtracted event spectra were obtained for each interval (Section 2.8). Only event intervals with peak count rate > 500 cps were chosen for analysis. Table 3.1 lists the time, geographic location, magnetic local time (MLT) and L value from the International Geomagnetic Reference Field (IGRF) model for 2000 and spectral power law index, α ,

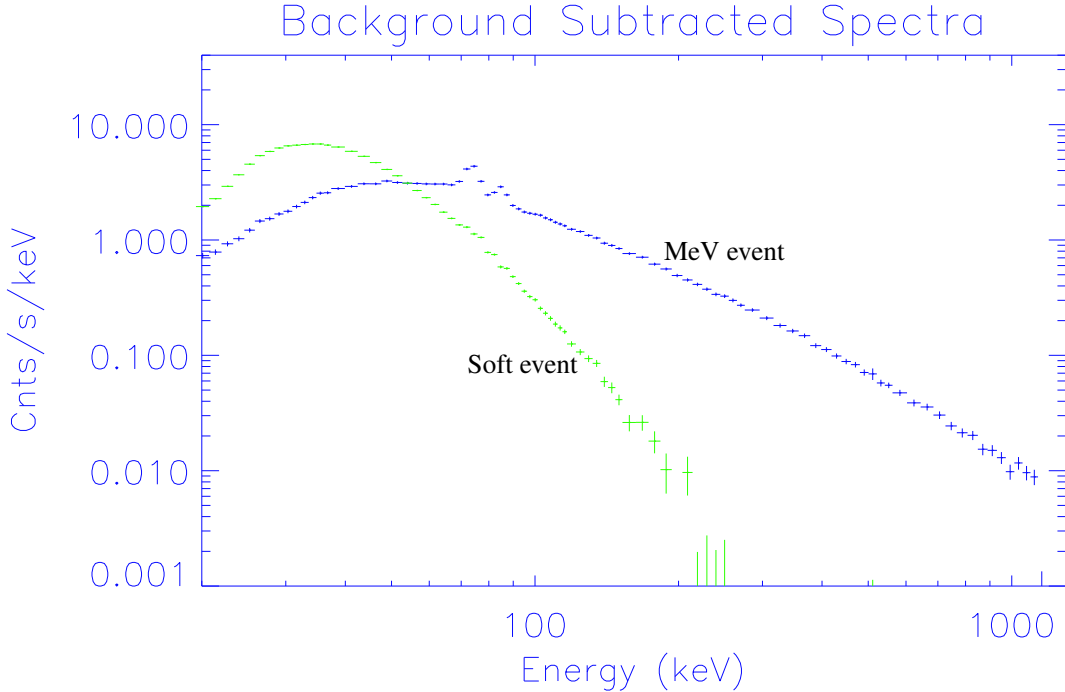


Figure 3.5: Background subtracted spectra for an MeV event and a soft event. The lead collimator lines are still evident in the background subtracted MeV event spectrum since the line strength is actually increased by the MeV event.

(described below) for each event interval. The event names simply reflect the method used to initially divide the data into smaller and more manageable intervals. The data were first divided into four intervals A-D and then subsequently divided into sub-intervals (i.e. B2), sub-sub-intervals (i.e. B2a) and even finer intervals (i.e. B2a_i).

Before analyzing the MeV events observed by MAXIS in detail, it was necessary to find an objective method for identifying MeV events. In most cases, distinguishing MeV events from softer precipitation is straightforward because the shape of the X-ray spectrum is very different as indicated by Figure 3.5 which shows spectra for a soft precipitation event and an MeV event. Like the 1996 Kiruna event, MeV events have a very flat (hard)

spectrum and significant flux extending to MeV energies while the lower energy events have no significant flux above 200-300 keV. However, MAXIS also observed several events with spectra of intermediate hardness making these events more difficult to classify. The intermediate events are due either to precipitation of medium energy electrons or to MeV and soft precipitation occurring simultaneously. The former would imply that the MeV and soft events are not distinct, rather there is a continuum of precipitating electron energies. It is important to establish whether there are two distinct classes of precipitation caused by different processes or whether the MeV events are just the high energy tail in a distribution of low energy precipitation (as would be suggested by a continuum of spectral shapes).

On January 25, MAXIS detected a short MeV event that occurred in the middle of a longer period of slowly varying lower energy precipitation as shown in Figure 3.6. The spectrum during the MeV event is nearly identical to that of the Kiruna event at high energies but there is an additional soft component at low energies indicating that the MeV event is superposed on the low energy precipitation. The difference in both the spectrum and temporal profile between the low energy and MeV events suggests that two different mechanisms are acting to precipitate particles simultaneously.

In order to characterize each event spectrum, a power law was fit to each between 100-180 keV to obtain the power law index, α . This energy range was chosen because the statistics were good enough to obtain a satisfactory fit even for soft events and high enough that the power law index isn't affected by the presence of a soft component. The power law index in this energy range picks out spectra with a hard tail independent of the presence of a soft component.

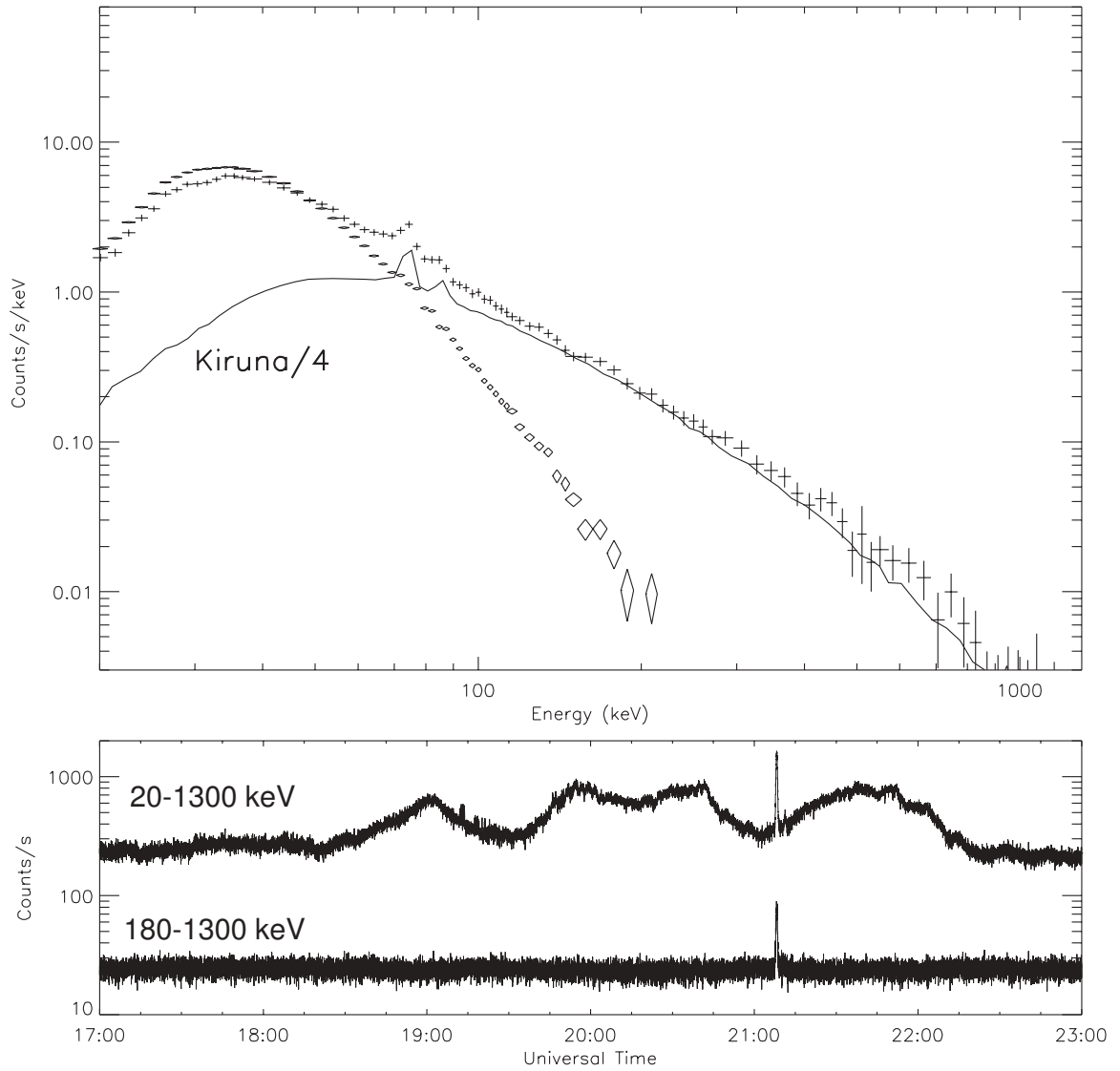


Figure 3.6: Spectrum and count rate for events on January 25, 2000. The short spike evident in the 180-1300 keV count rate is the MeV event (crosses) and occurred during a period of low energy precipitation (diamonds).

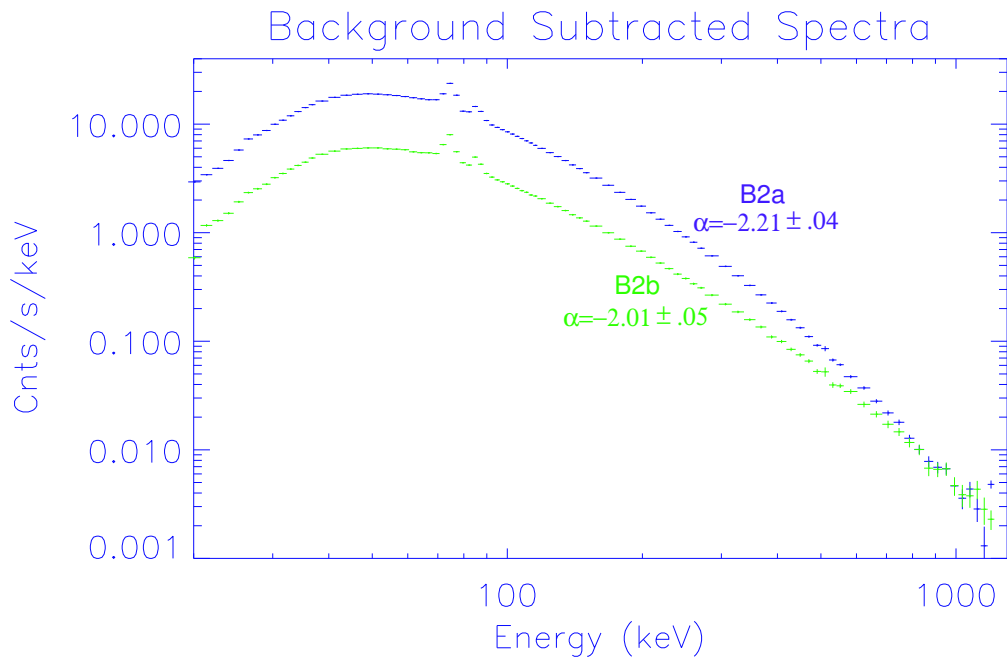


Figure 3.7: Count spectra and power law index between 100-180 keV

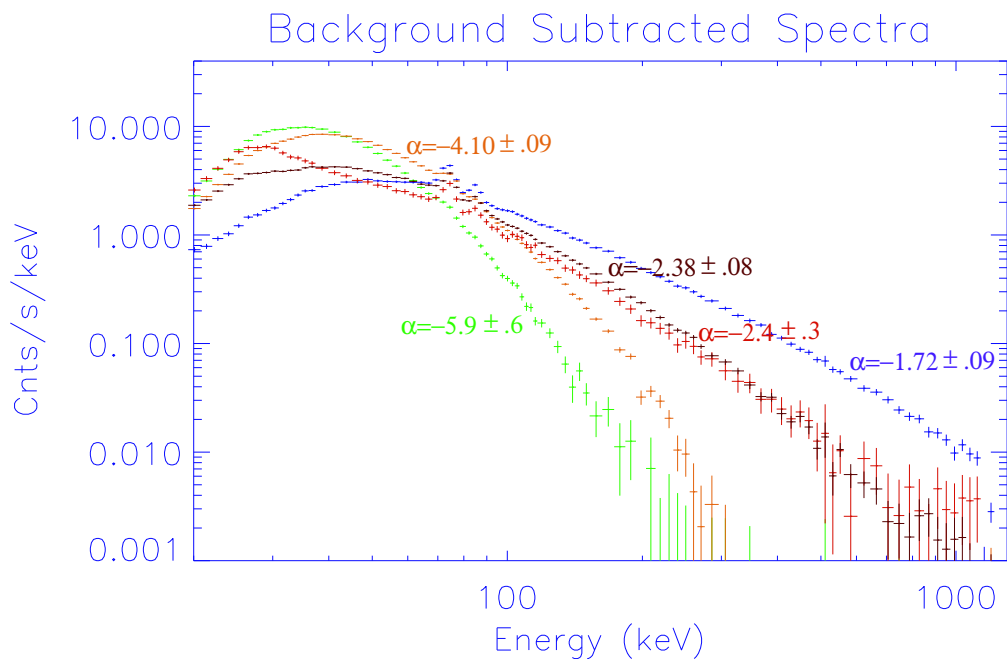


Figure 3.8: Count spectra and power law index between 100-180 keV

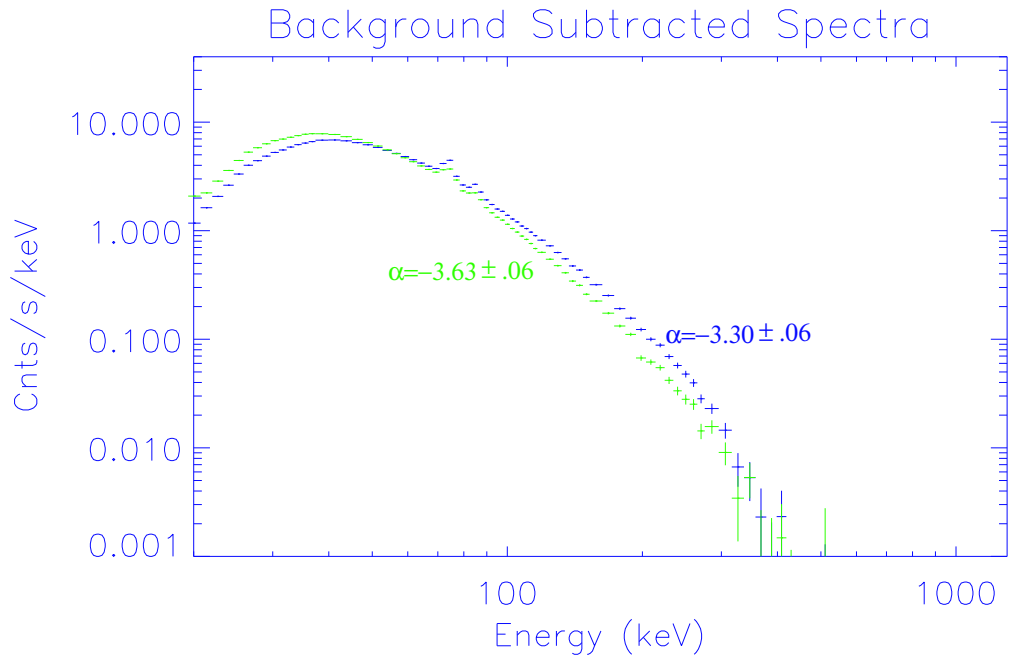


Figure 3.9: Count spectra and power law index between 100-180 keV

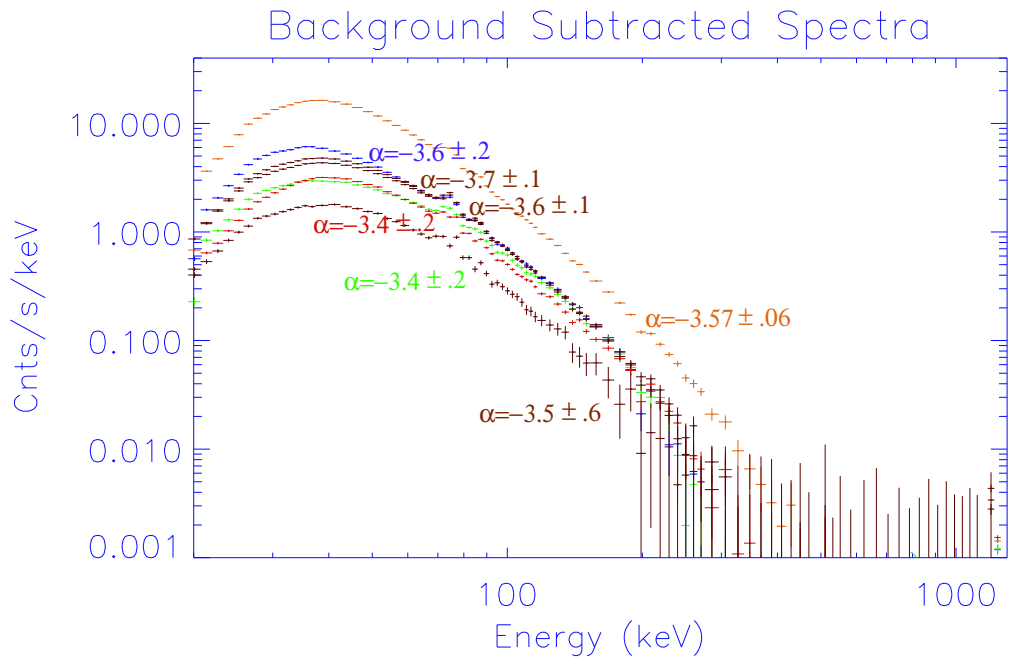


Figure 3.10: Count spectra and power law index between 100-180 keV

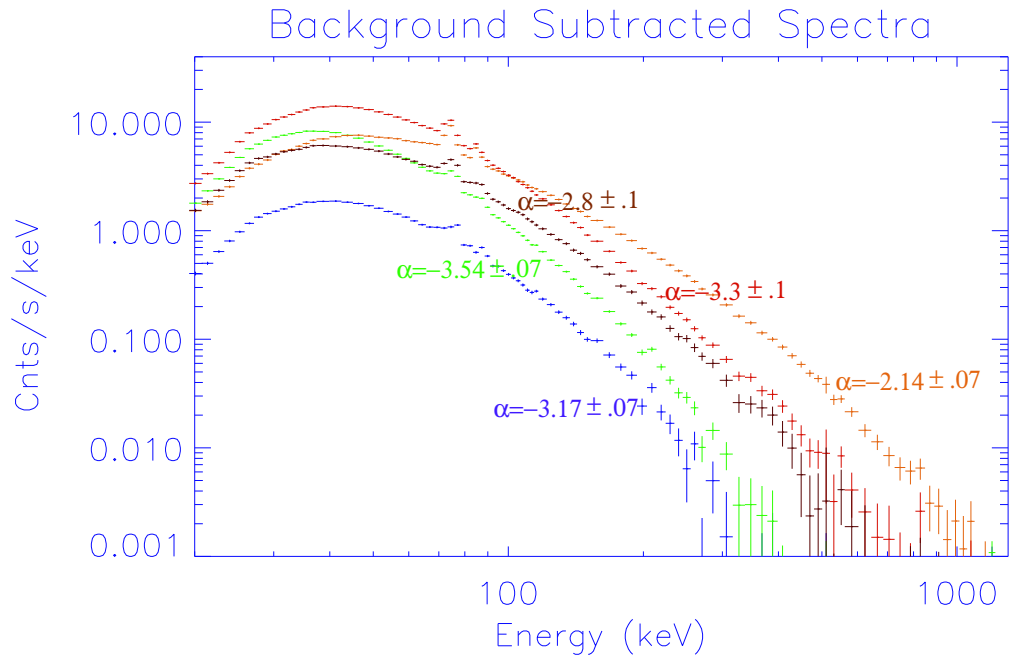


Figure 3.11: Count spectra and power law index between 100-180 keV

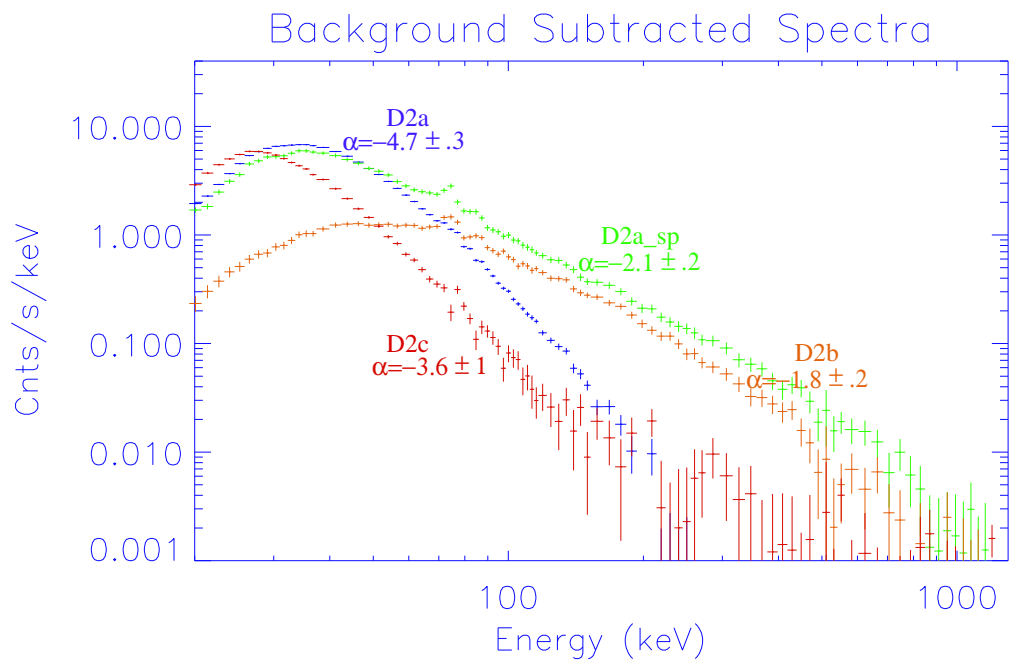


Figure 3.12: Count spectra and power law index between 100-180 keV

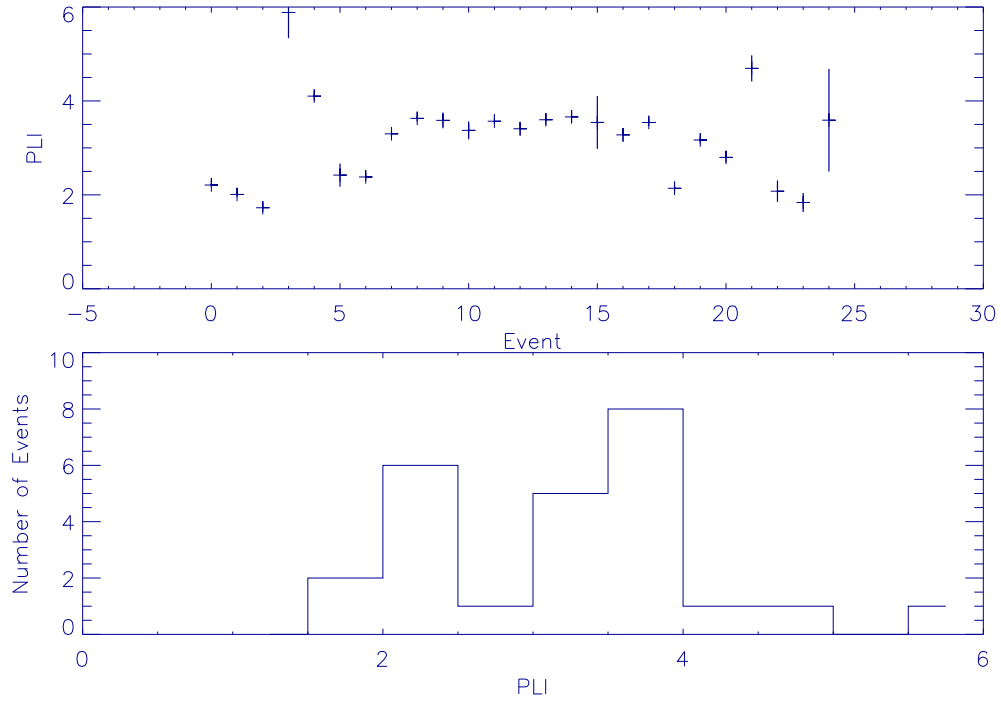


Figure 3.13: Spectral power law index (PLI) for each event and histogram for all of the 25 MAXIS event intervals

Figures 3.7-3.12 show spectra for every MAXIS event along with the power law index in the 100-180 keV band in each case. The power law index is shown in Figure 3.13 (top panel) along with the error in the fit for each of the 25 MAXIS events. Also shown is the histogram of α for all the events (bottom panel). The events were found to fall into two distinct groups with α peaking ~ 2 for the MeV events and ~ 3.5 for the soft events. There is also the suggestion of a third class with larger $\alpha \sim 5-6$ indicating very soft spectra. Two examples can be seen in Figure 3.8; the green points show a very soft spectrum with $\alpha = 5.9$, and a very soft component is also evident at low energies in the spectrum indicated in red. These ultrasoft events may be due to auroral precipitation. The bimodal distribution suggests that MeV and soft events are distinct classes of precipitation. For the following analysis, any event with $\alpha < 3$ is classified as an MeV event.

3.2 Magnetic Local Time Distribution

After classifying events based on the power law index, a local time distribution of events was created. As discussed in Section 1.3.2, the local time distribution can tell us about the processes responsible for the electron precipitation. The magnetic local time and magnetic latitude were calculated for each event using the IGRF model. Figure 3.14 shows the distribution of events on a polar plot with MeV events shown by asterisks and soft precipitation by triangles. MeV events occurred between MLT 1430-0000 while softer precipitation was observed at all local times. The solid line in the figure shows the balloon trajectory and indicates that all local times were sampled evenly. The different local time distributions of the MeV precipitation events and low energy precipitation events again suggests they are distinct classes of precipitation and different processes may be acting to precipitate particles in each case.

To determine the probability of occurrence as a function of local time, the number of hours of activity was divided by the number of observing hours at each latitude and local time. Figure 3.15 shows the occurrence probability for MeV events as a function of local time and latitude. The soft precipitation events are also shown for comparison. The average number of observing hours in each bin was \sim 10 hours for latitudes 58° - 64° , \sim 20 hours for latitudes 64° - 70° and \leq 5 hours at higher latitudes. MeV events occurred more frequently (\sim 16% of the time) at the lowest latitudes and from 18-21 MLT while lower energy precipitation occurred at all local times and up to \sim 50% of the time near local noon.

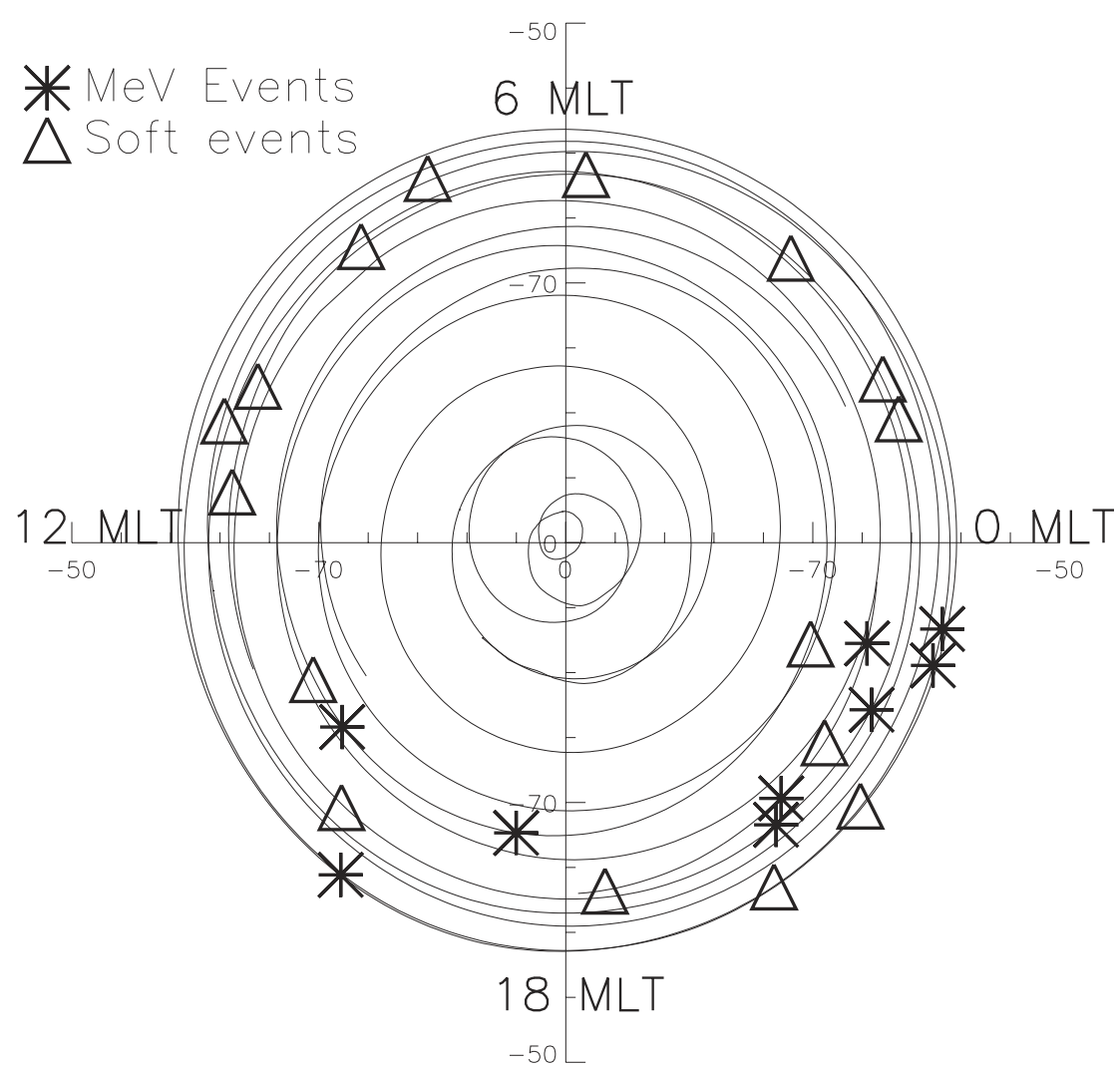


Figure 3.14: Magnetic local time distribution of 25 MAXIS events. MeV events are represented by an asterisk and soft events by triangles (the 1996 Kiruna event is also included).

Name	DOY	Kp	L
Kiruna		2	5.8
B2a	019	3	5.4
B2b	020	2	5.2
C2b	022	3	4.4
C2e_i	023	5	4.6
C2e_ii	023	5	4.6
D1b_i	025	2	6.0
D1b_iii	025	3	7.4
D2a_sp	025	2	6.8
D2b_ev	025	2	7.4

Table 3.2: Kp and L-value calculated from T89 magnetic field model for MeV events.

3.3 Magnetic Latitude and L Distribution

The precipitating electrons for the 1996 Kiruna event were thought to come from the outer radiation belts since the event occurred near L=5.8. In this section the latitude and L-shell of the MAXIS MeV events are examined to determine the source of the precipitating electrons.

As shown in Figure 3.15, all events (MeV and soft) were detected between magnetic latitudes of 58°-69° and no events were detected over the polar cap. These distributions could be very dependent on magnetic activity but more data are needed to make separate distributions for different levels of activity.

To determine the source of the precipitating electrons, the L-shell of each MeV event was calculated using the Tsyganenko 89 magnetic field model which is expected to be more accurate than the IGRF model described earlier (Table 3.2). The T89 model uses the Kp index as an input and includes effects of the cross-tail, magnetopause and ring currents which depend on magnetic activity. The MeV events detected by MAXIS were found to

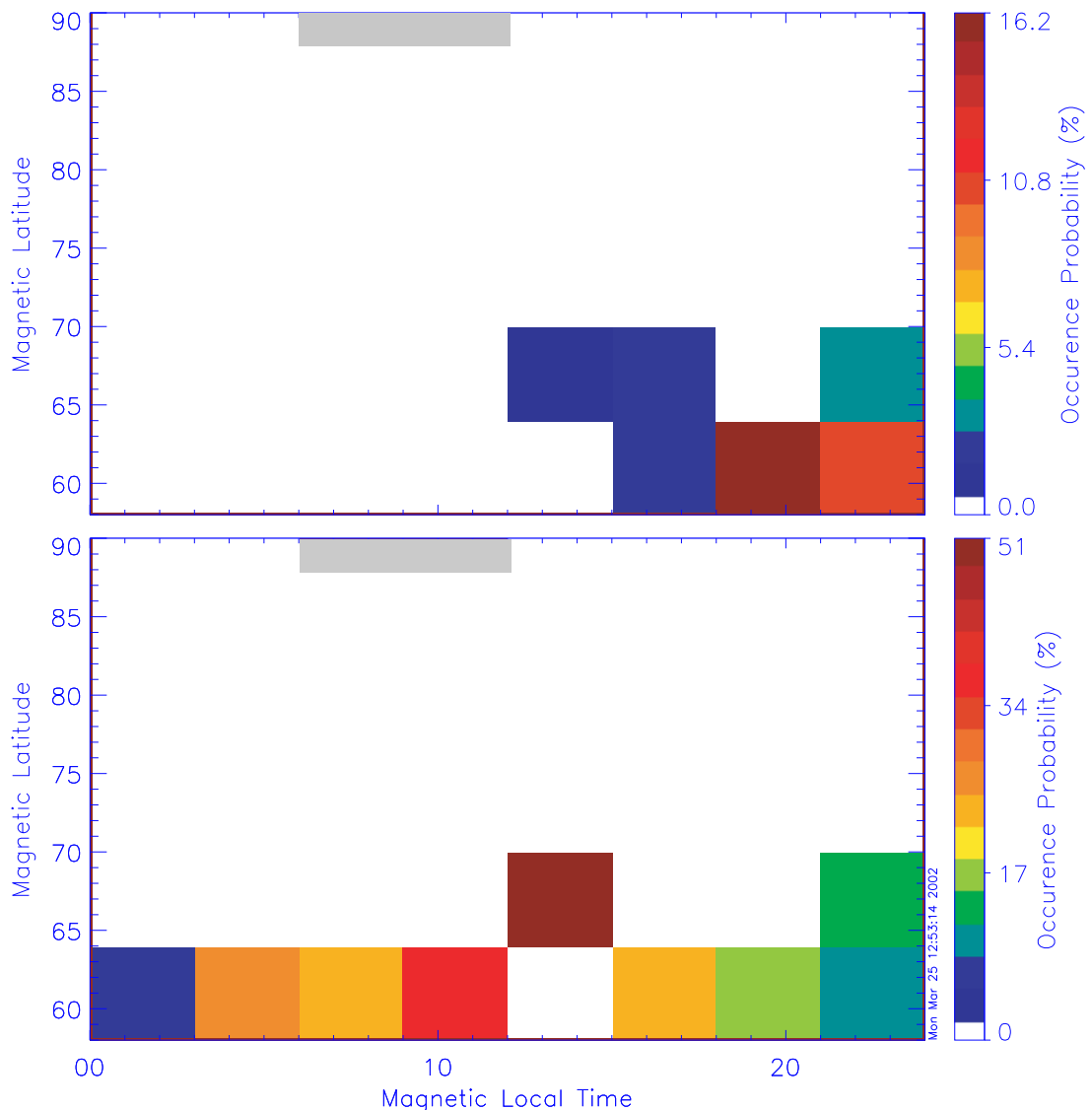


Figure 3.15: Occurrence probability as a function of magnetic latitude and magnetic local time for MeV events (top) and soft events (bottom). Grey indicates no data.

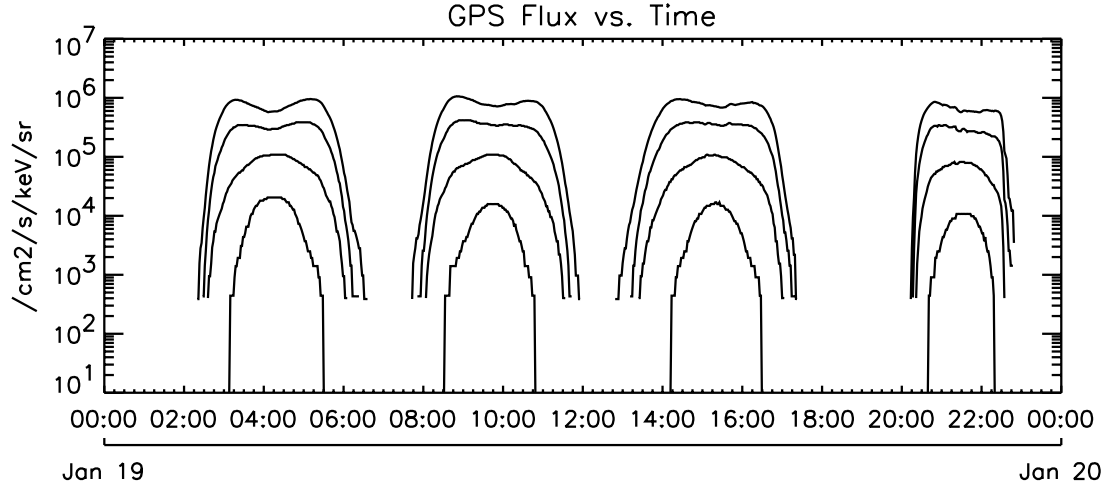


Figure 3.16: Electron flux measured in four energy channels for four GPS passes through the radiation belts. GPS data were provided courtesy of R. Friedel.

occur between L-values of 4.4-7.4 which is within the expected region of stable trapping in most cases, thus the most likely source of electrons for these events is the outer radiation belts. The events on Jan. 25-26 at L=6.8-7.4 are at higher L than would be expected for trapped MeV electrons and could be near or beyond the trapping boundary.

3.4 Location with respect to the Trapping Boundary

Electron precipitation near the midnight trapping boundary has been attributed to current sheet scattering (also called the Sergeev mechanism); when the radius of curvature of the magnetic field becomes smaller than ~ 10 times the electron gyroradius, the first adiabatic invariant is no longer conserved. Near local midnight, at L values ≥ 7 , the magnetic field begins to deviate from a dipole field and the Sergeev mechanism becomes important. During times of high activity, the field lines closer to Earth become “stretched” or more tail-like with smaller radius of curvature, and the trapping boundary moves to lower L.

The trapping boundary during the time of each MAXIS MeV event was measured directly using data from a particle detector on one of the GPS satellites in a 20,200 km altitude, 55° inclination orbit. The satellite passes through the radiation belts four times a day reaching L-values as low as $L \sim 4$ (Figure 3.16) and measures electrons in four energy channels between 0.34-3.6 MeV. The location of the trapping boundary in each energy channel was defined to be where the flux dropped by a factor of 100 from its peak value and is shown in Figure 3.17 for January 19-27. Note with this definition of the trapping boundary, there are still electrons outside the boundary but a factor of 100 fewer. Here the T89 magnetic field model was used with $K_p=2$ to calculate L. The locations of the MeV events (also using the T89 model with $K_p=2$) are also shown. The location of the trapping boundary at low energies varies substantially during this time period. The L-values shown were obtained with a quiet-time field model, so movement of the boundary inwards probably indicates that the real magnetic field is stretched thus effectively putting the spacecraft at higher L where it sees fewer particles. The trapping boundary location for 2.38-3.6 MeV electrons doesn't vary much probably because it occurs at lower L (closer to Earth) where the magnetic field configuration doesn't change as much.

The MeV events on Jan. 19/20 occurred near the trapping boundary as it was rapidly moving inward. The trapping boundary was also moving in during the event on Jan. 22 but this event was well within the region of stable trapping. The events on Jan. 23 occurred near the boundary for 2.38-3.6 MeV electrons but well within otherwise and, in this case, the boundary was moving in only slightly. The MeV events on Jan. 25 occurred outside the boundary for 2.38-3.6 MeV electrons and near boundary for lower energy electrons. The

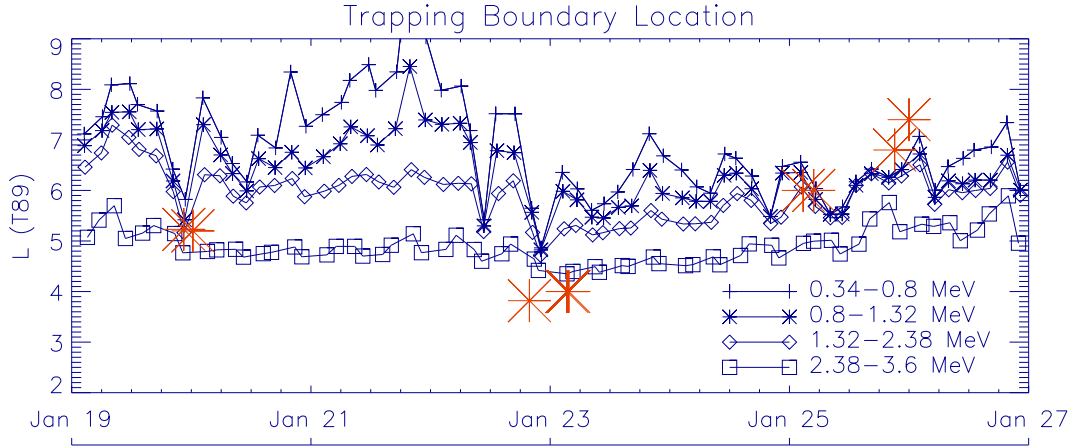


Figure 3.17: Trapping boundary location in four energy channels as measured by GPS. Asterisks mark the MeV X-ray event times and locations.

boundary was moving inward for the first two events but not during the last two events.

These observations suggest that the events at lower L are more likely to occur when the boundary moves in but those at higher L are already outside the boundary and don't require it to move. Thus it is possible that these events are associated with the trapping boundary and caused by the Sergeev mechanism acting in the dusk sector. However, it could also be that the events are associated with substorm activity which also causes the trapping boundary to move in; in other words, the movement of the trapping boundary and occurrence of an MeV event could both be results of something external rather than one being the cause of the other. In Section 3.6, the relation between MeV events and substorms is examined.

3.5 Location with respect to the Plasmapause

As described in Section 1.3.2, EMIC waves on the duskside occur near the boundary of the plasmapause and relativistic electrons can be resonant with the waves inside the plasmasphere. As magnetic activity increases, the plasmapause boundary moves in (to lower L). The plasmapause location for local times 0-15 MLT was determined empirically by Carpenter and Anderson (1992) and is given by

$$L_{ppi} = 5.6 - 0.46 * K_{pmax}$$

where K_{pmax} is the maximum value of Kp during the previous 24 hours. Thus for K_{pmax} ranging from 2 to 4 the plasmapause is located near $L=3.7-4.7$. However, in the dusk sector, the plasmapause extends to higher L and is not described by this model. The location of the plasmapause during the MAXIS flight was determined using POLAR EFI measurements of the spacecraft potential which responds to changes in plasma density. POLAR crossed the duskside plasmapause near 16:00 MLT roughly once every 18 hours (shown in Figure 3.18 along with the MeV event locations). In practice, the plasmapause was not found to be a very sharp boundary especially in the dusk sector, so its location was defined in two different ways. In one case, the location was defined where the spacecraft potential just began to decrease (solid line). In the second case, it was defined where the spacecraft potential reached a value of -5 V corresponding to a change in density by a factor ~ 50 (dashed line). For the duskside passes on January 21st, 22nd, and 25th, neither of these quantities was well defined. Five of the MeV events were found to lie well within the plasmasphere, and the other four were found to lie within or very near the plasmapause. Therefore, scattering by EMIC waves is a viable precipitation mechanism for the MeV events.

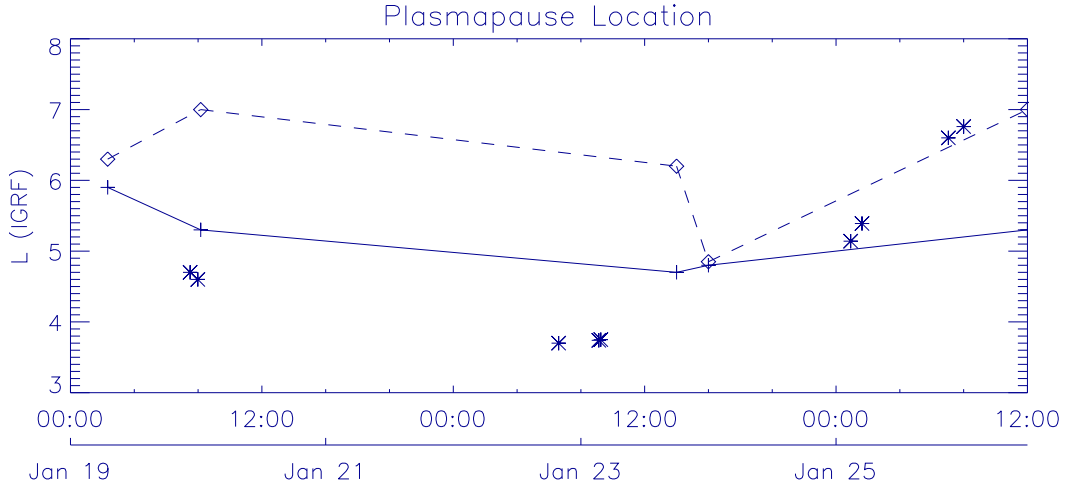


Figure 3.18: L-value of the inner edge of the plasmapause (solid line) and where density has fallen by a factor ~ 50 (dashed line) determined using POLAR EFI data. The MeV event locations are shown with asterisks.

3.6 Relation to Geomagnetic Activity

The MeV events detected by MAXIS occurred both during relatively quiet times, and during the main and recovery phases of a geomagnetic storm. More events were detected following a drop in Dst, however, since the events prior to the storm lasted for much longer, MeV events occurred for nearly the same percentage of time before and after the storm. The events prior to the storm also account for more precipitating flux. This indicates that geomagnetic storms are not a requirement for the occurrence of MeV events. However, the 1996 Kiruna event did occur following a small isolated substorm (see Section 1.4) and most of the MAXIS MeV events were observed during the recovery phase of the geomagnetic storm when substorms are more likely. In this section, spacecraft and ground-based observations are examined to determine whether the MAXIS MeV events are associated with substorms.

Figure 3.19 shows the AL index from January 17-26, 2000. As described in Sec-

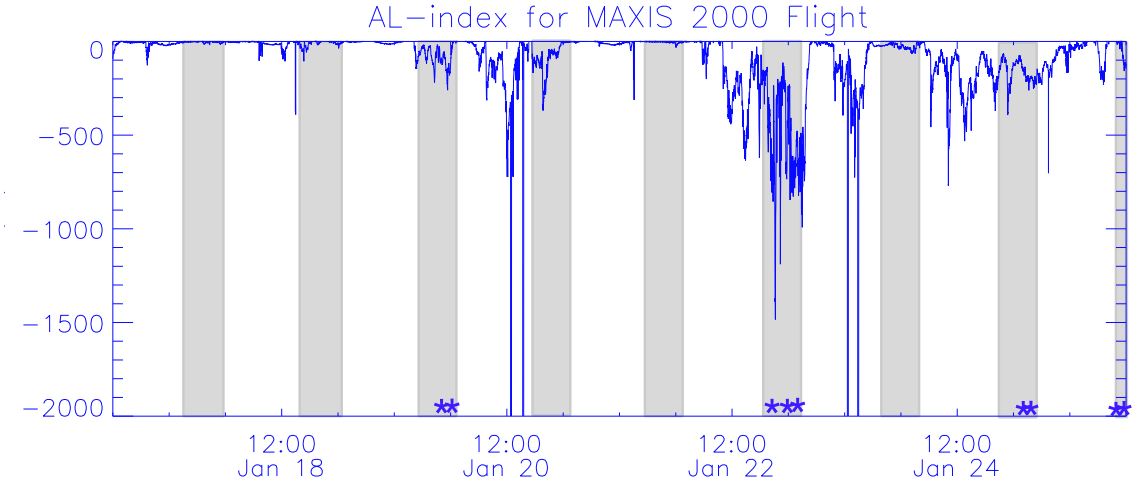


Figure 3.19: AL index from Jan 17-26,2000. The shaded regions indicate when the balloon was between $\sim 1500\text{-}0000$ MLT and stars show the location of the MeV events

tion 1.1.3, changes in the rate of decrease of AL indicate the onset of a substorm. The shaded regions indicate when the balloon was in the dusk sector (1500-000 MLT) and the nine MeV events are indicated by stars. In addition to these events, MAXIS detected a very weak MeV event during the dusk interval on January 20 but this was not included in the above analysis since the peak count rate was <500 counts/s (thus making spectral analysis difficult). MAXIS detected MeV events during every dusk interval that showed increased activity as indicated by AL but detected no MeV events outside of the dusk sector even when there was substorm activity. There were three dusk intervals during which no MeV events were detected and these occur when little or no substorm activity was present. This strongly suggests that MeV events occur in conjunction with substorms but only in the dusk sector. A detailed analysis of activity during the MeV events is now presented.

B2a/b: Jan. 19-20, 2000

The MeV X-ray event on January 19, 2000 was the strongest and longest event detected by MAXIS and was directly followed by a shorter but more energetic burst on January 20. A series of substorms starting at \sim 16:15 UT on January 19 is evident in the AL index (Figure 3.20). Also shown is the X-ray count rate and the horizontal component of the surface magnetic field measured at Narsarsuaq, Greenland which was nearly conjugate to the balloon location. The first two substorms are barely evident at the conjugate location but there is a positive bay signature beginning around 20:00 UT indicating that a substorm is occurring east of the magnetometer station (towards midnight). MAXIS detected two successive MeV events starting at 21:30 that appear to be associated with sharp increases in the horizontal component of the magnetic field.

At \sim 20:30 UT, the LANL geosynchronous spacecraft 1994-084 located in the post-midnight sector (3:30 LT) saw a sharp drop in both the proton and electron flux (Figure 3.21) which probably indicates a thinning of the plasma sheet during the substorm growth phase [G. D. Reeves, private communication]. The first MeV precipitation event was detected from 21:20-23:30 UT in the middle of the dropout when the LANL flux was varying rapidly. The rapid variations are possibly due to many dipolarizations of the magnetic field; as described in Section 1.1.3, during the expansion phase of a substorm, reconnection causes the stretched, tail-like magnetic field lines to snap back into a more dipolar configuration. The MeV event may have been associated with one or more of these dipolarizations. The flux dropout persisted until \sim 23:10 UT at which time a substorm injection is evident (Figure 3.21). A second MeV event was observed starting at \sim 23:45 and may be associated

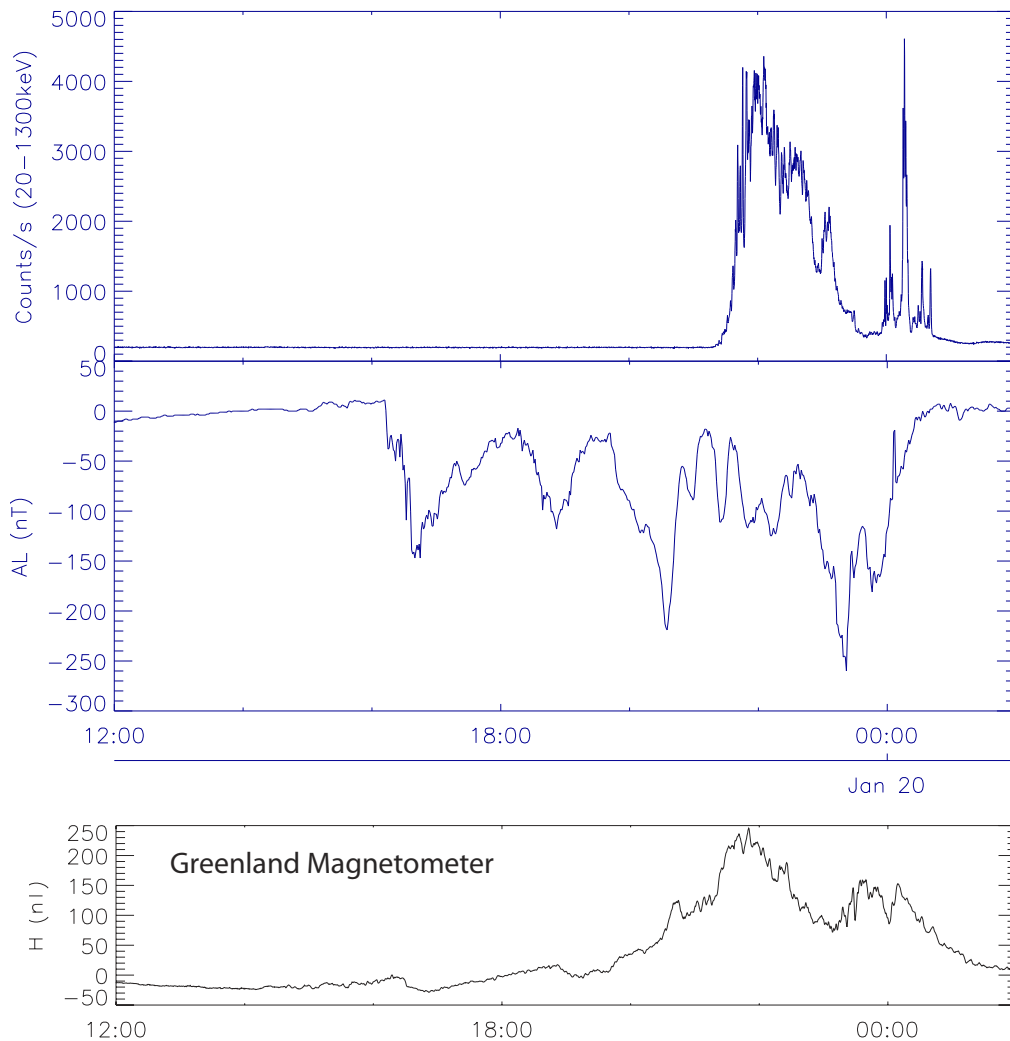


Figure 3.20: GeD count rate (top) AL index (middle) and horizontal component of surface magnetic field conjugate to balloon (bottom) on January 19, 2000. The Greenland ground-based magnetometer array is operated by the Danish Meteorological Institute (DMI). Magnetometer data for this study were provided by J. Watermann, DMI.

with the last substorm and particle injection.

Both of these MeV events are associated with substorm activity and with sharp changes in the magnetic field indicating rapid substorm expansion. In addition, both the X-ray count rate and surface magnetic field show temporal oscillations at ULF frequencies which will be discussed further in Chapter 5.

C2b,C2e_i/C2e_ii: Jan. 22-23,2000

The period January 22-23, 2000 was very active (Figure 3.22) and a moderate geomagnetic storm was indicated by Dst (Figure 2.10) which started to drop sharply at 17:00 UT reaching a minimum on January 23 at 0:00-1:00 UT. An injection of electrons and protons was observed at LANL 1994-084 in the post-midnight sector (2:30 LT) at \sim 19:30 UT (Figure 3.23). MAXIS detected a short MeV event at 20:05-20:10 UT during the main phase of the storm and following the substorm injection. Low energy X-ray activity was observed on January 23 until two successive MeV events at 3:20-4:05 UT. In this case, it is difficult to associate the MeV events with a particular substorm phase and MAXIS didn't observe MeV events with every change in AL. However, this could also just be a result of the MeV events being localized and some events occurring outside the GeD field of view. In addition, there doesn't seem to be any obvious difference between periods when MeV events were observed and periods when low energy precipitation was observed.

D1b_i,D1b_iii,D2a_sp,D2b: Jan 25, 2000

From January 24-26, 2000 activity was again nearly continuous (Figure 3.24). Changes in the MAXIS GeD count rate appear to follow the changes in AL during this

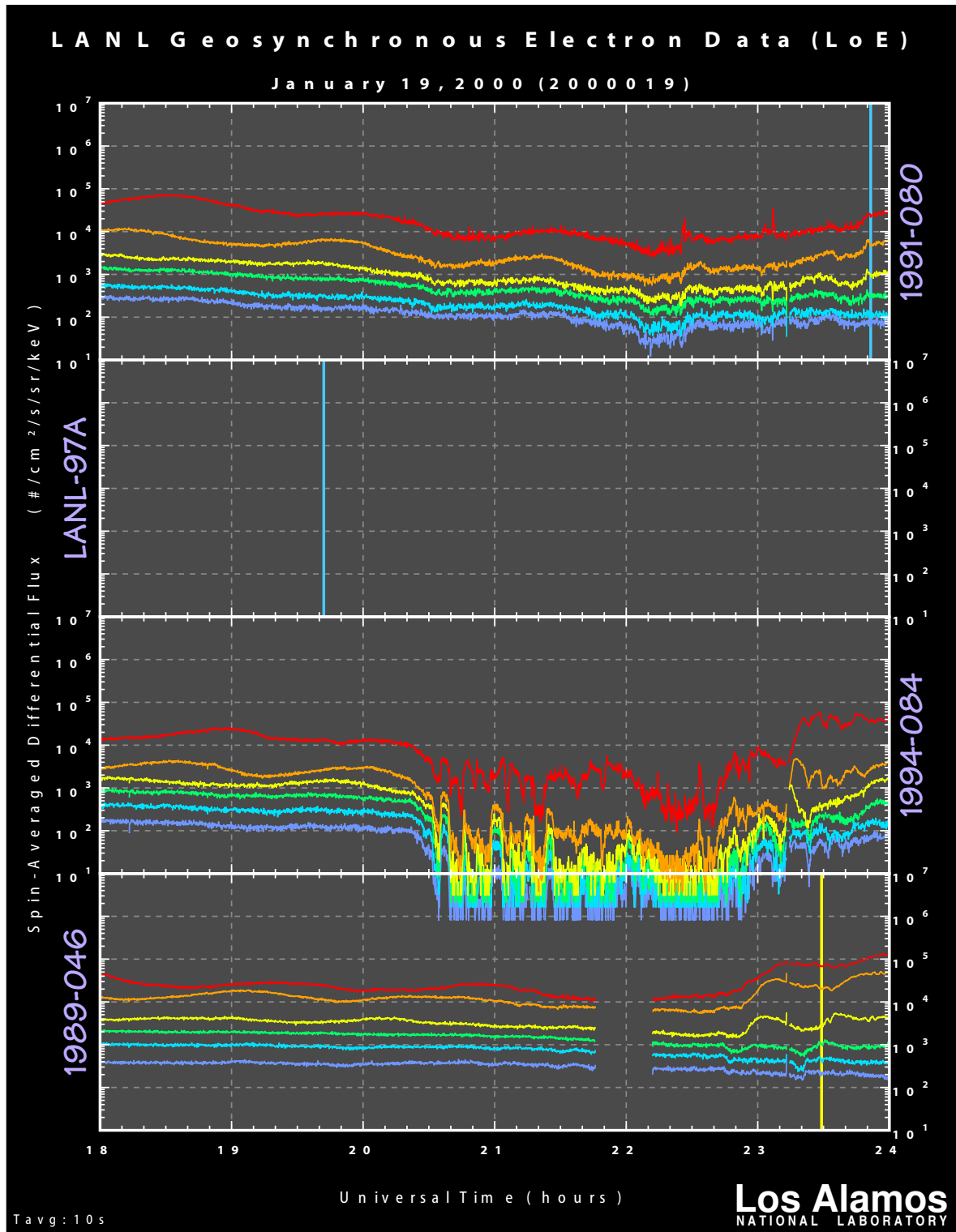


Figure 3.21: LANL electron flux 50-315 keV.

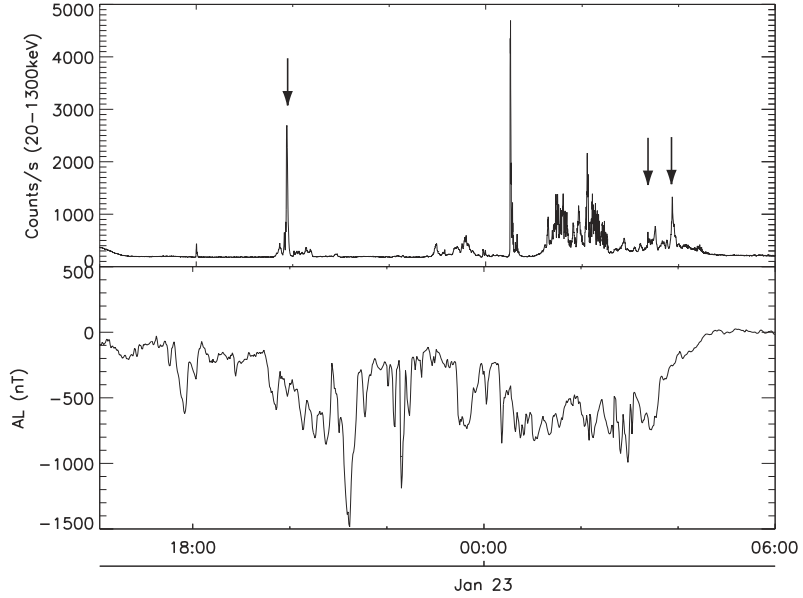


Figure 3.22: GeD count rate and AL index on January 22-23, 2000. MeV events are indicated by arrows.

time but most of the X-ray activity was due to low energy precipitation. MeV events were detected on January 25 at 2:25 UT, 4:40 UT, 21:05 UT, and 23:55 UT.

3.7 Summary

The observations presented in this chapter demonstrate that MeV electron precipitation is distinct from lower energy precipitation and the most likely source for the precipitating electrons is the radiation belts. The MeV precipitation events were observed only in the dusk/pre-midnight sector in association with substorm activity. Because the activity was nearly continuous during this period, it is difficult to associate each MeV event with a particular substorm or substorm phase although the events on January 19/20 were directly correlated with a substorm and occurred during the expansion phase. The MeV events also occurred near the trapping boundary as measured by GPS and often during

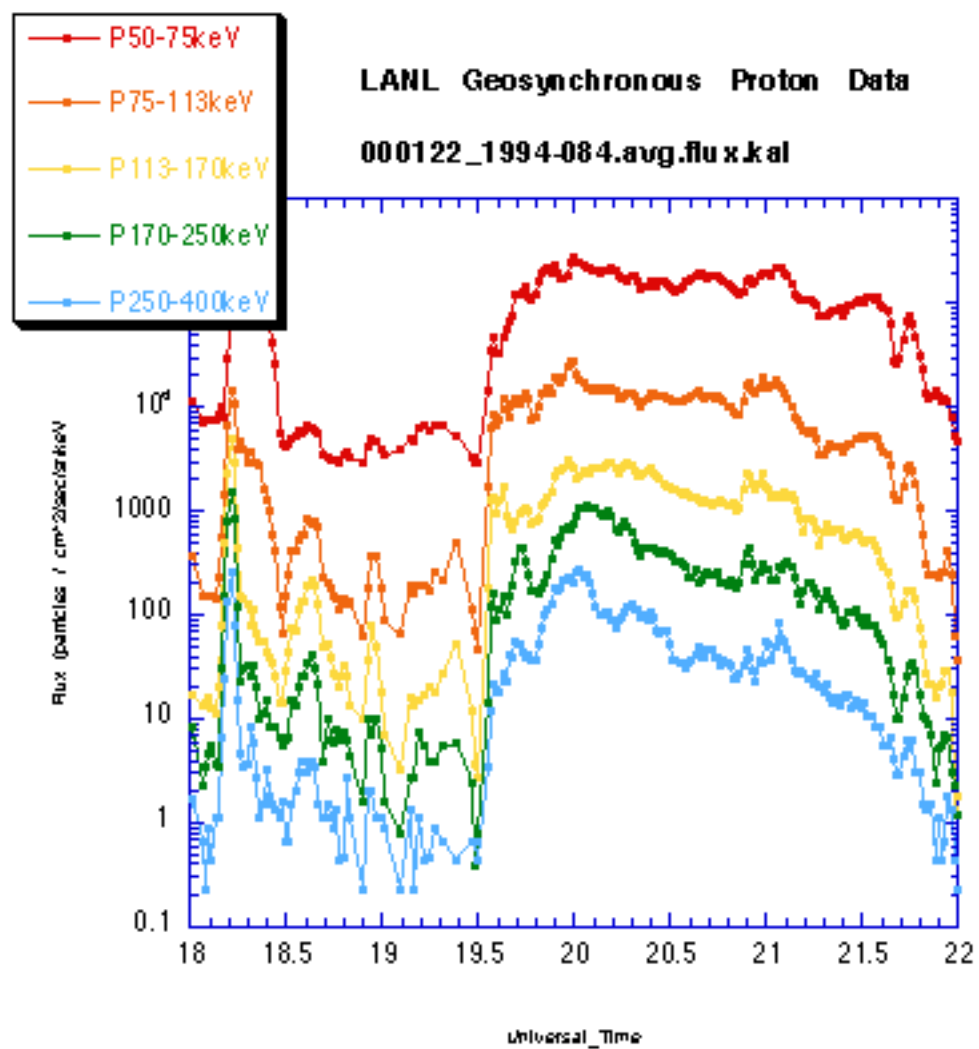


Figure 3.23: LANL proton flux

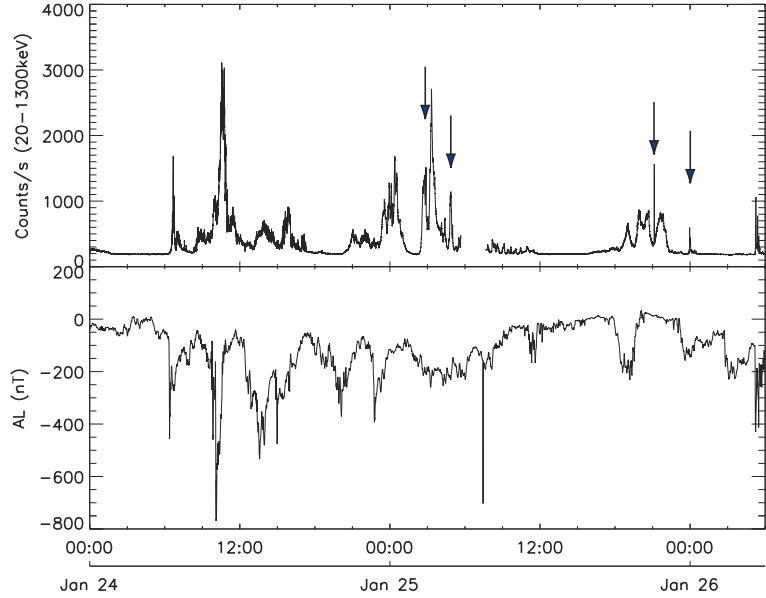


Figure 3.24: GeD count rate and AL index on January 24-26,2000. MeV events are indicated by arrows.

times when the trapping boundary was moving inward suggesting that current-sheet scattering could be the precipitation mechanism. However, this could just be a result of the association with substorms. It is not clear whether the trapping boundary motion somehow triggered the MeV events or whether substorms caused both the motion of the boundary and the MeV events. The duskside location near the plasmapause and the association with substorms are consistent with EMIC waves as the scattering mechanism. In the next chapter, the precipitating electron spectrum and flux are obtained from the X-ray spectrum for each event and compared with spacecraft measurements of the trapped electron distribution.

Chapter 4

Spectral Modeling of MAXIS MeV Events

The previous chapter demonstrates that MeV events are a distinct class of precipitation that occurs predominantly in the dusk sector and the most likely source of the precipitating electrons is the outer radiation belts. In order to understand the processes acting to scatter the electrons and to quantify the loss of electrons from the radiation belts due to MeV events, it is necessary to determine both the precipitating electron energy distribution and flux. There are two ways to infer the precipitating electron spectrum. In the forward-folding method, an input electron distribution is assumed and the count spectrum produced by this distribution is modeled and compared with the observed count spectrum. This process is carried out iteratively until a model that reproduces the observed spectrum is found. The count spectrum can also be directly inverted. This is preferable since it doesn't rely on a-priori assumptions about the precipitating electrons but this method

requires very good statistics. In this chapter, the modeling procedure is described and applied to several examples. Results from the forward-folding modeling are presented for each MAXIS MeV event and used to calculate the average precipitating >500 keV flux. After removing the effects of atmospheric and instrument scattering, the GeD and BGO photon spectra can be combined. The combined photon spectra are presented for selected MeV events in Section 4.3 along with the results of the direct-inversion modeling technique. In Sections 4.2.3 and 4.4, the results are compared with observations of the trapped electrons made by one of the GPS satellites.

4.1 Description of the Model

In both the forward-folding and direct-inversion methods, the effects of Coulomb scattering of electrons as they enter the atmosphere, bremsstrahlung production and scattering of photons in both the atmosphere and instrument must be modeled.

4.1.1 Ionization Losses

As they are precipitated, electrons suffer ionization losses to the atmosphere due to Coulomb interactions and as a result, the electron energy spectrum will be modified. An analytic model is used to describe the ionization losses. The electron distribution obeys a continuity equation

$$\frac{dN}{dt} = F(E) - \frac{d}{dE} \left(N(E) \frac{dE}{dt} \right)$$

where $F(E)$ is the incident electron distribution and $N(E)$ is the modified (bremsstrahlung-producing) distribution. Since the travel time for a single electron (which travels at close to

the speed of light for the energies of interest here) is very short compared to the duration of the X-ray events, we assume that an equilibrium distribution of electrons will be established.

Setting $\frac{dN}{dt} = 0$ and solving for $N(E)$, we have

$$N(E) = \left[\frac{dE}{dt} \right]^{-1} \int F(E) dE \quad (4.1)$$

Since actual losses due to production of bremsstrahlung are only $\sim 1\%$ for electrons ≤ 1 MeV, only losses due to Coulomb interactions are considered when determining the intermediate electron distribution. The energy loss of an electron as a function of distance traveled is given by the Bethe-Bloch formula [Jackson, 1975] thus

$$\frac{dE}{dt} = v \frac{dE}{dx} = -4\pi n Z \frac{e^4}{m_e v} \left[\ln \left(\frac{2\gamma^2 m_e v^2}{I} \right) - v^2/c^2 \right] \quad (4.2)$$

where n is the density, Z is the atomic number, and I the average ionization potential of the scattering medium (in this case air). Some examples of equilibrium distributions are shown in Section 4.2.1.

4.1.2 Bremsstrahlung Production

Bremsstrahlung X-rays of a given energy can only be produced by electrons at or above that energy. Given the electron distribution, the differential electron flux, dJ_e/dE , is obtained as a function of energy and integrated with the energy dependent cross section for bremsstrahlung production, $d\sigma/dk$, to give the differential photon flux, dJ/dk . Assuming an electron distribution independent of spatial position, we have

$$\frac{dJ}{dk}(k, t) = \frac{nV}{4\pi R^2} \int_k^\infty \frac{dJ_e}{dE}(E, t) \frac{d\sigma}{dk}(k, E) dE \quad (4.3)$$

where n is the density of the ambient medium (the atmosphere), R is the distance to the source, and V the source volume. The bremsstrahlung cross sections are taken from Koch and Motz [1959] and are accurate to 5% for 10-100 keV electrons and 20% for 100-2000 keV electrons but these uncertainties will affect only the overall scaling and not the shape of the spectrum [Johns and Lin, 1992].

4.1.3 Atmospheric and Instrument Response

The bremsstrahlung photons interact in both the atmosphere and instrument before finally being photoelectrically absorbed. This scattering depends on both the energy and incident angle of a photon. To simulate the atmospheric and instrument responses, a Monte Carlo simulation is performed using the method described by Smith et al. [1995].

The instrument is modeled as 20 regions of different materials. Photons in each energy bin with incident angles between 0° - 10° up to 95° - 105° are input into the simulation. The effects of Compton scattering, pair-production and photoelectric absorption are included and the final energy spectrum recorded for each input energy and angle. The result is a response matrix with elements for each set of incident angle and energy.

The atmosphere is modeled as ten concentric shells of air with varying densities. Photons are started isotropically from a point at 70 km altitude (the penetration depth of a \sim 1 MeV electron is \sim 60 km [Berger and Seltzer, 1972]). When the simulated photon reaches balloon atmospheric depths ($4.5\text{-}6 \text{ gcm}^{-2}$), the current angle and energy are recorded resulting in energy spectra for each incident angle, incident energy and final angle.

The instrument and atmospheric response matrices are then multiplied to give the full atmospheric/instrument response which gives the count spectrum in the detector

as a function of initial photon energy and angle. A response matrix is obtained for each atmospheric depth (4.5 and 6 gcm^{-2}) and the appropriate matrix can then be used for each event.

4.2 Forward-Folding Method

In the forward-folding method, a precipitating electron distribution, $F(E)$ is assumed and the equilibrium distribution, $N(E)$, is calculated with Equation 4.1. The electron flux, written here as $J_e(E)$ to simplify the notation, is integrated with the bremsstrahlung cross section to give the photon spectrum. Finally, assuming a spatial distribution of photons at the source (70 km), the bremsstrahlung spectrum is folded through the atmospheric/instrument response and divided by $4\pi R^2$ where R is the distance to the source (assumed to be isotropic). The result is a model count spectrum. A normalization factor is determined by requiring that the model and observed count spectra contain the same total number of counts. When modeling the MeV precipitation events, the spectra are integrated above 100 keV to get the normalization factor since we are interested in the high energy part of the spectrum. The normalization factor can then be used to find the precipitating electron flux.

4.2.1 Some Examples and Discussion

In this section, count spectra derived from different spectral shapes are compared and the ability to distinguish between them, given the uncertainties inherent in measuring count spectra, is discussed. Since the electron distribution is modified due to ionization

losses, similar final count spectra can result from a range of initial electron distributions. Several cases will be compared below.

Monoenergetic

In the monoenergetic case, the precipitating electron distribution is given by

$$F(E) = A\delta(E - E_0)$$

where A is a constant. With Equations 4.1 and 4.2 we have

$$N(E) = \left[\frac{dE}{dt} \right]^{-1} \int_E^\infty A\delta(E - E_0) dE$$

and $\frac{dE}{dt} \sim \frac{1}{v}$

At non-relativistic energies, we then have

$$N(E) \sim E^{1/2}$$

The electron flux as a function of energy in units of $\text{cm}^{-2}\text{s}^{-1}\text{keV}^{-1}$ is then

$$J_e^\delta(E) = vN(E) \sim \begin{cases} E & E \leq E_0 \\ 0 & E > E_0 \end{cases}$$

Notice that the equilibrium electron distribution in this case *rises* with energy up to the energy of the incident electrons, E_0 . This is due to the fact that lower energy electrons lose energy faster than higher energy electrons (since dE/dt goes like $E^{-1/2}$).

Exponential

For an exponential precipitating electron distribution,

$$F(E) = Ae^{-E/E_0}$$

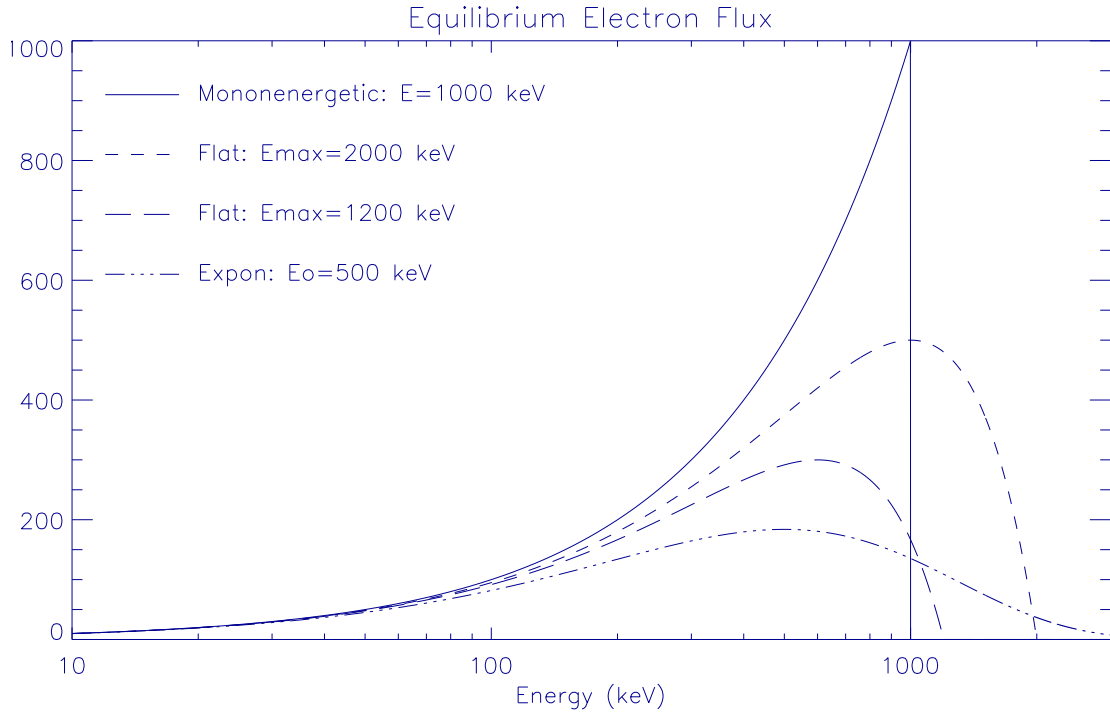


Figure 4.1: Equilibrium electron flux for monoenergetic, exponential and flat initial electron distributions.

where E_0 is the e-folding energy, the integral (Equation 4.1) gives

$$N(E) = \left[\frac{dE}{dt} \right]^{-1} A E_0 e^{-E/E_0}$$

and

$$J_e^{\text{exp}}(E) \sim A E E_0 e^{-E/E_0}$$

For energies well below the e-folding energy, we can expand this keeping only the zeroth order term

$$J_e^{\text{exp}}(E) \sim E \quad \text{for } \frac{E}{E_0} \ll 1$$

Thus, at energies well below the e-folding energy, the equilibrium electron distributions look identical in shape for both the monoenergetic and exponential cases (differing only

be a constant factor). For the exponential, $J_e^{exp}(E)$ has a maximum at $E = E_0$ similar to the mononenergetic case which is peaked at E_0 . The monoenergetic and exponential cases only differ appreciably near and above the e-folding energy, therefore the photon spectra they produce will only differ at the high energy end of the spectrum. In particular, the mononenergetic J_e^δ goes to zero at E_0 , while J_e^{exp} does not. Therefore, the bremsstrahlung produced by the exponential electron distribution has non-zero flux above E_0 and the roll-off of the photon spectrum is more gradual than in the monoenergetic case. Figure 4.1 shows the equilibrium electron distributions for a monoenergetic case with $E_0=1000$ keV and exponential with e-folding=500 keV. The equilibrium distributions assuming a flat precipitating electron spectrum up to cut-off energies, $E_{max}=1200$ and 2000 keV are also shown and are discussed next.

Flat

In the case of a flat electron distribution up to a cut-off energy, E_{max} ,

$$F(E) = \begin{cases} A & E \leq E_{max} \\ 0 & E > E_{max} \end{cases}$$

$$\Rightarrow J_e(E) \sim E(E_{max} - E)$$

In this case, the equilibrium distribution is a parabola with maximum at $E_{max}/2$ and is thus very sensitive to the choice of E_{max} . For energies well below E_{max} (since E_{max} is constant)

$$J_e^{flat}(E) \sim E \quad E \ll E_{max}$$

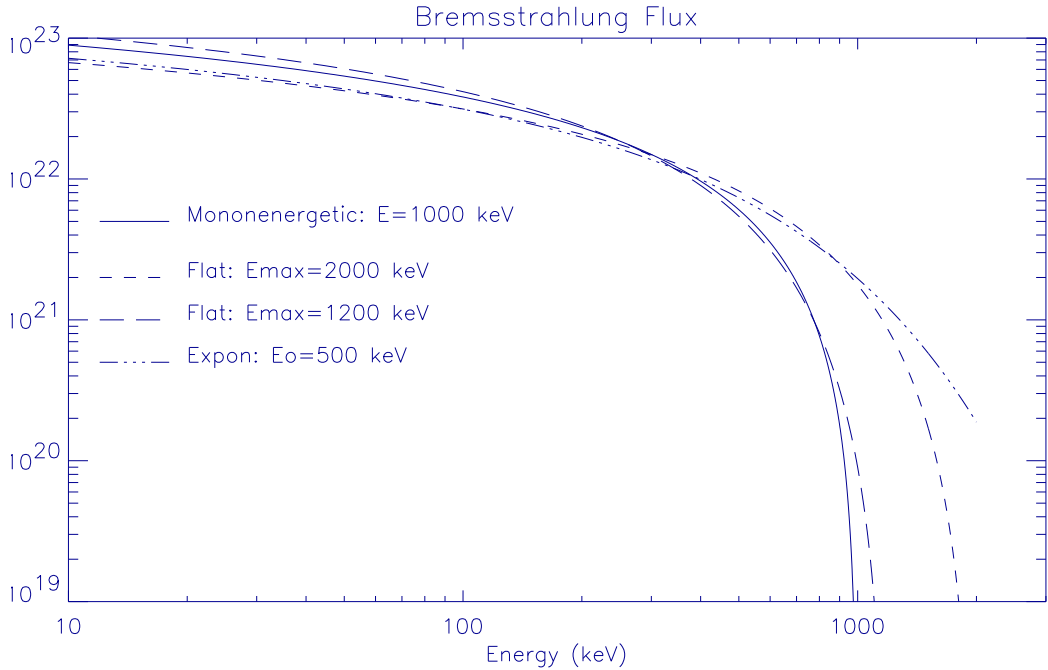


Figure 4.2: Bremsstrahlung spectra for monoenergetic, exponential and flat initial electron distributions.

With the right choice of E_{max} , we can produce a spectrum very similar to either the monoenergetic or exponential case. It isn't surprising that the flat case looks very similar to the exponential case presented since the exponential with a high e-folding energy looks very flat. However, one might expect the monoenergetic case to look very different. That it does not is simply the result of the $1/v$ dependence in the Bethe-Bloch formula that causes electrons to pile up at high energies in all three cases. Although the electron equilibrium distributions are all peaked, they have very different widths and this results in differences in the bremsstrahlung spectra and allows us to distinguish between them.

The bremsstrahlung spectrum can be approximated by [Longair, 1997]

$$J_\gamma(E) \sim \int_E^\infty J_e(E') E'^{-1/2} \ln\left(\frac{E'}{E}\right) dE'$$

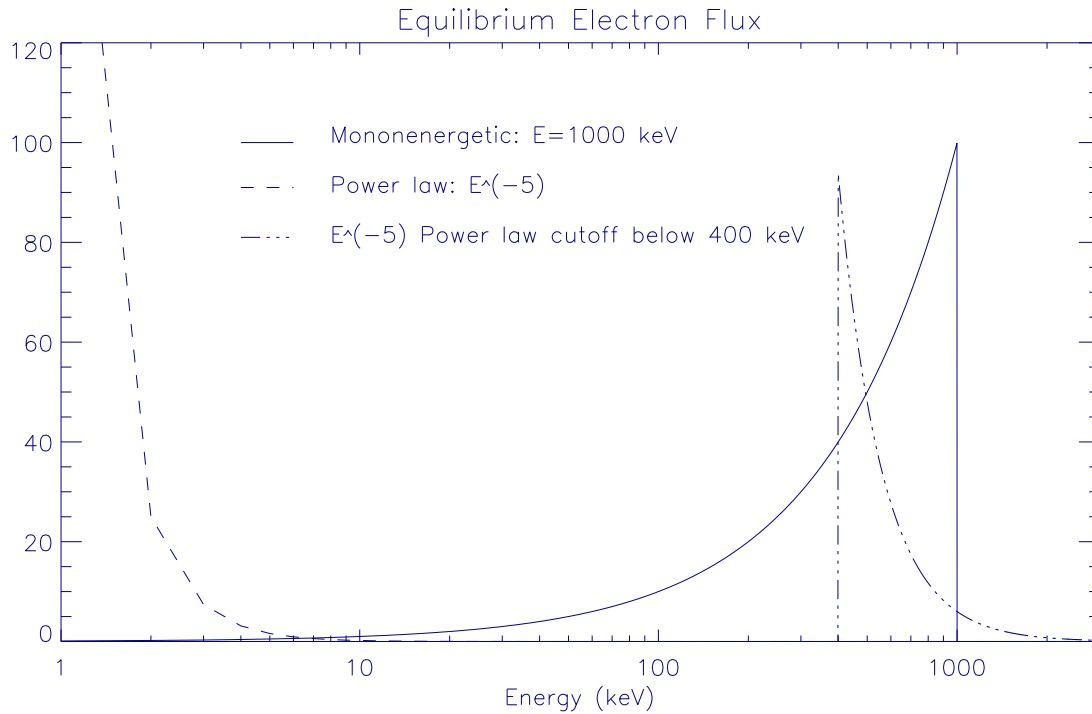


Figure 4.3: Equilibrium electron flux for monoenergetic, power law ($\alpha = 6$) and power law with a lower energy cutoff of 400 keV initial electron distributions.

This expression was integrated numerically for the monoenergetic, exponential and flat cases and the results are shown in Figure 4.2. Note that this approximate method is used here for illustration purposes and is not used for modeling the MeV events.

Power Law

Now consider a power law precipitating electron distribution which can be written

$$F(E) = AE^{-\alpha}$$

For $\alpha > 1$:

$$J_e^\alpha(E) \sim E^{2-\alpha}$$

In this case, as long as the power law index is greater than 2, the electron flux will

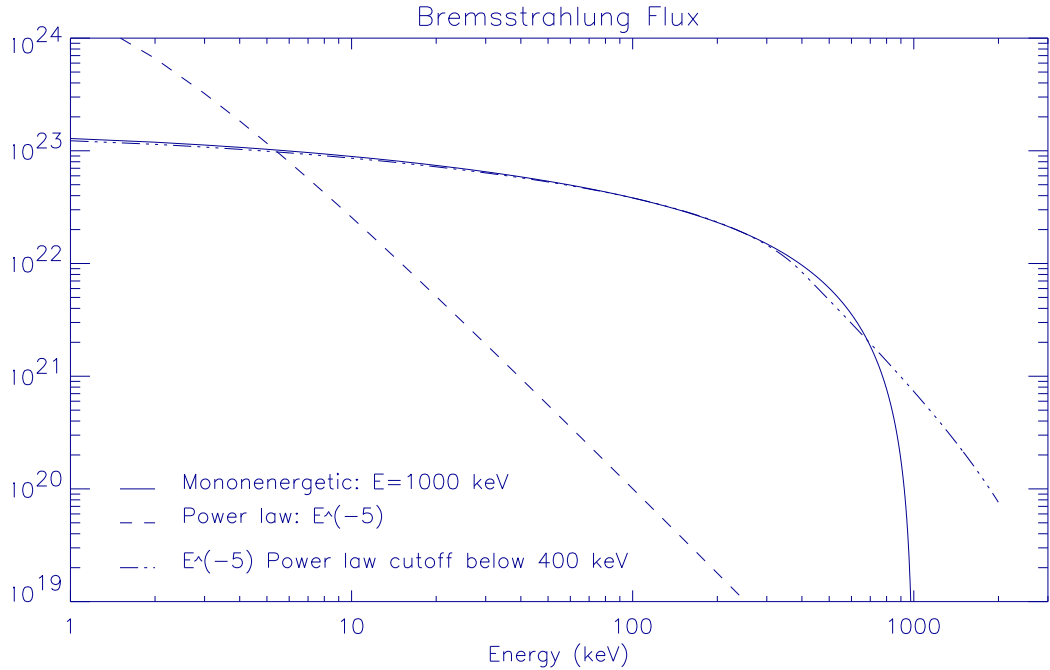


Figure 4.4: Bremsstrahlung spectra for monoenergetic, power law ($\alpha = 5$) and power law with a lower energy cutoff of 400 keV initial electron distributions.

decrease with energy (Figure 4.3) and the resulting photon spectrum (Figure 4.4) will be much steeper than in the monoenergetic case since most of the electrons are at low energies. If, however, the precipitating electron distribution is a power law with a lower cut-off energy, the spectrum once again can be made to look very similar to the monoenergetic case since the electron flux is concentrated near the cutoff energy. This might for example represent precipitating all the radiation belts electrons above some threshold energy.

From the above discussion, it is clear that a power law of precipitating electrons should be easily distinguishable from the other models presented. With the right choice of parameters, however, the monoenergetic, exponential, flat and cut-off power law electron distributions will all produce similar photon spectra at low energies; however major differences occur at the high energy part of the spectrum. The question is: can these different

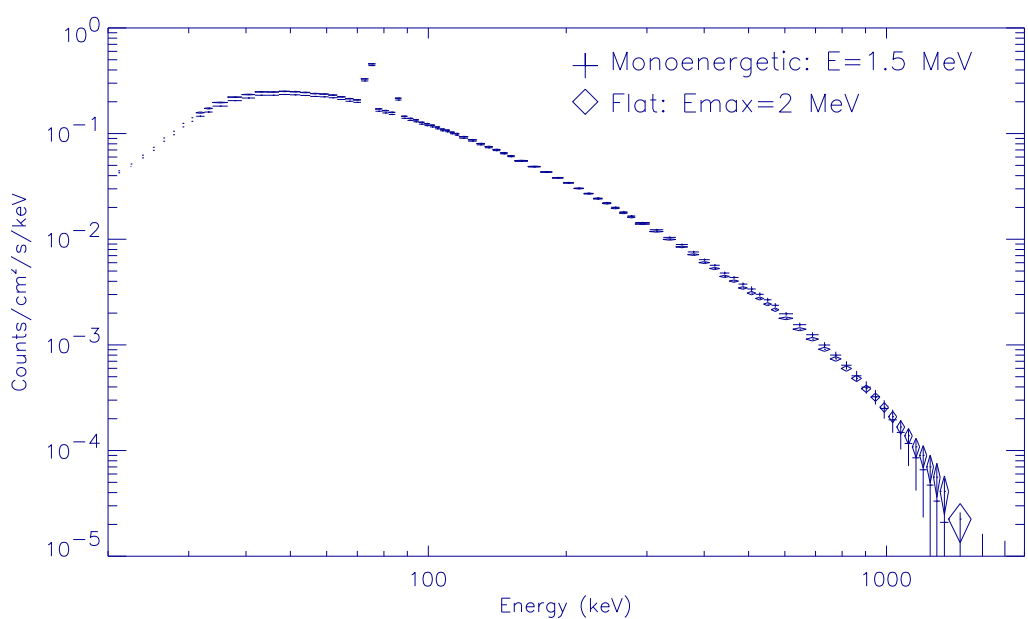
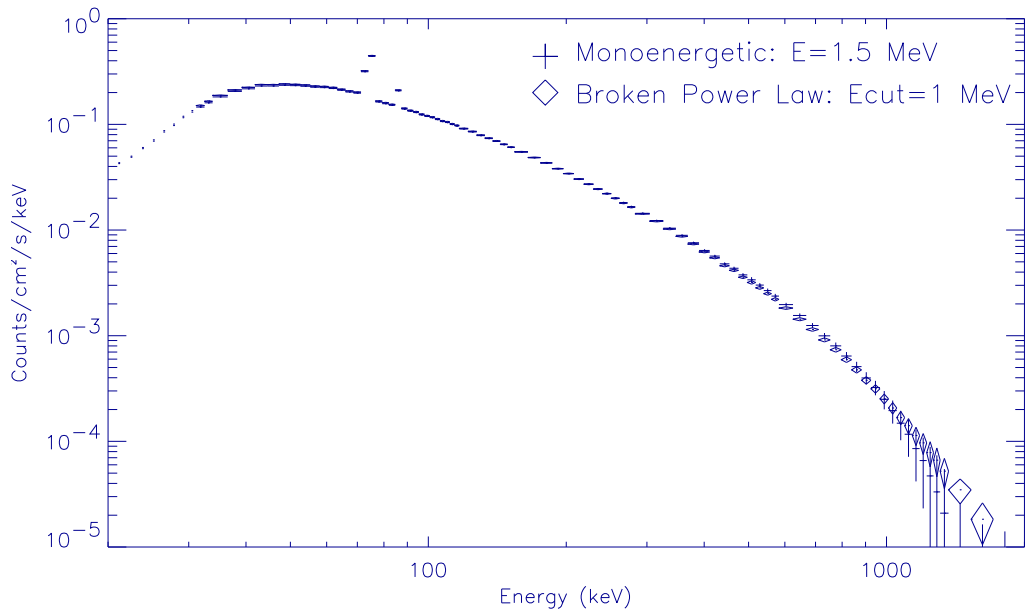
models be distinguished given the uncertainties in the measured count spectrum for a particular event or will each produce a model count spectrum consistent with the data? This question can be answered in the following way:

Using the Kiruna event as a “typical” event, a model count spectrum was obtained using the forward-folding method (including full relativistic expressions) for several different initial electron distributions. We assume that the model spectrum represents the true spectrum in each case and try to estimate the uncertainty in what would be measured. Any measured spectrum is governed by Poisson statistics (in the best case) and the uncertainty in measured counts, N , in each energy bin $\sim \sqrt{N}$. The measured spectrum is the sum of both the background, B , and event, M . The background can be estimated using the measured background during the balloon flight, then the statistical uncertainties for the model event count spectrum are given by

$$\sigma_M = \frac{1}{A^{1/2}\tau^{1/2}\Delta E^{1/2}} \left[M + B \left(1 + \frac{\tau}{\tau_B} \right) \right]^{1/2}$$

where A is the detector area, τ and τ_B the observing time for event and background, and ΔE the width of each energy bin. This represents the uncertainty in the event spectrum assuming the instrument and atmospheric responses are well understood and there are no systematic errors (such as bad background subtraction). In other words, these are the smallest uncertainties achievable.

Using the statistical uncertainties, we can compare the different models to see if they are distinguishable. Model count spectra were created with the forward-folding method for monoenergetic, flat, exponential and cut-off power law initial electron distributions. The cut-off power law in this case is a broken power law with indices $\alpha=3$ and $\alpha=6$ with a break



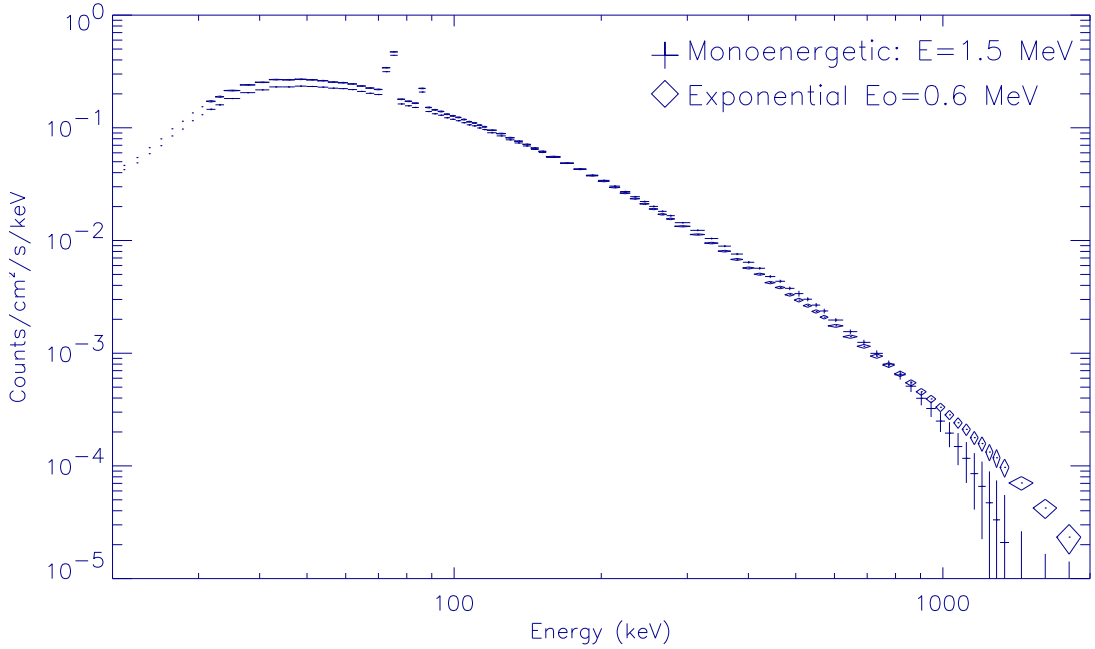


Figure 4.7: Simulated count spectra for an event similar to the Kiruna event. Models shown here use monoenergetic (1.5 MeV) and exponential (with e-folding at 600 keV) electron distributions.

at 1.5 MeV determined by the trapped electron distribution as measured by the LANL geosynchronous spacecraft. The model spectra and theoretical error bars are shown for each type of model in Figures 4.5-4.7 for an event with the duration and flux of the Kiruna event. From these results, the exponential model should be just distinguishable from the monoenergetic case, but the monoenergetic, flat and cut-off power law models will all be consistent with the data. However, the theoretical errors scale as $\tau^{-1/2}$, thus for an event with more counts (whether due to a larger detector, stronger event or longer observing time), we would be able to differentiate between the different models. One way to achieve this is to hope for a stronger or longer duration events but a more reliable method is to use a more sensitive instrument or reduce the background.

The BGO scintillator flown on MAXIS has nearly ten times the sensitivity of the GeD at 1 MeV (but a higher background) and can improve the modeling at the highest energies. The results of the forward-folding modeling for the GeD data are presented in the next section. In Section 4.3, the BGO and GeD data are combined for selected MeV events and the precipitating electron distribution is obtained using the direct-inversion method.

4.2.2 Model Results for MAXIS MeV Events

Model count spectra were created assuming monoenergetic, exponential, and flat initial electron spectra for each MAXIS MeV event. Since XRI images were unavailable, the spatial distribution of each event was unknown and was assumed to fill the field of view (zenith angles 0° - 45°). The best fit parameter for each model (i.e. e-folding for the exponential) was determined by changing the parameters until the minimum reduced χ^2 was found. Here, the reduced χ^2 was calculated for each model using only the data above 100 keV. The very last bin in the spectrum was excluded from the calculation since it is at the crossover point between two gain channels and was found to be systematically too low. In most cases, acceptable fits were found for a range of input parameters where “acceptable fit” is defined by requiring the χ^2 probability, Q , to be greater than 10^{-3} . The quantity Q gives the probability that the chi-square will exceed a particular value by chance, so very small values of Q indicate that the data are unlikely to be drawn from the model. However, if the measurement errors are not normally distributed, Q can be as small as 10^{-3} even for data that are drawn from the model [Press et al., 1992]. In some of the cases examined, acceptable fits could be found for more than one spectral shape due to poor statistics in the data (see above discussion and examples below).

Forward Modeling Results for MAXIS MeV Events

Event	Best fit	Acceptable Fit Parameters	>500 keV fluence	Fluence Range
B2a	E:330	E:325-340	$8.7 \times 10^{17} e^-/s$	$8.4-8.7 \times 10^{17} e^-/s$
B2b	E:550	E:490-580	$2.2 \times 10^{17} e^-/s$	$2.2-2.4 \times 10^{17} e^-/s$
C2b	F:10000	E:>3000, M:>2400, F:>5000	$1.4 \times 10^{16} e^-/s$	$1.4-5.1 \times 10^{16} e^-/s$
C2e_i	E:325	E:250-550, M:900-1000, F:1000-1600	$8 \times 10^{16} e^-/s$	$0.6-1.0 \times 10^{17} e^-/s$
C2e_ji	E:315	E:280-340	$9.7 \times 10^{16} e^-/s$	$0.9-1.0 \times 10^{17} e^-/s$
D1b_i	F:1300	E:360-400, F:1250-1350	$2.9 \times 10^{17} e^-/s$	$2.5-3.0 \times 10^{17} e^-/s$
D1b_iii	E:170	E:145-180	$9.9 \times 10^{16} e^-/s$	$0.9-1.0 \times 10^{17} e^-/s$
D2a_sp	F:5000	E:900-3000+, M:1500-2600+, F:>2100	$2.1 \times 10^{16} e^-/s$	$1.4-4.2 \times 10^{16} e^-/s$
D2b	F: 1600	E:390-700, M:900-1600, F:1200-2200	$5.5 \times 10^{16} e^-/s$	$2-7 \times 10^{16} e^-/s$

Table 4.1: Best fit and acceptable range of fit parameters (in keV) for MeV events (E signifies exponential, F flat, and M monoenergetic). Also listed is >500 keV electron fluence from best fit model and the range of model electron fluence from all acceptable models.

Table 4.1 lists the best fit, range of acceptable fit parameters and corresponding range of >500 keV electron fluence from the acceptable models for all nine MeV events. An exponential initial electron distribution was the only model that fit all nine MeV events with e-foldings ranging from 170 keV->3000 keV and was the best fit model for over half the events. All but one of the events showed e-folding energies above 300 keV. As described in Section 1.3.1, previous X-ray observations of precipitation showed much steeper exponential spectra with typical electron e-folding energies \sim 10-50 keV [Barcus and Rosenberg, 1966], and the highest e-folding previously reported was 200 keV [Parks et al., 1979]. The Kiruna 1996 event was best described by a monoenergetic distribution but an exponential with 650 keV e-folding also provided an acceptable fit. Below, some examples of the best fit exponential and monoenergetic model count spectra are shown superposed on the measured count spectrum for several events. The χ^2 probability for each model, Q, is shown on each plot for reference.

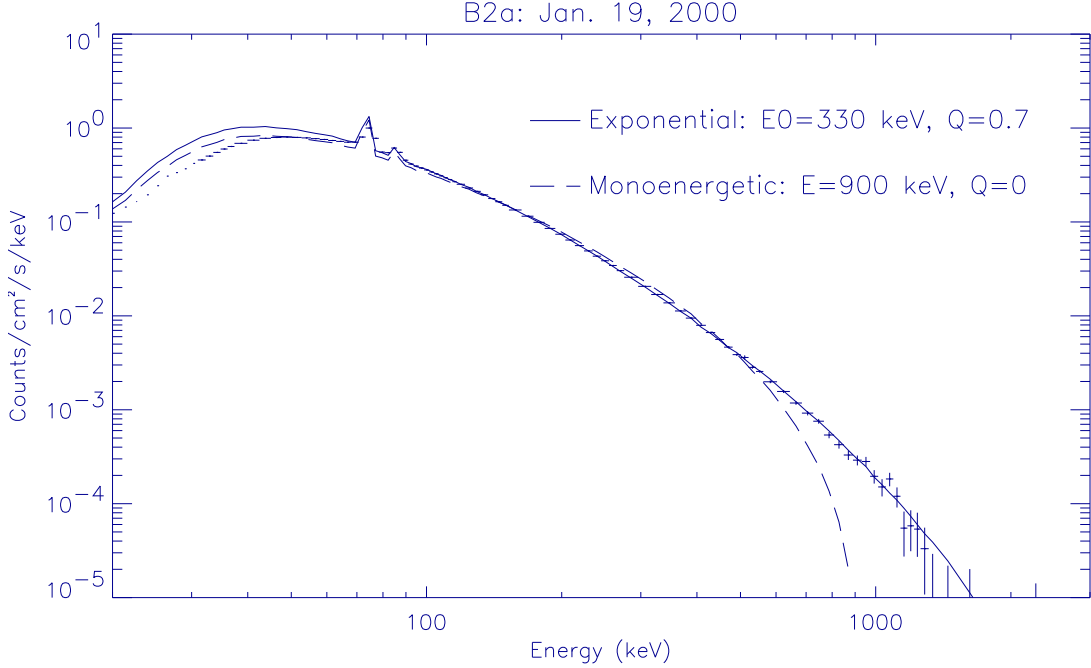


Figure 4.8: Observed and model count spectra. Q is the chi-square probability described in the text.

Figure 4.8 shows the best fit monoenergetic and exponential model count spectra for the event on January 19, 2000 which lasted for more than two hours. The event was not as hard as the Kiruna event and the statistics in the data are very good, therefore, the monoenergetic and exponential models are clearly distinguished in this case. The best fit is an exponential with e-folding, $E_0=330$ keV and all exponentials with e-foldings between 325-340 keV provided acceptable fits to the data. A monoenergetic input electron spectrum could not reproduce the measured spectrum. Below ~ 60 keV, the model does not reproduce the observed spectrum since the bremsstrahlung cross sections may no longer be valid [Koch and Motz, 1959] and corrections for absorption by both the atmosphere and GeD window are very sensitive.

Figure 4.9 shows the measured and model count spectra for the event on Jan-

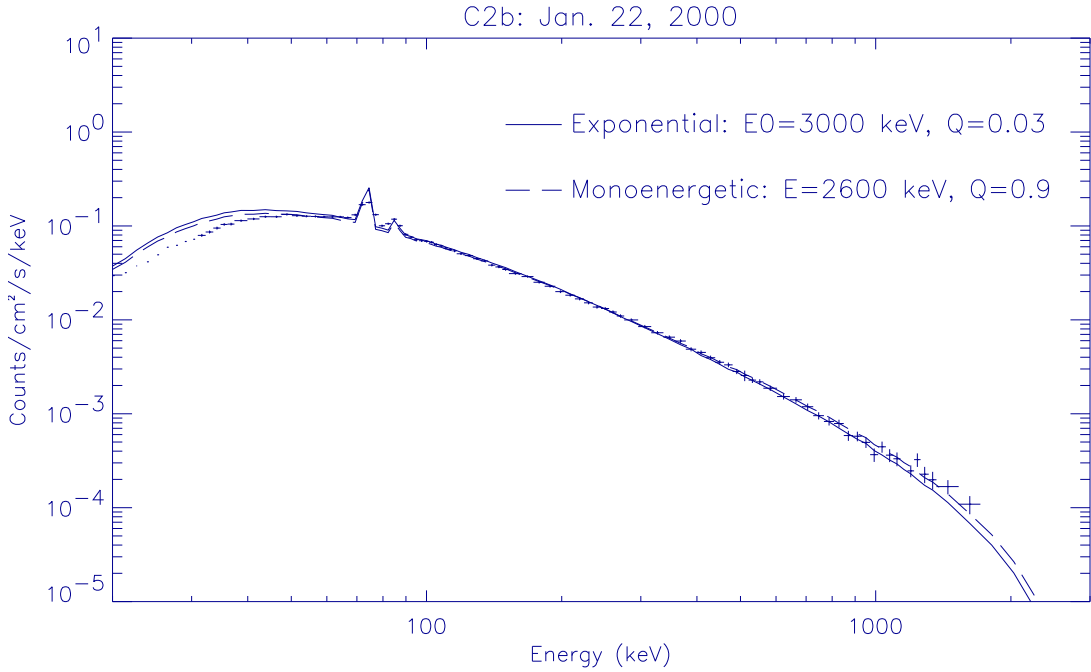


Figure 4.9: Observed and model count spectra

uary 22, 2000. The spectrum for this event is so hard that all the models are consistent with the data since differences in the model spectra lie above the range covered by the data. This event clearly illustrates the need for good measurements above 1 MeV.

The first event on January 23, 2000 was almost ten times weaker than the Kiruna event at high energies thus the statistics are poor enough that different models cannot be distinguished (Figure 4.10). A super-soft component is also evident in the spectrum and could be affecting the shape of the spectrum even above 100 keV. This example again illustrates the difficulty in distinguishing between different models for short, weak events which have poor statistics.

The event on January 25, 2000 occurred during a period of soft precipitation (Figure 3.6) and the soft component was subtracted before modeling the spectrum. The

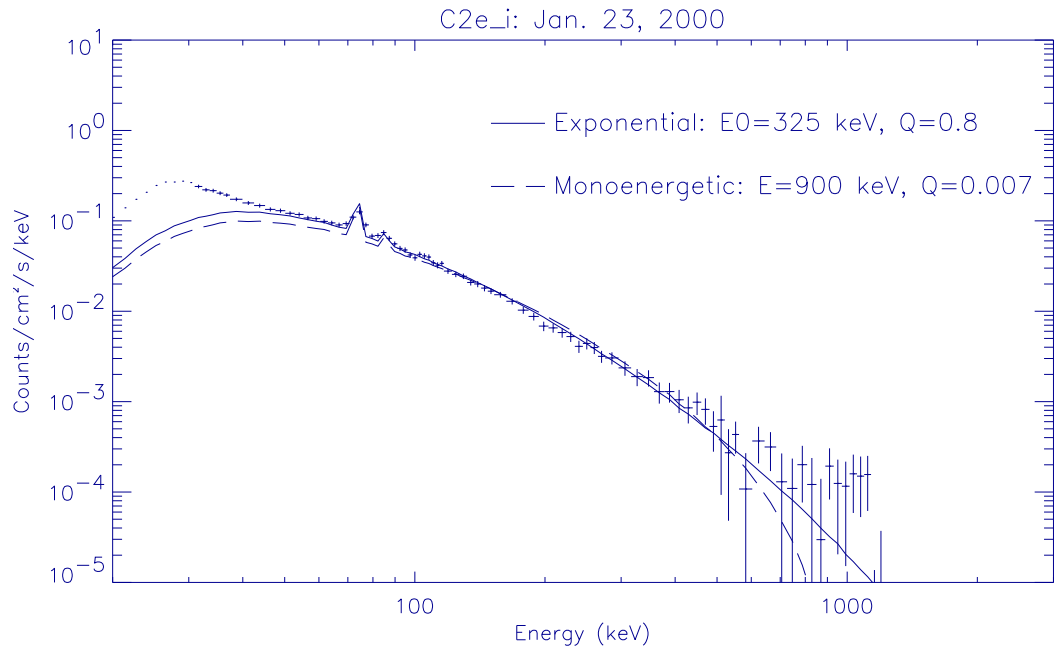


Figure 4.10: Observed and model count spectra

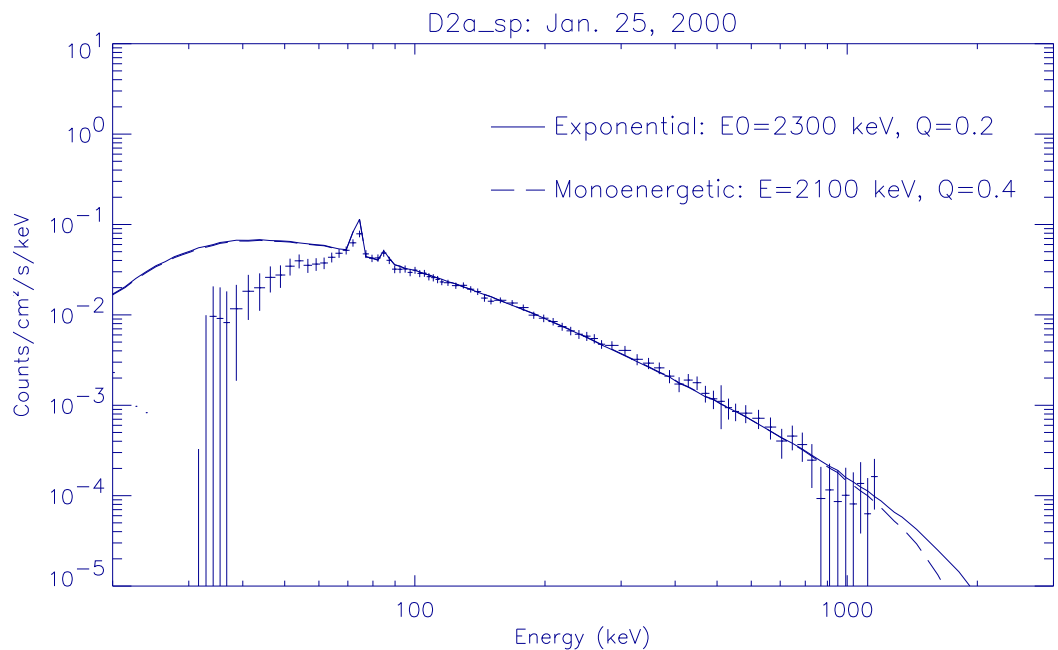


Figure 4.11: Observed and model count spectra

soft component was obtained by averaging the spectrum before and after the MeV event and then scaled by interpolating between the count rate before and after the event but appears to be slightly over-subtracted. Because this event was very short, the statistics are poor and several models fit the data. A monoenergetic electron distribution at 2100 keV, an exponential with e-folding of 2300 keV, and a flat distribution up to 5000 keV were all well fit to the data.

4.2.3 Average Precipitating Relativistic Electron Flux

MAXIS detected nine MeV bursts, with durations from \sim 2 minutes to 2.5 hours, during the eight days it spent between magnetic latitudes of 58° - 68° south. The total number of precipitating relativistic electrons observed was obtained by multiplying the event duration (see Table 3.1) by the best fit >500 keV model electron fluence obtained in the previous section for each event (Table 4.1) giving a total of $9.5 \pm 1.5 \times 10^{21}$ electrons observed by the GeD during the eight day interval. The event on January 19 accounted for four times as many precipitated electrons as all other events combined. The uncertainty in the number of precipitated electrons was estimated in the following way: the uncertainty due to the bremsstrahlung cross sections was taken to be 20% and this uncertainty dominated for the events B2a, B2b, C2e_ii, D1b_i, and D1b_iii. For the other events, the uncertainty was dominated by poor statistics in the observed count spectrum and the resulting large range in the model fit parameters. In these cases, the uncertainty used was taken from the range of >500 keV electron fluence for each event given in Table 4.1. The uncertainty for each event was multiplied by the event duration and these were added in quadrature.

Assuming the events filled the field of view (at 70km) of $3.8 \times 10^{13} \text{ cm}^2$ and dividing

by the observing time of 8 days, the average precipitating electron flux was found to be $j_p \sim 360 \text{ cm}^{-2} \text{ s}^{-1}$. Since the GeD field of view is small, it is assumed that precipitation events that were not observed directly also occurred. To estimate the total number of electrons lost, the average flux was multiplied by the total area between magnetic latitudes 58° - 68° , $2 \times 10^{17} \text{ cm}^2$, and the observing time (eight days). The total number of >500 keV electrons lost during the eight day interval is then $\sim 5 \times 10^{25}$.

Baker et al. [1998] estimated the total number of >500 keV trapped outer zone electrons before and after the January 1997 magnetic cloud event to be 10^{23} and 10^{26} respectively. To estimate the total number of trapped electrons during the MAXIS flight, measurements of the electron flux made by one of the GPS satellites on January 19 between 2:30-6:10 UT (Figure 3.16), prior to any observed MeV events, were used. The outer extent of the belts was defined using the definition of the trapping boundary given in Section 3.4 and was $L=7$ for the two lowest energy channels, $L=6.5$ for 1.32-2.38 MeV and $L=5$ for 2.38-3.6 MeV. The inner limit was taken to be $L=2$ which is the approximate inner extent of the outer radiation belts. There were no X-ray or GPS observations at L-values this low, but extending the calculation down to $L=2$ doesn't change the result since the volume contributed between $L=2$ and $L=4$ is small. For an isotropic pitch angle distribution, the flux of electrons, J , anywhere along the magnetic field line is constant. Therefore, the density of electrons is obtained with

$$n = \frac{J}{c}$$

where the speed of the electrons is taken to be the speed of light since the particles are relativistic. The volume of the shell between L_1 and L_2 can be calculated as follows. By

conservation of magnetic flux, the cross-sectional area of a flux tube at some position along the field line, s , can be written in terms of the cross-sectional area at the equator. In the case of a dipolar magnetic field

$$dA_\theta = \frac{B_{eq}}{B_\theta} dA_{eq} = \frac{\sin^6 \theta}{(1 + 3\cos^2 \theta)^{1/2}} dA_{eq}$$

where θ is the co-latitude (the usual spherical coordinate). The differential length of the field line is given by [Schulz and Lanzerotti, 1974]

$$ds = LR_e \sin \theta (1 + 3\cos^2 \theta)^{1/2} d\theta$$

where R_e is the radius of the earth. Thus the total volume of the shell between L_1 and L_2 can be written

$$V = \int ds dA_\theta = 2R_e^3 \int_0^{\pi/2} \sin^7 \theta d\theta \int_{L_1}^{L_2} L^2 dL \int_0^{2\pi} d\phi$$

where the integral is taken down to the center of the earth (θ from 0 to $\frac{\pi}{2}$) for simplicity since this will contribute very little to the volume. The total number of electrons in the shell between L_1 and L_2 is then

$$N = 0.46 \times \frac{4\pi R_e^3}{c} J \int_{L_1}^{L_2} L^2 dL \quad (4.4)$$

The median flux for each energy channel during the pass was determined and assumed to be isotropic and N was calculated for each energy channel. The total number of 0.5-3.6 MeV electrons measured in the radiation belts was found to be 2×10^{25} . Thus the MAXIS observations indicate that the outer zone could be depleted by MeV precipitation events in a few days if no new particles were accelerated. Although the flux of outer zone relativistic electrons is highly variable, the particles never disappear completely, therefore, they must also be replenished on the same timescale.

Previous estimates of the loss rate made using in-situ measurements of the electron flux found an e-folding decay time of ~ 6 days after a storm-related enhancement for >450 keV electrons [Schulz and Lanzerotti, 1974]. This is comparable to the loss rate measured by MAXIS indicating that MeV X-ray bursts are one of the primary mechanisms for the loss of relativistic electrons from the outer radiation belts.

Spacecraft observations indicate that the pitch angle distribution is more typically peaked near 90° rather than isotropic so the flux tends to be concentrated near the equator. Since most of the GPS measurements were taken away from the equator, the measured value could underestimate the trapped flux. This factor can be estimated as follows assuming a typically observed pitch angle distribution

$$J = J_\perp \sin^m \alpha$$

with $m \sim 1$ where J_\perp is the flux of 90° pitch angle particles [Baker et al., 2001]. Using Liouville's theorem, the flux at some position along a magnetic field line, s , can be expressed in terms of the flux at the equator ($s=0$)

$$J_\perp(s) \sin^m \alpha(s) = J_\perp(0) \sin^m \alpha_{eq}$$

Particles move along the magnetic field line conserving their first adiabatic invariant (Section 1.2.2) thus

$$\frac{\sin \alpha_{eq}}{\sin \alpha(s)} = \sqrt{\frac{B(0)}{B(s)}}$$

Therefore,

$$\frac{J_\perp(s)}{J_\perp(0)} = \left(\frac{B(0)}{B(s)} \right)^{m/2}$$

With $m=1$, the flux scales as the square root of the magnetic field ratio.

Since the particle density is no longer independent of θ , the magnetic field ratio as a function of θ must be included in the volume integral. To estimate the total number of particles assuming this pitch angle distribution, scale factors were first determined as a function of L using the magnetic field ratio determined by the measured field at the GPS location and model equatorial field given by the Tsyganenko 1989 model and were found to range from 1.0 at L=4 to 2.6 at L=7. The integral over θ doesn't change by much giving 0.37 instead of 0.46 that was found in the uniform density case (Equation 4.4). The total number of trapped electrons assuming this pitch angle distribution is then 3×10^{25} which is not much larger than the previous estimate.

In Section 4.4, the precipitating electron flux for individual events is compared with the GPS measurements in each energy band.

4.3 Direct Inversion Method

If the detector resolution and the statistics are sufficient, the X-ray spectrum can be directly inverted to obtain the precipitating electron spectrum. The direct inversion is still subject to the limitations described above but has the advantage that no a priori assumption is made about the electron distribution. To obtain the source photon spectrum from the observed count spectrum, the atmospheric/instrument response matrix described in Section 4.1.3 is inverted and applied to the observed count spectrum.

As mentioned in Section 2.2.3, the BGO scintillator flown on MAXIS is more sensitive than the GeD at high energies. Because the instrument response of the BGO is different than that of the GeD, the instrument response must be removed from each before the spec-

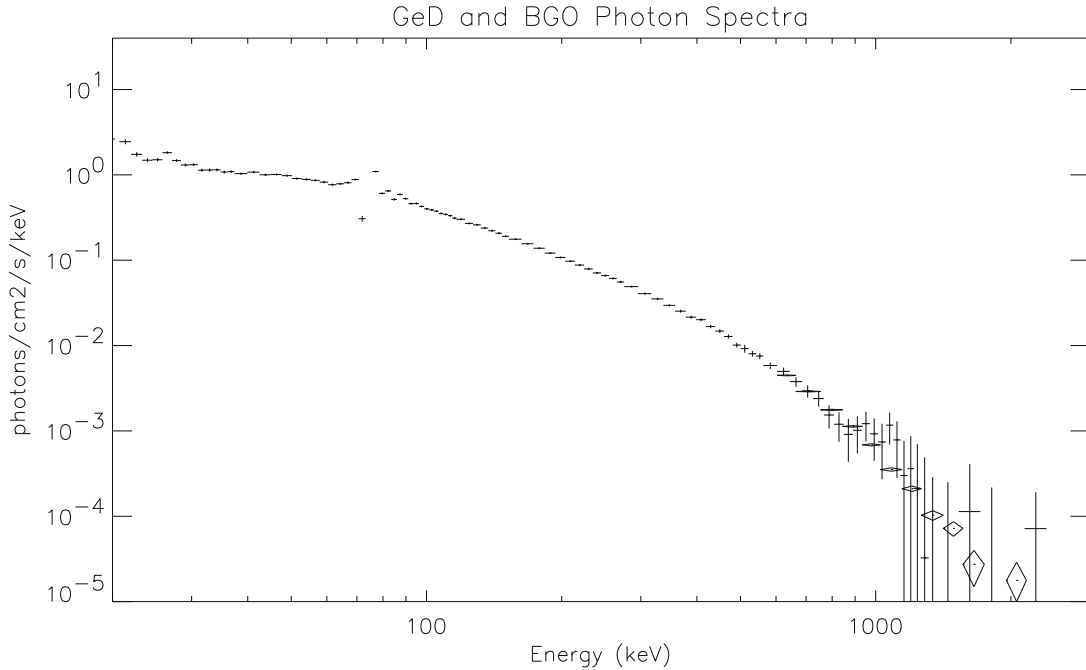


Figure 4.12: GeD (crosses) and BGO (diamonds) photon spectra on Jan. 19,2000.

tra can be combined. Background subtracted BGO spectra were provided by Dr. Michael McCarthy at the University of Washington for each MeV event. The spectra were binned into 23 energy bins with bin width approximately equal to the spectral resolution at each energy ($\sim 10\%$). A Monte Carlo simulation similar to that described for the GeD was carried out using a five component mass model of the instrument and the CERN Monte Carlo code, MGEANT V2.7. New atmospheric response matrices were calculated using the same method as for the GeD but with different input energy bins. The atmospheric and instrument response matrices were then multiplied and the spectrum was inverted as for the GeD. Since the BGO scintillator was uncollimated except for a thin lead shield surrounding the crystal, the angular distribution was chosen so the BGO spectrum matched the GeD where the two spectra overlapped. Figure 4.12 shows both GeD and BGO photon spectra for the

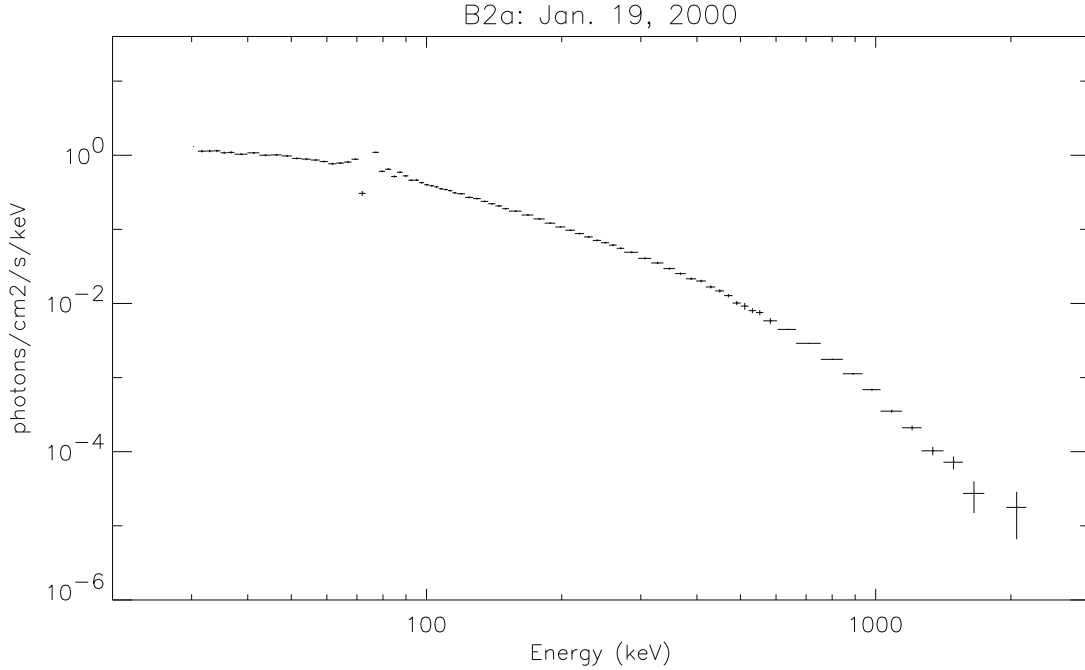


Figure 4.13: Combined GeD and BGO photon spectrum.

January 19 MeV event.

The photon spectra were then combined as follows. The GeD data were first rebinned above 600 keV to match the BGO energy bins. A weighted average of GeD and BGO data was then computed in each bin up to 1 MeV above which only the BGO data were used. Below 600 keV, only GeD data were used. Figure 4.13 shows the combined GeD and BGO photon spectrum for the event on January 19, 2000.

Once the photon spectrum is obtained, the equilibrium and precipitating electron distributions can be calculated following the method of Johns and Lin [1992]. To obtain the differential electron flux given the differential photon flux, Equation 4.3 must be inverted. Rewriting Equation 4.3 as a matrix equation

$$J_\gamma = \beta J_e$$

where J_γ is an $n \times 1$ matrix of the measured photon fluxes, $dJ/dk(k_i)$ in each energy bin, k_i , and J_e is the column matrix of electron fluxes. β is an $n \times n$ matrix with elements

$$\beta_{ij} = 0 \quad \text{for } j < i$$

and for $j \geq i$

$$\beta_{ij} = \frac{nV}{4\pi R^2} \int_{k_j}^{k_{j+1}} \frac{d\sigma}{dk}(k_i, E) dE$$

The matrix equation can be inverted to obtain the electron flux

$$J_e = \alpha J_\gamma$$

where, like β , α is an upper triangular matrix.

The uncertainties in the electron flux are given by

$$\delta \frac{dJ_e}{dE} = \left[\sum_{j=1}^n \left(\alpha_{ij} \delta \frac{dJ}{dk}(k_j, t) \right)^2 \right]$$

Because alpha is upper triangular, the uncertainty at one energy has contributions from the measured uncertainties at all higher energies. In other words, the errors propagate downward leading to very large uncertainties at the low energy end of the spectrum for the very flat spectra of MeV events. To reduce these uncertainties, the photon spectrum was first binned starting at the highest energy bin and working downwards. To avoid binning over such a large energy range that the cross sections would vary substantially within the bin, the photon spectrum was only binned to reduce the uncertainties somewhat and the

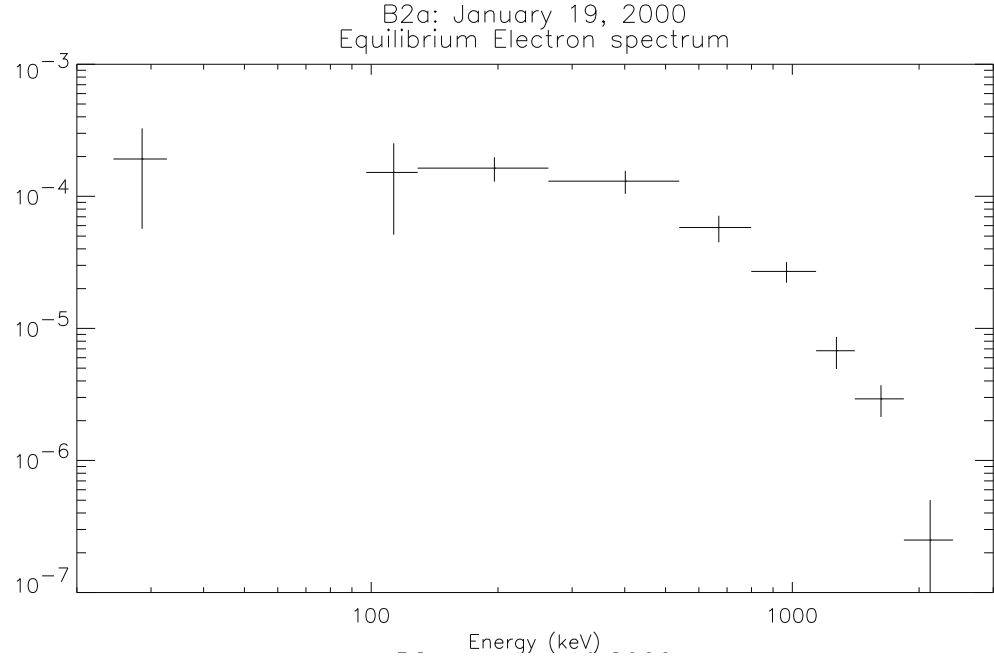


Figure 4.14: Equilibrium (bremsstrahlung-producing) electron spectrum.

resulting electron spectrum was further binned after doing the inversion. As discussed in Johns and Lin [1992], the photon spectrum must also be extrapolated at the high energy end since the data only extend to some finite energy but the X-ray flux may extend further. The extrapolation is carried out by fitting a power law to the last two photon fluxes and then extending the spectrum a few hundred keV beyond the last data point. Note that in doing this, an assumption about the electron distribution is being made; if the input electron distribution was monoenergetic with energy near the last data point, it would roll off very quickly and not follow the extrapolated power law.

The equilibrium electron distribution above 100 keV is shown in Figure 4.14 for the event on January 19, 2000. Because of imperfect modeling of the collimator lead lines in the GeD instrument response, the inversion was unreliable for all energies below 100 keV.

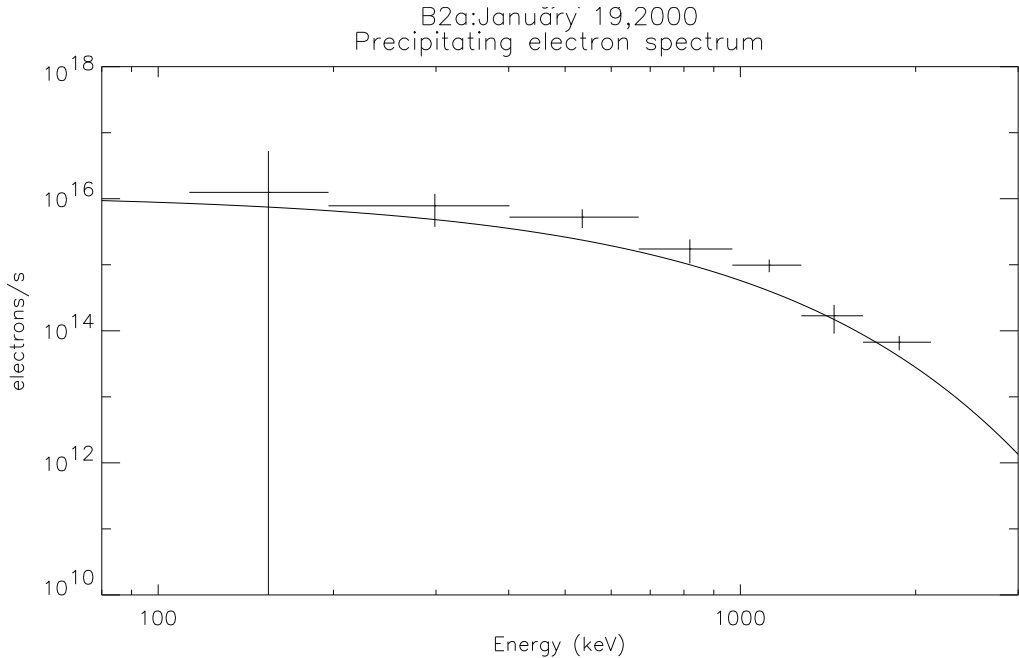


Figure 4.15: Precipitating electron spectrum.

After obtaining the photon-producing electron distribution, the precipitating distribution can be calculated. From Equation 4.1, solving for the precipitating electron distribution, we have

$$F(E) = \frac{d}{dE} \left(\frac{dE}{dt} N(E) \right)$$

which can be computed numerically. The precipitating electron distribution for the event on January 19 was very nearly exponential and is shown in Figure 4.15 along with the best fit exponential obtained with the forward modeling.

4.3.1 Direct Inversion results for MAXIS MeV Events

Only four of the MAXIS MeV events had statistics sufficient to carry out the direct inversion. The results for the event on January 19 were presented in the last section and

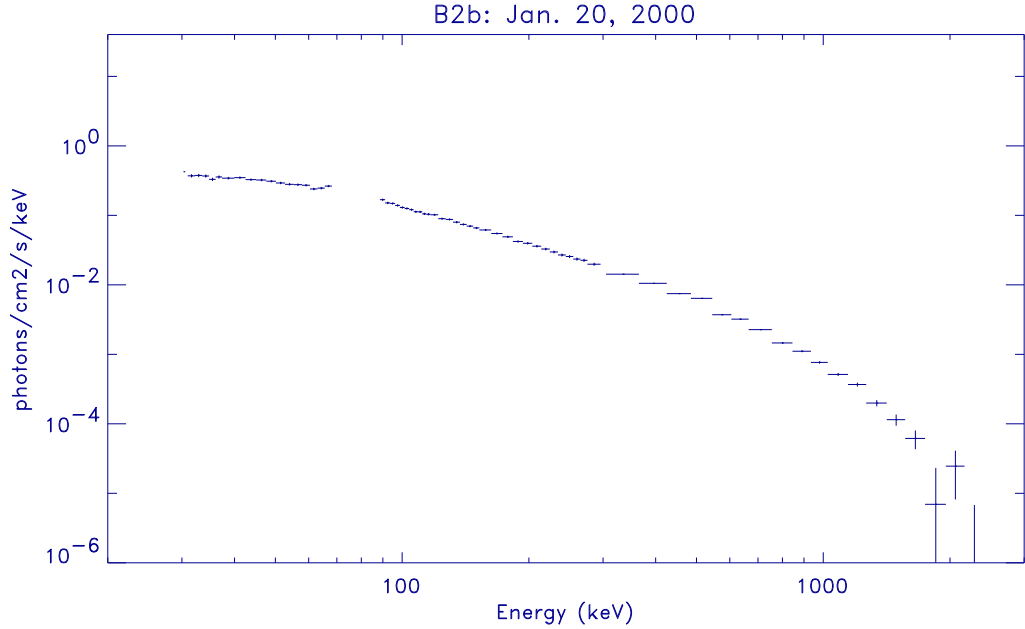


Figure 4.16: Combined GeD and BGO photon spectrum.

the results for the remaining three are shown in this section.

B2b: January 20, 2000

The event on January 20 was harder than the January 19 event (Figure 4.16) and the event was short so the errors are larger. The equilibrium and precipitating electron distributions are shown in Figure 4.17 and the results are consistent with the results from the forward modeling (solid line) except below 500 keV where the forward model gives slightly larger results. Below 500 keV, the direct inversion gives only an upper limit on the precipitating flux.

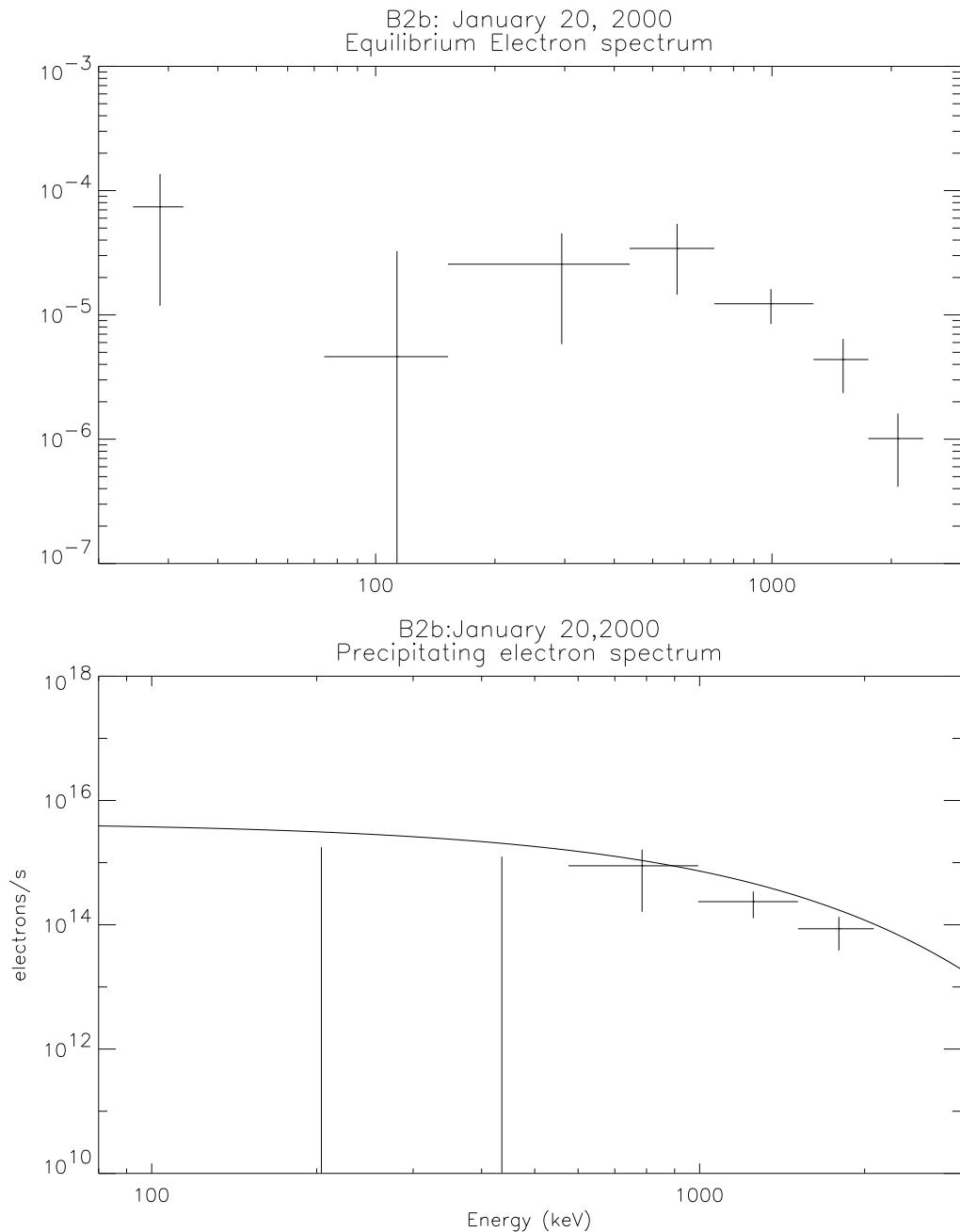


Figure 4.17: Equilibrium (bremsstrahlung-producing) and precipitating electron spectra.

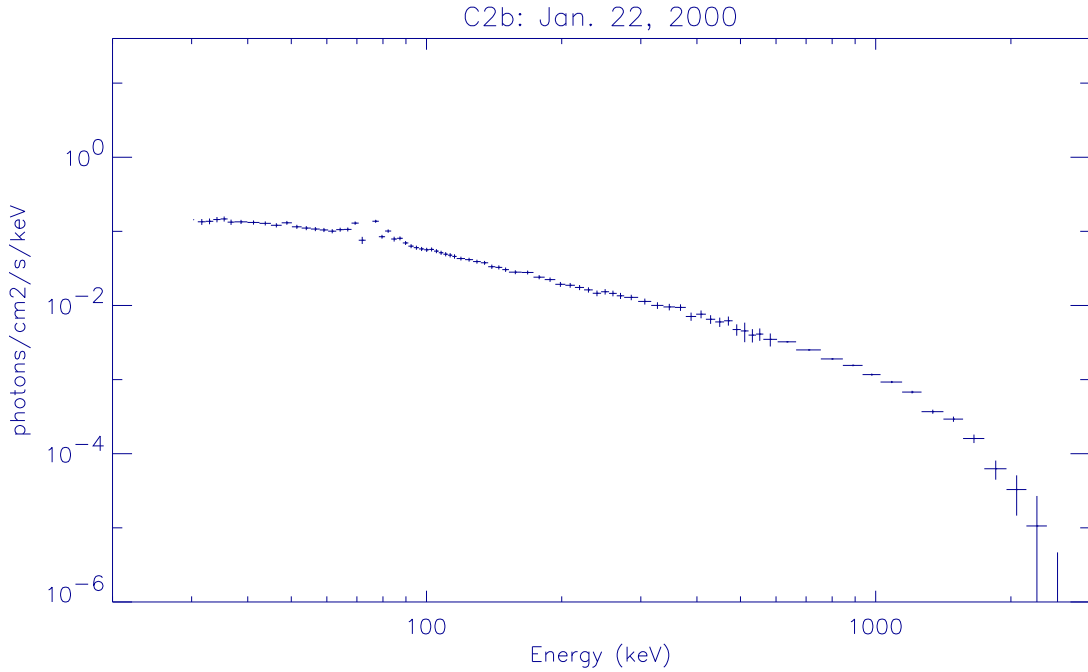


Figure 4.18: Combined GeD and BGO photon spectrum

C2b:January 22,2000

The event on January 22 was the hardest event detected by MAXIS and the combined photon spectrum is shown in Figure 4.18. The equilibrium and precipitating fluxes are shown in Figure 4.19 along with the best fit exponential. The precipitating distribution is consistent with a monoenergetic, flat or exponential distribution, however, the direct inversion does provide a good constraint on the precipitating flux above ~ 1.5 MeV. In this case, the direct inversion gives slightly larger results at high energies.

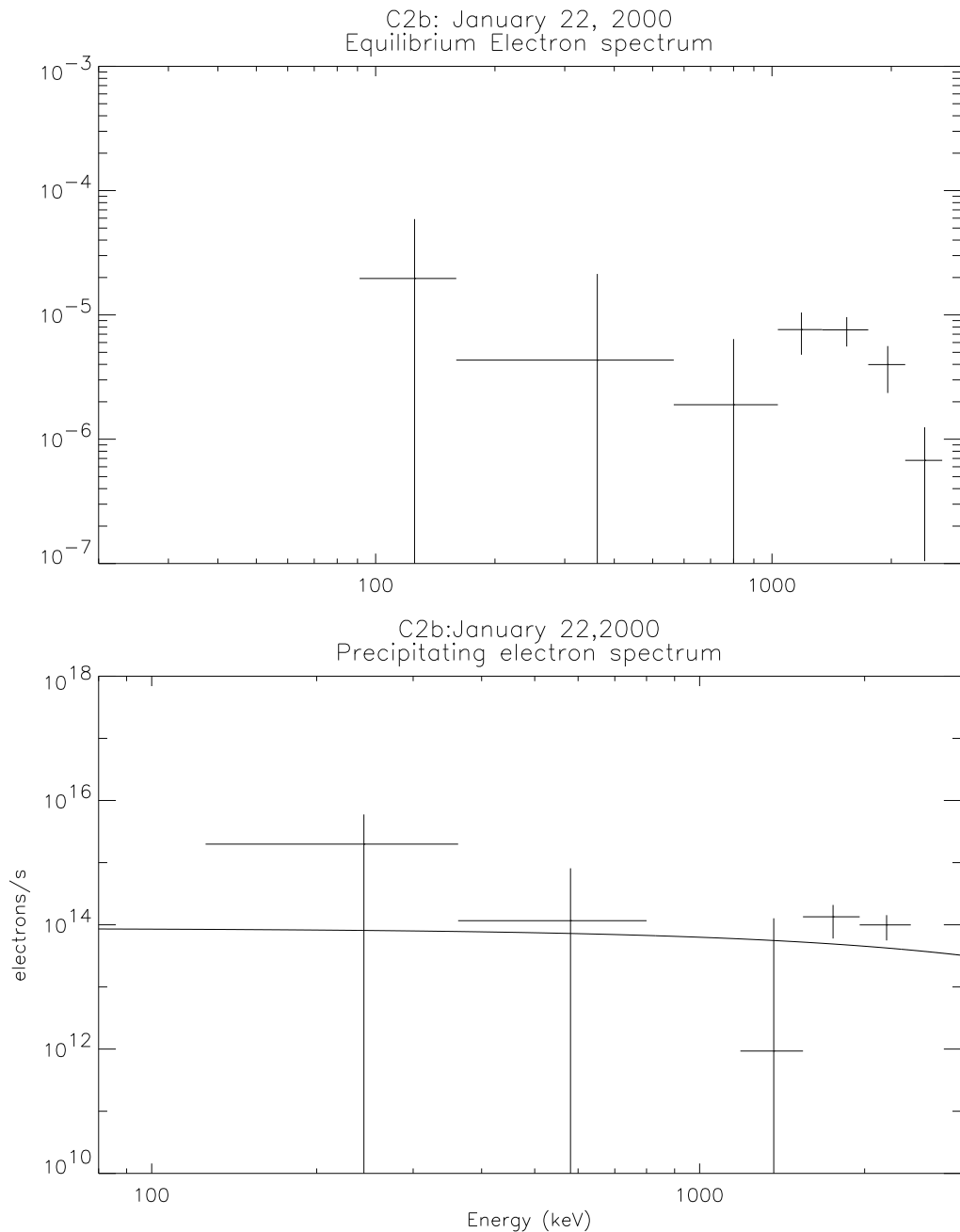


Figure 4.19: Equilibrium (bremsstrahlung-producing) and precipitating electron spectra.

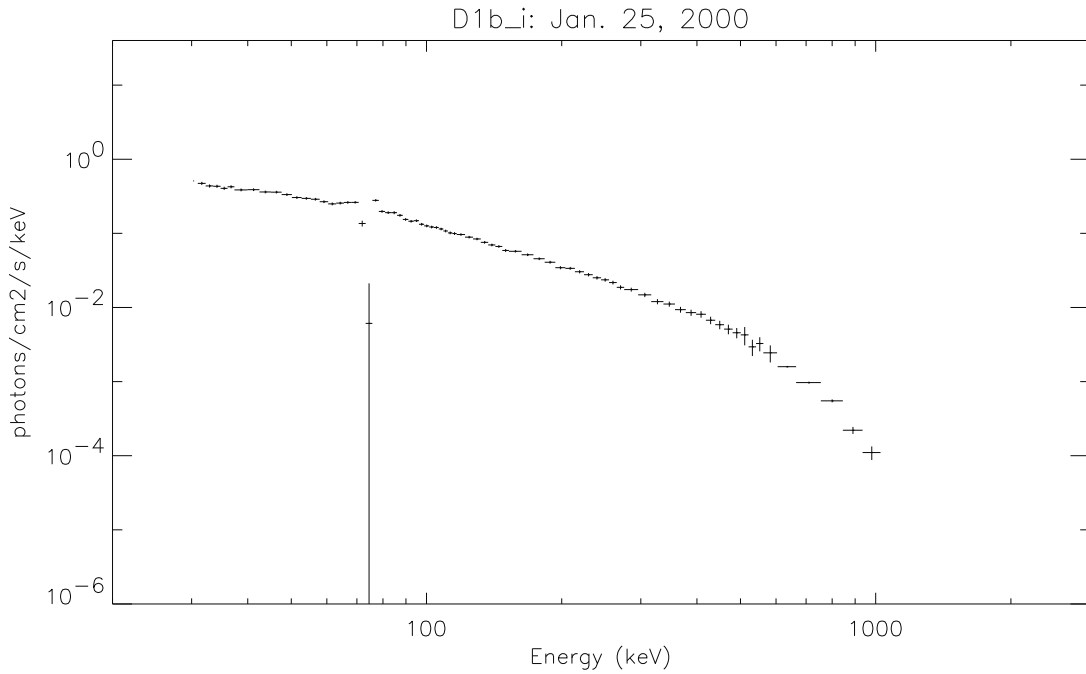


Figure 4.20: Combined GeD and BGO photon spectrum.

D1b_i:January 25,2000

The photon spectrum for this event doesn't extend much beyond ~ 1 MeV as shown in Figure 4.20. Results from the forward modeling indicated that this spectrum is consistent with either an exponential or flat precipitating electron distribution. The direct inversion results are shown in Figure 4.21 and are consistent with the forward modeling results except at low energies where, similar to the January 20 event, the forward modeling overestimates the flux.

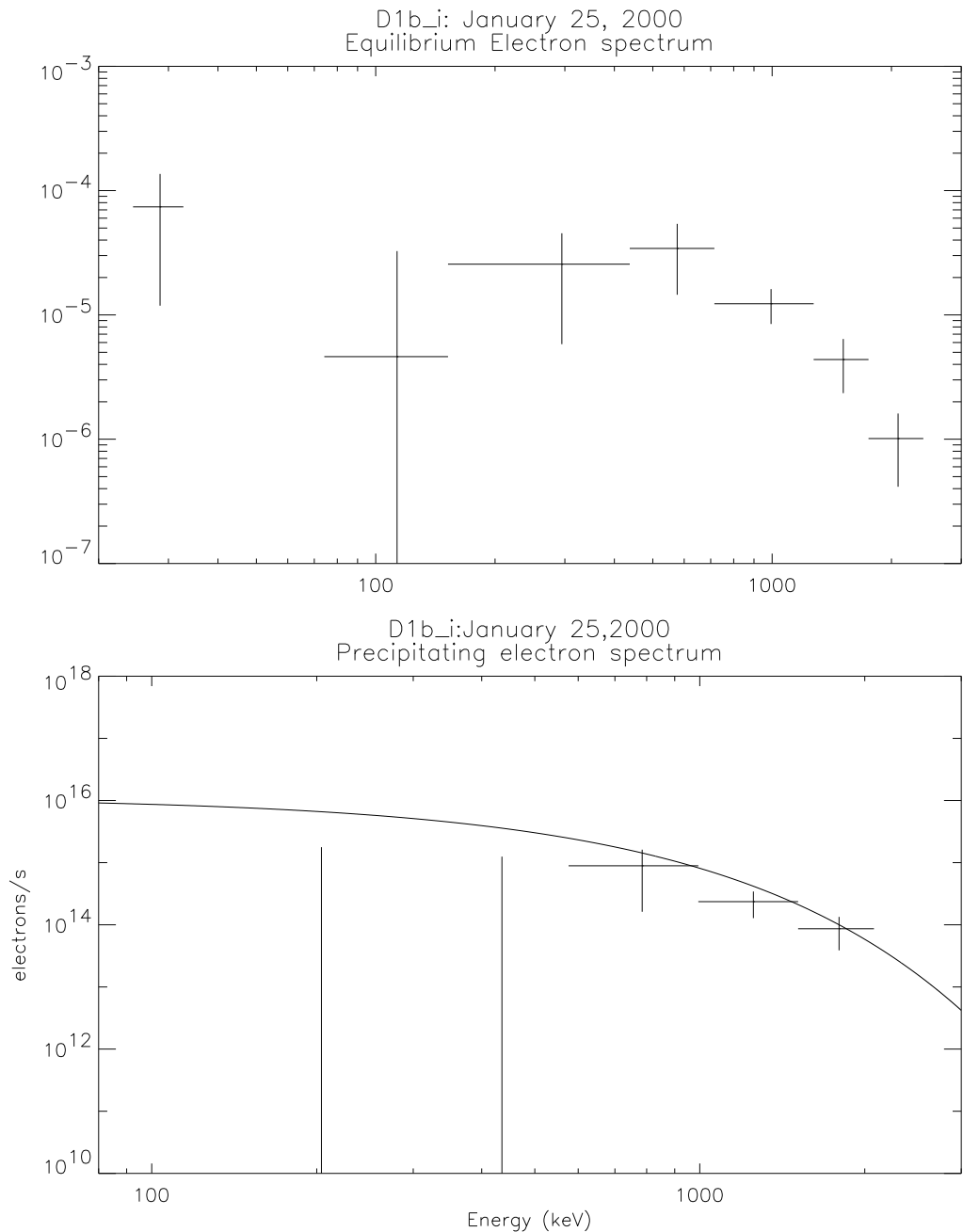


Figure 4.21: Equilibrium (bremsstrahlung-producing) and precipitating electron spectra.

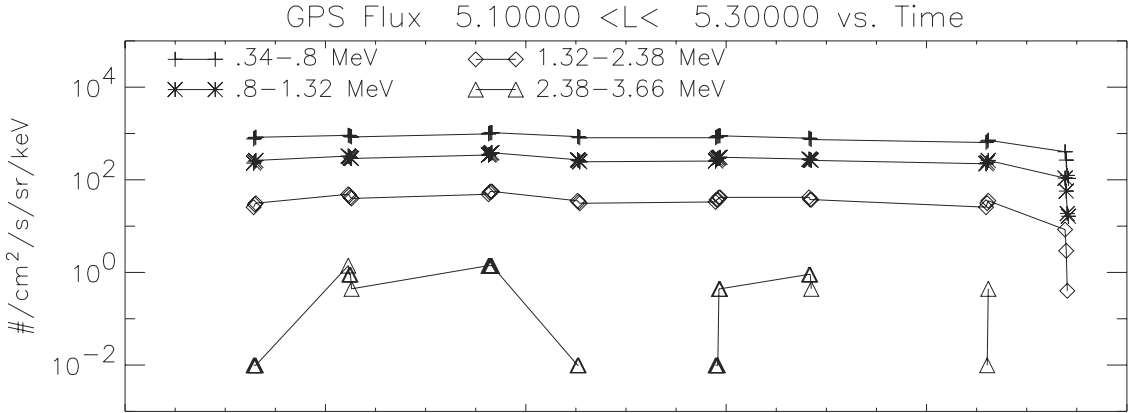


Figure 4.22: GPS electron flux in four energy channels averaged over $L=5.1-5.3$ on January 19, 2000.

4.4 Comparison with Measurements of Trapped Electrons

In this section the precipitating electron distribution is compared to in-situ measurements of the trapped electrons measured by one of the GPS satellites. The GPS measurements were first averaged over a small range of L-values near the balloon location; for the event on January 19, the flux was averaged between $L=5.1-5.3$ and is shown in Figure 4.22. A time interval before the MeV event was then chosen (13:10-18:00 UT on Jan. 19) and the flux averaged over that interval. The flux was assumed to be isotropic over the downward (toward Earth) hemisphere.

Figure 4.23 shows the average trapped electron flux measured by GPS with the precipitating electron distribution for the Jan. 19 event superposed. For an isotropic pitch angle distribution, the trapped and precipitating fluxes would be equal. This would be the case for strong pitch angle scattering and would be the maximum flux that could be precipitated (i.e the case where the loss cone is filled). For the event on January 19, the precipitating flux is a small fraction of the trapped flux which indicates that only a small

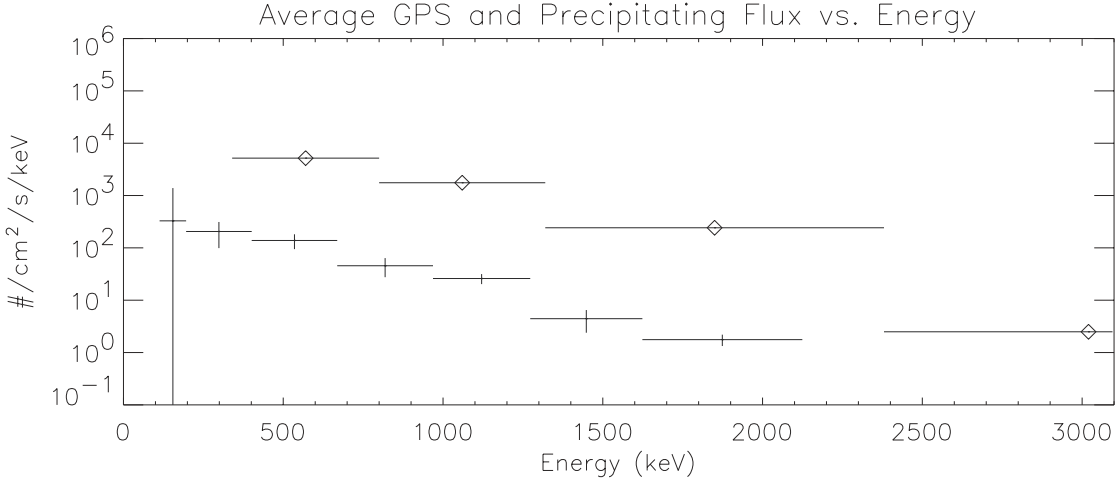


Figure 4.23: GPS electron flux averaged over $L=5.1-5.3$ on January 19, 2000 from 13:10-18:00 UT (bar with diamonds) and precipitating electron flux (crosses).

fraction of the particles are being scattered into the loss cone. If the scattering mechanism is wave-particle interactions, this implies that the interaction is not in the strong diffusion regime.

To quantify the scattering strength as a function of energy, the precipitated spectrum was first rebinned to match the GPS data and then divided by the trapped spectrum to obtain a scattering efficiency in each energy bin (Figure 4.24). For the event on January 19, $\sim 1\text{-}3\%$ of the particles that could have been were scattered into the loss cone and the scattering is strongest in the 340-800 keV channel.

The January 19 event occurred at $L\sim 5$ and the flux near the edge of the radiation belts falls steeply with increasing L . If the magnetic field model used is not accurate, the balloon location could map to a different L -value where the GPS measurements could be different. To quantify this uncertainty, the same scattering efficiency was calculated using different L -values, from 0.5 L below and 0.5 L above the original L interval. The efficiency

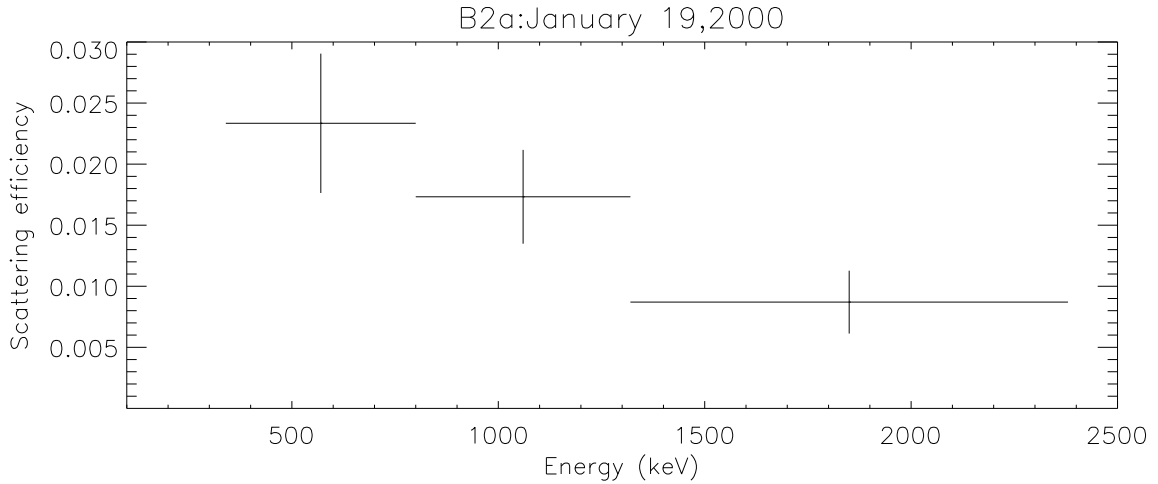


Figure 4.24: Scattering efficiency as a function of energy.

was found to vary by up to a factor of two. The time interval chosen was also varied since, just prior to this event, there was a drop in the electron flux as measured by GPS. Using the GPS measurements from the time interval 19:10-21:30 just prior to the MeV event, the efficiency was 1.5 times larger.

Although this event was the strongest detected, its spectrum was not very hard (not nearly as hard as the Kiruna event) suggesting that the scattering efficiency at high energies could be much larger for some of the other events. Figures 4.25-4.27 show the scattering efficiency for three other events. The event on January 20 was compared with GPS measurements between $L=5.1-5.3$, and the event on January 25 $L=5.9-6.1$. For these two events, the scattering was stronger at higher energies. The event on January 22 occurred at $L=3.8$ and was compared with GPS measurements at $L=4.1-4.5$ since the satellite didn't go below 4.1. Although this event was the hardest event detected, the scattering efficiency is not much larger at higher energies than the other events. This is probably because

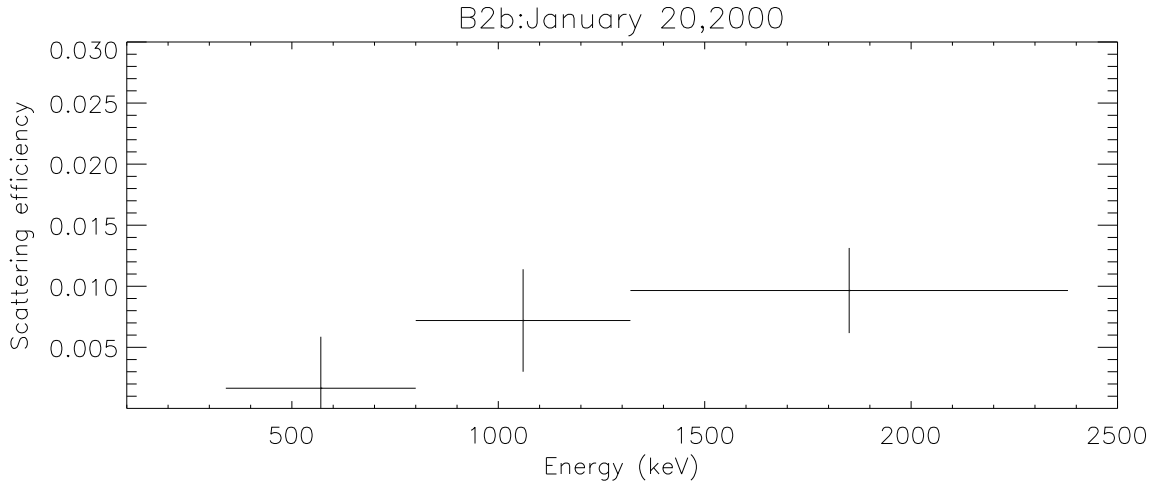


Figure 4.25: Scattering efficiency as a function of energy.

the trapped spectrum appears to be flatter at lower L values. The event on January 25 preferentially scattered higher energy electrons more than for any other event. This event also occurred at the highest L-value (L=6).

In the above calculations, the pitch angle distribution of the trapped electrons was assumed to be isotropic and the precipitating fluxes were compared directly to the measured fluxes. However, as mentioned in Section 4.2.3, the pitch angle distribution is usually observed to be concentrated near the equator thus the GPS measurements could be underestimating the trapped flux. Therefore, the above efficiencies really represent upper limits. Assuming the pitch angle distribution goes as $\sin\alpha$, the flux would be a factor of 1.5 higher at L~5 (Jan. 19 and Jan. 20 events), unchanged at L~4.2 (Jan. 22 event) and a factor of 2 higher at L~6 (Jan. 25 event). Therefore, the efficiencies shown above could be too high by up to a factor of two.

The average precipitating flux for these four events is only at the few percent level

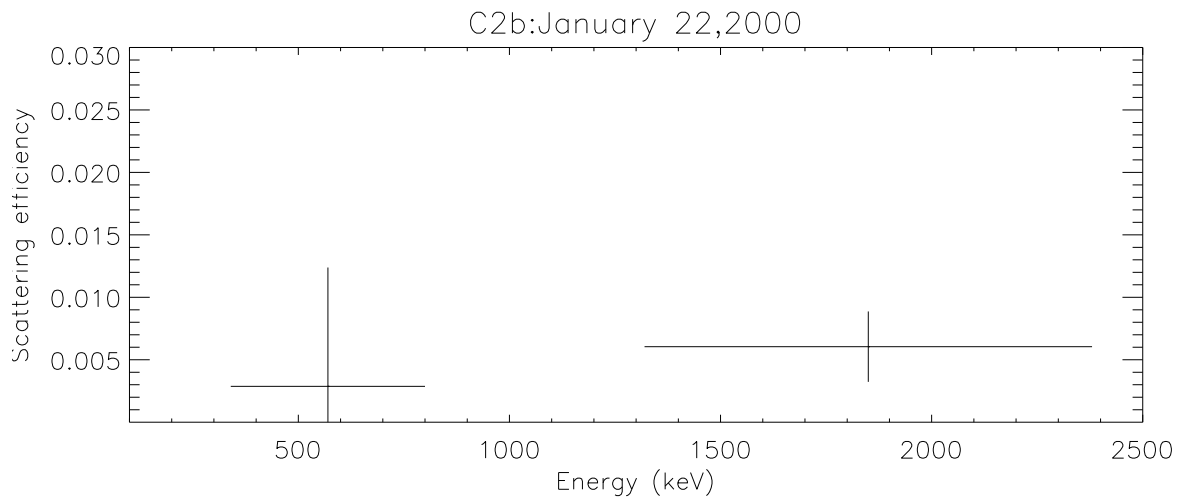


Figure 4.26: Scattering efficiency as a function of energy

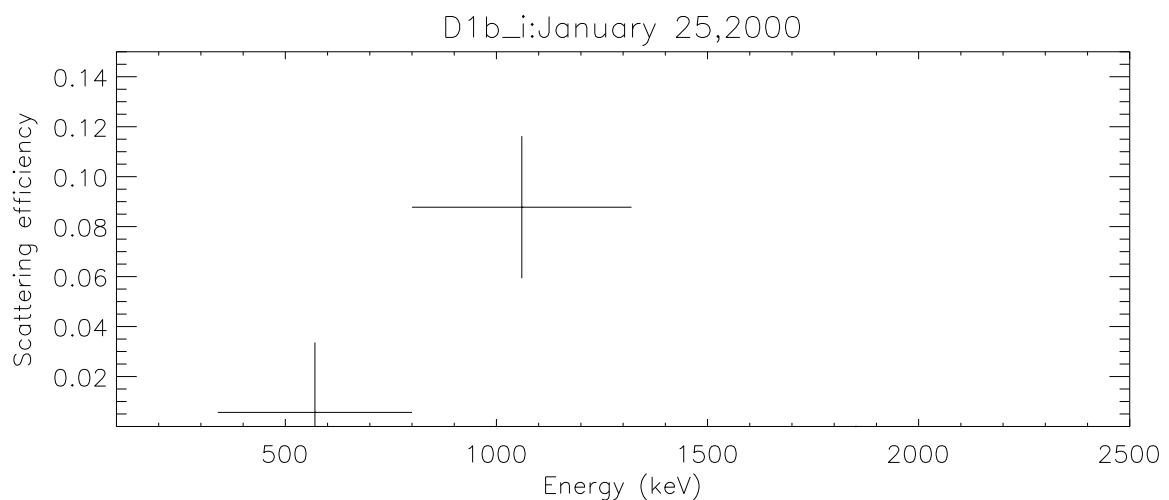


Figure 4.27: Scattering efficiency as a function of energy

with the exception of the January 25 event for which it is $\sim 5\text{-}10\%$. These observations indicate that the mechanism acting to precipitate particles is not strong scattering. However, these results are consistent with the loss rates presented in Section 4.2.3. This can be seen in the following way. The fraction of particles lost per second is

$$f = \epsilon \frac{\Delta\Omega}{2\pi} \frac{1}{\tau_b}$$

where ϵ is the scattering efficiency (or fraction of particles in the loss cone compared to an isotropic distribution), $\Delta\Omega$ is the size of the loss cone in steradians and τ_b is the particle bounce time. Here it is assumed that all particles in the loss cone are lost in one bounce period. For a relativistic electron ($\beta \approx 1$) with small pitch angle, the bounce time (Equation 1.4) is $\tau_b \approx 0.1L/\gamma$ and is 0.2 seconds for a 1 MeV electron at $L=5$. The loss cone is defined by particles mirroring at 60 km where, for a dipolar magnetic field, the mirror field is given approximately by

$$\frac{B_{eq}}{B_m} = \left(\frac{1.01}{L}\right)^3 \frac{1}{(4 - \frac{3.03}{L})^{1/2}}$$

Combining this with Equation 1.5, the loss cone angle, α_L , is given approximately by

$$\alpha_L = \left(\frac{1}{2L^3}\right)^{1/2}$$

and is about 3.6° at $L=5$. For small pitch angles,

$$\Delta\Omega \sim \pi\alpha_L^2 = .0124$$

The average MeV event duration is 40 minutes. Assuming $\epsilon=0.01$, the fraction of 1 MeV electrons lost from a given flux tube due to one event is then 0.2. On average, about 1 event occurs per day at any given location (i.e. for any flux tube). Therefore, it would take ~ 5 days to lose all the particles.

The above scattering efficiencies were computed using the average precipitating flux from each event rather than the peak flux. However, many of the MeV events consist of multiple bursts or a temporally modulated count rate. For example, the event on January 20, had a peak count rate five times as large as the average. Therefore, the scattering efficiencies could be as high as 10% during the strongest part of each MeV event, but still not in the strong diffusion regime.

4.5 Summary

In this chapter, the procedures for modeling the X-ray spectrum were discussed and used to derive the precipitating electron distribution and flux for each MeV event. A very flat exponential precipitating electron distribution was found to be consistent with every event though some were also well modeled by a monoenergetic or flat electron distribution. Therefore, EMIC waves are unlikely to be the scattering mechanism since, as discussed in Section 1.3.2, only electrons with energies ≥ 1 MeV are expected to be resonant with EMIC waves. The precipitating electron flux was compared to the trapped flux as measured by one of the GPS satellites and a scattering efficiency was calculated. These results show that the scattering is not in the strong diffusion regime. However, the average precipitating >500 keV electron flux due to MeV events was found to be $360 \text{ cm}^{-2}\text{s}^{-1}$ indicating that the entire outer zone could be depleted of relativistic electrons in a few days. This loss rate is comparable to previous estimates of the total loss rate indicating that the MeV events are one of the primary loss mechanisms for outer zone relativistic electrons.

Chapter 5

Temporal Analysis

Unlike low-Earth orbiting spacecraft which traverse through a precipitation region on time scales of seconds, balloons offer a nearly stationary platform from which the temporal structure of precipitation on all time scales, from microseconds to hours, can be studied. Thus they provide another tool for understanding the underlying physics of energetic electron precipitation. As discussed in Section 1.3.1, X-ray observations from balloons have commonly shown modulation of the X-ray count rate at timescales ranging from < 1 s to several minutes. The < 1 s “X-ray microbursts” occur on roughly the electron bounce timescale; a packet of electrons bouncing between mirror points could cause modulation on the bounce timescale if some of the electrons were precipitated near the mirror point during each bounce. SAMPEX observations of microburst precipitation also support this model [Blake et al., 1996]. The X-ray modulation on longer timescales has been attributed to modulation of the electron precipitation by plasma waves. The waves may be directly responsible for the precipitation or indirectly modulate the precipitation rate. For example,

the growth rate of plasma waves can be modulated by Ultra Low Frequency (ULF) waves [Coroniti and Kennel, 1970].

As described in Section 1.4, the 1996 Kiruna MeV X-ray event was modulated at both 10-20 s and 100-200 s. A 4.9 mHz Field Line Resonance was also observed with ground-based magnetometers suggesting a connection between ULF waves and the X-ray modulation. Lorentzen [1999] suggested that if the electrons were scattered by EMIC waves, modulation of the wave growth by ULF waves could cause the observed 100-200 s modulation. As discussed below, MAXIS observed several MeV events that show modulation at ULF timescales very similar to the Kiruna event.

In this chapter, the temporal structure of MeV electron precipitation is examined. In Section 5.1, the Fourier power spectrum is introduced and its limitations discussed. The wavelet transform is then introduced as an alternative method for analyzing temporal variations (Section 5.2) and the Kiruna event is used as an example to compare the two methods. Finally, the wavelet power spectrum is presented for two MAXIS MeV events. Correlated ground-based and spacecraft observations are also examined for evidence of wave activity near the time and location of the MeV events. Several mechanisms for modulating precipitation are then discussed.

5.1 Fourier Analysis

5.1.1 Overview

The Fourier transform and its inverse are defined as

$$\begin{aligned}\mathcal{F}(\omega) &= \int_{-\infty}^{\infty} f(t)e^{i\omega t}dt \\ f(t) &= \frac{1}{2\pi} \int_{-\infty}^{\infty} \mathcal{F}(\omega)e^{-i\omega t}d\omega\end{aligned}\tag{5.1}$$

and the power spectrum is given by

$$P(\omega) \equiv |\mathcal{F}(-\omega)|^2 + |\mathcal{F}(\omega)|^2\tag{5.2}$$

For discretely sampled data, we use the Fast Fourier Transform [Press et al., 1992].

In particular, we are interested in modulation of the X-ray count rate and also in the time evolution of that modulation (i.e frequency change, etc.). Therefore, a sliding window Fourier transform is used. An X-ray event is divided into intervals each containing N points and centered about some time, t . A power spectrum is computed for each interval given by

$$\begin{aligned}P(0) &= \frac{1}{N^2} |C(0)|^2 \\ P(f_k) &= \frac{1}{N^2} \left[|C_k|^2 + |C_{N-k}|^2 \right] \quad k = 1, \dots, (\frac{N}{2} - 1) \\ P(f_c) &= P(f_{N/2}) = \frac{1}{N^2} \left| C_{\frac{N}{2}} \right|^2\end{aligned}\tag{5.3}$$

where C_k are the Fourier coefficients at $N/2+1$ frequencies, f_k , given by

$$f_k = \frac{k}{N\Delta} = 2f_c \frac{k}{N} \quad k = 0, \dots, \frac{N}{2}\tag{5.4}$$

where Δ is the sampling interval. As N is increased, the frequency resolution is improved but at the expense of time resolution.

5.1.2 Example: Kiruna Event

In the case of a burst like the Kiruna event, the power at low frequencies (of order the duration of the burst) dominates. Since we are interested only in modulation of the burst, we first hi-pass filter the data by subtracting a 20 s running average to obtain the residual count rate which was shown in Figure 1.14 and is also shown again in Figure 5.1 (top). The power spectrum was computed every 5 seconds using a 35 s window.

There are several ways to normalize the power; for short timescale modulation we are interested in how the power contained at each frequency compares with the white noise power expected from Poisson statistics. The power spectrum shown in Section 1.4 (Figure 1.14) was normalized in the following way. Pre-event background counts were summed over an interval chosen to give the same average number of counts in each 35 s time window of the event data. The power spectrum was then computed in the same way as for the event and the 1σ level was defined for each time window as the power in the background spectrum at each frequency. This method is not very accurate, however, because of fluctuations in the background (inherent in Poisson statistics). If a different background interval was chosen, the background power spectrum would be different and the 1σ level would be defined differently. One should really perform the analysis on many background intervals and average the result. However, if we can verify that the background obeys Poisson statistics, the spectrum can instead be normalized by the theoretical power spectrum expected for white noise which is constant for all frequencies [Torrence and Compo, 1998]:

$$P_k = \frac{2\sigma^2}{N} \quad (5.5)$$

where σ^2 is the variance of the signal being analyzed. In the case of Poisson distributed

noise, the variance is equal to the mean, thus, P_k can be calculated for any event interval using the mean within that interval in place of the variance. Dividing the event power spectrum by the quantity, P_k , then normalizes the power spectrum such that the power for a white noise spectrum with the same mean is unity. In other words, we're asking how the power compares to the power in a white noise signal with the same mean. The power spectrum is χ^2 distributed with two degrees of freedom, thus after normalizing the spectrum as described above, the 1σ or 68.3% confidence level is defined as $\chi_2^2(.317)/2=1.1$ times the power in a white noise spectrum (equal to 1) [Torrence and Compo, 1998]. If the event count rate is unmodulated and just Poisson distributed, 31.7% of the values in the power spectrum would be expected to greater than 1.1 by chance. The 99.7% or 3σ level is equal to 5.8. Figure 5.1 shows the power spectrum for the Kiruna event normalized to the power spectrum expected by Poisson statistics. The MAXIS data were used to verify that the background obeys Poisson statistics. For comparison, the wavelet power spectrum is also shown and is discussed in the next section.

The normalization described above is useful for comparing the residual X-ray count rate to white noise. If the power at some frequency and time is found to be above 5.8, we can be 99.7% sure that the count rate is not Poissonian and therefore has some significant modulation at that frequency. For the Kiruna event, the lower frequency (100-200 s) modulation in the X-ray count rate is obviously significant. We don't need to prove the modulation exists, rather we just want to quantify the amplitude of the modulation since this may provide some clue to the physics taking place. In this case, the power spectrum is expressed in units of fractional modulation calculated by dividing the square root of the

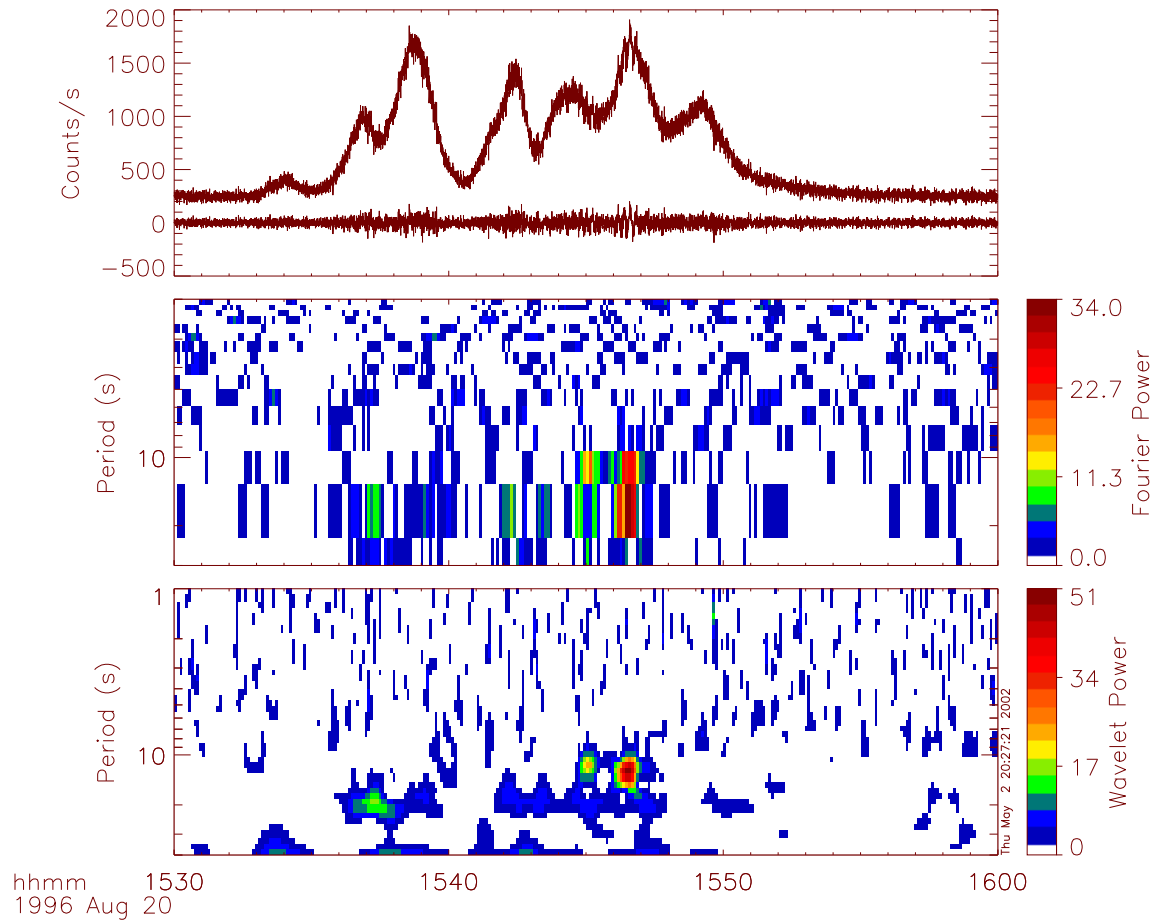


Figure 5.1: X-ray count rate (top), Fourier power spectrum (middle) and wavelet power spectrum (bottom) for the Kiruna Event. The 3σ level corresponds to a normalized power of 5.8.

power (proportional to the modulation amplitude) by the signal mean. This is another normalization that will be used in the next few sections.

5.1.3 Limitations of the Fourier Transform

The Fourier transform has disadvantages when working with signals localized in both frequency and time. The basis functions used in the Fourier transform are sinusoids that are localized in frequency but completely unlocalized in time. For a signal that goes on forever, this isn't a problem, but when dealing with a finite duration signal, the Fourier transform loses information about time localization of a single frequency component [Van den Berg, 1999]. The windowed Fourier transform localizes the basis functions somewhat but introduces other problems. In particular, the finite time window causes sidelobes in the frequency response. In the case of a burst like the Kiruna event, the low frequency power (timescale of the burst) dominates and much of this power leaks into the sidelobes and shows up at other frequencies. The sidelobes can be reduced by choosing a different windowing function but can't be eliminated. This is the reason for subtracting the running average and using the residual count rate described above. Subtracting a running average can however introduce artifacts if the smoothing time scale is not chosen very carefully. For a signal that is varying on several timescales such as the Kiruna event, this is difficult and the power present at frequencies lower than 57.1 mHz is most likely the result of these introduced artifacts.

With the windowed Fourier method, one must choose between spectral resolution and time resolution when choosing the window width. Moreover, this window width will only be appropriate for a small frequency range. A large window will improve spectral resolution

but smears the time profile. In order to examine the signal over a large frequency range, it is necessary to perform many different windowed transforms with different window sizes which is cumbersome and also requires the results to be interpreted very carefully since the signal is smoothed over a different timescale for each frequency range. The wavelet transform can overcome some of these difficulties and will be discussed in the next section.

5.2 Wavelet Analysis

As described above, Fourier analysis has limitations for signals that are localized in time or whose frequency components change in time such as the X-ray bursts being discussed here. The wavelet transform is a type of time or space-scale representation of a signal more suitable for non-stationary signals. In the last two decades, it has become a popular tool with applications in signal analysis and, in the 2-D case, image analysis and compression.

5.2.1 Overview: Time-Frequency analysis

In time-frequency analysis, a signal is represented by two parameters: the scale (or 1/frequency), a , and time, b . (Note: we have been discussing the case of a temporally varying signal but the analysis can apply equally well to a signal varying in space). In general, the linear time-frequency transform of the signal $f(t)$ is

$$f \rightarrow \mathcal{F} = \int (f(t) * \psi_{ab}(t)) dt \quad (5.6)$$

where ψ_{ab} are the analyzing or basis functions. Both the windowed Fourier transform and wavelet transform are special cases of this general transform with different basis functions.

In the case of the windowed Fourier transform which was discussed in Section 5.1 above,

$$\psi_{ab} = e^{ix/a} \psi(x - b) \quad (5.7)$$

where ψ is the window function. The window has constant width so there are more oscillations in the window at smaller scales (higher frequencies) [Fang and Thews, 1998].

In the case of the wavelet transform,

$$\psi_{ab} = \frac{1}{\sqrt{a}} \psi\left(\frac{x - b}{a}\right) \quad (5.8)$$

where ψ is the wavelet function also called the mother wavelet. The parameter, a , serves to dilate or contract the function ψ but the shape is unchanged. Thus, rather than changing the number of oscillations within a constant window to form a basis to represent the signal (windowed Fourier transform case), the basis is made by stretching or squeezing the mother wavelet thus keeping the number of oscillations within the window constant. The stretched and squeezed versions of the mother wavelet form a basis and are called baby wavelets. The time localization is achieved with the parameter, b , by translating the basis functions. The continuous wavelet transform of a function $f(t)$ can be written

$$W(t, s) = \int_{-\infty}^{\infty} f(t') \frac{1}{\sqrt{s}} \psi^*\left[\frac{t - t'}{s}\right] dt' \quad (5.9)$$

where the generic scale parameter, a , has been replaced by the wavelet scale parameter, s .

In other words, the wavelet and Fourier transforms break up the phase space (time-frequency in this case) in different ways. In the windowed Fourier transform case, the phase space is divided into equally sized squares independent of scale thus the time resolution is limited at small scales (large frequencies) since the window must be chosen large enough to fit a full period. For the wavelet transform, phase space is divided into rectangles with

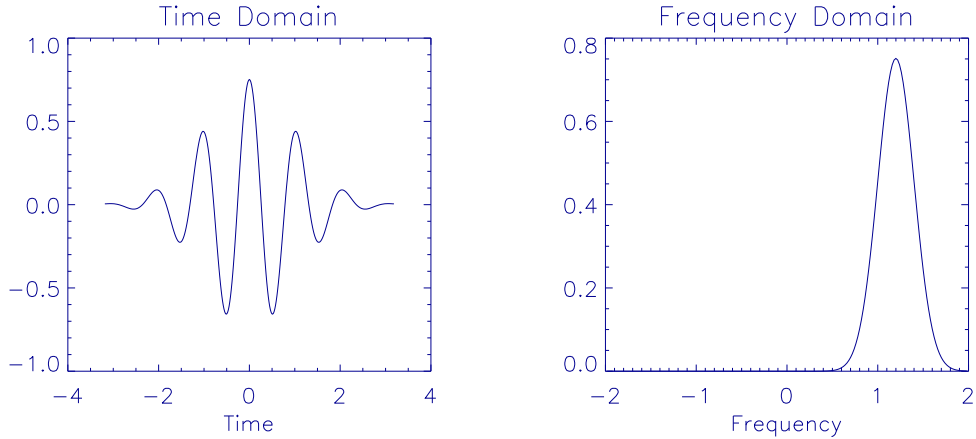


Figure 5.2: Morlet wavelet in time and frequency domains.

the rectangle size increasing with scale. Therefore, good time resolution is possible at small scales (large frequency) [Fang and Thews, 1998]. In essence, the wavelet transform uses the ideal window size for each scale.

There are many different choices of mother wavelet, ψ , and in some cases, the basis is not orthonormal. A detailed discussion is beyond the scope of this dissertation but can be found in [Fang and Thews, 1998] and references therein. A common choice which we use here is the Morlet wavelet which consists of a plane wave modulated by a Gaussian

$$\psi_0(\eta) = \pi^{-1/4} e^{i\omega_0 \eta} e^{-\eta^2/2} \quad (5.10)$$

where ω_0 is the non-dimensional frequency, taken to be 6, and η is a dimensionless “time” parameter [Torrence and Compo, 1998]

$$\eta = \frac{t - t'}{s}$$

Figure 5.2 shows the Morlet wavelet in the time and frequency domains; note that it is localized in both.

5.2.2 Analytic Example

In order to understand the wavelet transform, how the scale, s , relates to frequency and how the result depends on the choice of ω_0 , consider a simple example for which the wavelet transform can be computed analytically. Consider the function

$$f(t) = b \cos \omega t$$

Using the Morlet wavelet (Equation 5.10), Equation 5.9 becomes

$$W(t, s) = b \int_{-\infty}^{\infty} \cos \omega t' \frac{1}{\sqrt{s}} \pi^{-1/4} e^{-i\omega_0 \left(\frac{t-t'}{s}\right)} e^{-(t-t')^2/2s^2} dt'$$

and the wavelet power is then

$$|W(t, s)|^2 = \frac{b^2 \pi^{1/2} s}{2} [e^{-(\omega_0 - \omega s)^2} + e^{-(\omega_0 + \omega s)^2} + 2 \cos 2\omega t e^{-\omega_0^2 s^2}]$$

Only the first term is non-negligible and approaches unity near $\omega_0 = \omega s$ thus the power is approximately [De Moortel and Hood, 2000]

$$|W|^2 \approx \frac{\pi^{1/2} s b^2}{2} e^{-(\omega_0 - \omega s)^2}$$

The wavelet power scales as s and the square of the signal amplitude. The width depends on the choice of ω_0 and the maximum in wavelet power occurs at

$$s = \frac{\omega_0 + \sqrt{\omega_0^2 + 2}}{2\omega}$$

Therefore, for $\omega_0=6$, the period, P , and scale, s , are related by

$$P = \frac{\omega}{2\pi} = 1.03s \quad (5.11)$$

Discretely Sampled Data

For discretely sampled data, x_n , the continuous wavelet transform is
 [Torrence and Compo, 1998]

$$W_n(s) = \sum_{n'=0}^{N-1} x_{n'} \psi^* \left[\frac{(n' - n)\delta t}{s} \right] \quad (5.12)$$

where δt is the sample time, and N the total number of samples. It is computationally faster to calculate the wavelet transform in Fourier space where

$$W_n(s) = \sum_{k=0}^{N-1} \hat{x}_k \hat{\psi}^*(s\omega_k) e^{i\omega_k n \delta t} \quad (5.13)$$

and \hat{x}_k is the Fourier transform of x_n and

$$\omega_k = \begin{cases} \frac{2\pi k}{N\delta t} & k \leq \frac{N}{2} \\ \frac{-2\pi(N-k)}{N\delta t} & k > \frac{N}{2} \end{cases}$$

5.2.3 Example: The Kiruna Event

The wavelet power spectrum for the Kiruna event is shown in Figure 5.1 in comparison with the Fourier power spectrum. Both the Fourier and wavelet power spectra are normalized to the white noise case. In the case of the wavelet power, this is accomplished simply by dividing by the signal mean (which is approximated by the smoothed X-ray count rate) [Torrence and Compo, 1998]. The wavelet transform is clearly better at localizing the power.

The X-ray count rate for this event was modulated at ~ 20 seconds for the second and fourth peaks and ~ 10 seconds for the fifth and sixth peaks. The change in modulation frequency was also accompanied by a hardening of the X-ray spectrum (Section 1.4). For

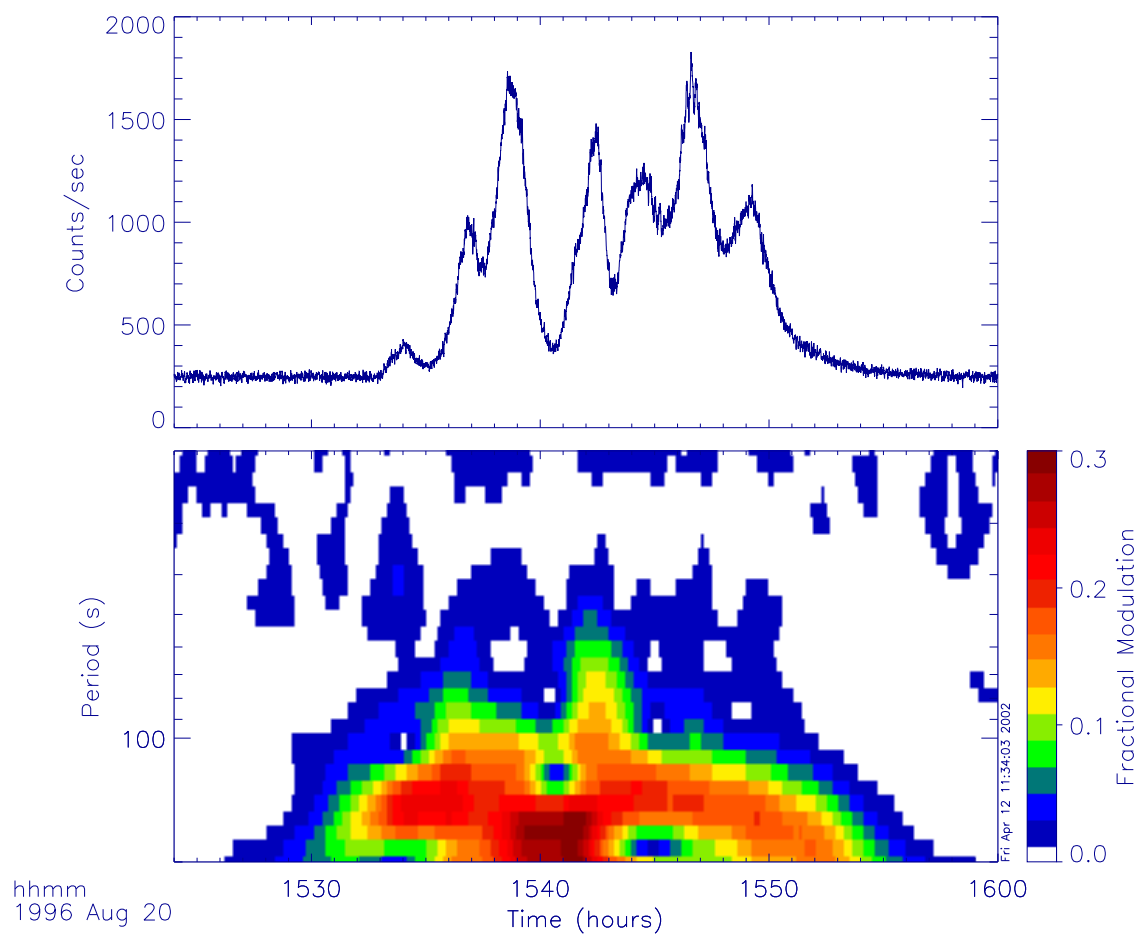


Figure 5.3: X-ray count rate (top) and wavelet power spectrum for periods between 20-200 seconds (bottom) for the Kiruna event.

the second peak, the modulation is strongest at the peak but for the fourth peak, it comes on the rising edge. For the fifth peak, the modulation is strongest on the falling edge. This suggests that the 10-20 second modulation is independent of the modulation at 100-200 seconds. The wavelet power spectrum at lower (ULF) frequencies is shown in Figure 5.3. The strong peak at 15:40 UT is due to the wide gap between the third and fourth peaks. The X-ray count rate is modulated at the \sim 20-25% level peaking near 170 s.

5.2.4 Wavelet Analysis of MAXIS MeV Events

In this section, wavelet power spectra are presented for the MAXIS MeV events detected on January 19 and January 20, 2000. These events show strong modulation at ULF timescales similar to the Kiruna event. Before calculating the wavelet power for each event, the X-ray count rate was corrected for short negative spikes caused by heavy cosmic ray nuclei passing through the detector and briefly overloading the system. These dropouts were not observed on the ground and the cadence (about 1 every 30 seconds) is consistent with that expected from cosmic rays. Any data point more than 3σ below the average of its nearest neighbors was identified as a spike and its value was replaced with the nearest neighbor average. This has the effect of smoothing the data on \sim 1 second timescale.

Before presenting the results for the MeV events, the wavelet power spectrum for the X-ray background is presented to illustrate that the background count rate is Poisson distributed.

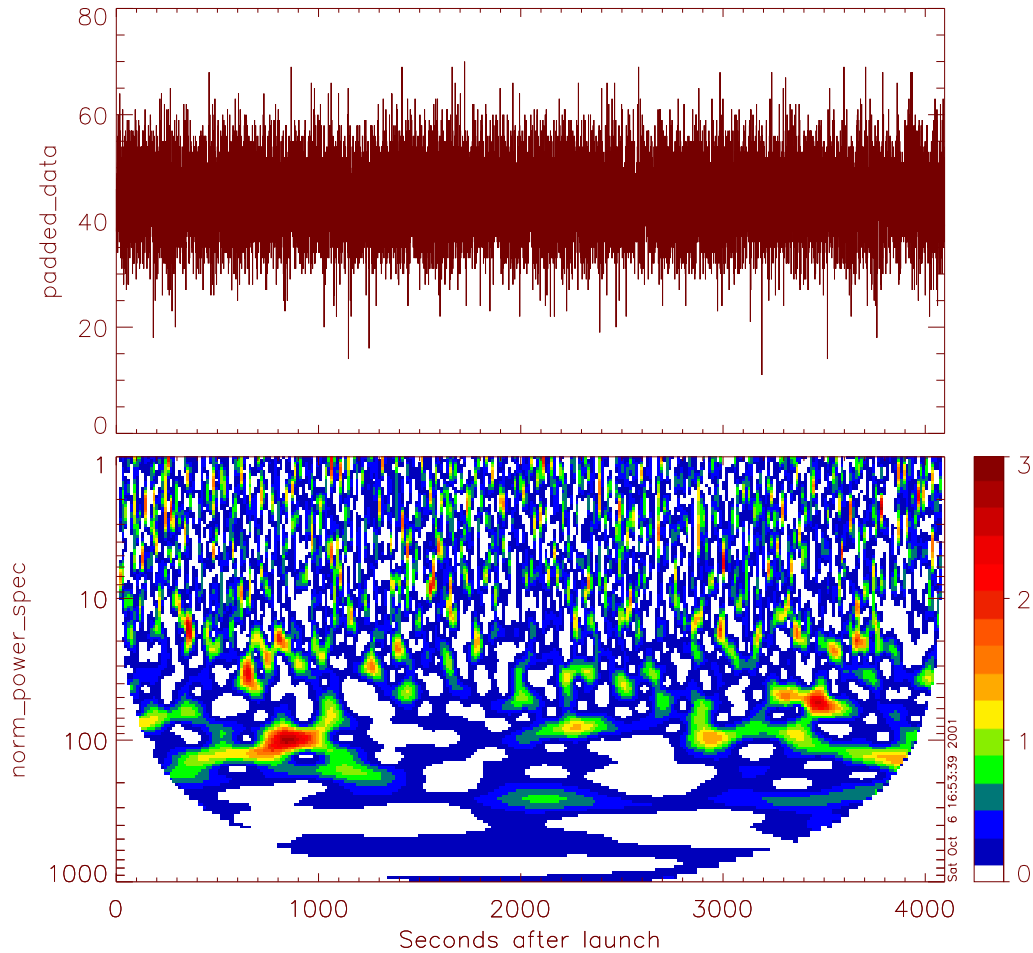


Figure 5.4: X-ray count rate (top) and wavelet power (in units of variance) (bottom) for one 4096 point background interval.

Background Interval: January 13-15, 20000

A 4096 point wavelet transform was calculated every 256 seconds for the GeD background count rate from January 13-15 during which no X-ray events were detected. The count rate and wavelet power spectrum are shown in Figure 5.4 for one of these intervals. To avoid edge effects, the spectrum for each of 1000 intervals was averaged over the central 100 points to obtain the wavelet power versus period for each interval. The re-

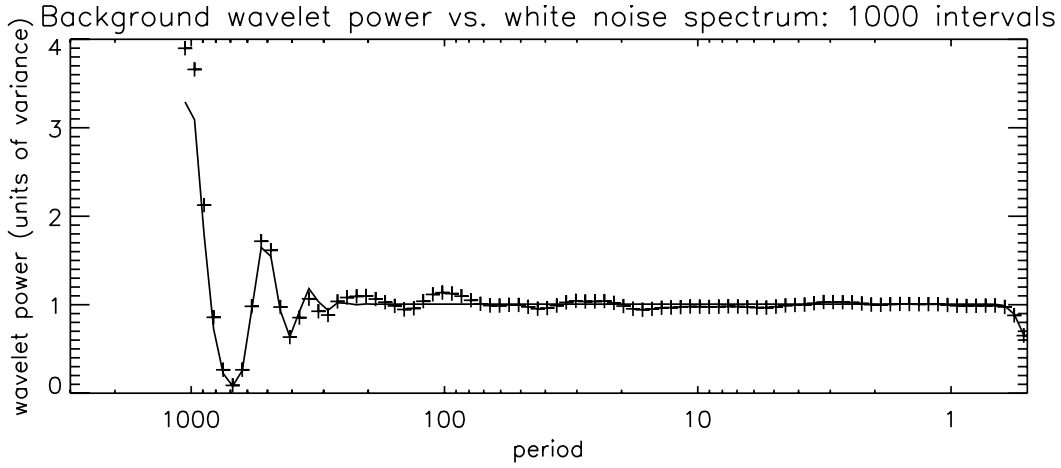


Figure 5.5: Average wavelet power (crosses) shown with theoretical curve for white noise (solid line).

sults for these intervals were then averaged resulting in a wavelet power spectrum averaged over 100,000 different spectra. Figure 5.5 shows the average spectrum superposed on the theoretical curve for white noise [Torrence and Compo, 1998]. The deviation from unity at large periods is due to edge effects and the background power spectrum from the MAXIS data follows that expected for white noise. Therefore, for the following analysis, the X-ray count rate is assumed to follow a Poissonian distribution in the absence of modulation or temporal structure and the wavelet power is normalized to a white noise spectrum unless the significance of the modulation is very high. In these cases, the power spectrum is presented in units of fractional modulation.

B2a: January 19, 2000

On January 19, 2000 MAXIS detected its strongest and longest duration X-ray event. The event lasted for over two hours and was ~ 4 times stronger than the Kiruna event. Figure 5.6 shows the count rate and wavelet power spectrum for timescales between 1-35

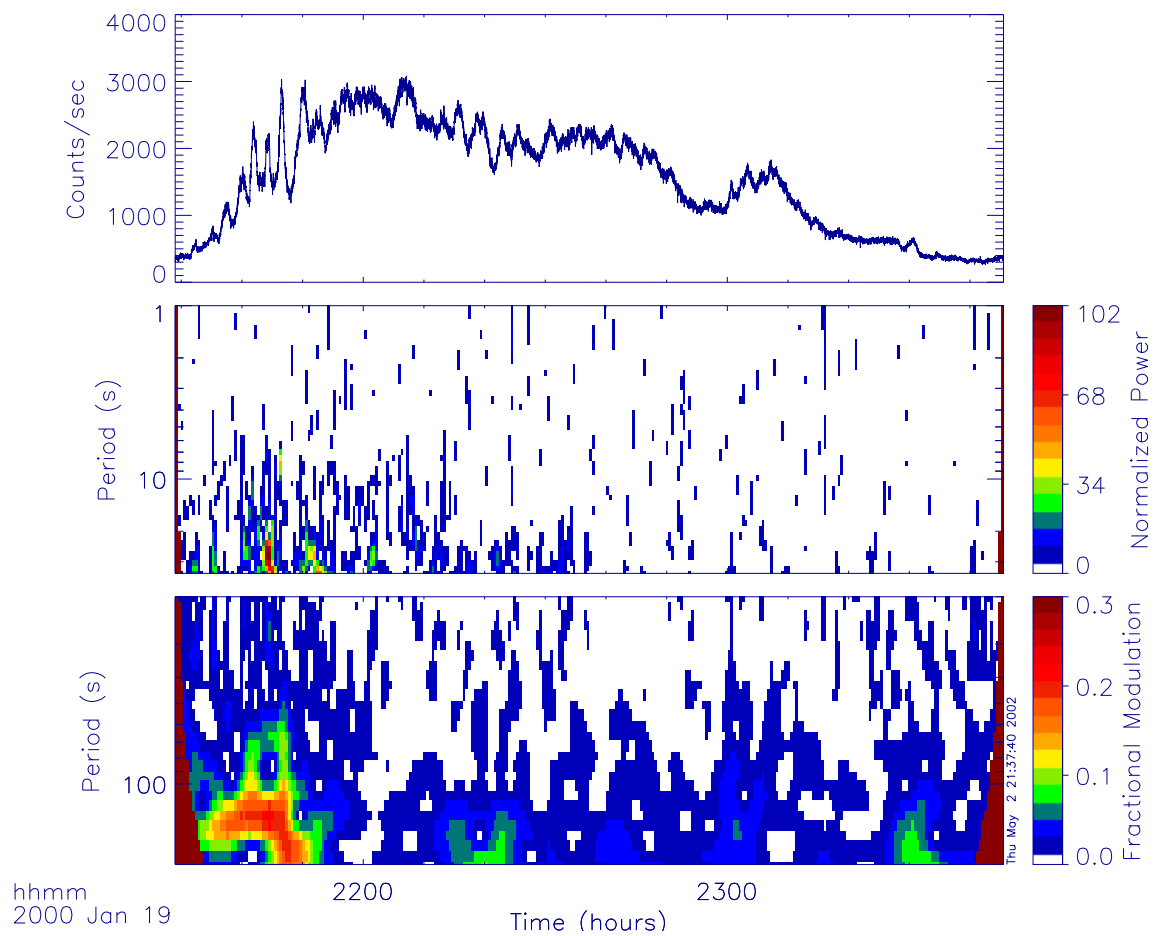


Figure 5.6: X-ray count rate (top) and wavelet power spectrum for periods between 1-35 s (middle) and 20-200 s (bottom) for event on Jan. 19, 2000.

and 20-200 seconds. Very localized power at 20-30 seconds is evident near the beginning of the event but appears to be associated with sharp features in the count rate rather than coherent modulation. The low frequency power on the rising edge of the event is evident in both the count rate and the wavelet power spectrum. The peak in power was determined by fitting a Gaussian to the power spectrum at 21:39 UT and was found to occur at a period of 140 s ($\sim 7\text{mHz}$) with a fractional modulation of 0.17. The period of modulation and fractional modulation for this event are both very similar to the slow modulation of the Kiruna event. The power at 200 seconds at 21:48 UT is due to the wide gap in the X-ray count rate and the “fingers” in the power spectrum at higher frequency arise because the modulation isn’t perfectly sinusoidal. The coherent modulation at 140 s disappears after the rise of the event but coherent 200 s modulation appears briefly at 22:20 UT.

B2b: January 20, 2000

The January 20, 2000 event occurred directly after the January 19 event when the X-ray count rate had not quite fallen to background level. The wavelet power spectrum for this event is shown in Figure 5.7. In this case, the count rate was modulated by 20-30% with the modulation peaking near 70 seconds. The 100 second modulation near the end of the event represents the width of the small bursts following the large burst. There is also significant power at 30 seconds but this appears to be an extension of the power at lower frequencies. There is no significant power below 20 seconds.

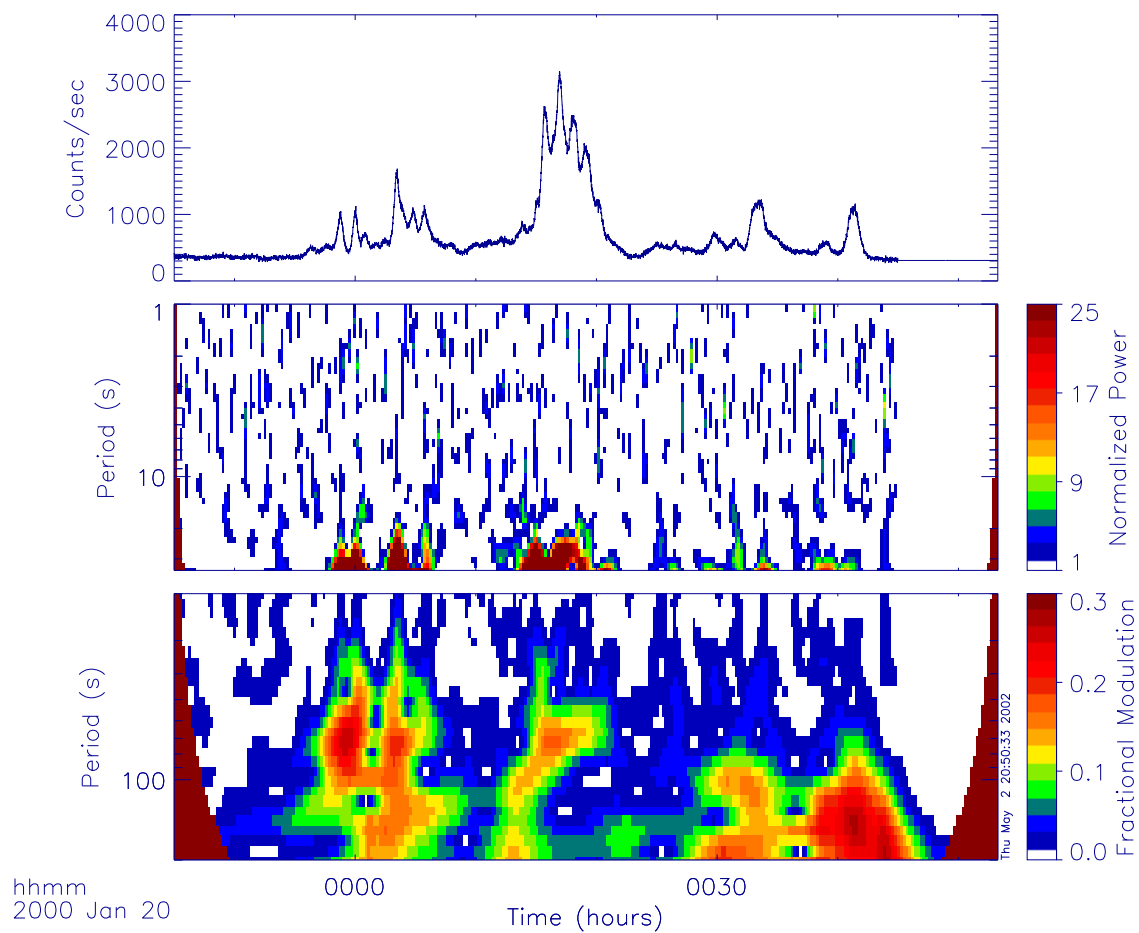


Figure 5.7: X-ray count rate (top) and wavelet power spectrum for periods between 1-35 s (middle) and 20-200 s (bottom) for the event on Jan. 20, 2000.

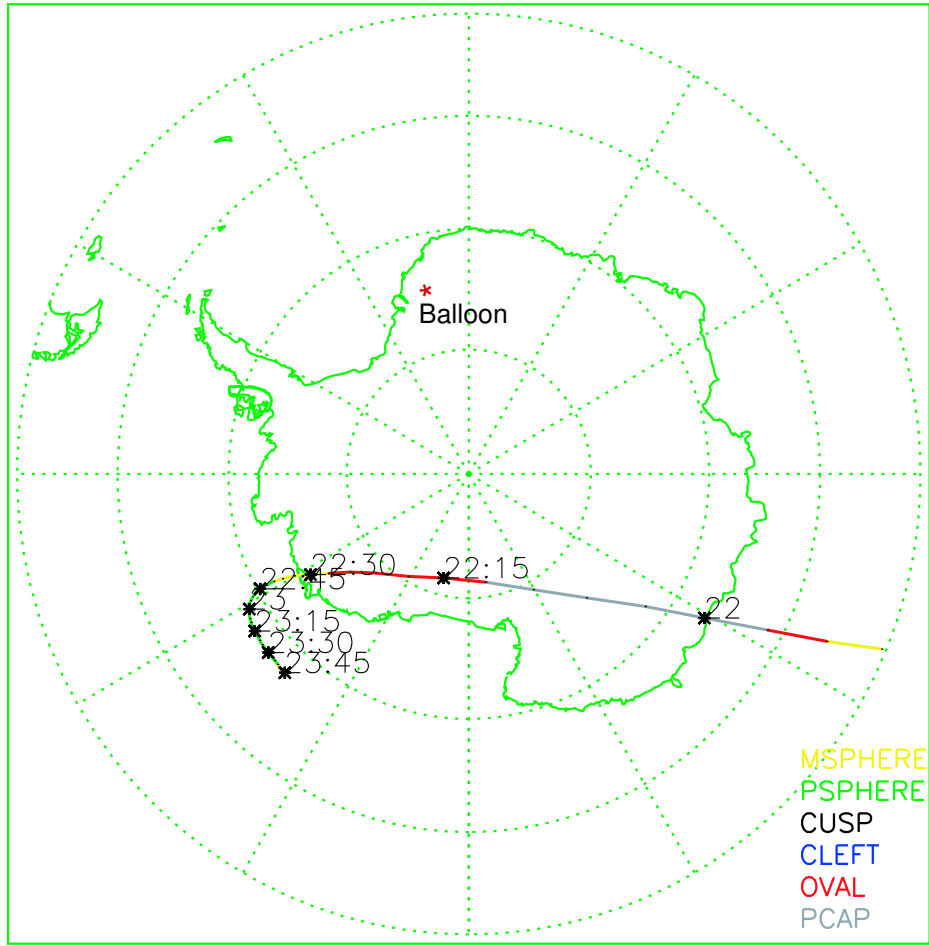


Figure 5.8: POLAR trajectory over Antarctica and balloon location (star) on January 19, 2000.

5.3 Spacecraft and Ground-Based Observations

On January 19, 2000, the Electric Field Instrument (EFI) on the POLAR spacecraft detected ULF timescale oscillations near the time and location of the Jan. 19 MeV X-ray event. Figure 5.8 shows the trajectory of POLAR over Antarctica. The X-ray event occurred at 21:20-23:45 UT when the balloon was located at $L=4.7$ (IGRF) and magnetic local time 19:20-21:45.

Figure 5.9 shows the EFI measurements which have been rotated into a frame

where the z-direction points along the magnetic field direction as determined using the IGRF model (x and y are arbitrary). The baseline has also been removed by subtracting the electric field smoothed over 10 minutes. Polar detected electric field oscillations from 23:10-23:40 UT at L=4.5, 16:40 MLT near the end of the X-ray event. The magnetic field experiment also observed oscillations at the same time (not shown). The observations indicate a transverse electromagnetic wave.

The wavelet power spectrum for the (unrotated) z-component of the electric field is shown in Figure 5.10. The oscillations have a period of 144 s or a frequency of ~ 7 mHz in the ULF range. In Section 5.2.4, the wavelet transform for the event on January 19 showed oscillations peaking at nearly the same frequency (140 s period) but near the beginning of the X-ray event ($\sim 21:20$ UT) prior to the electric field observations. Therefore, it is unclear whether the ULF oscillations detected by POLAR directly caused the X-ray modulation, however, the observations do indicate that ULF oscillations were present near the time of the event.

A ground-based magnetometer located in Narsarsuaq, Greenland nearly conjugate to the balloon location also observed ULF oscillations during the X-ray event but with longer period than the X-ray modulation. Figure 5.11 shows the GeD X-ray count rate, ten minute bandpass-filtered magnetometer data and the normalized wavelet power spectrum of the magnetometer data. Significant power at 300-500 s is present during the time of the X-ray event.

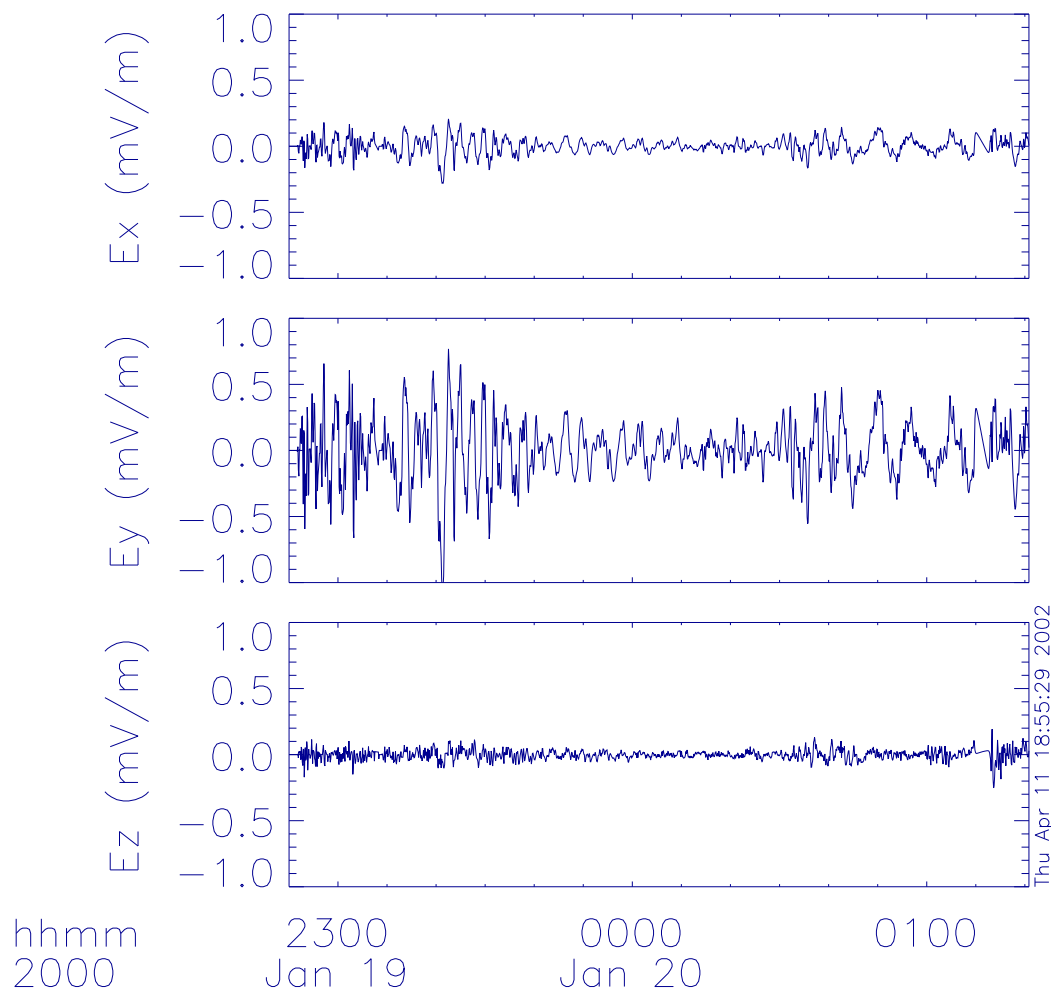


Figure 5.9: POLAR EFI data transformed into frame where z is in the direction of the magnetic field. The x and y directions are arbitrary.

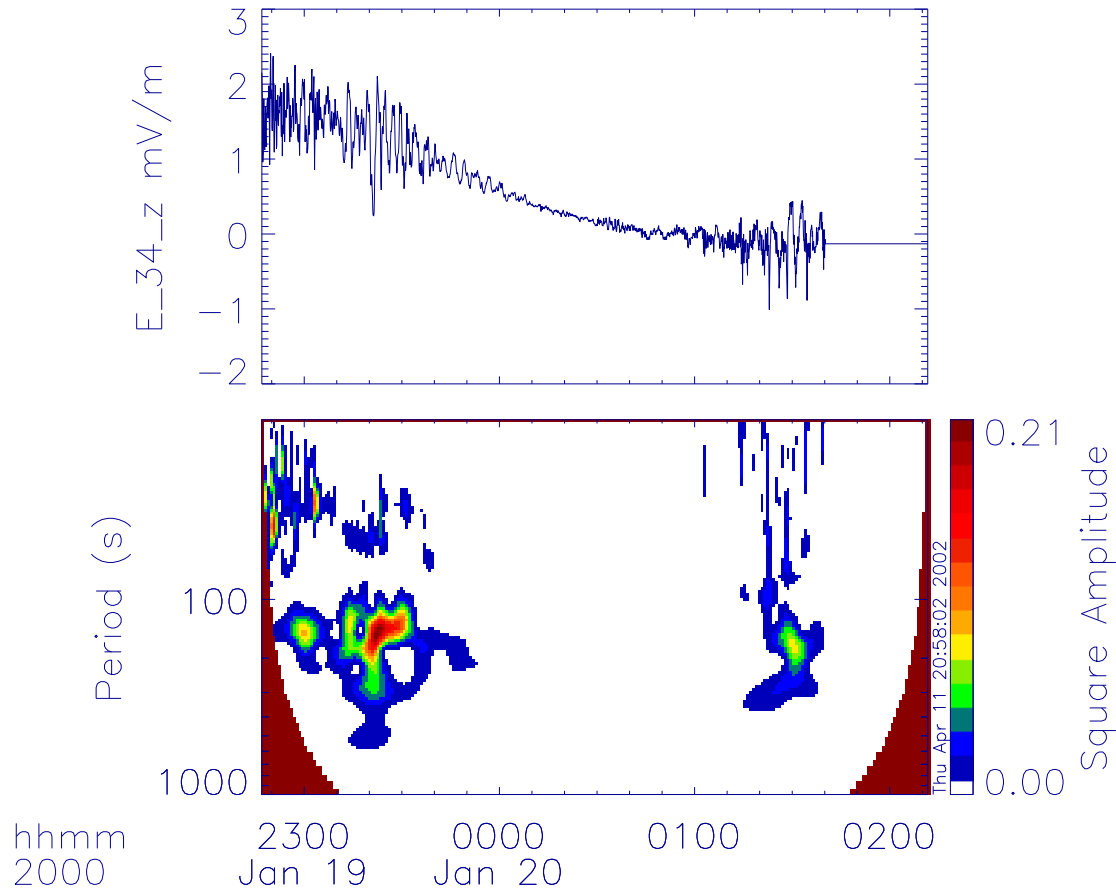


Figure 5.10: Raw electric field data (unrotated and without baseline removed) and it's wavelet power spectrum (from POLAR EFI). In this case, the z-direction is measured in the spacecraft frame not with respect to the magnetic field.

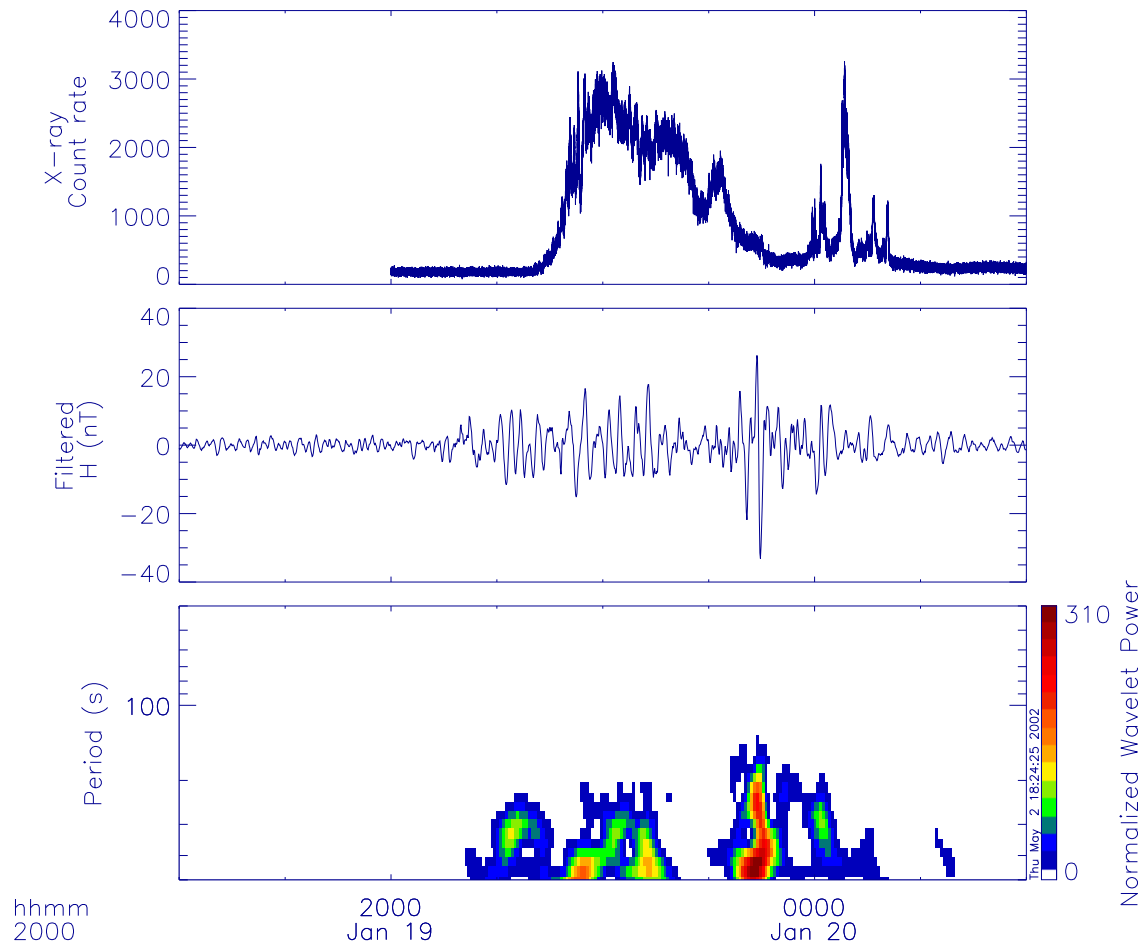


Figure 5.11: X-ray count rate (top), 10 minute bandpass-filtered (H-component) magnetometer data (middle) and normalized wavelet power for the magnetometer data (bottom). The Greenland ground-based magnetometer array is operated by the Danish Meteorological Institute (DMI). Magnetometer data for this study were provided by J. Watermann, DMI.

5.4 Mechanisms for Modulating Precipitation

The spacecraft and ground-based observations presented in the previous section suggest that ULF waves were present near the location and time of the X-ray events. In addition, the frequency of modulation of the X-ray count rate is in the ULF range suggesting that ULF waves could be the cause of the modulation. In this section several mechanisms related to ULF waves are discussed to explain the X-ray modulation.

Parallel electric fields can be associated with ULF waves [W. Lotko, priv. comm.] and Parks et al. [1979] suggested that a parallel electric field associated with ULF waves was responsible for modulating the X-ray count rate in a precipitation event they observed. In the presence of a parallel electric field, particles are accelerated along the magnetic field and their pitch angle is decreased. Therefore particles will have their mirror point lowered and particles near the loss cone will reach the atmosphere and be precipitated. In other words, the loss cone increases in size and thus more particles can be lost. An oscillating electric field would cause the loss cone size to oscillate and therefore could modulate the precipitating flux. Assuming the first adiabatic invariant of a particle remains constant (which is a valid assumption here since the modulation is occurring much slower than the gyromotion), one can easily show that the loss cone angle is given by

$$\sin^2 \alpha' = \left(\frac{B_{eq}}{B_m} \right) \left(1 + \frac{e\phi}{T} \right)$$

where ϕ is the electric potential and T is the particle kinetic energy. Assuming the loss cone angle is small and writing the loss cone angle in the presence of the electric field in terms

of the loss cone angle without the electric field, we have

$$\alpha' \approx \alpha \left(1 + \frac{e\phi}{2T} \right)$$

Therefore, in order to change the size of the loss cone substantially, the particle must gain an energy comparable to its kinetic energy. Observed parallel electric fields typically have $e\phi \sim 1$ keV [Parks et al., 1979] which is much less than the energies of interest here. For the Kiruna X-ray event, the ratio of the count rate at a peak of the modulation to the count rate in a valley is ~ 4 indicating that an unrealistically large electric field would be required to explain the observed modulation.

The magnetic field strength is also modulated in the presence of a wave. Since the particle motion is assumed to be adiabatic, a magnetic field at the equator will not affect the mirror point of a particle, and only a modulation of the field near the mirror point will have an effect. In this case, the loss cone angle is modified as

$$\alpha' \approx \alpha \left(1 + \frac{\Delta B}{2B_m} \right)$$

Typical ULF wave amplitudes are ~ 10 nT which is much smaller than the magnetic field at 60 km (the assumed mirror point). Therefore, an oscillating magnetic field would not be expected to change the loss cone size.

If the precipitation is caused by EMIC waves, the modulation could be caused by modulation of the EMIC wave growth [Lorentzen, 1999]. Ground-based observations of EMIC waves (in the Pc1 frequency range) have shown that the EMIC growth rate can be modulated by ULF waves [Fraser et al., 2001]. The precipitation rate is expected to depend on the wave amplitude, thus modulation of the growth rate could also modulate

precipitation. Another mechanisms relating to EMIC waves is modulation of the resonant energy and this could also change the precipitating flux. As discussed in Section 1.3.2 (Equation 1.10), the minimum energy for resonance between an electron and an EMIC wave depends on the magnetic field strength. An oscillating magnetic field due to the presence of ULF waves could modulate the resonant frequency; since the trapped electron spectrum is steeply falling with energy, changing the resonant frequency would change the number of particles in resonance and thus the precipitation rate. However, EMIC waves are only expected to interact with electrons with energy ≥ 1 MeV. In Chapter 4, the precipitating electron spectrum was shown to be consistent with a very flat exponential suggesting that EMIC waves are not the scattering mechanism. Therefore, the mechanism for modulating the X-ray count rate at ULF frequencies is still unknown but these results suggest that ULF waves play an important role.

The MAXIS observations provide several more examples in addition to the Kiruna event where the electron precipitation is modulated at ULF frequencies. Since ULF waves are much slower than the electron bounce or gyromotion, they are not expected to play a direct role in precipitating the particles. Unlike the Kiruna event, the MAXIS MeV events did not show strong, coherent modulation at shorter (10-20 s) timescales. The mechanism for modulating precipitation at these 10-20 s timescales is completely unknown since no waves were observed at these frequencies during the Kiruna event. However, the modulation mechanism was probably not directly responsible for causing the precipitation event since similar modulation was not observed in other MeV events.

Chapter 6

A Compton Telescope for Imaging MeV Electron Precipitation

This dissertation has so far discussed both the spectral and temporal characteristics of MeV electron precipitation but we have no information on its spatial scale and structure. The spatial structure of electron precipitation has never been measured at MeV energies; with current instrumentation, imaging can only be done below ~ 200 keV. This severely limits our knowledge of the spatial distribution since, at ≤ 100 keV, photons can be produced by any electron above this energy. In addition, electron scattering in the atmosphere is more severe at lower energies and can blur the image. There is evidence to suggest that the spatial distribution of precipitation may be different at high energies. For example, SAMPEX observations of electron microburst precipitation show a different spatial distribution at high energies with the latitudinal extent much more narrow at 1 MeV than at 150 keV [Blake et al., 1996]. This suggests that the mechanisms acting on relativistic

electrons may be different than at lower energies.

In addition to determining the spatial scale of the precipitation region, imaging is also important for distinguishing temporal modulations from spatial variations such as a moving source. Correctly interpreting and understanding the nature of temporal variations can help us understand the precipitation mechanism. Imaging also plays a key role in inverting the X-ray spectrum and thus determining the precipitating electron distribution and electron loss rates. Finally, imaging at higher energies may also provide unique information about the spatial and angular distributions since bremsstrahlung X-rays are polarized and strongly beamed in the forward direction at these energies.

For photons with energies >500 keV, the Compton scattering cross section dominates over photoelectric absorption and pair production. In this energy range, an imaging instrument called the Compton telescope is ideal. A Compton telescope can provide a low background, large field of view, good sensitivity at high energies and the potential for measuring polarization. Unlike the Anger type or coded mask imagers flown on MAXIS, a Compton telescope is also sensitive over a large range of spatial scales. In this chapter, we explore the potential of a Compton telescope for imaging terrestrial MeV X-ray bursts. In the following sections the principles of Compton telescopes are reviewed and simulations of a simple Compton telescope are presented. In Section 6.3 polarization measurements are discussed that could in principle provide information about the precipitating electron pitch angle distribution.

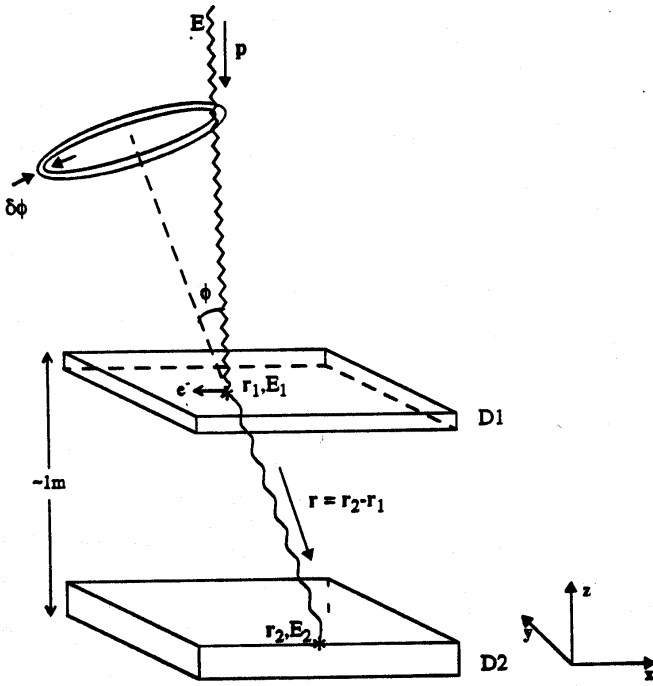


Figure 6.1: Schematic of a Compton telescope [Boggs, 1998].

6.1 Characteristics of the Compton Telescope

The Compton telescope was developed in the 1970's to image gamma rays with energies from several hundred keV to a few tens of MeV [Longair, 1997]. The technique has been employed on instruments such as COMPTEL on the Compton Gamma Ray Observatory to image hard X-rays and gamma rays from astrophysical sources such as nuclear line emission from the Galaxy [Schönenfelder, 1993]. Figure 6.1 shows a schematic of a simple Compton telescope which consists of two detector planes D1 and D2. The incident photon Compton scatters in D1 and the scattered photon is absorbed in D2. Assuming an energy, E_1 is deposited in the first interaction and the photon is fully absorbed so the incident

energy, E , is known, the scattering angle, ϕ is given by

$$\cos\phi = 1 - \frac{m_e c^2}{E} \left(\frac{E_1}{E - E_1} \right) \quad (6.1)$$

The scattering axis is given by the positions of the first and second interactions in the detector. Thus the photon incident direction is constrained to an annulus on the sky whose width is given by the uncertainties in the measured energies and scattering angle. An image of the source can be constructed using Fourier (synthesis imaging) techniques similar to those used in radio interferometry (e.g., Taylor et al. [1999]).

The first Compton telescopes employed scintillators for each detector plane thus the angular resolution was limited by poor energy resolution ($\geq 10\%$). However, recent work by Boggs has demonstrated the feasibility of using high resolution germanium detectors [S. E. Boggs, private communication]. In order to take advantage of the energy resolution of germanium, the photon interactions in the detector must be localized to ~ 1 mm. This is achievable with position-sensitive germanium strip detectors which have long thin electrodes or “strips” on each side with a pitch of ~ 2 mm. The strips on opposite sides are orthogonal thus allowing for x-y localization of the photon interaction in the detector. The z-position of the interaction can also be determined, to an accuracy of < 1 mm, by comparing the arrival time of the signal on the anode and cathode.

Another interesting application of position-sensitive germanium detectors is the ability to measure polarization at gamma ray energies since the Compton scattering process is sensitive to linear polarization. This will be discussed in more detail in Section 6.3.

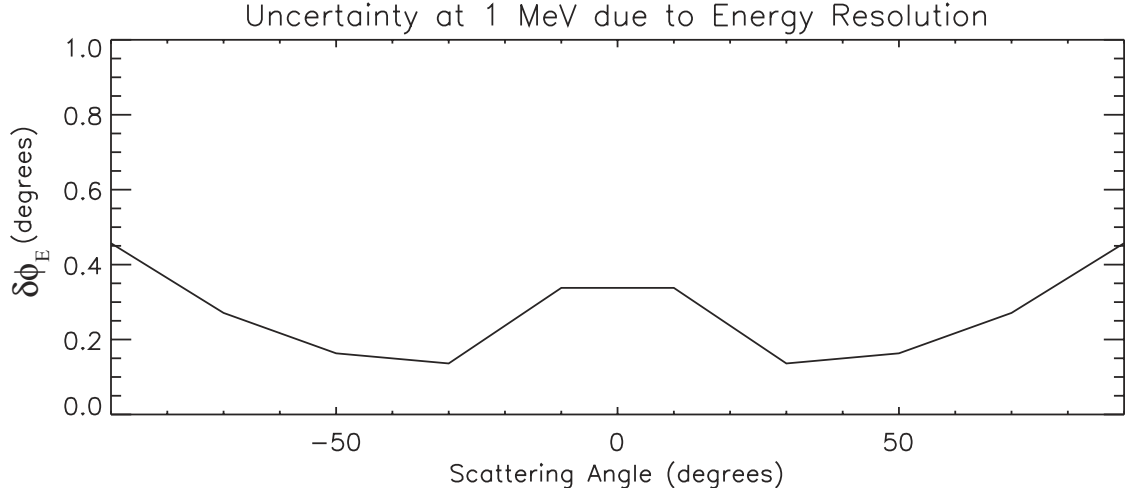


Figure 6.2: Uncertainty in the reconstructed scattering angle for a 1 MeV photon as a function of scattering angle due to energy resolution of detector (assumed to be 2 keV).

6.1.1 Angular Resolution

The angular resolution of a Compton telescope is determined by the uncertainty in the reconstructed photon scattering angle which depends on the energy and spatial resolutions of the detector and the lever arm or distance between the first and second interaction sites. The contribution due to the finite energy resolution is given by [Boggs and Jean, 2000]

$$\delta\phi_E = \frac{1}{\sin\phi} \left[\left(\frac{\delta W_0^2}{W_0^4} \right) + \delta W_1^2 \left(\left(\frac{1}{W_1^2} - \frac{1}{W_0^2} \right)^2 - \frac{1}{W_0^4} \right) \right]^{1/2} \quad (6.2)$$

where

$$W_i = \frac{1}{m_e c^2} \sum_{j=i+1}^N E_j \quad (6.3)$$

and

$$\delta W_i = \frac{1}{m_e c^2} \sum_{j=i+1}^N \delta E_j^2 \quad (6.4)$$

where N is the number of interaction sites. Figure 6.2 shows this contribution to the uncertainty as a function of scattering angle for a 1 MeV photon and $N = 2$ assuming a typical

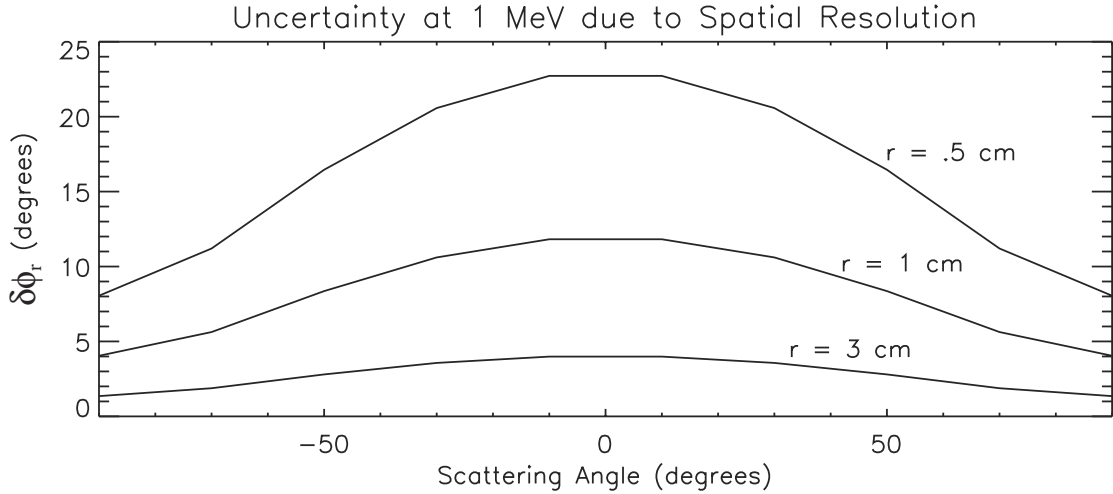


Figure 6.3: Uncertainty in reconstructed scattering angle for a normally incident 1 MeV photon as a function of scattering angle due to spatial resolution of detector ($x,y=1.5$ mm, $z=0.5$ mm). Shown for three different values of distance, r , between the first and second scatter.

germanium detector energy resolution of 2 keV (here taken to be independent of energy).

In a real detector, the energy resolution will be a function of energy and thus a function of scattering angle but won't deviate from this value by much. The contribution to the uncertainty due to finite energy resolution is less than 0.5° for all scattering angles and is smaller than the fundamental limit set by Doppler broadening ($\sim 0.8^\circ$) [Boggs and Jean, 2001] in which the scattered photon energy is modified due to interacting with bound instead of free electrons [DuMond, 1933].

The contribution to the uncertainty due to uncertainty in the spatial location of an interaction is given by

$$\delta\phi_r = \sqrt{\delta\phi_x^2 + \delta\phi_y^2 + \delta\phi_z^2} \quad (6.5)$$

where

$$\tan(\delta\phi_x) = \sqrt{2} \left(\frac{\delta x}{r} \right) \sqrt{1 - (\hat{r} \cdot \hat{x})^2} \quad (6.6)$$

r is the distance between the first and second interaction sites (lever arm), and similar expressions give $\delta\phi_y$ and $\delta\phi_z$. The spatial resolution currently achievable with a germanium strip detector is ~ 1.5 mm in x and y and ~ 0.5 mm in z [S. E. Boggs, private communication]. Figure 6.3 shows the uncertainty due to the spatial resolution for several different lever arms. The uncertainty is strongly dependent on the lever arm and can be reduced dramatically by processing only events with a minimum lever arm [Boggs and Jean, 2000]. This, however, comes at the cost of instrument effective area. The total uncertainty in the scattering angle is given by

$$\delta\phi = \sqrt{\delta\phi_E^2 + \delta\phi_r^2} \quad (6.7)$$

but with the lever arms shown above, the spatial resolution dominates.

The effective angular resolution of an instrument is given by the distribution of the uncertainties in reconstructed scattering angle since different events will have different lever arms and number of interactions. The angular resolution can be described in terms of the angular resolution measure (ARM) which is defined as the difference between the initial photon scattering angle and reconstructed scattering angle [Boggs and Jean, 2001]. The ARM distribution is shown for a particular configuration and choice of minimum lever arm in Section 6.2.3. The angular resolution can in principle be chosen during the analysis of each event depending on the event statistics. The desired resolution for imaging MeV precipitation events is $\leq 10^\circ$ which corresponds to ~ 4 km for a source at 60 km assuming a balloon and detector altitude of 35 km. In Section 6.2.2 the effects on effective area of imposing a minimum lever arm are discussed for a particular instrument configuration.

6.1.2 Field of View

The field of view of the instrument is determined by integrating the angular response over all angles and is highly dependent on the instrument configuration. In addition, the field of view can be restricted by only accepting events within a chosen zenith angle range. This reduces the instrument effective area but also reduces the background.

The 1996 Kiruna MeV event was about 200 km in spatial extent as measured by an imaging riometer that also observed the event. Therefore, the ideal instrument would have good sensitivity at large zenith angles. The angular response for a particular instrument configuration is shown in the next section.

6.2 Monte Carlo Simulation of a Compton Telescope

In this section, results from a Monte Carlo simulation of a Compton telescope are presented. The CERN GEANT Monte Carlo code was used to simulate the instrument effective area and background in order to calculate the instrument sensitivity. The results are compared with the MAXIS GeD and BGO.

6.2.1 Instrument Configuration

Boggs and Jean [2001] have demonstrated that a compact Compton telescope configuration is more sensitive than the classical configuration (with detector separation ~ 1 m) since placing the detectors as close together as possible prevents the escape of many photons out the sides. A compact configuration also provides a larger field of view. Figure 6.4 shows a schematic of the configuration chosen which is a simple Compton telescope

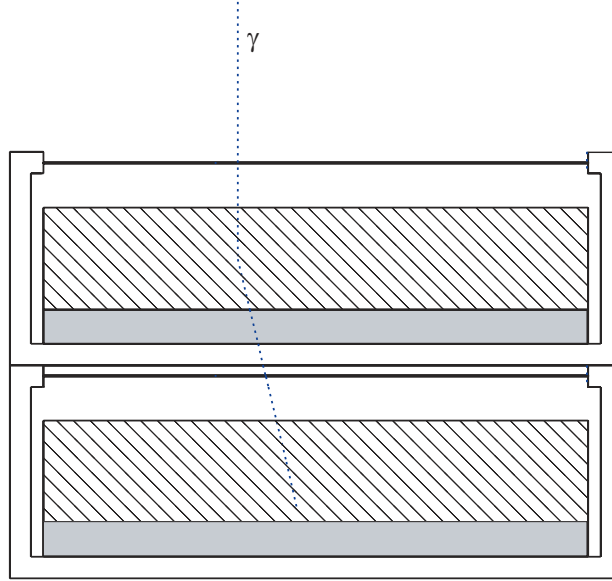


Figure 6.4: Schematic of model instrument geometry. Germanium detectors are shaded with angled lines and cold plates are shaded gray. A normally incident 1 MeV photon is also shown.

with two germanium detector planes separated by 3.135 cm. Each 1.5 cm thick detector plane is 8 cm \times 8 cm (40 2 mm pitch strips) and housed in a 0.3175 cm (1/8") thick aluminum cryostat along with a 0.5 cm thick aluminum cold plate (necessary for cooling the germanium to LN₂ temperatures). The top of each cryostat consists of a 0.025 cm thick Be window which is nearly transparent to energetic photons. The instrument is unshielded since much of the background can be rejected (see Section 6.2.5) and instrument electronics and other passive material outside the cryostat are not included in the model.

6.2.2 Effective area

The effective area for this instrument configuration was simulated with 4000 γ/cm^2 normally incident at energies between 20-2000 keV. The interaction location and energy

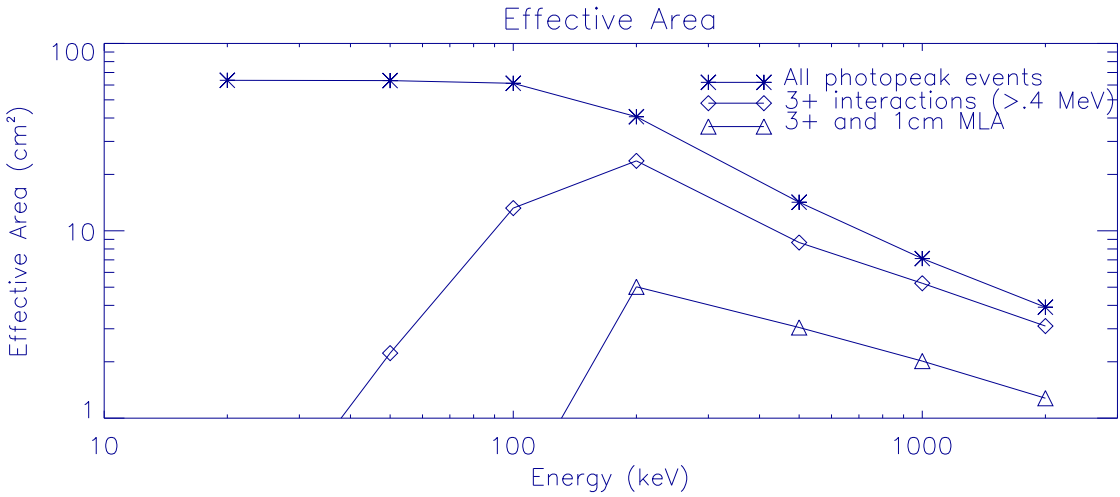


Figure 6.5: Effective area for three cases: all photopeak (fully absorbed) events, events with 3 or more interactions, and events with 3+ interactions that have a 1 cm minimum lever arm (MLA).

deposited was recorded for each interaction and all photons that were fully absorbed in either detector plane were included (photopeak events). The resulting effective area is shown (asterisks) in Figure 6.5.

In order to correctly reconstruct a photon's incident angle, the order of the interactions must be known and in germanium, this is a difficulty since the signal rise times are longer than the time of flight of the photon. Therefore, it is not possible to measure the interaction order directly. Below 0.4 MeV, single scatter (two site) events usually only have one ordering for which there is a valid solution for the scattering angle. However, above this energy, single scatter events have ambiguous ordering in most cases and including these events acts to increase the background since many of the single scatter events are incorrectly reconstructed. A statistical technique known as Compton Kinematic Discrimination (CKD) can be used to find the most probable ordering for events with two or more scatters (3+

sites) and is successful 60-70% of time below 10 MeV [Boggs and Jean, 2000]. In addition, multiple scatters are likely at high energies in germanium because of its high atomic number. Therefore, the instrument sensitivity will be improved by keeping only events with 3 or more interactions above 0.4 MeV although the effective area will be reduced. Figure 6.5 also shows the effective area when only photons that undergo three or more interactions are included (diamonds). The effective area is severely reduced at lower energies since the Compton scattering cross section is small, but this isn't a problem since we are only interested in imaging at energies above a few hundred keV. At low energies, the instrument can still be used for high resolution spectroscopy.

Finally, as described in Section 6.1.1, in order to achieve a desired angular resolution, a minimum lever arm must be chosen. For this instrument configuration, a minimum lever arm of 1 cm corresponds to an angular resolution $\sim 5^\circ$ (see next section) and when events are further restricted by this requirement, the effective area is again reduced as shown in Figure 6.5 (triangles). However, with sufficient data storage or telemetry, each interaction in the detector could be recorded, and all of these "cuts" imposed during the data analysis. Therefore, one could choose the parameters appropriate for individual events; a smaller minimum lever arm for coarser imaging, or a larger minimum lever arm for very strong events to look for fine spatial structure.

Assuming a 1 cm minimum lever arm, the effective area at 1 MeV is 2.0 cm^2 . For comparison, the 5.5 cm diameter MAXIS GeD effective area is $\sim 5 \text{ cm}^2$ at 1 MeV and that of the MAXIS BGO is 36 cm^2 (7.6 cm diameter \times 7.6 cm detector). Thus, the Compton telescope has a smaller effective area than a single GeD with smaller active volume. However,

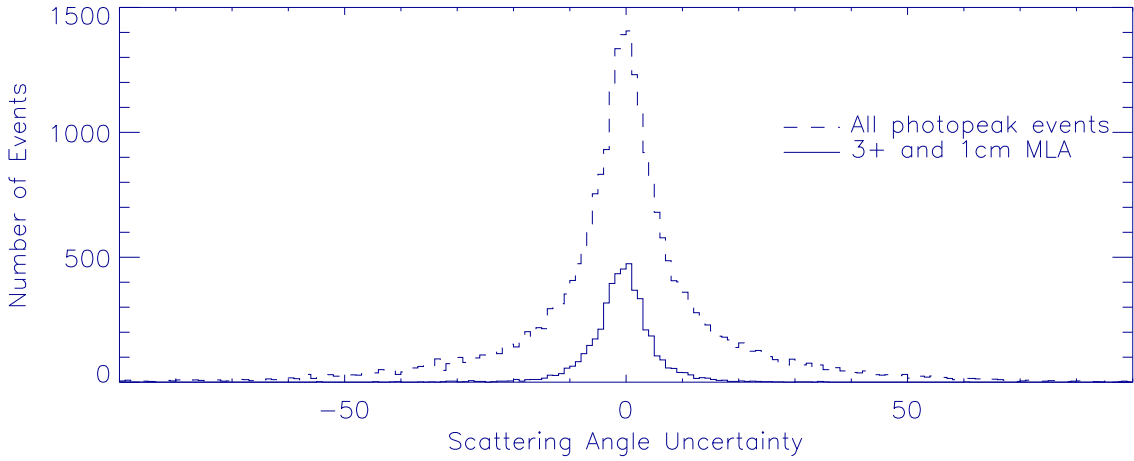


Figure 6.6: The ARM (angular resolution measure) distribution for normally incident 1 MeV photons.

though the BGO scintillator has seven times the effective area of the GeD, it is only about three times as sensitive because it also has a larger background. The instrument background plays an important role in determining the sensitivity and a major strength of the Compton telescope is its ability to reject background events that do not satisfy the Compton formula. The instrument background is modeled in Section 6.2.5 and the sensitivity is calculated in Section 6.2.6 below. We will see that this Compton telescope is more sensitive than the GeD but not as sensitive as the BGO at 1 MeV.

6.2.3 Angular Resolution

Figure 6.6 shows the ARM distribution for over 530,000 simulated 1 MeV normally incident photons including all photopeak events (dashed line) and only those events with three or more interactions and >1 cm lever arm. The angular resolution is defined to be the width of this distribution which contains 76% of the events. When all events are included,

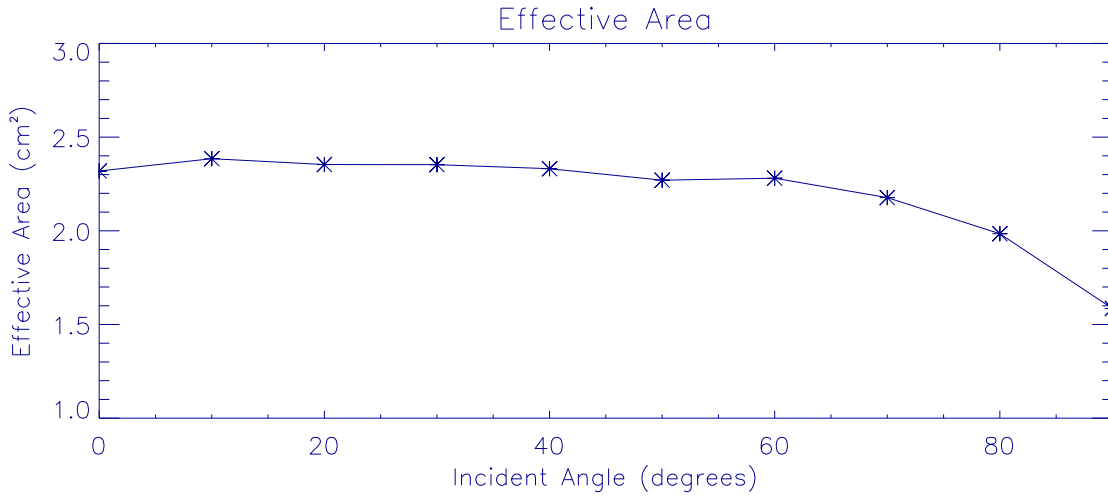


Figure 6.7: Effective area at 1 MeV as a function of incident angle. Only events with 3 or more interactions and 1 cm minimum lever arm were included.

the width is $\sim 17^\circ$ but when only 1 cm lever arm events are included, 76% of the events are within 5° .

6.2.4 Field of View

The angular response of the instrument was simulated in the same way as the effective area but with photons incident at varying zenith angles. Figure 6.7 shows the angular response of the instrument at 1 MeV which is nearly flat. The compact configuration of this instrument has good response even out to large zenith angles thus the instrument field of view can be defined during the analysis of a particular event and can be quite wide.

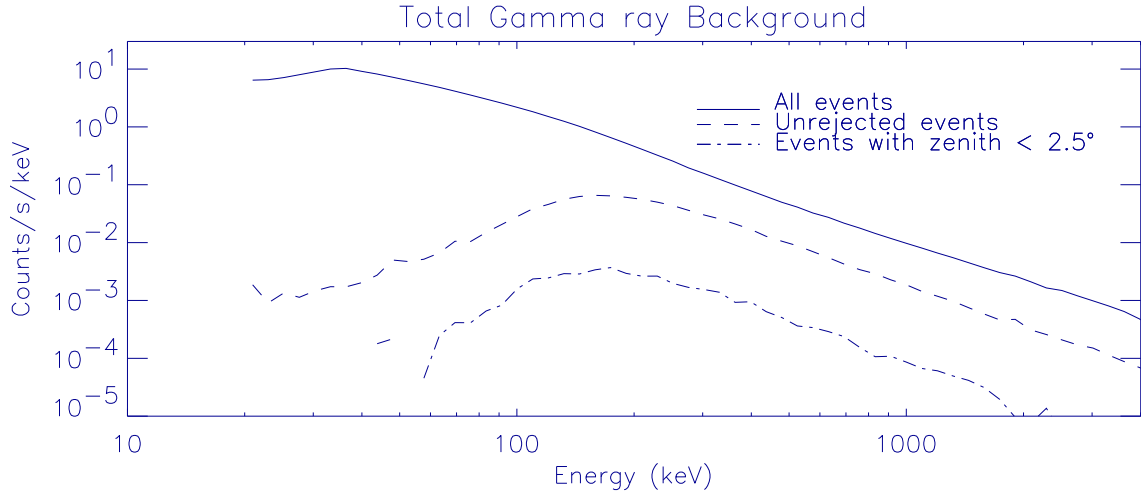


Figure 6.8: Background component for zenith angles 0° - 70° including all events (solid), unrejected events that satisfy 3+ interaction site, 1 cm minimum lever arm, and valid event requirements (dashed) and unrejected events within 2.5° of zenith (dot-dashed). Calculated assuming 5gcm^{-2} atmospheric depth in Antarctica.

6.2.5 Instrument Background

Cosmic and Atmospheric Gamma Rays

The primary source of background for a balloon-borne instrument is atmospheric gamma rays with a small contribution from cosmic gamma rays. The energy spectrum of this background component is harder at large zenith angles. Between zenith angles 0° - 70° , the flux ($\text{cm}^{-2}\text{s}^{-1}\text{sr}^{-1}\text{MeV}^{-1}$) is given by a broken power law ; $2.19 \times 10^2 E^{0.7}$ between 0.024-0.035 MeV and $5.16 \times 10^{-2} E^{-1.81}$ from 0.035-10 MeV assuming an atmospheric depth of 3.5 gcm^{-2} and magnetic latitude of 42° [Gehrels, 1985].

Using these expressions, the 0° - 70° background component was simulated with an observing time of 10^4 seconds. The result was scaled by a factor of 1.2 for an atmospheric depth of 5 gcm^{-2} and by a factor of two for observations over Antarctica. (Since the atmospheric gamma rays dominate the background and are produced by cosmic rays, the

background varies with magnetic latitude.) The total flux from 0° - 70° is shown in Figure 6.8. The solid line shows the background when all interactions are included and the dashed line shows the background when only those events that satisfy the 3+ interaction site, minimum lever arm and valid event requirements are included. The 3+ interaction and minimum lever arm requirements were described in Section 6.2.2. The background can be suppressed further by requiring that each event satisfies $|\cos\phi_1| \leq 1$ which will not be satisfied if, for instance, the photon was not fully absorbed in the detector (Compton continuum).

The imaging sensitivity (i.e sensitivity to a point source which is in this case any source smaller than ~ 3 km) of the instrument depends on the background in an image “pixel” rather than the total background in the field of view. In this case, the pixel size is 5° and the background must include any photon that is falsely imaged into the pixel. Since the incident direction of a photon is only constrained to an annulus on the sky, part of this annulus will intersect a given pixel even in the case that the photon didn’t actually come from that direction. A conservative estimate of the background component includes all photons that have their incident direction consistent with the pixel of interest. The 0° - 70° background flux for a 5° on-axis pixel is also shown in Figure 6.8 (dot-dashed line).

The background components from larger zenith angles were modeled at an atmospheric depth of 5 gcm^{-2} for three different zenith angle ranges as ($\text{cm}^{-2}\text{s}^{-1}\text{sr}^{-1}\text{MeV}^{-1}$) $0.094\text{E}^{-1.61}$ from 70° - 95° , $0.15\text{E}^{-1.47}$ from 95° - 130° , and $0.047\text{E}^{-1.45}$ from 130° - 180° and were again scaled by a factor of two for magnetic latitudes in Antarctica. Figure 6.9 shows the background components from all zenith angles for an on-axis source along with the total background obtained by adding all the components. The total background count rate at

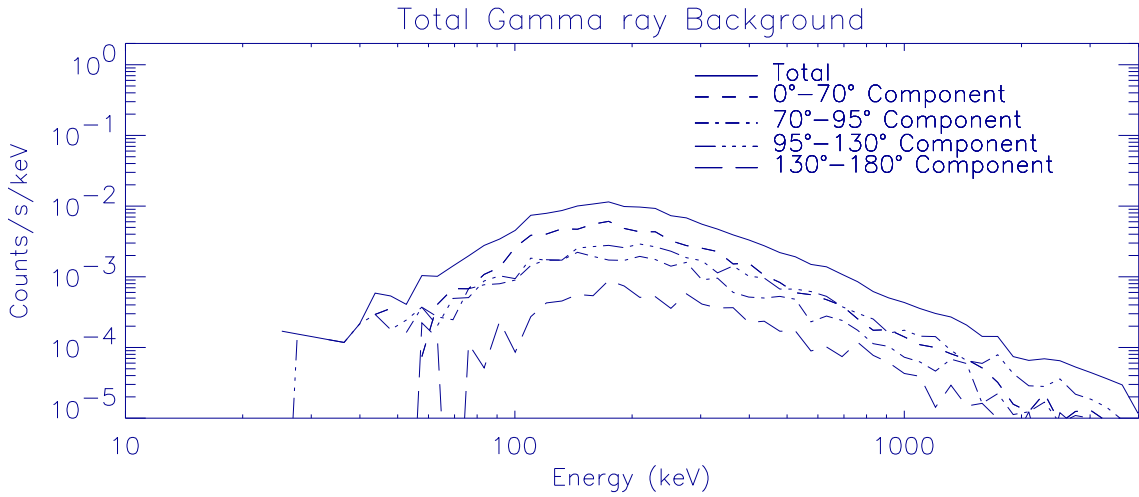


Figure 6.9: Total background (solid) and background components for different zenith angle ranges at 5 gcm^{-2} atmospheric depth in Antarctica assuming an on-axis point source.

1 MeV is 2.6×10^{-4} counts/s/keV.

The background components from 70° - 130° are comparable to the 0° - 70° component, thus the background could be further reduced by adding a side shield to the instrument. This, however, would also increase the internal background component which will be described in the next section.

Internal Background

An additional source of background is caused mostly by atmospheric neutrons and protons that interact in the detector. A detailed discussion of the internal background components is given in Gehrels [1985]. β^- unstable nuclides are produced by these interactions and the decay electron contributes one source of background as it rapidly deposits its energy in the detector. β^+ decays are another source of background. Neutrons incident on the detector also scatter elastically off Ge atoms in the detector. The recoil of the Ge atom

is an additional source of background.

The internal background component is actually increased by the presence of a shield thus it is expected to be small in the case of the unshielded instrument being considered. The internal background components can be estimated by scaling the result of Boggs and Jean [2001]. The internal background scales with the instrument active volume which in this case is 192 cm^2 compared to their active volume of $7.5 \times 10^4 \text{ cm}^2$. In addition, Boggs and Jean included only events that were consistent with a $\sim 1^\circ$ on-axis error circle. In the case being considered here, events consistent with a 5° on-axis error circle must be considered so the result was additionally scaled by a factor of 25. Therefore, the internal background at 1 MeV is estimated to be 6×10^{-5} counts/s/keV, five times smaller than the external background. Thus the internal background component is not important in this case.

6.2.6 Instrument Sensitivity

The sensitivity of an instrument depends both on its effective area and the total background. For a point source with flux, F , in units of $\text{cm}^{-2}\text{s}^{-1}\text{keV}^{-1}$, the number of detector counts is

$$N_s = F A_{eff} \tau \Delta E$$

where A_{eff} is the effective area, τ is the observing time (event duration) and ΔE is the energy channel width. The number of background counts is given by

$$N_b = b \tau \Delta E$$

where b is the simulated background in counts/s/keV described in the previous section. The signal-to-noise ratio is then given by

$$\begin{aligned} SNR \equiv k &= \frac{N_s}{\sqrt{N_s + N_b}} \\ \Rightarrow k &= \frac{FA_{eff}\tau\Delta E}{\sqrt{FA_{eff}\tau\Delta E + b\tau\Delta E}} \end{aligned}$$

Solving for F , and setting $k = 3$, the 3 sigma sensitivity is

$$F_{3\sigma} = \frac{3^2 + 3\sqrt{3^2 + 4b\tau\Delta E}}{2A_{eff}\tau\Delta E} \quad (6.8)$$

Imaging Sensitivity

For this instrument configuration, the simulated background for an on-axis source is $\sim 3 \times 10^{-4}$ counts/s/keV at 1 MeV (including external and internal components) and $A_{eff}=0.75*2 \text{ cm}^2$ where an atmospheric transmission of 0.75 has been included to account for absorption of the source photons by the atmosphere. Therefore, assuming an average event duration of 40 minutes, and the same energy bin width used for MAXIS ($\Delta E = 90$ keV)

$$F_{3\sigma} = 9 \times 10^{-5} \text{ cm}^{-2} \text{ s}^{-1} \text{ keV}^{-1}$$

Spectroscopy Sensitivity

In order to compare the sensitivity of this instrument with the MAXIS instruments, it is more useful to calculate the sensitivity for spectroscopy without imaging. In this case, no minimum lever arm is imposed since high angular resolution is not necessary. However, in order to reject much of the background entering through the sides of the instrument, the 3+ site requirement must still be imposed so the scattering angles can be reconstructed. The

background was re-simulated assuming a 90° field of view and no minimum lever arm giving a total background of 0.01 counts/s/keV. Keeping only the 3+ site events, the effective area at 1 MeV is 5.2 cm^2 and the 3 sigma sensitivity is

$$F_{3\sigma} = 2.4 \times 10^{-4} \text{ cm}^{-2} \text{ s}^{-1} \text{ keV}^{-1}$$

For comparison, the photon flux of the January 22, 2000 MAXIS event was $\sim 1 \times 10^{-3} \text{ cm}^{-2} \text{ s}^{-1} \text{ keV}^{-1}$ however that event only lasted for twenty minutes. This Compton telescope would detect the January 22 event at 11σ compared to the detection at 7σ for the GeD and 30σ for the BGO. Therefore, the instrument is more sensitive than the GeD but not as sensitive as the BGO.

6.2.7 Other Configurations

The sensitivity of the Compton telescope simulated here is not quite satisfactory since we would like to have measurements as sensitive as the MAXIS BGO but with the addition of imaging capability and the advantage of using a single instrument. One way to improve the sensitivity is to add a side shield to the instrument to reduce the cosmic and atmospheric gamma ray background. This will also increase the internal background component but since that component was small in the unshielded case, the shield will most likely still improve the sensitivity. Detailed modeling of the internal background including a shield is needed to determine the improvement.

Another possible solution is to add a third detector plane below the second detector. A simulation of this was carried out as described earlier and the results showed only a very small increase in effective area. It was found that placing the third detector sideways

actually provided a greater improvement since much of the loss of effective area is due to photons escaping out the sides.

This suggests that the best improvement would be obtained by moving the detector planes closer together which could be achieved if the two detector planes could be housed in the same cryostat. If the cold plate between the two detector planes could be moved to the sides of the detectors, the effective area would also be increased since many of the events scattering in the cold plate would be fully absorbed instead. This instrument configuration should be achievable with current cryostat designs.

These different telescope configurations will need to be investigated further to find the ideal instrument, but the above results demonstrate the feasibility of using a simple Compton telescope for imaging MeV bursts while maintaining good sensitivity at MeV energies.

6.3 Polarization

A Compton telescope has the ability to not only image but also to measure polarization since the cross section for Compton scattering depends on the incident electric field direction. In addition, the bremsstrahlung produced by precipitating MeV electrons is polarized and strongly beamed in the forward direction. In this section, the Compton telescope is examined as a tool for measuring polarization and thus gaining information about the pitch angle distribution of precipitating electrons.

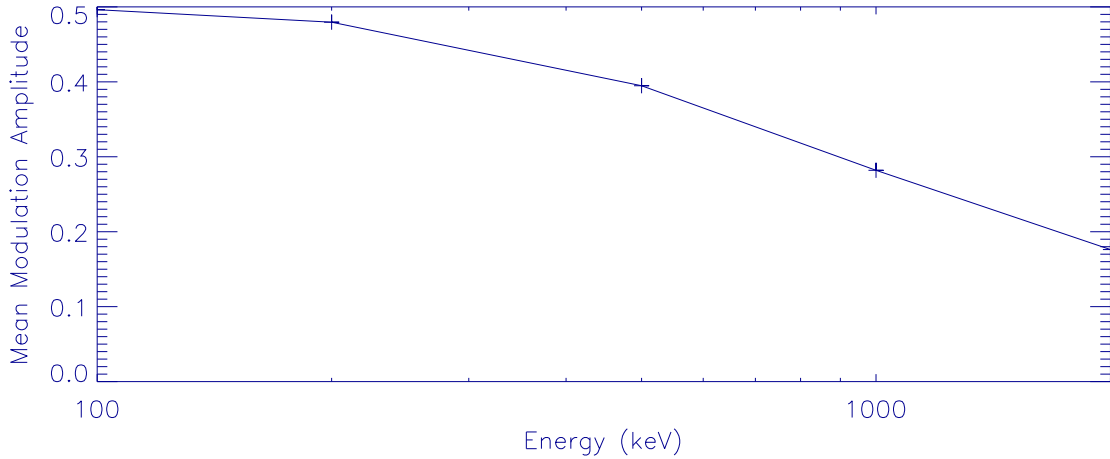


Figure 6.10: Mean modulation amplitude as a function of energy for normally incident photons.

6.3.1 Measuring Polarization

In the case of polarized radiation, a Compton scattered photon is more likely to be ejected perpendicular to the electric field vector of the incident radiation [Evans, 1955]. Therefore, the distribution of scattering angles in the detector provides information about both the polarization direction and fraction. The Klein-Nishina differential cross section can be written

$$d\sigma = \frac{r_0^2}{2} \left(\frac{E'}{E} \right)^2 \left(\frac{E}{E'} + \frac{E'}{E} - 2\sin^2\phi\cos^2\eta \right) d\Omega \quad (6.9)$$

where r_0 is the classical electron radius, E and E' are the incident and scattered photon energies, ϕ is the scattering angle and η is the angle between the plane of incident polarization and the scattering plane. From this expression, it is not only evident that the cross section is largest at $\eta=90^\circ$ but also that the preference for scattering in a particular direction will be strongest for scattering angles (ϕ) near 90° .

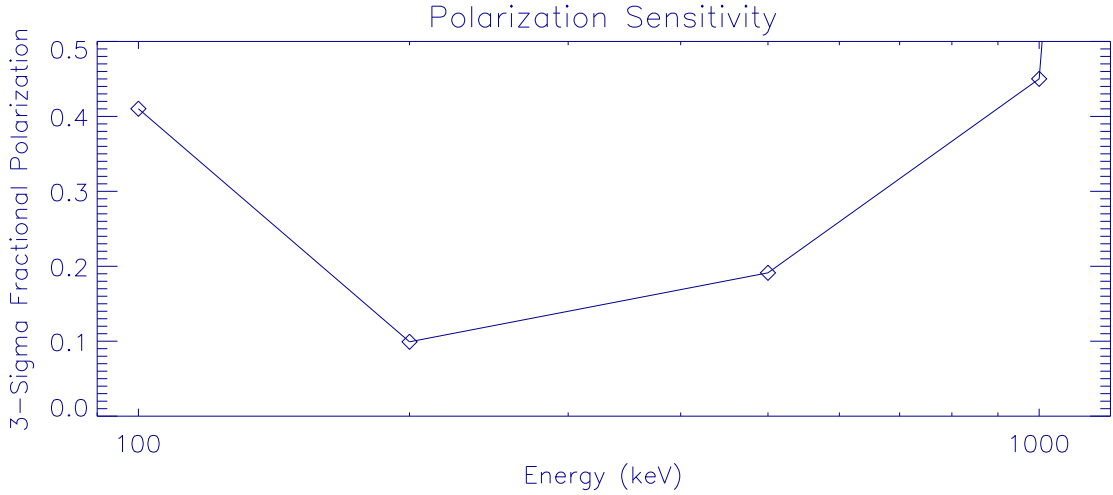


Figure 6.11: Fractional polarization sensitivity as a function of energy for an on-axis source.

Polarization Sensitivity

In a Compton telescope, photons will scatter at many angles but the sensitivity to polarization is greatest for scattering angles near 90° . The modulation amplitude gives the maximum variation in the cross section as a function of energy and scattering angle and is defined using the Klein-Nishina cross section as [S. E. Boggs, private communication]

$$\mu(\phi, E) = \frac{d\sigma(\eta = 90^\circ) - d\sigma(\eta = 0^\circ)}{d\sigma(\eta = 90^\circ) + d\sigma(\eta = 0^\circ)} \quad (6.10)$$

$$= \frac{\sin^2 \phi}{E/E' + E/E - \sin^2 \phi}$$

For the instrument configuration described in Section 6.2.1, the mean modulation amplitude was simulated at different energies and is shown in Figure 6.10. The modulation is largest for energies between 200-500 keV.

Given the mean modulation amplitude, the n-sigma instrument sensitivity to polarization can be calculated for a given source flux, F , and event duration, τ and is given

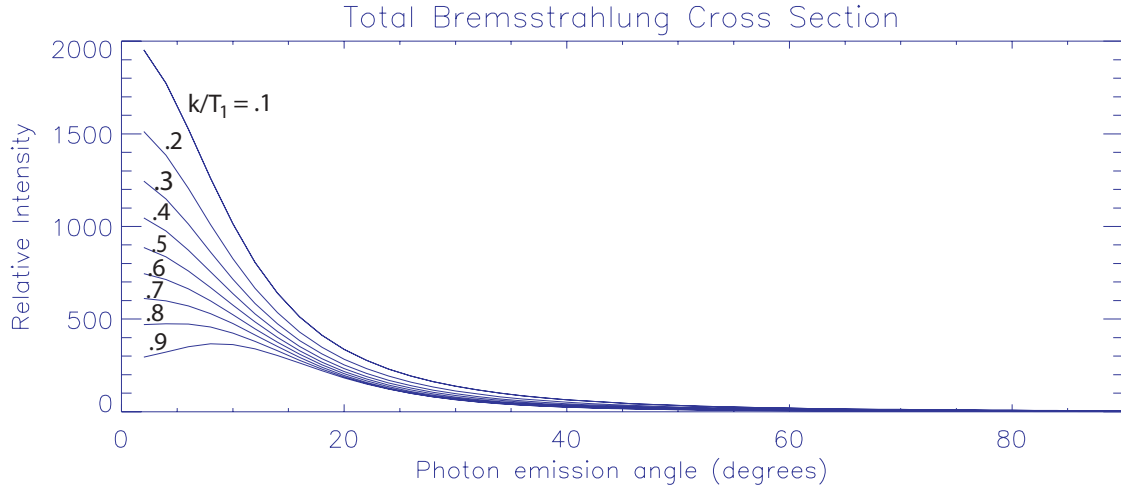


Figure 6.12: Total bremsstrahlung cross section as a function of photon emission angle for photon energies ranging from 0.1 to 0.9 of the initial electron energy (1 MeV).

by [Lei et al., 1997]

$$X_{n\sigma} = \frac{n}{\mu} \frac{\sqrt{(FA_{eff} + B)\tau\Delta E}}{FA_{eff}\tau} \quad (6.11)$$

where B is the background count rate. Using the background count rate simulated in Section 6.2.5 and assuming the source flux for the January 22, 2000 event and event duration of 40 minutes, the polarization sensitivity was calculated and is shown in Figure 6.11 for energies between 100-1000 keV. It is also assumed here that the energy band is 10% of the energy in each case. The 3 sigma sensitivity to polarization is best near 200 keV (~ 0.1) and decreases to about 0.45 at 1 MeV.

6.3.2 Polarization of an Overhead Source

For a terrestrial source, precipitating relativistic electrons produce bremsstrahlung which is polarized and beamed in the forward direction. The cross sections for the each polarization component of bremsstrahlung are given in Gluckstern and Hull [1953] and

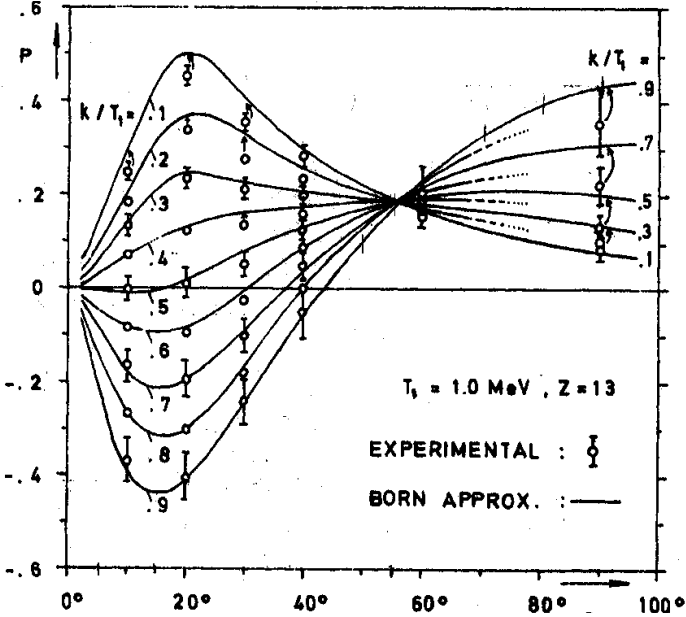


Figure 6.13: Fractional polarization as a function of emission angle for different values of the emitted photon energy (expressed as a fraction of initial electron energy) [Lichtenberg et al., 1975].

Figure 6.12 shows the total cross section for photons with energies ranging from 0.1 to 0.9 of the initial electron energy (here 1 MeV) which is summed over polarizations. The polarization fraction is defined as

$$P = \frac{d\sigma_{\perp} - d\sigma_{||}}{d\sigma_{\perp} + d\sigma_{||}} \quad (6.12)$$

Here “parallel” refers to the plane containing the initial electron and emitted photon directions and “perpendicular” is perpendicular to that plane. Figure 6.13 shows both theoretical curves and experimental values for the polarization fraction taken from Lichtenberg et al., [1975] for a 1 MeV initial electron energy and different values of the ratio k/T_1 where k is the emitted photon energy and T_1 is the initial electron energy. The curves shown are for bremsstrahlung produced in aluminum, but the fractional polarization is independent of Z for low Z materials, thus the curves shown are also valid for bremsstrahlung in air.

[Lichtenberg et al., 1975]. In the low frequency limit (small k/T_1), the polarization fraction is positive for all emission angles (angle between the initial electron direction and emitted photon direction) but becomes increasingly more negative at small emission angles for higher photon energies. Near the short wavelength limit where the photon takes away almost all the electron's energy, the bremsstrahlung is polarized in the parallel direction with the fractional polarization reaching a maximum of $\sim 45\%$ for emission angles near 20° .

Since the direction of polarization and fractional polarization depend strongly on the angle between an observer and the initial electron direction, polarization measurements may provide information about the electron direction and thus the pitch angle distribution of the electrons. Assuming a source directly overhead, two different pitch angle distributions are now considered and their expected polarizations compared.

Isotropic Distribution

In the case of strong pitch angle scattering, the pitch angle distribution of precipitating particles is nearly isotropic since the loss cone is filled. For a source overhead, the angle between the observer and the velocity vector for a particle with pitch angle, α , is just α and the fractional polarization can be read off Figure 6.13 for each electron. However, the radiation is also beamed in the forward direction with average emission angle $\sim 20^\circ$ for a 1 Mev electron (Figure 6.12) thus the contribution to the polarization should be largest for pitch angles near this value. For photon energies near the initial electron energy, the polarization is negative (polarized in the parallel direction) near $\sim 20^\circ$ emission angle with fractional polarization $\sim 45\%$.

To determine the average fractional polarization integrated over the all particles

for an isotropic pitch angle distribution

$$\begin{aligned} \langle P \rangle &= \frac{1}{\sigma} \int P(\alpha) \frac{d\sigma}{d\Omega}(\alpha) d\Omega \\ &= \frac{2\pi}{\sigma} \int \left(\frac{d\sigma_{\perp}}{d\Omega} - \frac{d\sigma_{\parallel}}{d\Omega} \right) \sin\alpha d\alpha \end{aligned}$$

where σ is the total cross section integrated over all angles. For a 1 MeV electron and $k/T_1=0.9$, $\langle P \rangle = -0.3$

Pancake Distribution

Now consider a pancake pitch angle distribution where all particles have 90° pitch angle just before producing the observed bremsstrahlung. This would correspond to the weak scattering case where the loss cone is nearly empty except for particles diffusing in at the very edge so that all particles are just mirroring when they're lost. For simplicity, assume the magnetic field points vertically, then the electrons will gyrate in a horizontal plane. In this case, it is easy to show that the angle between the electron velocity vector and the direction to the balloon is 90° for an overhead source. For photon energies near the initial electron energy, the radiation will be perpendicularly polarized with fractional polarization near 40%.

Comparing these results, the polarization is negative in the case of an isotropic distribution and positive in the case of a pancake distribution. These results indicate that, in principle, a pancake pitch angle distribution should be distinguishable from an isotropic distribution. A more detailed analysis is needed to determine the polarization fraction for a more realistic spatial distribution of precipitation. For complicated distributions, it is not yet clear that there will be a unique combination of spatial and pitch angle distributions

for a given intensity and polarization measurement but the above results are encouraging. However, with this Compton telescope configuration, polarization fractions of ~ 0.4 would be not quite detectable at the 3 sigma level.

6.3.3 Electron Scattering

In the previous section, the issue of electron and photon scattering in the atmosphere was ignored. In order to measure any angular information about the precipitating electrons, the directional information must be preserved as they enter the atmosphere. If the electrons are heavily scattered in direction, this information will be lost. In the multiple-scattering regime, the mean square angle for a single scatter is given by [Jackson, 1975]

$$\langle \theta^2 \rangle = 2\theta_{min}^2 \ln \left(\frac{1}{\theta_{min}} \right) \quad (6.13)$$

where θ_{min} is a cut-off angle at small angles and finite nuclear size effects, which are only important above ~ 50 MeV for electrons in air, have been ignored. The Quantum Mechanical expression for θ_{min} is given by

$$\theta_{min} = \frac{Z^{1/3}}{192} \frac{1}{\beta\gamma} \quad (6.14)$$

With these equations and $Z=7.2$ for air, the mean square scattering angle for a 1 MeV electron is then 1.5×10^{-4} radians. After many collisions, the distribution of scattering angles is nearly Gaussian with mean square angle [Jackson, 1975]

$$\langle \alpha^2 \rangle = N \langle \theta^2 \rangle \quad (6.15)$$

The average number of collisions suffered by an electron as it traverses an absorber of thickness, d , and number density, n , is given by

$$N = nd\sigma \quad (6.16)$$

where σ is the total scattering cross section in this case due to coulomb collisions with atmospheric nuclei. Following Jackson,

$$\sigma = 4\pi r_0^2 Z^{4/3} \left(\frac{192}{\beta} \right)^2 \quad (6.17)$$

where r_0 is the classical electron radius and $4\pi r_0^2 = 1 \times 10^{-24} \text{ cm}^2$. In terms of the column density, ξ , traversed by the electron, Equation 6.16 can be rewritten

$$N = \frac{\xi \sigma}{Am_p}$$

where A is the atomic mass number and m_p is the mass of the proton. In the case, of air, $Z=7.2$, $A=14$ and the penetration depth of a 1 MeV electron is 0.5 g/cm^2 [Berger and Seltzer, 1972].

Therefore at 1 MeV, the mean scattering angle is ~ 1.9 radians and it appears that the average electron will be scattered too much to preserve its directional information. However, there will be many electrons that are scattered less; photons near the electron energy are those produced before the electron has been scattered substantially and are those photons that have not been Compton scattered. By restricting the observations to energies near the precipitating electron energy, the directional information should be better preserved. For observations made at 1 MeV, based on the flattest observed spectrum for an MeV event (January 22 event), photons at 1 MeV are produced by electrons between 1-2 MeV. The worst case for losing directional information is a 2 MeV electron that loses 1 MeV before producing a 1 MeV photon. Such an electron would have traversed about 0.6 gcm^{-2} which corresponds to a mean scattering angle of 0.87 radians. Assuming a Gaussian distribution of scattering angles, about 40% of the electrons will be scattered by less than

0.3 radians which is roughly the width of the bremsstrahlung beam for a 1 MeV electron. Lower energy electrons will be scattered even less in order to produce a 1 MeV photon. For example, about 58% 1.25 MeV electrons will preserve their directional information to within 0.3 radians.

A detailed simulation that includes both electron scattering and Compton scattering of photons in the atmosphere is required to accurately determine the fraction of photons that preserve the directional information. These results suggest that the fractional polarization will be reduced by about a factor of two due to electron scattering which would make the predicted fractional polarizations undetectable with this Compton telescope. However, the other configuration discussed in Section 6.2.7 may have smaller backgrounds and a more compact instrument will have a larger effective area. In addition, the fractional polarization of bremsstrahlung is larger at lower energies and the instrument sensitivity is also better. Increasing the energy band of the observations may also improve the instrument sensitivity though electron scattering may negate this effect.

Chapter 7

Conclusion and Future Work

7.1 Summary

This dissertation presents X-ray observations of MeV electron precipitation made with the MAXIS long-duration balloon payload during its flight over Antarctica in January 2000. The MAXIS GeD detected nine MeV X-ray bursts similar to the 1996 Kiruna event demonstrating that these events are common, occurring on average about once per day at any location between 58°-68° latitude. The average event duration was found to be about 40 minutes, thus such precipitation occurs about 3% of the time at any given location. The events were found to occur during magnetospheric substorms though more observations are needed to confirm the association.

The precipitating electron spectrum and flux were determined by modeling the X-ray spectrum for each event and the average precipitating flux for >500 keV electrons was found to be $360 \text{ cm}^{-2}\text{s}^{-1}$ indicating that a total of 5×10^{25} electrons could be lost from the outer radiation belts in eight days. By comparing this loss rate with GPS measurements

of the trapped electrons, it was shown that the entire outer zone could be depleted by these precipitation events alone in less than one week. This is comparable to the loss rate estimated by in-situ measurements indicating that MeV X-ray bursts are one of the primary mechanisms for the loss of relativistic electrons from the outer radiation belts. The MAXIS observations provide a direct measurement of the loss rate and demonstrate that balloon observations could provide loss rates during both quiet and active times.

The MeV precipitation events detected by MAXIS occurred only in the dusk sector while lower energy precipitation occurred at all local times. In addition, the events were found to occur inside or very near the location of the duskside plasmapause. These observations suggest that EMIC waves could be responsible for pitch angle scattering the electrons into the loss cone as was suggested for the 1996 Kiruna MeV event. However, improved statistics obtained by combining the GeD and BGO spectra have allowed for better constraints on the precipitating electron spectrum and a direct inversion of the observed spectrum was possible for a few events. The results show that the precipitating electron spectrum is consistent with a very flat exponential with e-folding energies ranging from 170-3000 keV. In three out of four cases examined, this spectrum was found to be flatter than the trapped spectrum observed by a particle detector on one of the GPS satellites indicating that the pitch angle scattering mechanism acts more efficiently at higher energies but that low energy electrons are also being precipitated. EMIC waves are only expected to interact with energetic (\sim MeV) electrons, suggesting that EMIC is not responsible for the precipitation. Therefore, the precipitation mechanism is still not known.

7.2 Future Work

The MAXIS balloon flight greatly enhanced our understanding of MeV X-ray bursts and relativistic electron losses, but there are still many questions remaining. In particular, the precipitation mechanism is still not known and the relation of MeV bursts to other types of precipitation is not clear.

7.2.1 Relation to Other Types of Precipitation

During the MAXIS MeV event on January 22, 2000, in the main phase of a geomagnetic storm, the SAMPEX satellite observed relativistic electron microburst precipitation about 12 hours away in local time but near the same L-shell as the MAXIS MeV burst. Based on similar SAMPEX observations of microburst precipitation during three different geomagnetic storms, Lorentzen et al., [2001] estimated the loss rate due to microbursts as $\sim 10^{25}$ in the week following each storm. This is the same order of magnitude that was obtained with the MAXIS observations of MeV events, however microbursts are observed more frequently on the dayside, not at dusk.

These observations suggest a possible relation between microbursts and the MeV X-ray bursts. One suggestion is that the MeV bursts are the particles scattered into the drift loss cone during a microburst event on the dayside. As mentioned previously, particles scattered into the bounce loss cone are lost within the particle bounce time. However, some particles will be scattered close to, but not into, the bounce loss cone. These particles will gradient-curvature drift around the earth. Near the South Atlantic Anomaly, where the earth's magnetic field is weakest, the particles' mirror point is lowered and the loss cone

becomes wider. In this region, those particles that were previously near the bounce loss cone will mirror low enough in altitude to collide with the atmosphere and be lost; these particles are in the drift loss cone. For the event on January 22, MAXIS was located very close to the South Atlantic Anomaly. Therefore, particles scattered into the drift loss cone on the dayside by the microburst precipitation could have been precipitated at the balloon location producing the X-ray burst.

If microbursts are the source of the MeV X-ray bursts, one might expect to see drift dispersion in the X-ray spectrum since high energy particles drift faster than low energy particles. The spectrum should appear to soften in time, but this was not seen. In addition, both the Kiruna MeV event and several of the MAXIS MeV events were not very close to the South Atlantic Anomaly. A new balloon campaign planned for launch in December 2004 will be able to investigate the relationship between MeV X-ray bursts and microbursts. The experiment will consist of a long duration balloon payload similar to MAXIS (MAXIS II) and in addition, several very small payloads launched at a remote location near the South Atlantic Anomaly. Multi-point measurement will allow us to measure how the spectrum changes as a function of longitude as the particles drift and will also provide more opportunity for correlated measurements with SAMPEX.

Another type of precipitation events observed in the dusk sector are called “dusk-side spikes” and are measured with riometers. A riometer measures the radio opacity of the ionosphere by measuring the absorption of cosmic radio waves. During a precipitation event, increased ionization in the ionosphere causes an increase in the absorption. During the MAXIS flight, there were observations of duskside spikes at several Automated Geo-

physical Observatories in Antarctica, but these were observed far away from the balloon location so correlating these with the MeV bursts was difficult. With multiple balloon payloads launched in 2004 near Halley Bay or SONAE stations in Antarctica, which both have imaging riometers, better correlations will be possible. Correlating the MeV bursts with the duskside spikes would allow for a statistical study of the events since riometers operate year-round. The association between MeV events and substorms could then be investigated in more detail since the riometer stations also have magnetometers.

7.2.2 Other Observations

In addition to the X-ray instrumentation, The MAXIS II payload will consist of electric and magnetic field instruments to detect plasma waves. Measuring waves may shed some light on the X-ray modulation at both ULF and shorter timescales and may provide more information about the precipitation mechanism. For example, EMIC waves observed during an MeV event with wave amplitude modulated at the same frequency as the X-ray count rate would provide good evidence that EMIC waves are the scattering mechansim.

Finally, the Compton telescope presented in Chapter 6 would allow us to image MeV bursts at high energies and possibly gain information about the particle pitch angle distribution. The MAXIS observations of MeV electron precipitation indicated a nearly empty loss cone. Since the time for an electron to be scattered into the loss cone is longer than the time to empty the loss cone, the precipitating pitch angle distribution is likely to be pancake with all the precipitating particles near the edge of the loss cone. The results from Chapter 6 show that it should be possible to distinguish between an isotropic and pancake pitch angle distribution by measuring the polarization of the bremsstrahlung.

Bibliography

- [Bailey, 1968] Bailey, D. K. (1968). Some quantitative aspects of electron precipitation in and near the auroral zone. *Rev. Geophys. Space Phys.*, 6:289.
- [Baker et al., 1979] Baker, D. N., Higbie, P. R., Belian, R. D., and Hones, Jr., E. W. (1979). Do Jovian electrons influence the terrestrial outer radiation zone? *Geophys. Res. Lett.*, 6:531.
- [Baker et al., 2001] Baker, D. N., Kanekal, S. G., Blake, J. B., and Pulkkinen, T. I. (2001). The global efficiency of relativistic electron production in the earth's magnetosphere. *J. Geophys. Res.*, 106:19,169–19,178.
- [Baker et al., 1997] Baker, D. N., Li, X., Turner, N., Allen, J. H., Bargatze, L. F., Blake, J. B., Sheldon, R. B., Spence, H. E., Belian, R. D., Reeves, G. D., Kanekal, S. G., Klecker, B., Lepping, R. P., Ogilvie, K., Mewalt, R. A., Onsager, T., Singer, H. J., and Rostoker, G. (1997). Recurrent geomagnetic storms and relativistic electron enhancements in the outer magnetosphere: ISTP coordinated measurements. *J. Geophys. Res.*, 102:14141–14148.
- [Baker et al., 1998] Baker, D. N., Pulkkinen, T. I., Li, X., Kanekal, S. G., Blake, J. B.,

- Selesnick, R. S., Henderson, M. G., Reeves, G. D., Spence, H. E., and Rostoker, G. (1998). Coronal mass ejections, magnetic clouds, and relativistic magnetospheric electron events: ISTP. *J. Geophys. Res.*, 103:17,279–17,291.
- [Barcus and Rosenberg, 1966] Barcus, J. R. and Rosenberg, T. J. (1966). Energy spectra for auroral-zone x rays. *J. Geophys. Res.*, 71:803–823.
- [Berger and Seltzer, 1972] Berger, M. J. and Seltzer, S. M. (1972). Bremsstrahlung in the atmosphere. *Journal of Atmospheric and Terrestrial Physics*, 34:85–108.
- [Blake et al., 1992] Blake, J. B., Kolasinski, W. A., Fillius, R. W., and Mullen, E. G. (1992). Injection of electrons and protons with energies of tens of mev into $l < 4$ on 24 march 1991. *Geophys. Res. Lett.*, 19:821.
- [Blake et al., 1996] Blake, J. B.,Looper, M. D., Baker, D. N., Nakamura, R., Klecker, B., and Hovestadt, D. (1996). New high temporal and spatial resolution measurements by SAMPEX of the precipitation of relativistic electrons. *Adv. Space Res.*, 18(8):171–186.
- [Boggs, 1998] Boggs, S. E. (1998). *Gamma Ray Spectroscopy: Galactic Center Observations and Germanium Detector Development*. PhD thesis, University of California at Berkeley.
- [Boggs and Jean, 2000] Boggs, S. E. and Jean, P. (2000). Event reconstruction in high resolution Compton telescopes. *Astron. Astrophys. Suppl. Ser.*, 145:311–321.
- [Boggs and Jean, 2001] Boggs, S. E. and Jean, P. (2001). Performance characteristics of high resolution Compton telescopes. *Astronomy and Astrophysics*, 376:1126–1134.

- [Brown and Stone, 1972] Brown, J. W. and Stone, E. C. (1972). High-energy electron spikes at high latitudes. *J. Geophys. Res.*, 77:3384–3396.
- [Carpenter and Anderson, 1992] Carpenter, D. L. and Anderson, R. R. (1992). An ISEE/whistler model of equatorial electron density. *J. Geophys. Res.*, 97:1097.
- [Coroniti and Kennel, 1970] Coroniti, F. V. and Kennel, C. F. (1970). Electron precipitation pulsations. *J. Geophys. Res.*, 75:12791289.
- [Daglis, 2001a] Daglis, I. A., editor (2001a). *Proceedings of the NATO Advanced Study Institute on Space Storms and Space Weather Hazards*, Heidelberg, Germany. Kluwer Academic Publishers.
- [Daglis, 2001b] Daglis, I. A. (2001b). Space storms, ring current and space-atmosphere coupling. In [Daglis, 2001a], pages 1–42.
- [De Moortel and Hood, 2000] De Moortel, I. and Hood, A. W. (2000). Wavelet analysis and the determination of coronal plasma properties. *Astronomy and Astrophysics*, 363:269–278.
- [DuMond, 1933] DuMond, J. W. M. (1933). The linear momenta of electrons in atoms and in solid bodies as revealed by X-ray scattering. *Reviews of Modern Physics*, 5:1–14.
- [Elkington et al., 1999] Elkington, S. R., Hudson, M. K., and Chan, A. A. (1999). Acceleration of relativistic electrons via drift-resonant interaction with toroidal-mode Pc-5 ULF oscillations. *Geophys. Res. Lett.*, 26:3273.

[Evans, 1955] Evans, R. D. (1955). *The Atomic Nucleus*. McGraw-Hill Book Company, Inc., New York, NY.

[Fang and Thews, 1998] Fang, L.-Z. and Thews, R. L. (1998). *Wavelets in Physics*. World Scientific, Singapore.

[Foat et al., 1998] Foat, J. E., Lin, R. P., Smith, D. M., Fenrich, F., Millan, R., Roth, I., Lorentzen, K. R., McCarthy, M. P., Parks, G. K., and Treilhou, J. P. (1998). First detection of a terrestrial MeV X-ray burst. *Geophys. Res. Lett.*, 25(22):4109–4112.

[Fraser et al., 2001] Fraser, B. J., Hu, T. D., Korth, A., Singer, H. J., Hardy, D. A., and Anderson, R. R. (2001). Stormtime Pc5 hydromagnetic waves in the middle magnetosphere: Modulation of Pc1 ion cyclotron waves and the role of medium energy ions. *American Geophysical Union: Fall Meeting 2001*.

[Friedel et al., 2002] Friedel, R. H. W., Reeves, G. D., and Obara, T. (2002). Relativistic electron dynamics in the inner magnetosphere - a review. *Journal of Atmospheric and Terrestrial Physics*, 64:265–282.

[Fujimoto and Nishida, 1990] Fujimoto, M. and Nishida, A. (1990). Energization and anisotropization of energetic electrons in the earth's radiation belt by recirculation process. *J. Geophys. Res.*, 95:4265.

[Gehrels, 1985] Gehrels, N. (1985). Instrumental background in balloon-borne gamma-ray spectrometers and techniques for its reduction. *Nuclear Instruments and Methods in Physics Research*, A239:324–349.

- [Gluckstern et al., 1953] Gluckstern, R. L., Hull, Jr., M. H., and Breit, G. (1953). Polarization of bremsstrahlung radiation. *Physical Review*, 90:1026–1029.
- [Horne, 2001] Horne, R. B. (2001). The contribution of wave-particle interactions to electron loss and acceleration in the earth's radiation belts during geomagnetic storms. *URSI Reviews of Radio Science*.
- [Horne and Thorne, 1998] Horne, R. B. and Thorne, R. M. (1998). Potential waves for relativistic electron scattering and stochastic acceleration during magnetic storms. *Geophys. Res. Lett.*, 25:3011.
- [Imhof et al., 1991] Imhof, W., Voss, H. D., Mobilia, J., Datlowe, D. W., and Gaines, E. E. (1991). The precipitation of relativistic electrons near the trapping boundary. *J. Geophys. Res.*, 96:5619.
- [Imhof et al., 1990] Imhof, W. L., Mobilia, J., Datlowe, D. W., Voss, H. D., and Gaines, E. E. (1990). Longitude and temporal variations of energetic electron precipitation near the trapping boundary. *J. Geophys. Res.*, 95:3829–3839.
- [Imhof et al., 1986] Imhof, W. L., Voss, H. D., Reagan, J. B., Datlowe, D. W., Gaines, E. E., and Mobilia, J. (1986). Relativistic electron and energetic ion precipitation spikes near the plasmapause. *J. Geophys. Res.*, 91:3077.
- [Jackson, 1975] Jackson, J. D. (1975). *Classical Electrodynamics*. John Wiley & Sons, New York, NY, second edition.
- [Johns and Lin, 1992] Johns, C. M. and Lin, R. P. (1992). The derivation of parent electron spectra from bremsstrahlung hard X-ray spectra. *Solar Physics*, 137:121–140.

- [Kamide, 2001] Kamide, Y. (2001). Geomagnetic storms as a dominant component of space weather: Classic picture and recent issues. In [Daglis, 2001a], pages 43–78.
- [Kennel and Petschek, 1966] Kennel, C. F. and Petschek, H. E. (1966). Limits on stable trapped particle fluxes. *J. Geophys. Res.*, 71:1.
- [Kivelson and Russell, 1995] Kivelson, M. and Russell, C. (1995). *Introduction to Space Physics*. Cambridge University Press, New York, NY.
- [Knoll, 1989] Knoll, G. F. (1989). *Radiation Detection and Measurement*. John Wiley & Sons, New York, NY, second edition.
- [Koch and Motz, 1959] Koch, H. W. and Motz, J. W. (1959). Bremsstrahlung cross-section formulas and related data. *Reviews of Modern Physics*, 31:920.
- [Lei et al., 1997] Lei, F., Dean, A. J., and Hills, G. L. (1997). Compton polarimetry in gamma-ray astronomy. *Space Science Reviews*, 82:309.
- [Lemaire, 2001] Lemaire, J. F. (2001). From the discovery of the radiation belts to space weather perspectives. In [Daglis, 2001a], pages 79–102.
- [Li et al., 1997] Li, X., Baker, D. N., Temerin, M., Larson, D., Lin, R. P., Reeves, G. D.,Looper, M., Kanekal, S. G., and Mewalt, R. A. (1997). Are energetic electrons in the solar wind the source of the outer radiation belt? *Geophys. Res. Lett.*, 24:923–926.
- [Li et al., 1996] Li, X., Hudson, M. K., Blake, J. B., and Roth, I. (1996). Observation and simulation of the rapid formation of a new electron radiation belt during march 24, 1991 ssc. *AIP Conference Proceedings*, 383:109–117.

- [Lichtenberg et al., 1975] Lichtenberg, W., Przybylski, A., and Scheer, M. (1975). Bremsstrahlung linear polarization at incident electron energies of 0.5-1.5 MeV. *Physical Review A*, 11:480–487.
- [Longair, 1997] Longair, M. S. (1997). *High Energy Astrophysics*, volume 1. Cambridge University Press, Cambridge, U.K., second edition.
- [Looper et al., 1994] Looper, M. D., Blake, J. B., Mewalt, R. A., Cummings, J. R., and Baker, D. N. (1994). Observations of the remnants of the ultrarelativistic electrons injected by the strong SSC of 24 march 1991. *Geophys. Res. Lett.*, 21:2079–2082.
- [Lorentzen, 1999] Lorentzen, K. R. (1999). *Duskside Relativistic Electron Precipitation*. PhD thesis, University of Washington.
- [Lorentzen et al., 2001] Lorentzen, K. R., Looper, M. D., and Blake, J. B. (2001). Relativistic electron microbursts during the GEM storms. *Geophys. Res. Lett.*, 28:2573–2576.
- [Lorentzen et al., 2000] Lorentzen, K. R., McCarthy, M. P., Parks, G. K., Foat, J. E., Millan, R. M., Smith, D. M., Lin, R. P., and Treilhou, J. P. (2000). Precipitation of relativistic electrons by interaction with electromagnetic ion cyclotron waves. *J. Geophys. Res.*, 105:5381.
- [Lyons et al., 1972] Lyons, L. R., Thorne, R. M., and Kennel, D. F. (1972). Pitch-angle diffusion of radiation belt electrons within the plasmasphere. *J. Geophys. Res.*, 77:3455.
- [Matthews et al., 1988] Matthews, D. L., J.Rosenberg, T., R.Benbrook, J., and Bering III, E. A. (1988). Dayside energetic electron precipitation over the south pole ($\lambda = 75^\circ$). *J. Geophys. Res.*, 93(A11):12,941–12,945.

- [Nakamura et al., 1995] Nakamura, R., Baker, D. N., Blake, J. B., Kanekal, S., Klecker, B., and Hovestadt, D. (1995). Relativistic electron precipitation enhancements near the outer edge of the radiation belt. *Geophys. Res. Lett.*, 22:1129.
- [Nemiroff et al., 1997] Nemiroff, R. J., Bonnell, J. T., and Norris, J. P. (1997). Temporal and spectral characteristics of terrestrial gamma flashes. *J. Geophys. Res.*, 102:9659–9665.
- [Panasyuk, 2001] Panasyuk, M. I. (2001). Cosmic ray and radiation belt hazards for space missions. In [Daglis, 2001a], pages 251–284.
- [Parks, 1991] Parks, G. K. (1991). *Physics of Space Plasmas: An Introduction*. Addison-Wesley Publishing Company, Redwood City, CA.
- [Parks et al., 1993] Parks, G. K., Freeman, T. J., McCarthy, M. P., and Werden, S. (1993). The discovery of auroral X-rays by balloon-borne detectors and their contributions to magnetospheric research. In *Auroral Plasma Dynamics*, Geophysical Monograph 80, pages 17–23, Washington, D. C. American Geophysical Union.
- [Parks et al., 1979] Parks, G. K., Gurgiolo, C., and West, R. (1979). Relativistic electron precipitation. *Geophys. Res. Lett.*, 6:393–396.
- [Press et al., 1992] Press, W. H., Teukolsky, S. A., Vetterling, W. T., and Flannery, B. P. (1992). *Numerical Recipes in C*. Cambridge University Press, New York, NY, second edition.
- [Reeves, 1998] Reeves, G. D. (1998). Relativistic electrons and magnetic storms:1992-1995. *Geophys. Res. Lett.*, 25:1817.

- [Rosenberg et al., 1972] Rosenberg, T. J., Lanzerotti, L. J., Bailey, D. K., and Pierson, J. D. (1972). Energy spectra in relativistic electron precipitation events. *J. Atm. and Terr. Phys.*, 34:1977–1990.
- [Schönenfelder, 1993] Schönenfelder, V. e. a. (1993). Instrument description and performance of the imaging gamma ray telescope COMPTEL aboard the Compton gamma ray observatory. *APJS*, 86:657–692.
- [Schulz and Lanzerotti, 1974] Schulz, M. and Lanzerotti, L. J. (1974). *Particle Diffusion in the Radiation Belts*. Springer-Verlag, Heidelberg, Germany.
- [Sergeev and Tsyganenko, 1982] Sergeev, V. A. and Tsyganenko, N. A. (1982). Energetic particle losses and trapping boundaries as deduced from calculations with a realistic magnetic field model. *Plan. Space Sci.*, 30:999.
- [Smith et al., 1995] Smith, D. M., Lin, R. P., Anderson, K. A., Hurley, K., and Johns, C. M. (1995). High-resolution spectra of 20–300 keV hard X-rays from the electron precipitation over Antarctica. *J. Geophys. Res.*, 100(A10):675–685.
- [Spjeldvik and Rothwell, 1985] Spjeldvik, W. N. and Rothwell, P. L. (1985). *Handbook of Geophysics and the Space Environment*, chapter 5, pages 5–1:5–55. United States Air Force.
- [Summers et al., 1998] Summers, D. R., Thorne, R. M., and Xiao, F. (1998). Relativistic theory of wave-particle resonant diffusion with application to electron acceleration in the magnetosphere. *J. Geophys. Res.*, 103:20487.

[Taylor, 1999] Taylor, G. B., editor (1999). *Synthesis Imaging in Radio Astronomy II. Collection of Lectures from the Sixth NRAO/NMIMT Synthesis Imaging Summer School*, volume 180 of *Astronomical Society of the Pacific Conference Series*. Astronomical Society of the Pacific.

[Thorne and Kennel, 1971] Thorne, R. and Kennel, C. F. (1971). Relativistic electron precipitation during magnetic storm main phase. *J. Geophys. Res.*, 76:4446.

[Thorne and Andreoli, 1980] Thorne, R. M. and Andreoli, L. J. (1980). Mechanisms for intense relativistic electron precipitation.

[Torrence and Compo, 1998] Torrence, C. and Compo, G. P. (1998). A practical guide to wavelet analysis. *Bulletin of the American Meteorological Society*, 79:61–78.

[Tsurutani, 2001] Tsurutani, B. T. (2001). The interplanetary causes of magnetic storms, substorms and geomagnetic quiet. In [Daglis, 2001a], pages 103–130.

[Van den Berg, 1999] Van den Berg, J. C. (1999). *Wavelets in Physics*. Cambridge University Press, New York, NY.

[Walt, 1996] Walt, M. (1996). Source and loss processes for radiation belt particles. In *Radiation Belts: Models and Standards*, Geophysical Monograph 97, pages 1–13, Washington, D. C. American Geophysical Union.

[Winckler et al., 1958] Winckler, J. R., Person, L., Arnoldy, R., and Hoffman, R. (1958). X-rays from visible aurora at minneapolis. *Phys. Rev.*, 110:1221.

Appendix A

Geomagnetic Activity Indices

Magnetic field measurements at many locations on Earth provide a way to monitor the currents in the magnetosphere and ionosphere. A series of useful magnetic indices have been developed over the years based on these measurements as a way of monitoring geomagnetic activity. Different indices probe different current systems, and are thus useful for different purposes. The indices used in this dissertation are briefly described below. A full description of geomagnetic activity indices and how they are calculated is given in Kivelson and Russell [1995].

A.1 Indices

AU Auroral Upper index: measures changes in the horizontal component of the earth's magnetic field due to ionospheric currents. AU is the maximum positive disturbance measured at any given magnetometer station.

AL Auroral Lower index: similar to AU but measures the minimum disturbance.

K_p planetary K index: measures the magnitude of magnetic disturbances over a three hour interval. K_p is the K index averaged over 13 standard observatories around the earth.

D_{st} Disturbance storm time index: Measures the decrease of the earth's surface magnetic field averaged over equatorial magnetometer stations around the earth. During a magnetic storm, the magnetic field is decreased due to an increase in the energy density of the ring current, thus the D_{st} index is a measure of the energy contained in the ring current.

Appendix B

Frequently Used Acronyms

ARM Angular Resolution Measure

BG0 Bismuth germanate scintillator flown on MAXIS

CGM Corrected Geomagnetic (latitude)

CXRI Coded mask X-ray imager flown on MAXIS

DMI Danish Meteorological Institute

DPU Data Processing Unit

EIC Electrostatic ion cyclotron (plasma wave)

EMIC Electromagnetic ion cyclotron (plasma wave)

FLR Field Line Resonance

GeD Germanium detector flown on MAXIS

GPS Global Positioning Satellite

GSFC Goddard Space Flight Center

IGRF International Geomagnetic Reference Field

IMF Interplanetary Magnetic Field

LANL Los Alamos National Lab

LDB Long duration balloon

LLD Low Level Discriminator

LN₂ Liquid Nitrogen

MAXIS MeV Auroral X-ray Imaging and Spectroscopy balloon experiment

MLA Minimum lever arm

MLT Magnetic local time

NSBF National Scientific Balloon Facility

PHA Pulse Height Analyzer

PMT Photomultiplier tube

PXRI Pinhole X-ray imager flown on MAXIS

REP Relativistic electron precipitation

SAMPEX Solar, Anomalous and Magnetospheric Particle Explorer (spacecraft)

SIP Science instrument package

T89 Tsyganenko 1989 (magnetic field model)

ULF Ultra Low Frequency

UT Universal Time